12-2009

# SYNTHESIS AND DEVELOPMENT OF NOVEL FULLERENE-BASED STRUCTURES FOR PHOTOVOLTAICS, ELECTRONIC APPLICATIONS AND MRI CONTRAST AGENTS

Manuel Chaur
*Clemson University*, manuelc@clemson.edu

# SYNTHESIS AND DEVELOPMENT OF NOVEL FULLERENE-BASED STRUCTURES FOR PHOTOVOLTAICS, ELECTRONIC APPLICATIONS AND MRI CONTRAST AGENTS

---

A Dissertation
Presented to
the Graduate School of
Clemson University

---

In Partial Fulfillment
of the Requirements for the Degree
Doctor of Philosophy
Chemistry

---

by
Manuel N. Chaur
December 2009

---

Accepted by:
Dr. Luis Echegoyen, Committee Chair
Dr. Steven J. Stuart
Dr. William Pennington
Dr. Rhett C. Smith

## ABSTRACT

Metallic nitride endohedral metallofullerenes (EMFs) are one of the most interesting types of metallofullerenes due to their high yields and interesting electronic properties. The synthesis of these compounds allows the encapsulation of different metals inside fullerenes making it possible to combine the properties of the metal with those of the fullerene. Their interesting electrochemical and optical features make them potential candidates for several applications such as molecular electronics, biomedical imaging, non-linear optical devices, and magnetic resonance imaging (MRI) agents. This thesis reports the synthesis of novel metallic nitride EMFs based on Gd, Nd, Pr, Ce and La. These families of metallofullerenes were characterized by different techniques such as X-ray diffraction, MALDI-TOF mass spectrometry, HPLC, electrochemistry and UV/Vis-NIR spectroscopy. The reactivity study of the Gd nitride EMF family and the synthesis of a third generation dendrimer that is attached to EMFs in order to obtain water soluble structures that can be used in MRI applications is also covered. Finally, a comprehensive electrochemical study of carbon rich macrocycles is reported.

# DEDICATION

I dedicate this work and every accomplishment of my life to my father Mr. Aldemar Chaur and my mother Mrs. Gloria Valencia, I am blessed for being their son.

To my wife Ana Maria and my son Sebastian, they are my happiness and the owners of my heart.

ACKNOWLEDGMENTS

I want to deeply thank my advisor Professor Echegoyen for all his guidance during my time in his laboratory. It was a pleasure to work for him and I am very thankful that he received me and offered me beautiful projects that caught my attention and made me love all the research I did during the past years at Clemson. Professor Echegoyen also helped me tremendously in getting a postdoc position; many thanks Dr. Echegoyen. I am also very thankful to professors Alan L. Balch, Josep-Maria Poblet and Rik Tykwinski, our collaborators, for the different and fruitful projects we were involved in and that make up part of this dissertation.

I would also like to thank Dr. Lourdes Echegoyen and Dr. Steven J. Stuart; they brought me here to spend a summer in 2005 for Clemson's SURP program and, honestly, it was the best summer of my life. Thanks to them I came back for graduate school and I have always received their support and guidance. I owe them much gratitude.

I would like to thank my parents, Aldemar Chaur and Gloria Valencia, because they strongly encouraged me to go to school and even though the economic situation in my family was not the most convenient they both spared no expense in raising my brother, my sister, and me with education, honesty and hard work values that are the most valuable legacy that a son can ever receive. I am very grateful to my wife Ana Maria and her unconditional love and support. She was always with me through this long journey; she and my son are everything to me. I am thankful to my sister, my brother, and my aunt for all their support in the hard times as well as my grandmother Enelia Vargas who has always been like a mother to me.

I am very grateful to all the people in Prof. Echegoyen's lab, especially Dr. Frederic Melin, it was a very productive and enjoyable time working with him, Dr. Bevan Elliott and Dr. Amit Palkar and all the people who have been in our lab, these include Marta, Claudia, Drew, Tianming, Rachana, Ning, Fang-Fang, Carla, Angy, Julio, Adrian and Cheryl. I am very thankful to my friends Martin, Anshuman, Angy, Susan and all those who have given me their friendship and helped me tremendously the many times I needed it, many thanks guys, you made this time even more enjoyable.

Finally I would like to thank my committee members Prof. Dr. Stuart, Prof. Dr. Pennington and Prof. Dr. Smith for the help and time they spent during the achievement of this dissertation.

TABLE OF CONTENTS

Table of Contents (Continued)

Page

LIST OF TABLES

List of Tables (Continued)

Table Page

LIST OF FIGURES

List of Figures (Continued)

Figure Page

List of Figures (Continued)

Figure Page

List of Figures (Continued)

Figure Page

List of Figures (Continued)

Figure Page

List of Figures (Continued)

Figure Page

List of Figures (Continued)

Figure Page

List of Figures (Continued)

Figure Page

List of Figures (Continued)

Figure Page

List of Figures (Continued)

Figure Page

List of Figures (Continued)

Figure Page

List of Figures (Continued)

Figure Page

CHAPTER ONE

# INTRODUCTION

Since the early stages of fullerene research it was shown that fullerenes in general were able to host atoms and even small molecules in their interior.[1] Lanthanum was the first metal successfully encapsulated inside carbon cages and other atoms have been also trapped, including those from groups II and III, all the lanthanides as well as their corresponding metallic nitride clusters, metal carbides, noble gases, phosphorous, nitrogen and even metal oxides.[3-13] The search for the encapsulation of metals, metallic clusters and small molecules inside fullerenes has been driven not only by curiosity but also because endohedral metallofullerenes (EMFs) are novel carbon-based materials offering a broad range of properties of potential use in different fields such as materials science and medicine. For instance gadolinium based EMFs have been widely studied due to their magnetic contrast-enhancing properties and thus potential applications in magnetic resonance imaging (MRI).[8, 14-15] The highly paramagnetic and radioactive character of some EMFs enables them to have potential applications in medicine.[16-19] On the other hand their low HOMO-LUMO gaps as well as their electronic properties can be exploited in molecular electronics and electron donor/acceptor systems.[6,8,20-26]

As noted from the beginning of metallofullerene research, EMFs exhibit interesting and intriguing electronic properties that can be explained by an electron transfer process from the encapsulated moiety to the carbon cage.[2-9, 27] This electron donation makes possible the encapsulation of very unstable moieties that have never been independently isolated. It is well known that fullerenes tend to follow the Isolated

Pentagon Rule (IPR) which states that fullerenes with adjacent pentagons have higher formation energy than those with isolated pentagons.[28] While no exception to this rule has ever been reported for empty fullerenes, it turns out that this rule becomes more of a suggestion when considering EMFs, because several non-IPR carbon cages encapsulating metallic moieties have been prepared and characterized.[29]

The chemical functionalization of EMFs is a key step for the development of these compounds for potential applications.[29] The first EMF derivative was reported in 1995 by Akasaka and co-workers where La@$C_{82}$ was photochemically induced to react with disilirane.[30a] Besides photochemical reactions other types of reactions have been reported, among them Diels-Alder, 1,3-dipolar cycloadditions, Bingel-Hirsh, free radical, and other addition reactions.[29] Exohedral functionalization of EMFs has provided the opportunity of characterizing different metallofullerenes due to the fact that functionalized EMFs are relatively easier to crystallize than their unfunctionalized precursors.[29] Also the addition of polar groups that render EMFs soluble has made it possible to study their properties in biological systems.[14-19]

In this chapter we will discuss the synthesis of EMFs, especially the synthesis of metallic nitride EMFs, and their purification and characterization prior to 2007. Then we will discuss some applications of these compounds and conclude with a brief summary and outlook of the field.

## Synthesis and Purification of EMFs

The first proposal of an endohedral metallofullerene was given days after the discovery of [60]fullerene ($C_{60}$) by Kroto and coworkers.[30] The same authors found a

series of $C_n^+$ and $LaC_n^+$ ions in the mass spectrum of a sample prepared by the vaporization of graphite rods impregnated with $LaCl_2$.[1] However the mass production of $C_{60}$ and EMFs was not accomplished until 1990, when Krätschmer and co-workers successfully synthesized $C_{60}$ by resistive heating of graphite rods under a helium atmosphere.[31] Since then, many methods for the production of EMFs have been reported.[2-9] The most common method is the modified arc-discharged Krätschmer-Huffman reactor (Figure 1.1). In this synthesis process graphite rods are packed with the desired metal oxide (or a combination of metal oxides if mixed EMFs are wanted), then the packed rods are annealed for several hours before finally being burned in the presence of He or Ar.[2-9]

In the synthesis of metallic nitride (MN) EMFs, a nitrogen source is added, commonly, nitrogen or ammonia.[29] The first synthesis method was serendipitously discovered by Dorn and co-workers when they reported the Trimetallic Nitride Template (TNT) method for the synthesis of the first metallic nitride EMF, $Sc_3N@C_{80}$ in 1999.[29] The second method for the synthesis of MN EMFs is the "reactive gas atmosphere" method introduced by Dunsch and co-workers, where ammonia is used as a reactive gas. With this method for the first time MN EMFs were synthesized almost exclusively with less than 5% of empty fullerenes.[29] Other synthetic methods include the use of solid sources of nitrogen but these methods afford lower yields of EMFs and are not reproducible.[7-9] Figure 1.1(top) shows a simple sketch of an arcing reactor for the synthesis of EMFs and a picture (bottom) of the arc-reactor used for the production of

MN EMFs. More sophisticated arc reactors have enabled anaerobic collection and sampling methods.

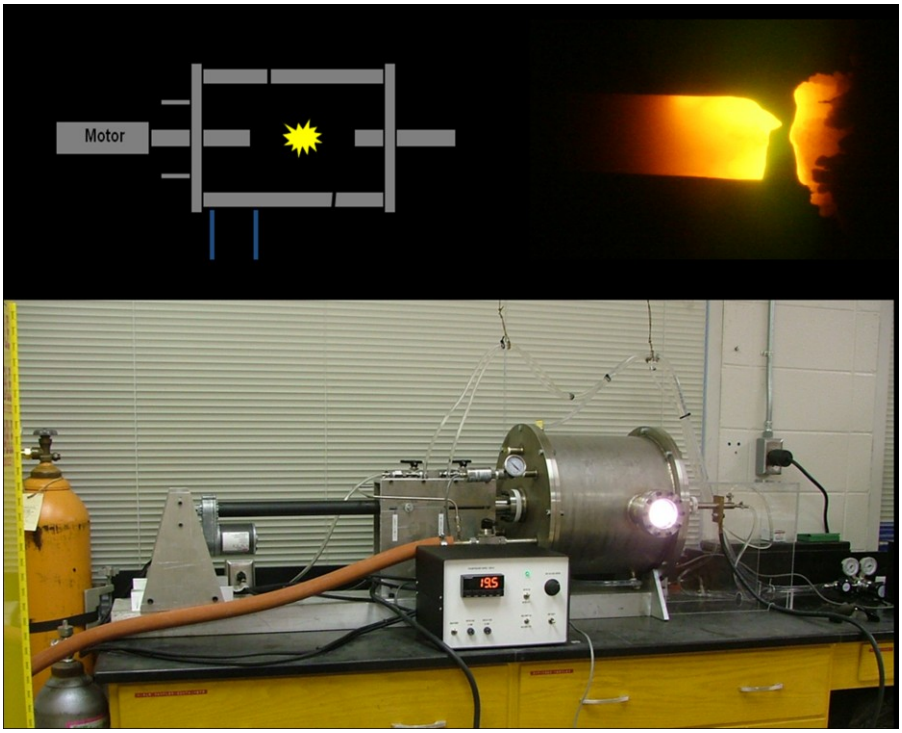


**Figure 1.1**. Schematic drawing of the arc-discharge reactor for the production EMFs (top) and a picture of the reactor used in our laboratory for the synthesis of MN EMFs (bottom).

## Families of EMFs

The synthesis process of EMFs allows the formation of different types of endohedral compounds such as:

- Classical EMFs ($M@C_{2n}$ and $M_2@C_{2n}$, M=metal and $60 \leq 2n \leq 88$)
- Metal Carbide EMFs ($M_2C_2@C_{2n}$ and $M_3C_2@C_{2n}$, M=metal and $68 \leq 2n \leq 104$)
- Metallic Nitride EMFs ($M_3N@C_{2n}$, M=metal and $68 \leq 2n \leq 96$)
- Metal Oxides EMFs $M_4O_2@C_{80}$

The symmetry and structures of most of these EMFs have been successfully characterized mainly by NMR spectroscopy and X-ray diffraction. The latter is especially essential when characterizing EMFs with paramagnetic metals/clusters. In the case of the metallofullerenes for which no X-ray analysis is available, IR and Raman spectroscopy supported by Density Functional Theory (DFT) calculations have provided valuable information about symmetries and structures of many EMFs, some of them have been later confirmed by X-ray.[2,7-8] Other characterization tools include electrochemistry, UV-vis-NIR spectroscopy and electron paramagnetic resonance (EPR), which have contributed to the understanding of the electronic properties of EMFs.[2]

**Classical EMFs**

As mentioned before, Kroto and co-workers proposed for the first time the existence of an endohedral metallofullerene in 1985,[1] but it was not until 1995 that the first structural characterization of an EMF by synchrotron powder X-ray diffraction (XRD) and the maximum entropy method (MEM)/Rietveld analysis was reported.[32] Since then many EMFs with up to four encapsulated metals have been isolated and characterized by mass spectrometry (MS), UV/Vis-NIR, cyclic voltammetry (CV), electron energy-loss spectroscopy, Electron Paramagnetic Resonance (EPR) spectroscopy, DFT calculations, Nuclear Magnetic Resonance (NMR), XRD measurements and some other characterization techniques.[2-8]

As reviewed before,[2-6] the most abundant classical EMF family is the M@$C_{82}$, the first example being La@$C_{82}$, followed by Y@$C_{82}$, Sc@$C_{82}$ and encapsulated lanthanides inside $C_{82}$.[2-6]

**Metal Carbide EMFs**

Metal carbide EMFs are a special type of fullerenes that encapsulate in their interior a metal carbide moiety (see Figure 1.2). The first structural characterization of a metal carbide EMF was reported in 2001 by Shinohara et al.[33] Both $^{13}C$ NMR and synchrotron X-ray structural analyses were used to determine the endohedral character of the $Sc_2C_2$ unit inside the $C_{84}$ [$D_{2d}$] (inside square brackets are the cage isomer labels) carbon cage.[33] The same metallofullerene had been isolated previously by the same group but erroneously they assigned it to $Sc_2@C_{86}$ (Isomer I).[97] In a similar way theoretical calculations, $^{13}C$ NMR and refined X-ray analyses have revealed in the past years other metal carbide EMFs such as $Y_2C_2@C_{82}$ (isomers [$C_s$], [$C_{2v}$] and [$C_{3v}$]), $Ti_2C_2@C_{78}$ [$D_{3h}$], $Sc_2C_2@C_{68}$ [$C_{2v}$], $Sc_2C_2@C_{82}$ [$C_{3v}$], $Sc_3C_2@C_{80}$ [$I_h$], and $Gd_2C_2@C_{92}$ [$D_3$].[36-37, 98-106] Interestingly, among all of these EMFs, only $Sc_2C_2@C_{68}$ [$C_{2v}$] was found to have a non-IPR carbon cage.[29]

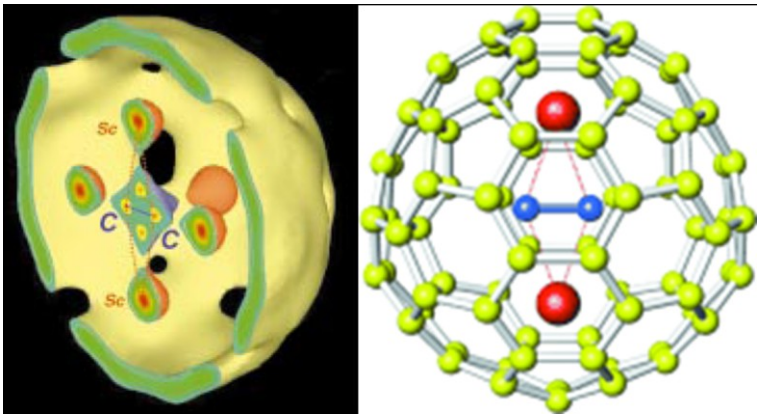


**Figure 1.2**. Left) Half section of the equicontour (1.9 e $Å^{-3}$) surface of the MEM charge density for $Sc_2C_2@C_{84}$. Right) Representation of $Sc_2C_2@C_{84}$ based on XRD and $^{13}C$ NMR spectroscopy.

Crystallographic data together with calculations have strongly suggested that the metal carbide unit is more stable in the bent geometry. In this conformation the carbon-carbon bond distance in $Sc_2C_2@C_{82}$ [$C_{3v}$] was measured to be 0.127 nm, corresponding to two carbons bonded by a triple bond.[29] Using $^{13}C$-enriched samples Nagase reported the chemical shifts of several metal carbide EMFs.[107] The chemical shifts of the $C_2$ unit were found at δ=249.2, 253.2 and 328.3 ppm for $Sc_2C_2@C_{84}$ [$D_{2d}$], $Sc_2C_2@C_{82}$ [$C_{3v}$], and $[Sc_3C_2@C_{80}]^-$ [$I_h$] respectively. Such low field resonances were explained by the presence of the two $Sc^{3+}$ cations and the dianion character of the $C_2$ unit.

A special type of metal carbide EMF is $Sc_3C_2@C_{80}$ [29] being the first and only metal carbide EMF isolated to date with three metals in the endohedral cluster. When first reported in 1994 this EMF presented a well resolved equally spaced 22 hyperfine splitting due to the equivalency of the three Sc metals inside the carbon cage.[29] In 2005 Nagase et al. reported the chemical functionalization of this EMF and found that it was actually a metal carbide. [29]

The electronic structure of metal carbide EMFs such as $M_2C_2@C_{82}$ was studied by Poblet and co-workers.[29] In this report Poblet proposed that empty cages with a large (LUMO+3)-(LUMO+2) gap are more suitable to encapsulate the $M_2C_2$ moiety because of the stabilization obtained by the formal transfer of four electrons from the cluster to the LUMO+1 and LUMO+2 of the carbon cage. This methodology suggested that isomer **85** with $D_3$ symmetry of the $C_{92}$ empty fullerene would be energetically more favored to host the $M_2C_2$ cluster, and this was confirmed experimentally for $Gd_2C_2@C_{92}$ [$D_3$].[26]

**Metallic Nitride EMFs**

Undoubtedly, these relatively new compounds, discovered only ten years ago, are among the most interesting EMFs. The reasonably high yield of $Sc_3N@C_{80}$, reported by Dorn and co-workers [29] emphasized the stabilization provided by the electron transfer between the internal cluster and the carbon cage. Neither the metallic nitride cluster nor the $C_{80}$ [$I_h$]carbon cage have been prepared independently but together they form a very stable compound, which can be obtained in even higher yields than the empty $C_{84}$ carbon cage, which was considered until that moment as the third most abundant fullerene obtained during the arcing process.[29] The large increase in stability from the charge transfer makes $Sc_3N@C_{80}$ the most thermodynamically, and thus, chemically stable of all the fullerenes, empty or filled. In fact, in the arc synthesis of this molecule, it is formed by far in the largest yield of any fullerene, excluding $C_{60}$ and $C_{70}$. The synthesis of scandium nitride EMFs also allows the formation of carbon cages with smaller size such as $Sc_3N@C_{68}$ and $Sc_3N@C_{78}$ as well as the two isomers of $Sc_3N@C_{80}$, the [$I_h$] symmetric one, which is the major product and the [$D_{5h}$]. [7-9, 29]

Experimentally and theoretically it has been shown that the metallic nitride cluster donates 6 electrons to the carbon cage. Poblet and co-workers rationalized the formation of $Sc_3N@C_{68}$, $Sc_3N@C_{78}$ and $Sc_3N@C_{80}$ on this basis. Based on this electron transfer they demonstrated that only certain carbon cage isomers have the most favored molecular orbital distribution to accommodate the cluster electrons.[29] Based on this ionic model possible host cages for metallic nitride clusters were also predicted by generalizing a rule of stabilization that states that only fullerenes with large enough (LUMO+3)-(LUMO+4)

gap would be suitable to accommodate the metallic nitride cluster. Dunsch and Popov extensively analysed the structures of larger metallic nitride EMFs based on the stability of fullerenes in their hexaanionic state, and by this methodology they were able to predict the symmetry of metallic nitride EMFs that were later confirmed experimentally.[29]

Certainly the discovery of these large endohedral cluster fullerenes has caused a significant shift in fullerene research since 1999. Due to its availability and the interest in its novel chemical and electronic properties, the $M_3N@C_{2n}$ families have received by far the most attention of any class of endohedral fullerene compounds.

Metallic nitride EMFs have been prepared with metals from group III and lanthanides either as homogenous metallic nitride EMFs or as mixed metallic nitride EMFs, and in all these families a wide cage-size distribution is usually observed, from $C_{68}$ to $C_{104}$.[7-9, 29] Because of its very low ionic radius scandium forms a small cluster nitride that fits perfectly inside the $C_{80}$ [$I_h$] cage, and this favourable fit along with the stabilization resulting from the electron transfer from the cluster to the carbon cage make $Sc_3N@C_{80}$ the most abundant EMF prepared so far.[7-9, 29] When the ionic radius of the metal is increased the yield of EMFs is considerably decreased while the $C_{80}$ cage is still favored. As will be shown later, the work reported in this thesis shows the first examples of larger cages templated preferentially by larger metals.

The structural, electrochemical and chemical properties of metallic nitrides EMFs of general formula $M_3N@C_{80}$ have been extensively studied and as of 2007, nothing was known about larger fullerene cages encapsulating a metallic nitride moiety.

**Metal Oxide EMFs**

Stevenson and co-workers recently reported the synthesis of an EMF encapsulating a metal oxide cluster consisting of 6 atoms, $Sc_4(\mu_3\text{-}O)_2@C_{80}$ [$I_h$] by vaporizing graphite rods packed with scandium oxide in the presence of helium and a small amount of air. The yield of this compound was considerably increased by the addition of copper nitrate in the packed rods. High resolution mass spectrometry revealed the presence of two other metal oxide EMFs with general formula $C_{80}O_2Sc_4$ and $C_{80}O_3Sc_4$. Figure 1.3 shows the structure of $Sc_4(\mu_3\text{-}O)_2@C_{80}$ [$I_h$] complexed with a nickel octaethylporphyrin $Ni^{II}$(OEP)obtained from crystallographic data.[10]

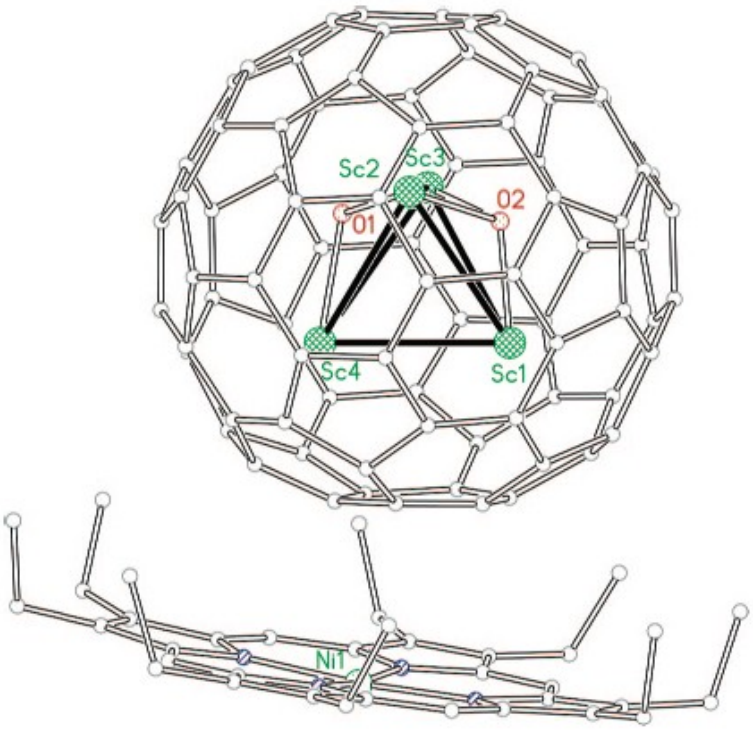


**Figure 1.3**. A drawing of $Sc_4(\mu_3\text{-}O)_2@C_{80}$ [$I_h$] $Ni^{II}$(OEP) $2C_6H_6$. Reproduced with permission from reference 10. Copyright 2008 American Chemical Society.

## Violations of the IPR with EMFs

Fullerene structures normally conform to the IPR due to the fact that violations result in higher strain energy. For this reason the five-membered rings should be surrounded by six-membered rings,[28] however, the encapsulation of metals and metallic clusters have made possible the synthesis of non-IPR EMFs. The first reports of EMFs with carbon cages containing fused pentagon systems were those of $Sc_2@C_{66}$ and $Sc_3N@C_{68}$ [$D_3$(6140)].[29] Other examples are $Sc_2C_2@C_{68}$ [$C_{2v}$(6073)], $Sc_3N@C_{70}$ [$C_{2v}$(7854)], $La_2@C_{72}$ [$D_2$(10611)], $La@C_{72}$, and $DySc_2N@C_{76}$ [$C_s$(17490)]. On the other hand, spectroscopy along with DFT calculations strongly suggested that the major isomer of $Dy_3N@C_{78}$ and $Tm_3N@C_{78}$ both have the non IPR carbon cage of symmetry $C_2$:22010[122] and that $Ce_2@C_{72}$ possesses a non-IPR carbon cage of $D_2$ symmetry as in the case of $La_2@C_{72}$ .[29]

Crystallographic data together with theoretical calculations have shown that there is a strong interaction between the encapsulated metal(s) and the fused pentagon system. The electronic donation of the metal or metallic cluster is localized mainly in the fused pentagon system making it more aromatic in character and therefore more stable. Akasaka and co-workers have studied the chemical reactivity of $La_2@C_{72}$ and demonstrated that the C-C bonds of the fused pentagon system adjacent to the [5,5] bond hold higher electron density than other C-C bonds of the fullerene cage, while the [5,5] bond itself has the lowest electron density.[34b] Figure 1.4 shows the HOMO/LUMO distributions of $La_2@C_{72}$, from these orbital distributions it is observed that the HOMO is mainly localized on the carbon cage but it does not contain the two [5,5] bonds

corresponding to each fused pentagon system. The LUMO, on the other hand, contains the two La atoms and the two [5,5] bonds . These features of the fused pentagon system can be used to understand the reactivity of non-IPR EMFs as described by Akasaka and co-workers.[34b-c]

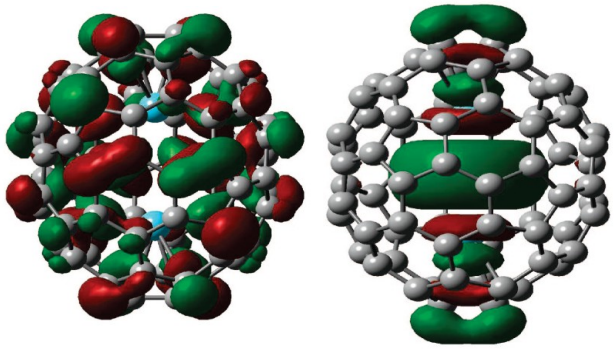

**Figure 1.4**. Scheme of the HOMO (left) and LUMO (right) of $La_2@C_{72}$. Reproduced with permission from reference 34b. Copyright 2008 American Chemical Society.

**Purification of EMFs**

Separation of isomers and different cage-sized EMFs has traditionally been accomplished by High Performance Liquid Chromatography (HPLC) using columns specific for fullerenes such as Buckyprep, Buckyprep-M, Buckyclutcher, PBB and PYE. Linear combinations of these columns, multistep separations or recycling HPLC chromatography allow the isolation of different EMF isomers.[2-9] Figure 1.5 shows some common chromatographic stationary phases used in HPLC columns for the separation of EMFs. Although over the years HPLC has been the most powerful technique to separate EMFs, this separation process is usually time consuming and expensive. The main reason for this is that empty cages such as $C_{60}$ and $C_{70}$ are usually two orders of magnitude more abundant than EMFs in the extracts from the raw soot. On the other hand, mixtures of

isomers usually have very similar retention times thus requiring longer separation times. Consequently it is necessary to use multistep chromatographic separations. So efforts to avoid HPLC as much as possible have been made by several groups and will continue in the future.[29]

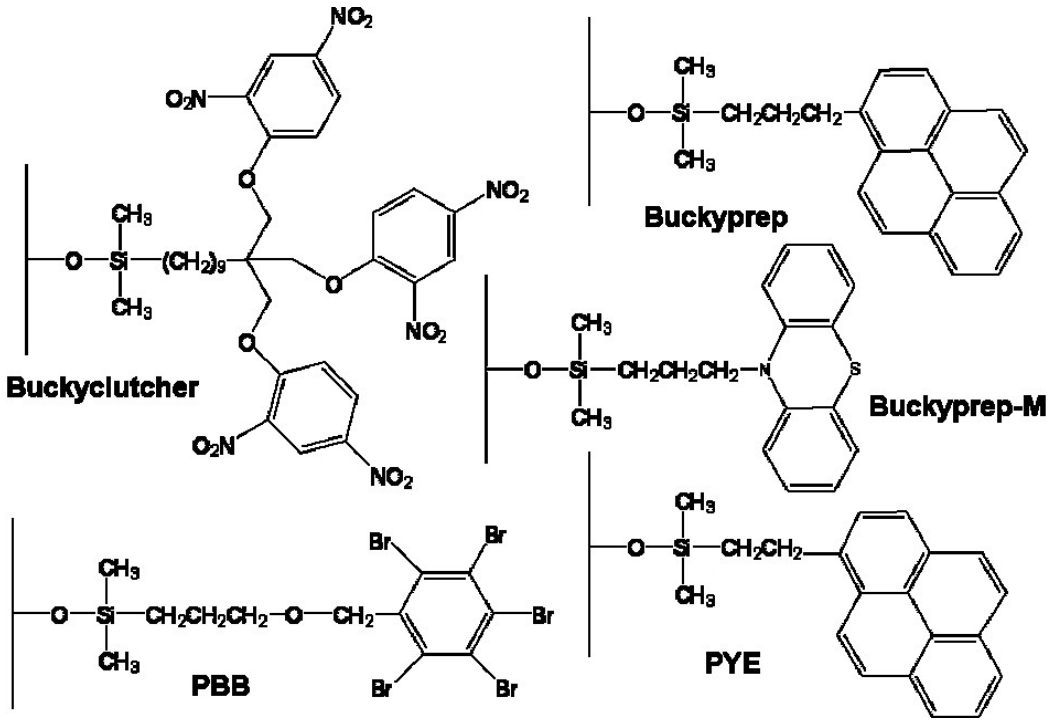


**Figure 1.5**. Some common chromatographic stationary phases used in HPLC column for the separation of EMFs.

### Chemical Functionalization of EMFs

After the synthesis and isolation of EMFs, their chemical functionalization has been the main focus of many researchers for two important reasons. First, to improve the characterization of those compounds that could not be isolated or studied by spectroscopy and X-ray crystallography. The second reason is to generate materials that are easy to process for multiple potential applications such as in optics, molecular electronics and

medicine. This section will focus on the different exohedral modifications of EMFs, beginning with the first functionalized La@$C_{82}$ derivative reported in 1995 by Akasaka and co-workers [35a] and reviewing the different types of reactions reported to date such as Diels-Alder reactions, 1,3-dipolar cycloadditions, Bingel-Hirsh reactions, photochemical reactions, free radical reactions and some other addition reactions.

Even though the aforementioned reactions have given insight into the chemical properties of EMFs, a complete study of the structure-reactivity relationships of EMFs is still lacking. Generally, EMFs seem to be quite reactive to organic functionalization, giving rise to multiple adducts or to a high number of mono-adduct regioisomers. However, a remarkable regioselectivity has been observed in a few cases for both mono and bis-adducts, depending on the nature of the encapsulated metal(s), or metallic cluster. The isolation of the obtained isomers is never an easy task, especially in the case of multi-adducts, making it difficult to study their properties and highlighting the need a regioselective functionalization protocol.

A significant number of studies have dealt with the [$I_h$] isomer of the $C_{80}$ carbon cage. Due to the high symmetry of this carbon cage, only two possible [1,2] addition sites (i.e. involving two adjacent carbons) are available (Figure 1.6): the double bonds located at a junction between a 5-membered ring and a 6-membered ring (defined as [5,6]) and the double bonds located at a junction between two 6-membered rings (defined as [6,6]). [1,4] additions (e.i, involving two opposite carbons of a 6-membered ring) have also been reported. Lower symmetry IPR carbon cages have multiple addition sites, either of

the [5,6] or [6,6] types, and therefore, after functionalization a mixture of several mono-adducts that are hard to isolate and characterize is usually obtained.

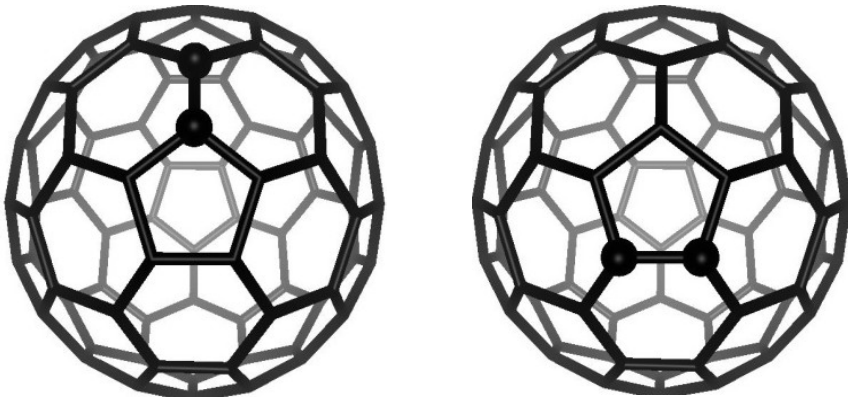

**Figure 1.6**. Possible [1,2] addition sites on the $I_h$-$C_{80}$ carbon cage: the [6,6] ring junction (left) and the [5,6] ring junction (right).

**Electrochemistry of EMFs and their derivatives**

Electrochemical methods provide very valuable information about the interaction between the entrapped species and the carbon cages in these special supramolecular structures. Fortunately, the high sensitivity of these methods is well adapted to the microgram quantities in which these materials are sometimes available. When coupled to EPR spectroscopy, electrochemistry also allows the determination of HOMO and LUMO levels and localization on the entrapped moieties, on the cage, or on both. Finally, electrochemistry has also proved to be a faster and cheaper alternative to conventional chromatographic methods for purification of some of these compounds.[29]

**Potential applications of EMFs**

The rich electronic properties of these materials offer very promising applications which have just started to be exploited. Electrochemistry has shown that the HOMO-

LUMO gap of these materials is highly dependent on the nature of the entrapped moiety, the size and symmetry of the cage and on exohedral derivatization, and therefore can by finely tuned. This is obviously an asset for potential molecular electronic applications. On the other hand, the relative inertness of the carbon cage could lead to medical applications for some EMFs with highly paramagnetic or radioactive entrapped species. We are reporting here the most recent advances of potential uses of EMFs in electric or electro-optical devices and in medicine.

**EMFs for molecular electronics and photonics**

Aside from the large range of HOMO-LUMO gaps exhibited by these compounds, some show very interesting electronic and electro-optical properties which have widened their potential applications. Only a few reports of the full incorporation of endohedral metallofullerenes in nanoelectronic devices have been published so far.

Fullerenes, in particular higher order ones ($C_{70}$ and above) usually show large non linear optical (NLO) responses, due to their highly polarizable π-electron cloud. In metallofullerenes, the charge transfer between the encapsulated moiety and the cage leads to an even larger π-electron density on the cage, and therefore these compounds are expected to show even better NLO properties. These properties have been measured or calculated with DFT for some metallofullerenes.[29] Encapsulation of one metal seems to effectively enhance NLO properties of fullerenes such as $C_{74}$ and $C_{82}$.[29] The size of the metal encapsulated is an important factor, and large metals, such as La, are preferable to smaller ones like Sc.[29] Interestingly and quite unfortunately, the encapsulation of a second metal leads to a weaker NLO response than that of the empty cage.[29]

Yang et al. showed that the photocurrent efficiency of a device based on a poly(3-hexylthiophene) film can be enhanced by doping with EMF Dy@$C_{82}$.[20] This effect was attributed to a facile photoinduced electron transfer between the film and the EMF. In a ferrocene adduct of $Sc_3N@C_{80}$ [$I_h$], recently reported by Echegoyen et al.[21] photoinduced electron transfer between the ferrocene moiety and the fullerene was detected, and the radical ion pair obtained was significantly stabilized relative to a similar ferrocene-$C_{60}$ dyad. Therefore, the contribution of metallofullerenes to the field of photovoltaics seems even more promising than that of the more conventional fullerenes.

Some films of EMFs were shown to have semiconductive properties, depending on the number of functional groups on the carbon sphere and the temperature, as demonstrated recently with the Gd@$C_{82}(OH)_x$ compounds.[22] The n-type field effect transistor (FET) behavior of thin films of $La_2@C_{80}$ has been known since 2003,[29] and some very recent calculations suggest that it may function as a single molecule transistor.[151b] Several factors influencing the efficiency of a EM-based nanotransistor were predicted, such as the nature and geometry of the endohedral-metal nanojunction and the total charge present in the system.

These properties can be further modified by incorporation of EMFs into carbon nanotubes to form so-called "peapods". In these, the EMFs modulate the bandgap of the nanotubes. Both classical[23-25] and nonclassical[6-7, 26] metallofullerenes have been inserted in carbon nanotubes, leading to a modulation of the bandgap by up to 0.5 eV in the case of Gd@$C_{82}$, resulting from a combination of elastic strain and charge transfer between the metallofullerene and the nanotube. FETransistor circuits based on Gd@$C_{82}$

peapods were designed and an ambipolar behavior with both p- and n-type characteristics was observed.[23] This interesting behavior is directly related to the unique properties of $Gd@C_{82}$ since it was not observed in the case of $C_{60}$ peapods.

**Application of EMFs in medicine**

The advantages of using endohedrals as contrast agents in magnetic resonance imaging (MRI) are now well recognized and have been reviewed several times.[8, 14] Their ability to reduce the spin relaxation time of water protons, quantified by their substantial relaxivity factors ($R_1$), is better than the currently used Gd(III) chelates.[29] (see Table 1.1 and Figure 1.7). In addition, their surface can be derivatized as much as needed and the presence of the carbon cage prevents the release of toxic Gd in organisms. Most of the studies involve classical EMFs, such as the derivatives of $Gd@C_{2n}$,[14-16, 18-19, 29] but most recent reports also involve non-classical EMFs, such as the derivatives of $Gd_3N@C_{2n}$.[29]

**Table 1.1**. R1 relaxivities (effect on the inverse of relaxation time T1) of some Gd classical and non classical endohedral fullerenes; comparison with a Gd chelate compound currently used as a MRI contrast agent (Gd-DTPA) (inside brackets is given the magnetic field used for the measurements).

| Compound | $R_1$ relaxivities ($mM^{-1}s^{-1}$) |
|---|---|
| $Gd@C_{60}$-$(OH)_x$ | 83.2-97.7 (1.4 T) |
| $Gd@C_{60}$-$[C(COOH)_2]_{10}$ | 15-24 (1.4 T) |
| $Gd@C_{82}$-$(OH)_{40}$ | 81 (1 T) |
| $Gd@C_{82}$-$O_6(OH)_{16}(NHCH_2CH_2COOH)_8$ | 9.1 (1.5 T) -8.1 (0.35 T) |
| $Gd@C_{82}$-$O_6(OH)_{16}(NHCH_2CH_2CO$-antiGFP$)_5$ | 12 (0.35 T) |
| $Gd_3N@C_{80}$–[DIPEG5000$(OH)_x$] | 102 (0.35 T) -143 (2.4 T) -32 (9.4 T) |
| $ScGd_2N@C_{80}$–$O_{12}(OH)_{26}$ | 20.7 (14.1 T) |
| $Sc_2GdN@C_{80}$–$O_{12}(OH)_{26}$ | 17.6 (14.1 T) |
| Gd-DTPA | 3.9 (1 T) |

The even better relaxivities of the polyethylene glycol (PEG) derivatives of $Gd_3N@C_{80}$, (i.e, $Gd_3N@C_{80}$-[DIPEG5000$(OH)_x$]) compared to those of $Gd@C_{82}$ derivatives arose not only from the higher number of gadolinium atoms inside the carbon cage but also, because the functionality of these compounds can influence the interaction between water and the endohedral paramagnetic metals and because of aggregation that occurs for these compounds.[14, 29] However the very low-yield production of $Gd_3N@C_{80}$ is a serious limitation to its commercial development. Therefore the more abundant mixed metallic nitride EMFs $Sc_xGd_{3-x}N@C_{80}$ were recently reported.[29] Even if their relaxivities are lower than that of $Gd_3N@C_{80}$, these compounds are still potentially useful when compared to the commercially available Gd(III) chelates (see table 1.1). Another interest of the mixed MN EMFs is that they could lead to multifunctional contrast agents for X-Ray and MRI.[29] Gd is good for MRI, and Gd, Lu and Ho provide good X-Ray contrast, hence the idea to mix these metals inside the same $C_{80}$ cage seems very attractive. The recent synthesis of new trimetallic nitride EMFs, with larger cages, and other paramagnetic metals such as Nd, Pr and Ce should lead to an even greater number of compounds suitable for medical imaging. Finally, a very interesting article recently reported that the coupling of $Gd@C_{82}$ -$O_6(OH)_{16}(NHCH_2CH_2COOH)_8$ to the antibody of the green fluorescent protein (anti-GFP)[29] resulted in higher relaxivity efficiencies (see table 1.1). The future coupling of gadolinium endohedral fullerides to tumor antibodies could therefore facilitate the early diagnosis of tumors.

The therapeutic use of water soluble EMFs, which has been considered for a long time,[15] could become a reality with the recent report of their reacting oxygen species

(ROS) scavenging effect.[29] $Gd@C_{82}(OH)_{22}$ showed a better capacity than $C_{60}(OH)_{22}$ and $C_{60}(C(COOH)_2)_2$ for scavenging superoxide radical anion ($O_2^{\cdot-}$), hydroxyl radical ($HO^{\cdot}$) and singlet oxygen, presumably due to the higher electron affinity of $Gd@C_{82}$ compared to $C_{60}$. As these reactive oxygen species are the mediators of oxidative stress, which is linked to diseases as varied as cancer, HIV, athereosclerosis… the therapeutic potential of EMFs looks very promising. Additionally, EMFs could be suitable for radioimmunotherapy, since their carbon cage prevents the leakage of radionuclides in organs. Diener et al. recently reported the encapsulation of α-emitting radionuclides such as $^{212}Pb$ and $^{213}Bi$ in $C_{60}$, and the exohedral functionalization of these endohedrals.[29] Preliminary studies in mice confirmed the absence of accumulation of $^{212}Pb$ in bones.

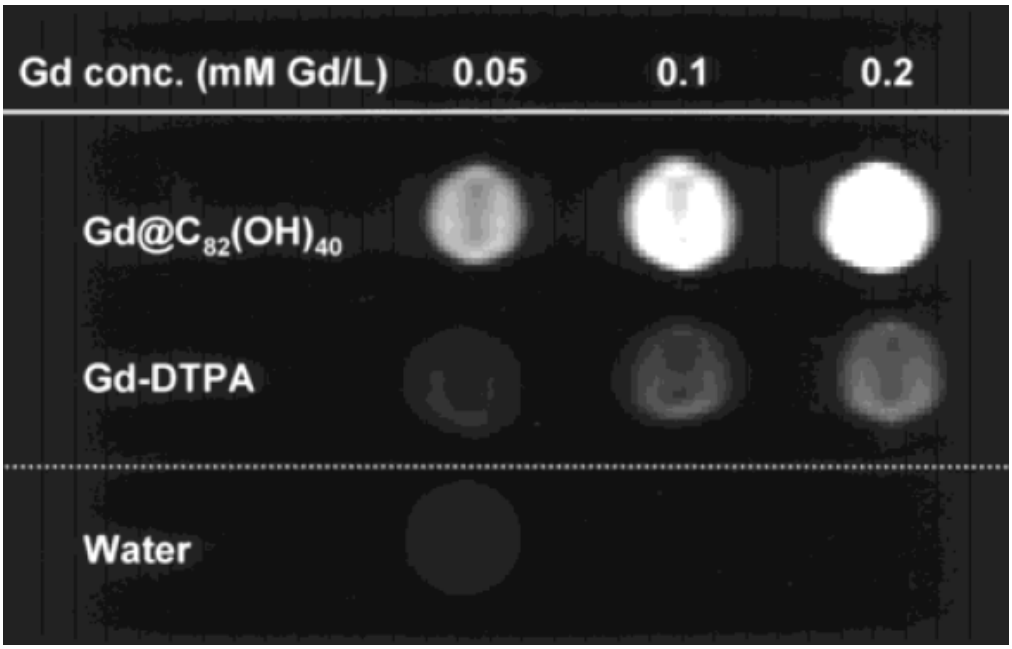


**Figure 1.7**. Enhancement of the MRI signals by $Gd@C_{82}(OH)_{40}$ compared to Gd-DTPA and water under the same conditions. Reproduced with permission from reference 16. Copyright 2001 American Chemical Society.

## Summary and Outlook

EMFs are fullerenes that encapsulate metals in their interior. These types of compounds combine the metallic properties of the incarcerated moiety with those of the fullerene host. The interaction between the metallic cluster and the carbon cage is mostly ionic since there is an electron transfer from the encapsulated moiety to the carbon cage and this electron transfer accounts for their stability and most of their electronic properties. So far, several types of EMFs have been synthesized, which include single and multiple metals (classical EMFs), metal carbides, trimetallic nitrides and metal oxide EMFs. From all these families of EMFs the trimetallic nitride is the largest family of EMFs. To date metals from group III and lanthanides have been found to form trimetallic nitride EMFs offering a broad variety of metals with properties of potential use in different fields. One of the most interesting properties of EMFs is the strong interaction between the entrapped metal(s) and the carbon cage, this interaction accounts for the formation of carbon cages that have never been isolated independently. For instance, many violations of the IPR rule have been reported for EMFs, another example is the formation of the $I_h$-$C_{80}$ that encapsulates most of the metallic nitrides.

Chemical functionalization has also revealed that EMFs are chemically different from empty cages. It seems that the metallic cluster has a considerable influence on the carbon cage, making certain bonds more reactive towards specific reactions. However, the low yields of some EMFs and the difficulty of isolating and purifying mono and bis-adducts have slowed the progress in this field. On the other hand, functionalized and non-

functionalized EMFs feature interesting electrochemical properties that expand the number of possible applications of these compounds.

Even though there are many significant contributions in the field of EMF research, there are still many questions that need to be addressed in the near future such as the influence of the metal on the carbon cage, what are the rules of stabilization of non-IPR EMFs, which other types of endohedral confinement are possible, how to selectively control the synthesis of EMFs and how to increase their yields. Clearly the EMF field remains as a fascinating, challenging and still largely unexplored arena with multiple potential applications.

## References


[1] J.R. Heath, S.C. O'Brien, Q. Zhang, Y. Liu, R.F. Curl, H.W. Kroto, F.K. Tittel, R.E. Smalley, *J. Am. Chem. Soc*. **1985**, 107, 7779-7780.

[2] H. Shinohara, *Rep. Prog. Phys*. **2000**, 63, 843-892.

[3] S. Nagase, K. Kobayashi, T. Akasaka, T. Wakahara, In Fullerenes: Chemistry, Physics and Technology (Eds. K.M. Kadish and R.S. Ruoff), John Wiley, New York (2000), Chapter 9, 396-436.

[4] S. Liu, S. Sun, *J. Organom. Chem*. **2000**, 599, 74-86.

[5] Endofullerenes: A New Family of Carbon Clusters, ed. T. Akasaka, S. Nagase. Kluwer Academic Publishers, **2002**.

[6] R. Kitaura, H. Shinohara, *Jpn. J. Appl. Phys*. **2007**, 46, 881-891.

[7] L. Dunsch, S. Yang, *Phys. Chem. Chem. Phys*. **2007**, 9, 3067-3081.

[8] L. Dunsch. S, Yang, *Small* **2007**, 3, 1298-1320.

[9] M.N. Chaur, A.J. Athans, L. Echegoyen, *Tetrahedron* **2008**, 64, 11387-11393.

[10] S. Stevenson, M.A. Mackey, M.A. Stuart, J.P. Phillips, M.L. Easterling, C.J. Chancellor, M.M. Olmstead, A.L. Balch, *J. Am. Chem. Soc*. **2008**, 130, 11844-11845.

[11] (a) M. Saunders, H.A. Jimenez-Vazquez, R.J. Cross, R.J. Poreda, *Science*, **1993**, 259, 1428-1430. (b) M.Saunders, H.A. Jimenez-Vazquez, R. J. Cross, M. Mroczkowski, M. L. Gross, D.E. Giblin, R.J. Poreda, *J. Am. Chem. Soc*. **1994**, 116, 2193-2194. (c) M.S. Syamala, R.J. Cross, M. Saunders, *J. Am. Chem. Soc*. **2002**, 124, 6216-6219.

[12] H. Mauser, A. Hirsch, N.J.R. van Eikema Hommes, T. Clark, B. Pietzak, A. Weidinger, L. Dunsch, *Angew. Chem. Int. Ed. Engl*. **1997**, 36, 2835-2838.

[13] J.A. Larsson, J.C. Greer, W. Harneit, A. Weidinger, *J. Chem. Phys*. **2002**, 116, 7849-7854.

[14] R.D. Bolskar, *Nanomedicine* **2008**, 3, 201-213.

[15] V.K. Koltover, *Prog. Fullerene Res*. **2007**, 199.

[16] M. Mikawa, H. Kato, M. Okumura, M. Narazaki, Y. Kanazawa, N. Miwa, H. Shinohara, *Bioconjugate Chem*. **2001**, 12, 510-514.

[17] H. Kato, Y. Yanazawa, M. Okumura, A. Taninaka, T. Yokawa, H. Shinohara, *J. Am. Chem. Soc*. **2003**, 125, 4391-4397.

[18] R.D. Bolskar, A.F. Benedetto, L.O. Husebo, R.E. Price, E.F. Jackson, S. Wallace, L.J. Wilson, J.M. Alford, *J. Am. Chem. Soc*. **2003**, 125, 5471-5478.

[19] S. Laus, B. Sitharaman, E. Toth, R.D. Bolskar, L. Helm, S. Asokan, M.S. Wong, L.J. Wilson, A.E. Merbach, *J. Am. Chem. Soc*. **2005**, 127, 9368-9369.

[20] S.F. Yang, L.Z. Fan, S.H. Yang, *Chem*. *Phys. Lett*. **2004**, 388, 253-258.

[21] J.R. Pinzon, M.E. Plonska-Brzezinska, C.M. Cardona, A.J. Athans, S.S. Gayathri, D.M. Guldi, M.A. Herranz, N. Martin, T. Torres, L. Echegoyen,. *Angew. Chem. Int. Ed*. **2008**, 47, 4173-4176.

[22] J. Tang, G. Xing, Y. Zhao, L. Jing, H. Yuan, F. Zhao, X. Gao, H. Qian, R. Su, K. Ibrahim, W. Chu, L. Zhang, K. Tanigaki, *J. Phys. Chem. B*. **2007**, 111, 11929-11934.

[23] J. Lee, H. Kim, S.J. Kahng, G. Kim, Y.W. Son, J. Ihm, H. Kato, Z.W. Wang, T. Okazaki, H. Shinohara, Y. Kuk, *Nature* **2002**, 415, 1005-1008.

[24] T. Okazaki, T. Shimada, K. Suenaga, Y. Ohno, T.Mizutani, J. Lee, Y. Kuk, H. Shinohara,. *Appl. Phys. Mater. Sci. Process*. **2003**, 76, 475-478.

[25] J.H. Warner, A.A.R. Watt, L. Ge, K. Porfyrakis, T. Akachi, H. Okimoto, Y. Ito, A. Ardavan, B. Montanari, J.H. Jefferson, N.M. Harrison, H. Shinohara, G.A.D. Briggs, *Nano Lett*. **2008**, 8, 1005-1010.

[26] M. Kalbac, L. Kavan, M. Zukalova, S.F. Yang, J. Cech, S. Roth, L. Dunsch, *Chem. Eur. J*. **2007**, 13, 8811-8817.

[27] Y. Chai, T. Guo, C. Jin, R.E. Haufler, L.P.F. Chibante, J. Fure, L. Wang, G.M. Alford, R.E. Smalley, *J. Phys. Chem*. **1991**, 95, 7564-7568.

[28] a) P.W. Fowler and D.E. Monolopoulos, *An Atlas of Fullerenes*, Clarendon Press, Oxford, 1995; b) K. Kobayashi, S. Nagase, M. Yoshida, E. Osawa, *J. Am. Chem. Soc*., **1997**, 119, 12693-12694.

[29] Chaur, M.N.; Melin, F.; Ortiz, A.L.; Echegoyen, L. *Angew. Chem. Int. Ed.* **2009**, 48, 7514-7538.

[30] H. Kroto, J.R. Heath, S.C. O'Brien, R.F. Curl, R.F. Smalley, *Nature* **1985**, 318, 162-163.

[31] a) W. Krätschmer, K. Fostiropoulos, D.R. Huffman. *Chem. Phys. Lett*. **1990**, 170, 167-170. b) W. Krätschmer, W. Fostiropoulos, L.D. Lamb, D.R. Huffman. *Nature* **1990**, 347, 354-358.

[32] M. Takata, B. Umeda, E. Nishibori, M. Sakata, Y. Saitot, M. Ohno, H. Shinohara. *Nature* **1995**, 377, 46-49.

[33] C.R. Wang, T. Kai, T. Tomiyama, T. Yoshida, Y. Kobayashi, E. Nishibori, M. Takata, M. Sakata, H. Shinohara, *Angew. Chem. Int. Ed*. **2001**, 40, 397-399.

[34] a) B. Cao, H. Nikawa, T. Nakahodo, T. Tsuchiya, Y. Maeda, T. Akasaka, H. Sawa, Z. Slanina, N. Mizorogi, S. Nagase, *J. Am. Chem. Soc.* **2008**, *130*, 983-989. b) X. Lu, H. Nikawa, T. Nakahodo, T. Tsuchiya, M.O. Ishitsuka, Y. Maeda, T. Akasaka, M. Toki, H. Sawa, Z. Slanina, N. Mizorogi, S. Nagase. *J. Am. Chem. Soc*. **2008**, 130, 9129-9136. c) X. Lu, H. Nikawa, T. Tsuchiya, Y. Maeda, M.O. Ishitsuka, T.

Akasaka, M. Toki, H. Sawa, Z. Slanina, N. Mizorogi, S. Nagase. *Angew. Chem. Int. Ed*. **2008**, 47, 8642-8645.

[35] a) T. Akasaka, T. Kato, K. Kobayashi, S. Nagase, K. Yamamoto, H. Funasaka, T. Takahashi, *Nature*, **1995**, *374*, 600-601; b) T. Kato, T. Akasaka, K. Kobayashi, S. Nagase, K. Kikuchi, Y. Achiba, T. Suzuki, K. Yamamoto, *J. Phys. Chem Solids*, **1997**, *158*, 1779-1783; c) M. Yamada, L. Feng, T. Wakahara, T. Tsuchiya, Y. Maeda, Y. Lian, M. Kako, T. Akasaka, T. Kato, K. Kobayashi, S. Nagase, *J. Phys. Chem. B*, **2005**, *109*, 6049-6051.

CHAPTER TWO

# SYNTHESIS, ISOLATION AND CHARACTERIZATION (STRUCUTURAL AND ELECTROCHEMICAL) OF THE GADOLINIUM NITRIDE ENDOHEDRAL METALLOFULLERENE $Gd_3N@C_{2n}$ ($78 \leq 2n \leq 88$) FAMILY

Gadolinium-based compounds are of great utility in tomographic magnetic resonance imaging (MRI) applications due to the high paramagnetic character of this lanthanide nucleus. Although there are other candidates in the lanthanide series that have high magnetic moment, the intrinsic relaxation time of the electron-spin state of the corresponding cation has to be long enough for efficient transfer of magnetic information to the bulk water. The uniqueness of $Gd^{3+}$ ion relies not only on its high magnetic moment (7.9 BM) resulting from seven unpaired f-electrons, but also on the totally symmetric electronic state ($^8S_{7/2}$ ground state), which makes the electronic relaxation time much longer than for other $Ln^{3+}$ ions, $10^{-8}$-$10^{-9}$ s.[1]

However, the main problem when using heavy metals ions like $Gd^{3+}$ in MRI applications is the significant toxicity of the "free" (aqua-ion) form. Therefore, the clinical use of $Gd^{3+}$, demands that it be bound in a complex of high stability and, even more importantly, it must show a long-term resistance to a transmetallation/transchelation loss of the $Gd^{3+}$ ion.[2] For the aforementioned reasons, Gd-based metallofullerenes are a very promising new type of MRI contrast enhancing agents, not only because of the encapsulated Gd but also because the fullerene cages offer an almost infinite stability to these compounds. This characteristic has motivated several researchers to synthesize

metallofullerenes containing trapped $Gd^{3+}$ ions. In this chapter the synthesis of the gadolinium nitride endohedral fullerenes is described as well as the isolation and the characterization of each member of this family of metallofullerenes.

## Isolation and Identification

In 2004 Stevenson and co-workers reported the synthesis and isolation of $Gd_3N@I_h$-$C_{80}$, the first metallic nitride EMF containing a cluster of three $Gd^{3+}$ ions.[3] Interestingly, the metallic nitride cluster in this EMF was not planar as other metallic nitride clusters reported before, in fact, the nitrogen atom deviated 0.522 Å away from the plane defined by the three gadolinium atoms (see Figure 2.1).[3] Later Dunsch and co-workers reported the encapsulation of the $Gd_3N$ cluster inside cages as small as $C_{80}$ and as large as $C_{88}$;[4] however, no isolation of cages larger than $C_{80}$ was reported. Even though $Gd_3N@I_h$-$C_{80}$ is the most abundant metallic nitride EMF within the Gd family it is also the lowest yielding EMF. This low yield has been largely attributed to the size of the metallic nitride cluster that does not fit well within the $C_{80}$ carbon cage, leading to pyramidalization of the cluster and an increase in the energy of formation of this compound.

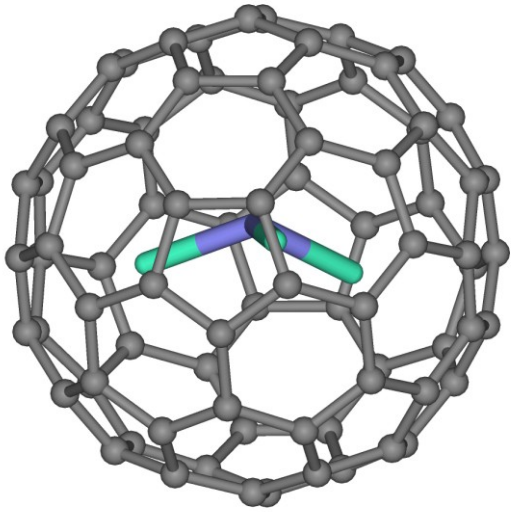

**Figure 2.1**. A drawing of $Gd_3N@I_h$-$C_{80}$ that emphasizes the pyramidal nature of the $Gd_3N$ cluster.

The synthesis of the $Gd_3N@C_{2n}$ family was accomplished by arc-burning graphite rods packed with $Gd_2O_3$, graphite powder and $Fe_xN$ (x=2-4) in a weight ratio 1:1:0.1 respectively in the presence of Helium (200 torr) and Nitrogen (20 torr) gases. Fullerenes from the collected soot were then extracted with toluene using a Soxhlet apparatus. Empty cage fullerenes were removed by passing the extracted solution through a column containing a cyclopentadiene-functionalized resin. In this procedure, first introduced by Dorn and co-workers,[5] the most reactive fullerenes react with the cyclopentadiene groups *via* Diels-Alder reaction with the resin and the less reactive fullerenes (such as metallic nitride EMFs) are eluted. Figure 2.2 shows the schematic production of the $Gd_3N@C_{2n}$ mixture.

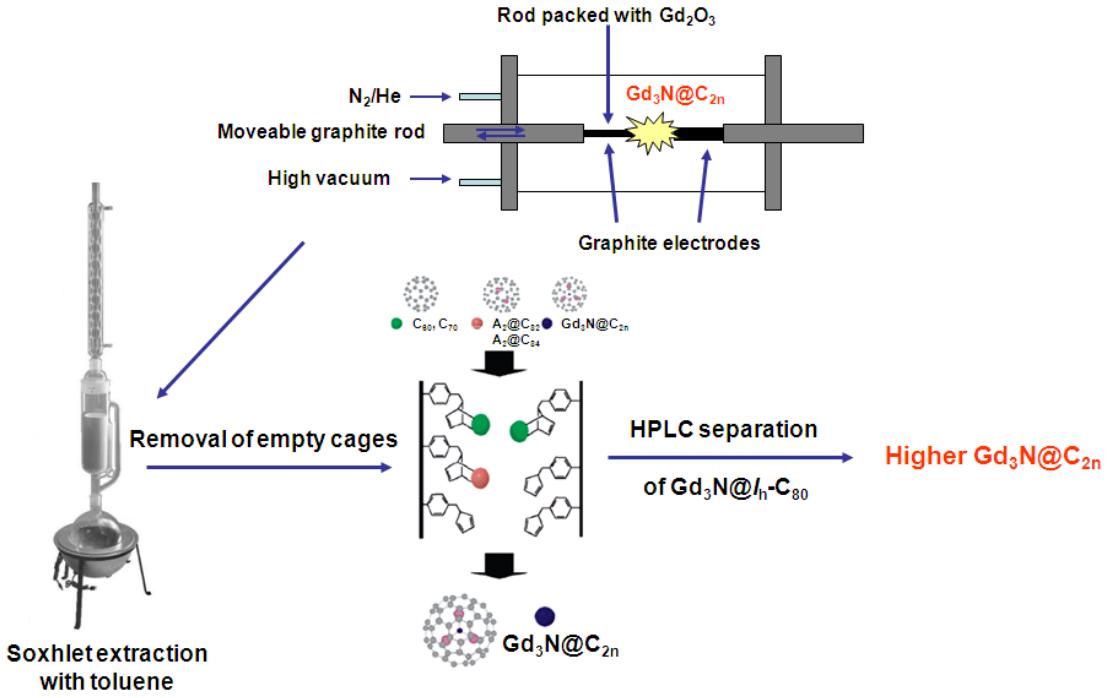


**Figure 2.2**. Schematic representation of the synthesis and purification of $Gd_3N@C_{2n}$ metallofullerenes.

A mixture of higher order metallic nitride EMFs and some $Gd_3N@C_{80}$ were separated from pure $Gd_3N@I_h$-$C_{80}$ by HPLC. The mixture contained metallic nitride EMFs with cages as small as $C_{78}$ and as large as $C_{88}$ (see Figure 2.3). The most significant advantage with respect to the current work was the production volume at Luna Innovations (nanoWorks division) that allowed the collection of significant amounts of very low yielding species.

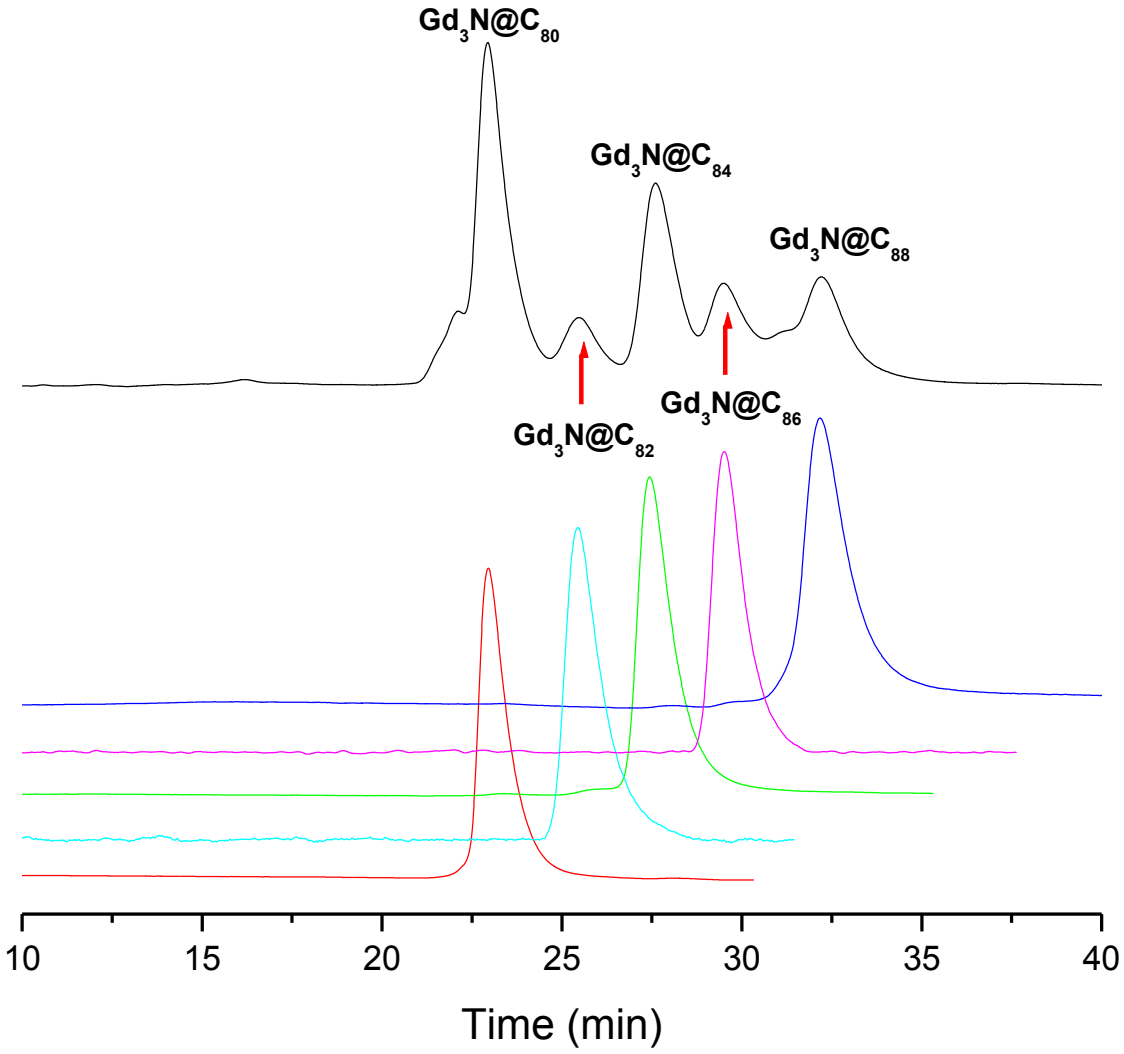


**Figure 2.3**. HPLC chromatograms of the $Gd_3N@C_{2n}$ mixture and isolated fractions. Buckyprep-M column, mobile phase toluene, flow rate 4.0 mL/min, detection 370 nm.

The identity of each isolated fraction was established by MALDI-TOF MS (see Figure 2.4). This first-stage separation was accomplished with a preparative (20 x 250 mm) Buckyprep-M column using toluene as eluent with a flow rate of 10 mL/min. From

this separation stage only $Gd_3N@C_{80}$, $Gd_3N@C_{84}$ and $Gd_3N@C_{88}$ were obtained in a 98% purity.[6]

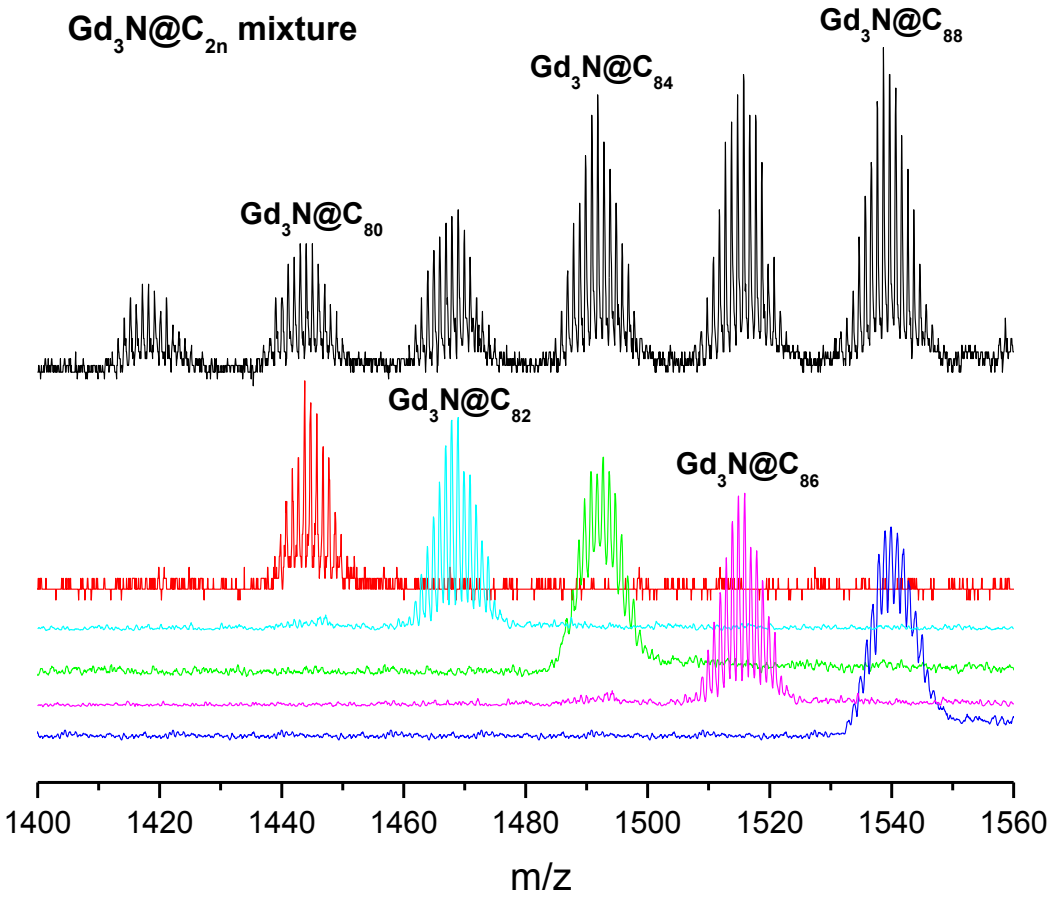


**Figure 2.4**. MALDI-TOF MS of the $Gd_3N@C_{2n}$ mixture and isolated fractions.

From the first stage separation a first fraction containing $Gd_3N@C_{78}$ was collected and then analyzed in a Buckyprep column using toluene as an eluent with a flow rate of 4 mL/min. At this point, three different fractions were collected; the middle fraction corresponded to $Gd_3N@C_{78}$ and no other column or linear combination of columns showed other peaks in the sample (Figure 2.5).

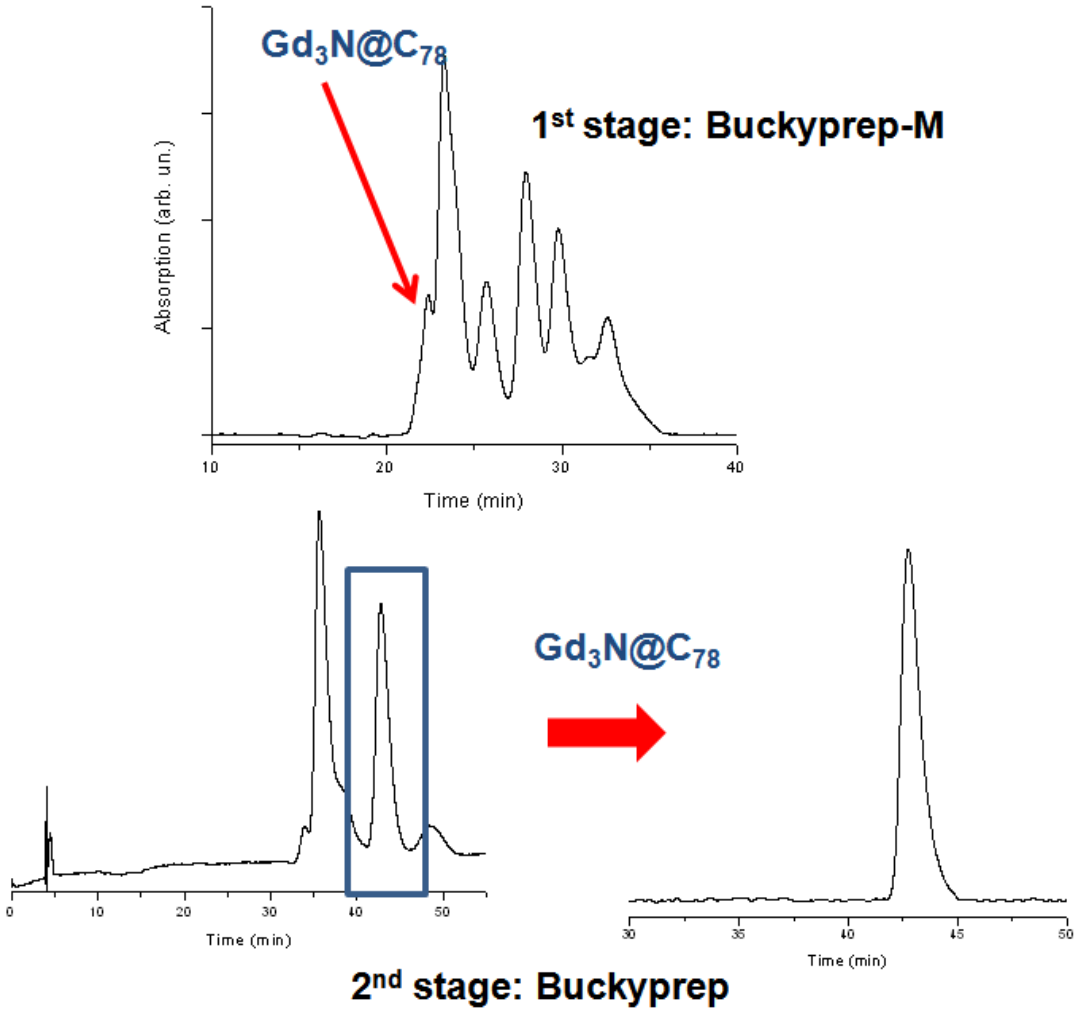


**Figure 2.5**. HPLC separation of $Gd_3N@C_{78}$. Upper trace corresponds to the initial HPLC extract on a Buckyprep-M column (mobile phase, toluene; flow rate, 4 mL/min). Lower trace corresponds to the second and third stages on a Buckyprep column (mobile phase, toluene; flow rate, 4 mL/min).

In Figure 2.5 (bottom traces) at least three different fractions eluting from the Buckyprep column can be observed, the first one corresponds to a mixture of $Gd_3N@C_{80}$ and $Gd@C_{82}$, the second fraction to $Gd_3N@C_{78}$ and the third one to $Gd_3N@C_{82}$. Mass

spectrometry analysis of fraction two shows clearly the corresponding peak at m/z=1421.75, the experimental isotopic distribution of this compound matches very well with its corresponding calculated isotopic distribution as observed in Figure 2.6.

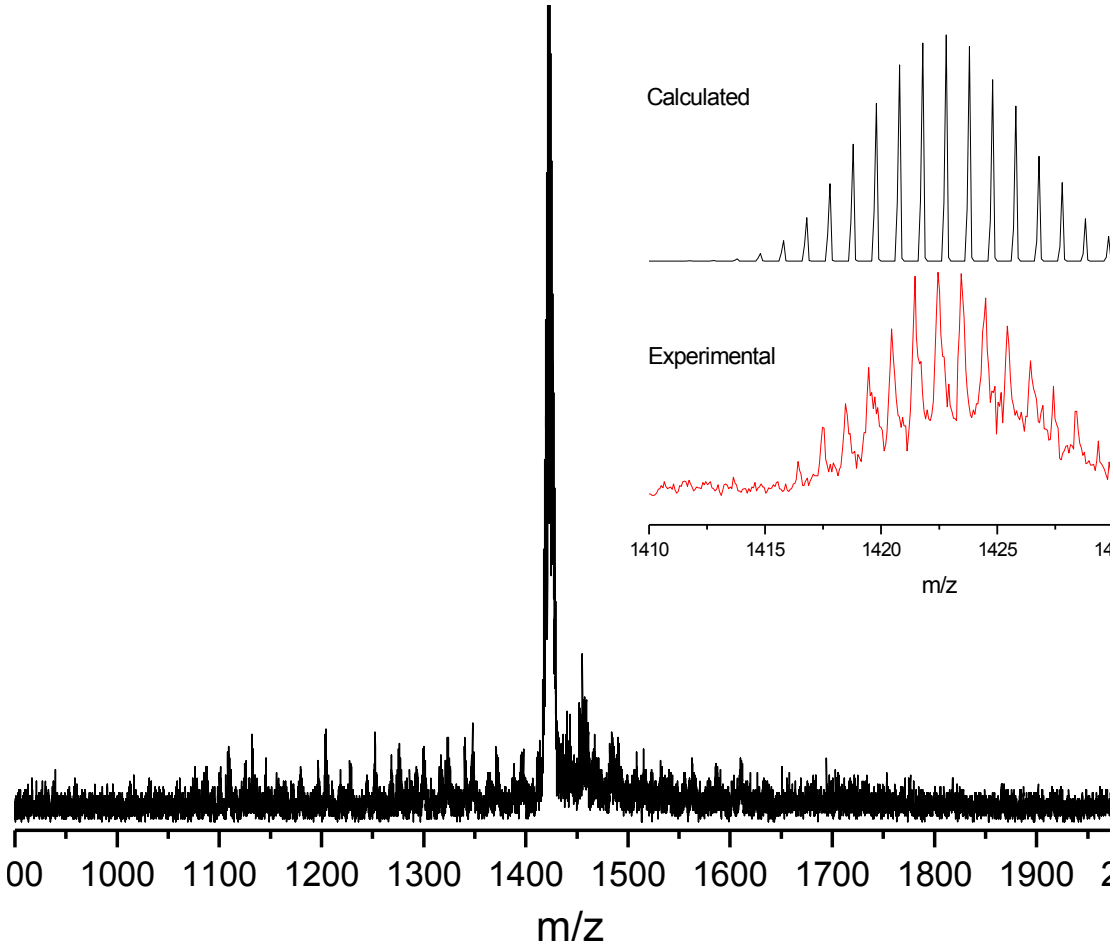


**Figure 2.6**. MALDI-TOF mass spectrum of the purified sample of $Gd_3N@C_{78}$. (Inset) Expansions of the calculated and experimental spectra for $Gd_3N@C_{78}$.

In a similar way, the isolation of $Gd_3N@C_{82}$ was accomplished in two separation stages. The first stage by collecting the second main fraction (see Figure 2.3) using a

Buckyprep-M column and the second stage using the same column to remove the small $Gd_3N@C_{80}$ fraction. This separation procedure is described in Figure 2.7.

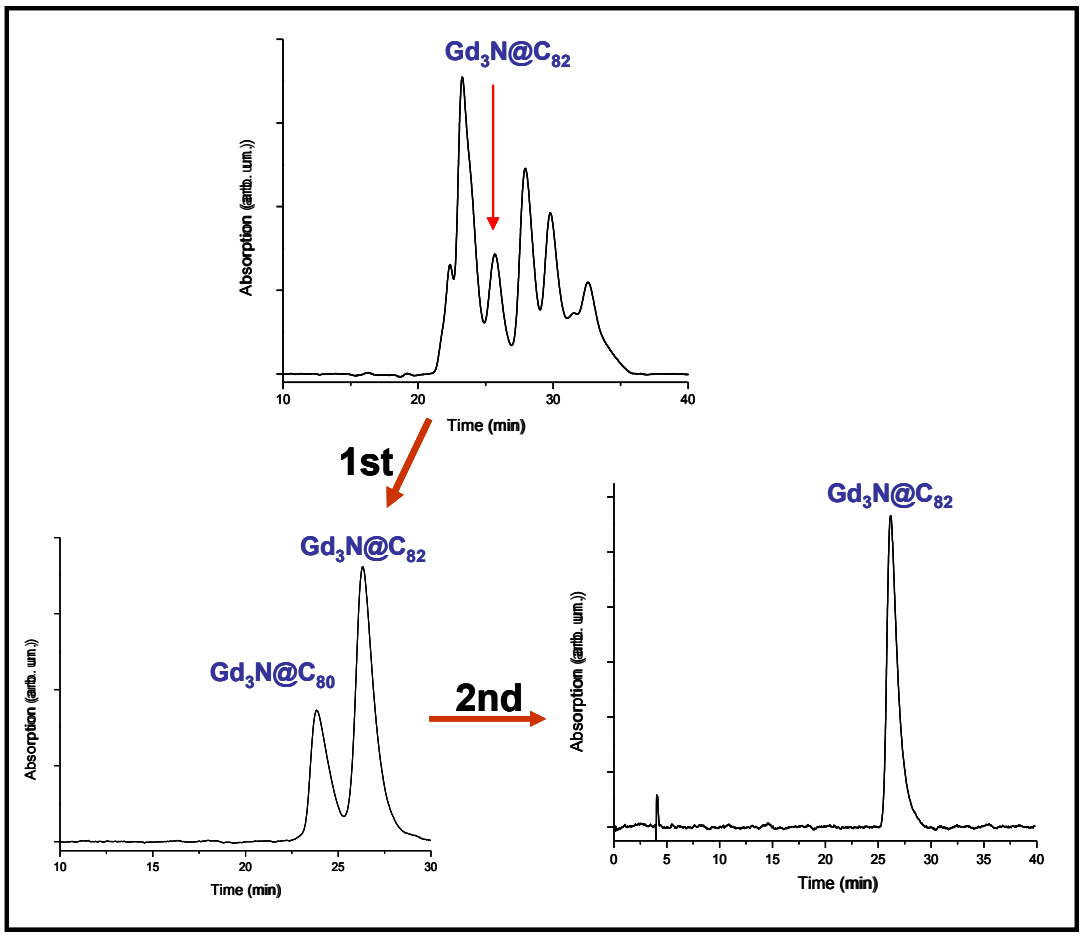


**Figure 2.7**. HPLC separation of $Gd_3N@C_{82}$. Upper trace corresponds to the initial HPLC extract on a Buckyprep-M column (mobile phase, toluene; flow rate, 4 mL/min). Lower traces correspond to the second and third stages on a Buckyprep-M column (mobile phase, toluene; flow rate, 4 mL/min).

The identity of this compound was confirmed by MALDI-TOF mass spectrometry, with the parent peak at m/z=1469.75. The isotopic distribution of the

experimentally obtained mass spectrum matches very well the calculated distribution for $Gd_3N@C_{82}$. Figure 2.8 shows the MALDI-TOF mass spectrum and the corresponding isotopic distributions for the isolated sample and for the calculated one.

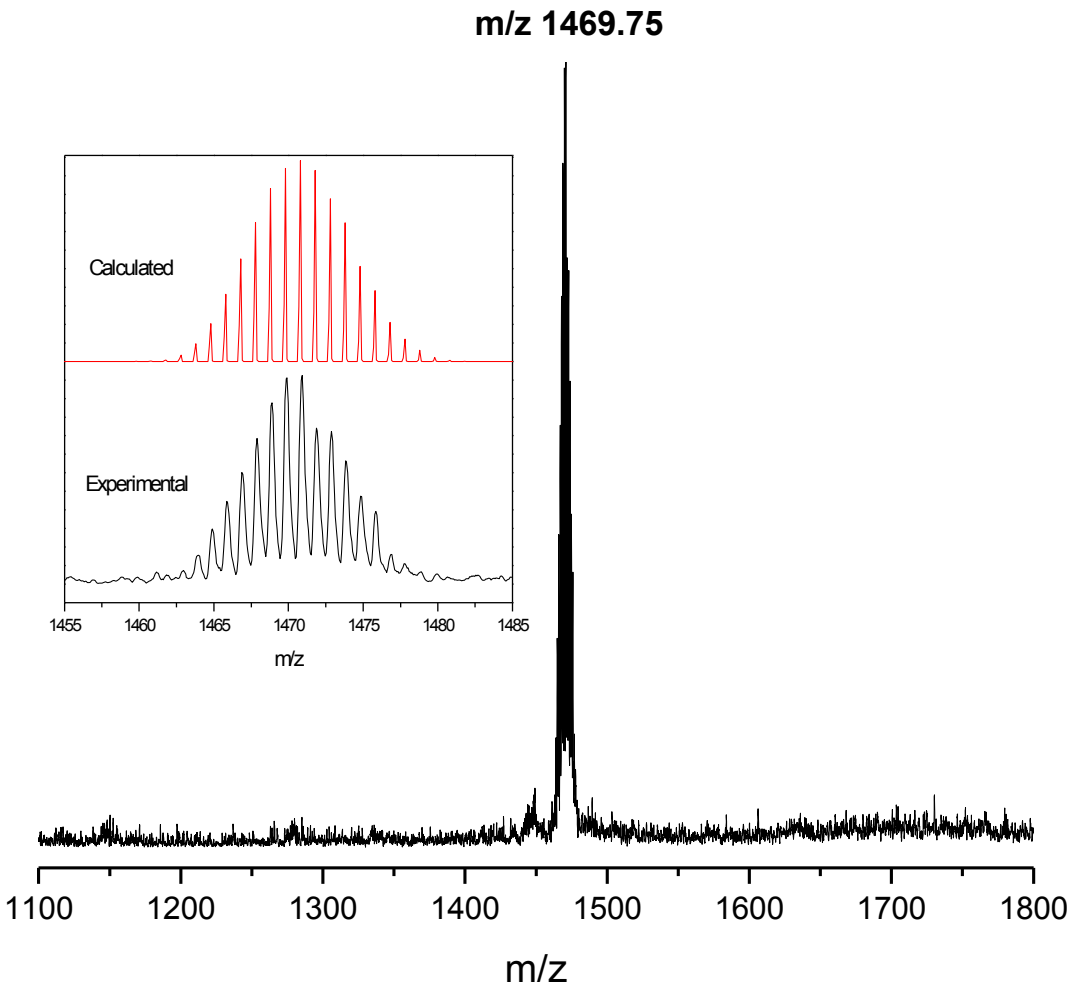


**Figure 2.8**. MALDI-TOF mass spectrum of the purified sample of $Gd_3N@C_{82}$. (Inset) Expansions of the calculated and experimental spectra for $Gd_3N@C_{82}$.

The fourth fraction from the process shown in Figure 2.2 corresponds mainly to $Gd_3N@C_{86}$ and a second isomer of $Gd_3N@C_{84}$. This fraction appears as a single peak in the Buckyprep-M column but it splits into at least five more peaks when analyzed in a linear combination of the Buckyprep-M and Buckyprep columns (Figure 2.9). The first fraction of the chromatogram corresponds to $Gd_3N@C_{86}$, the second to a $Gd_3N@C_{84}$ (II), the third one to $Gd_3N@C_{88}$, the fourth one to $Gd_2C_{90}$ and the last fraction to $Gd_2C_{92}$.

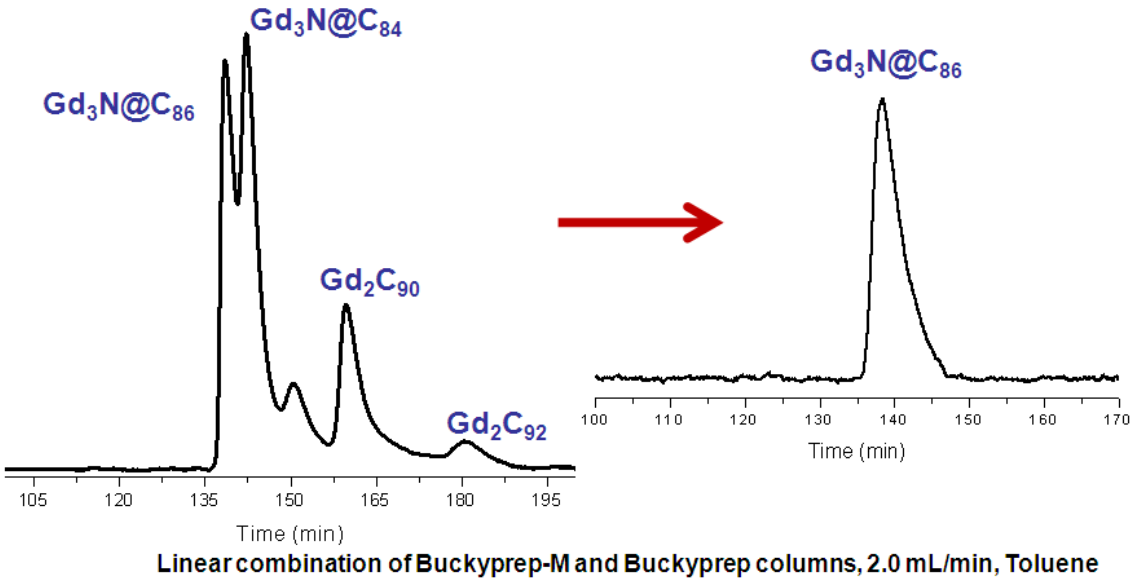


**Figure 2.9**. HPLC separation of $Gd_3N@C_{86}$. Left trace corresponds to the initial HPLC extract on a linear combination of the Buckyprep-M and Buckyprep columns (mobile phase, toluene; flow rate, 2 mL/min). Right trace corresponds to the isolated compound on the linear combination of columns (mobile phase, toluene; flow rate, 2 mL/min).

The first isolated fraction was identified as $Gd_3N@C_{86}$ by MALDI-TOF mass spectrometry. The calculated and experimental isotopic distributions match very well as

observed in Figure 2.10. The other fractions were also identified by MALDI-TOF mass spectrometry and isolated in a similar way using a linear combination of the Buckyprep-M and Buckyprep columns.

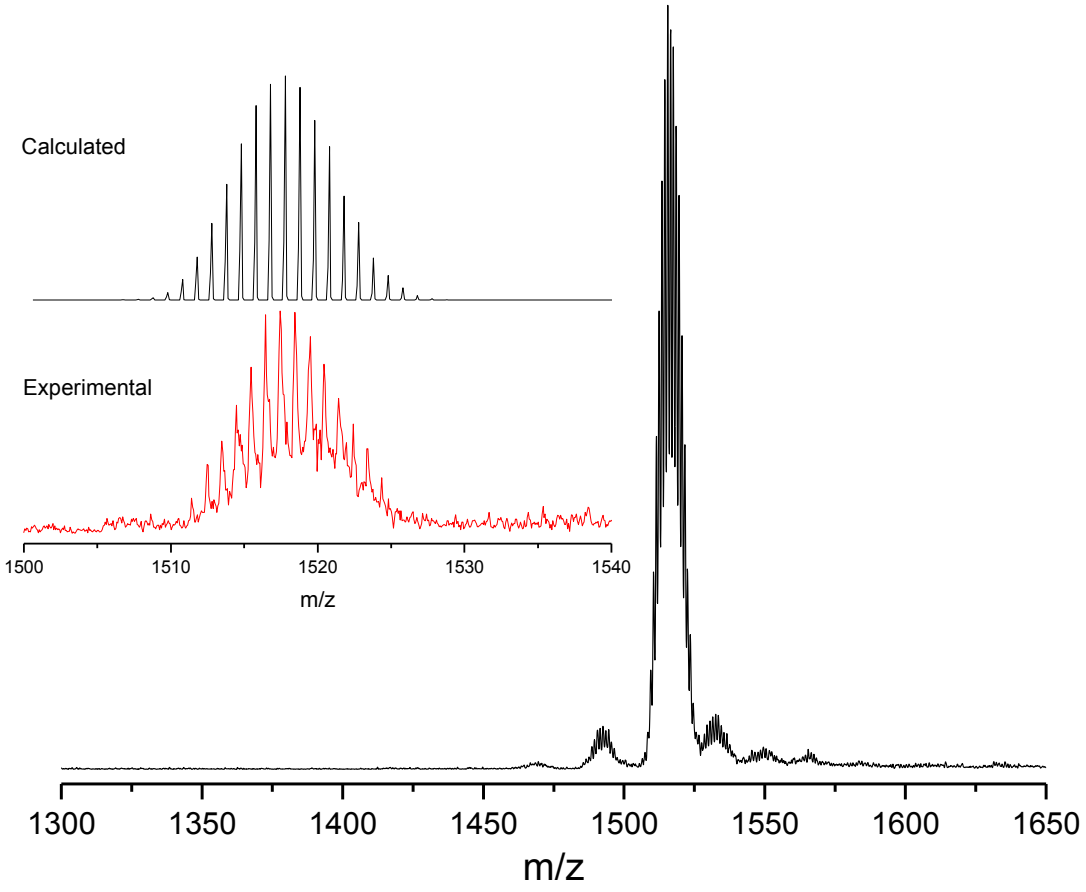


**Figure 2.10**. MALDI-TOF mass spectrum of the purified sample of $Gd_3N@C_{86}$. (Inset) Expansions of the calculated and experimental spectra for $Gd_3N@C_{86}$.

Figures 2.3 and 2.4 summarize the HPLC separation results as well as their corresponding MALDI-TOF MS spectra. Despite its low yield the $Gd_3N@C_{2n}$ family is one of the widest families of metallic nitride EMFs allowing the encapsulation of the

metallic nitride cluster inside cages as small as $C_{78}$ and as large as $C_{88}$. Considerable amounts of $Gd_2C_{90}$ and $Gd_2C_{92}$ that presumably correspond to metal carbide structures ($Gd_2C_2@C_{88}$ and $Gd_2C_2@C_{90}$) were also obtained. This type of fullerenes encapsulate in their interior a metal carbide unit ($M_2C_2$) and due to their unique electronic structures are of great interest.[7]

## Structural Characterization

As mentioned in the introduction chapter, fullerenes are closed carbon-cage molecules containing only five- and six-membered rings, and these rings consist of twelve pentagon rings and a variable number of hexagonal rings (depending on the size of the fullerene). [8] The fullerene archetype, $C_{60}$, possesses twelve pentagonal rings and 20 hexagonal rings forming a soccer ball-like structure with icosahedral ($I_h$) symmetry. Experimentally it has been found that the abundance of empty fullerenes is ruled by the intrinsic energy strain. The most important consequence of this concept in fullerenes is the Isolated-Pentagon Rule (IPR), which basically states that the most stable fullerenes are those in which all the pentagons are isolated, in other words, the arrangement of the rings must avoid fused connections between pentagons.[8] This rule has been successfully used to predict the structures of a large number of empty fullerene cages and the adducts that they form.[9] Therefore, the number of possible isomers to be expected in fullerenes is considerably decreased by the use of the IPR. For instance $C_{78}$ only has five possible IPR isomers, $C_{80}$ seven, $C_{82}$ nine, $C_{84}$ twenty four, $C_{86}$ nineteen and $C_{88}$ thirty five. However, the sacrosanct IPR for empty fullerenes seems to be more of a suggestion than

a rule for metallofullerenes, since a constantly growing number of metallofullerenes has been found to contain one or more pairs of fused pentagon rings.[7]

In the next section we shall analyze the structural features of the $Gd_3N@C_{2n}$ family, beginning with the structural characterization of $Gd_3N@C_{78}$, the smallest member of the $Gd_3N@C_{2n}$ family. Then the structures of $Gd_3N@C_{84}$ and $Gd_3N@C_{82}$ will be discussed; this arbitrary order is chosen to follow the chronological order in which they were reported and more importantly to connect the analysis of these two structures due to their similarities. Finally the structure of the $Gd_3N@C_{86}$ will be presented.

**Large Metal Ions in a Relatively Small Fullerene Cage: The Structure of $Gd_3N@C_2$(22010)-$C_{78}$ Departs from the Isolated Pentagon Rule[10]**

As can be observed in Figure 2.11, there are five isomers of the $C_{78}$ cage that obey the IPR: one with $D_3$ symmetry, two with $C_{2v}$ symmetry ($C_{2v}$ (2)-$C_{78}$ and $C_{2v}$(3)-$C_{78}$) and two with $D_{3h}$ symmetry ($D_{3h}$(4)-$C_{78}$, and $D_{3h}$(5)-$C_{78}$) and 24,105 isomers that do not obey the IPR (but still have a surface comprised of hexagons and twelve pentagons).[8] From the IPR isomers three soluble isomers of empty $C_{78}$ fullerene can be successfully extracted from the carbon soot formed during the arcing process: $D_3$-$C_{78}$, $C_{2v}$(2)-$C_{78}$, and $C_{2v}$(3)-$C_{78}$. [11-13] Furthermore, high temperature trifluoromethylation of the arc-burning generated carbon soot allows the synthesis of an adduct of $D_{3h}$(5)-$C_{78}$.[14] Consequently, $D_{3h}$(5)-$C_{78}$ is present in the carbon soot after sublimation and extraction to remove the soluble isomers. Up to the present moment there is no indication for the existence of $D_{3h}$(4)-$C_{78}$ in an arc-generated carbon soot.

Some endohedral metallofullerenes that utilize a $C_{78}$ carbon cage have been structurally characterized. Most of them possess the $D_{3h}(5)$-$C_{78}$ cage, for instance, $Sc_3N@D_{3h}(5)$-$C_{78}$ where the planar $Sc_3N$ cluster lies in the horizontal mirror plane as seen in Figure 11.[15] On the other hand, for $La_2@D_{3h}(5)$-$C_{78}$[16]and $Ce_2@D_{3h}(5)$-$C_{78}$,[17] the metal ions lie on the $C_3$ axis near the polar caps of the carbon cage. With this arrangement the separation between the two metal atoms is maximized. Finally re-analysis of the $^{13}C$ NMR spectrum of $Ti_2C_{80}$ and computational studies suggest that this compound has the metal carbide structure $Ti_2C_2@D_{3h}(5)$-$C_{78}$.[18-20] In contrast, computational and spectroscopy studies of the major isomers of $Dy_3N@C_{78}$ and of $Tm_3N@C_{78}$ have suggested that these molecules use the non-IPR fullerene cage isomer $C_2(22010)$-$C_{78}$ as a consequence of the large sizes of $Dy^{3+}$ and $Tm^{3+}$ ions.[21-22]

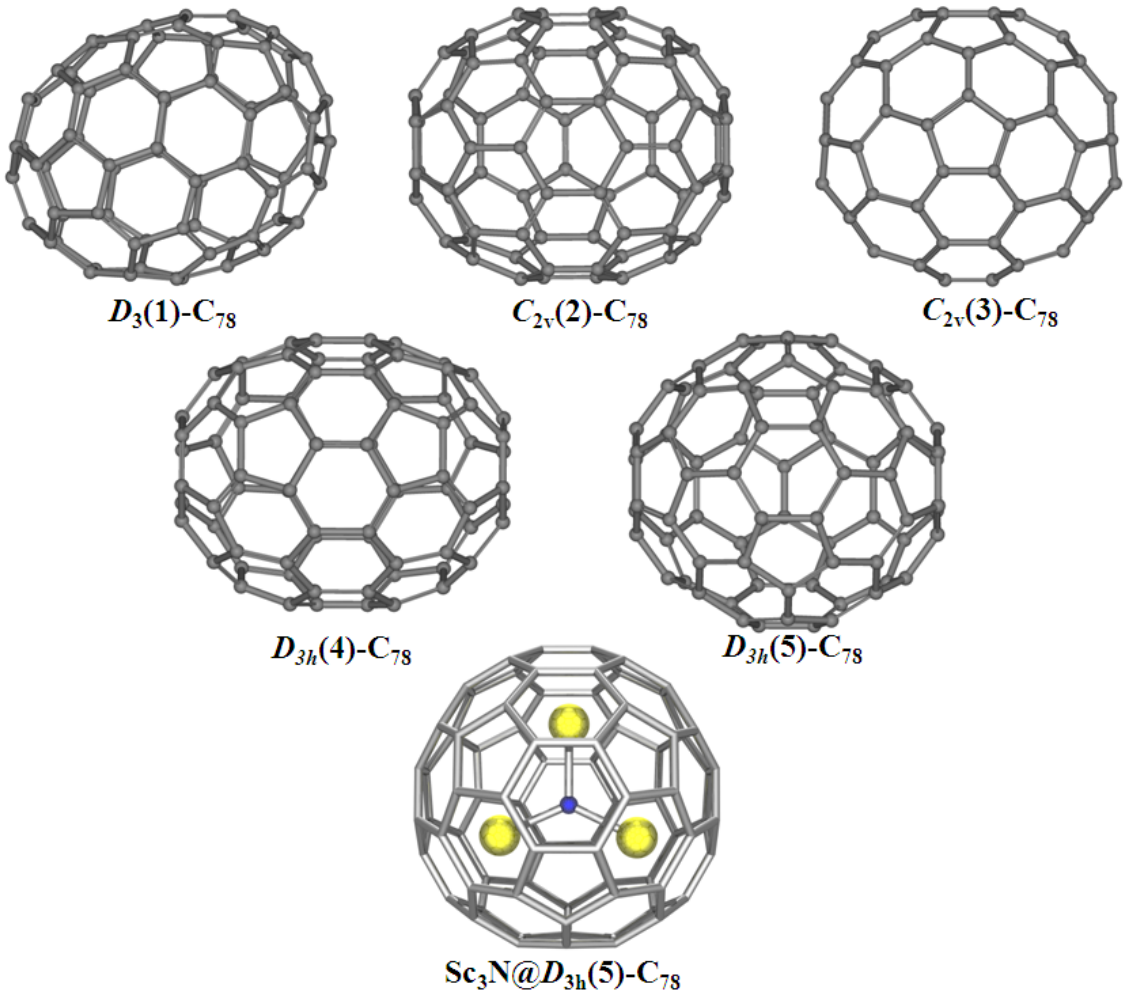


**Figure 2.11**. IPR isomers of the $C_{78}$ carbon cage and a drawing of the $Sc_3N@D_{3h}(5)$-$C_{78}$ MNEMF.

Black crystals of $Gd_3N@C_2(22010)C_{78}$ were obtained by slow diffusion of a solution of ~0.4 mg of $Gd_3N@C_2(22010)C_{78}$ dissolved in a minimum of benzene over a benzene solution of $Ni^{II}$(OEP) in a NMR tube constricted in the middle and kept at 4 $^{o}$C. Crystals grew during a period of approximately two weeks.. The fullerene cage in $Gd_3N@C_2(22010)$-$C_{78}$ does not obey the IPR. Rather it has a structure with $C_2$ symmetry

and two locations where two pentagons abut. Figure 2.12 shows the structure of the metallic nitride EMF and its relationship to the nickel porphyrin.

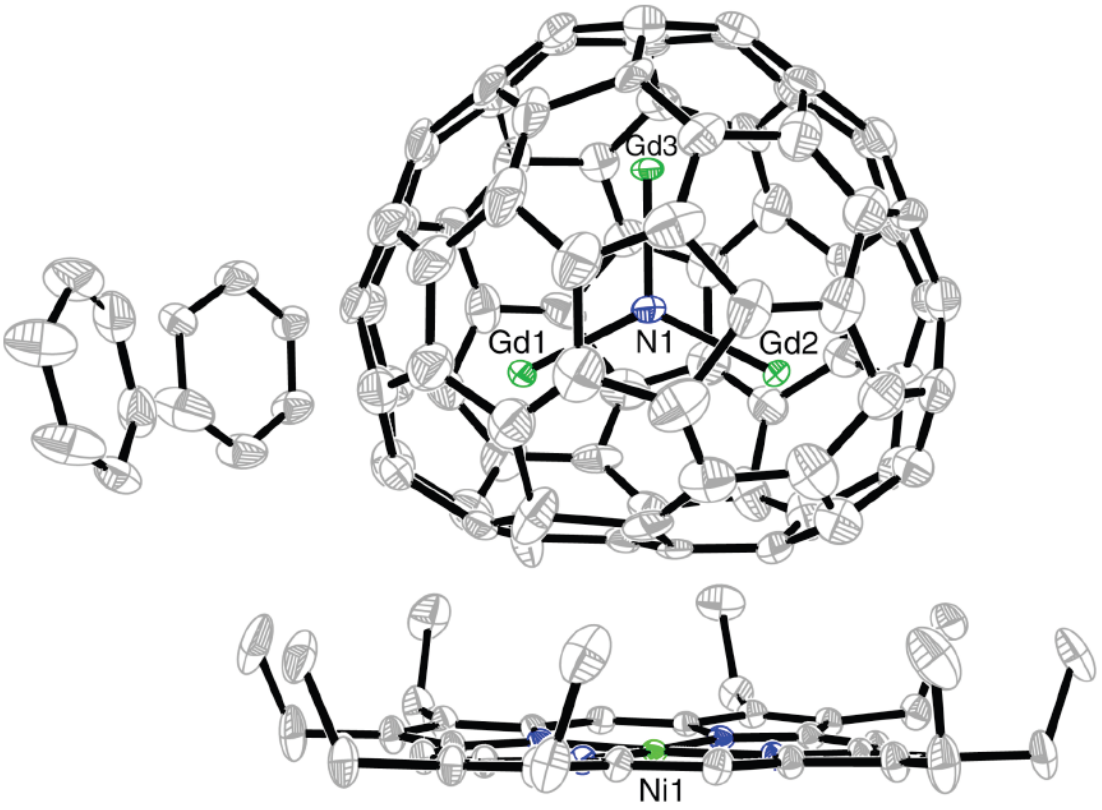


**Figure 2.12**. View of the asymmetric unit in crystaline $Gd_3N@C_2(22010)$-$C_{78}{\cdot}Ni^{II}(OEP){\cdot}1.5\ C_6H_6$ showing the spacial relationship between the fullerene and the porphyrin.

Figure 2.13 shows an orthogonal view of the metallic nitride EMF with the abutting pentagons highlighted in turquoise. The cage is disordered. There are four overlapping orientations of the cage with refined occupancies of 0.402(2), 0.232(3), 0.181(3) and 0.184(3). The gadolinium cluster is also subject to disorder. The major sites with occupancies of 0.36 for Gd1, 0.23 for Gd2 and 0.25 for Gd3 are shown in Figures 2.12 and

2.13 along with the major cage orientation. There are an additional twenty-two sites that are fractionally occupied by gadolinium ions. [23]

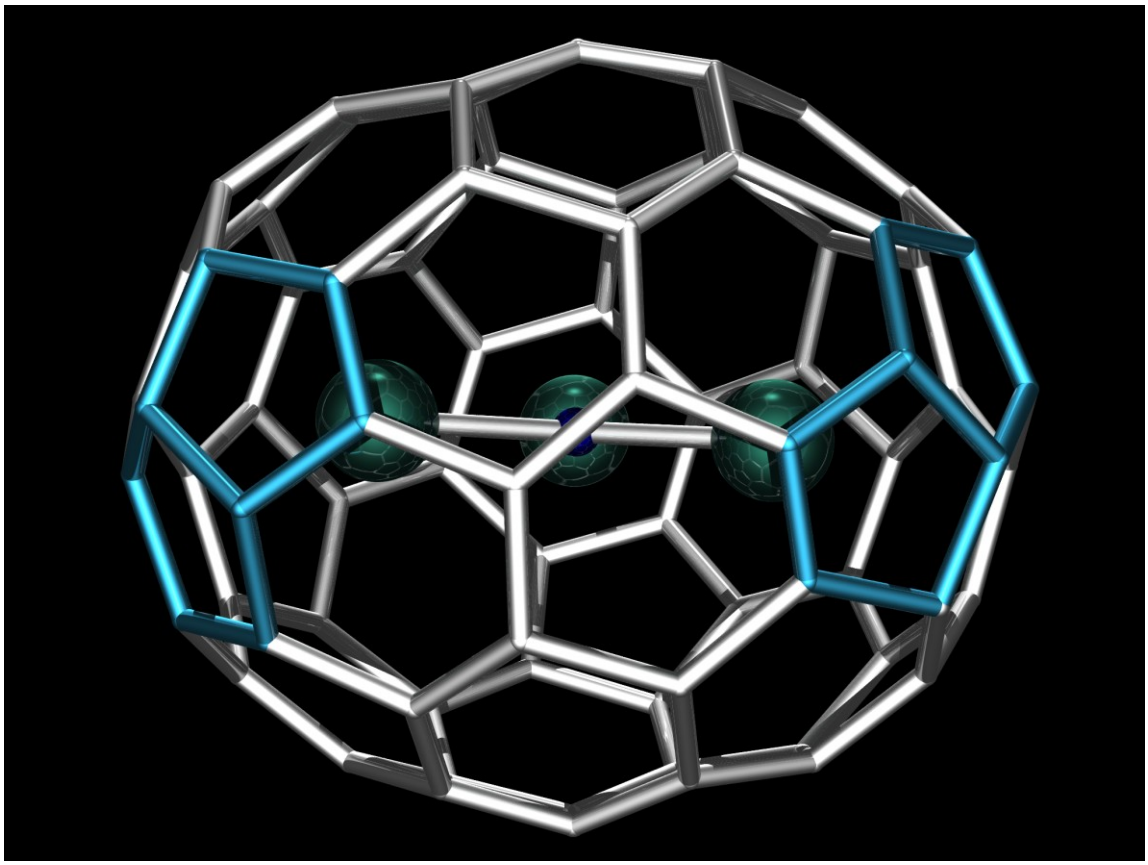

**Figure 2.13**. An orthogonal side view of $Gd_3N@C_2(22010)$-$C_{78}$ with abutting pentagons highlighted in turquoise, the nitrogen atom in blue and the gadolinium atoms in green. Only the major gadolinium sites and the major cage orientation are shown.

Figure 2.14 shows the relationship between the principal $Gd_3N$ site and the adjacent carbon atoms. The Gd-N distances are 2.037(2), 2.103(2) and 2.133(2) Å, which are similar to the Gd-N distances (2.038(8), 2.085(4), and 2.117(5) Å) observed for $Gd_3N@I_hC_{80}$.[3] In comparison the Sc-N distances in $Sc_3N@D_{3h}(5)$-$C_{78}$ are shorter: 1.981(6), 1.967(15), and 2.127(4) Å. The $Gd_3N$ unit is planar. The sum of the three Gd-

N-Gd angles (Gd1-N1-Gd2, 127.37(11); Gd2-N1-Gd3, 116.59(11); Gd1-N1-Gd3 116.03(11) °) is 359.99 ° and the nitrogen atom is only 0.01 Å out of the $Gd_3$ plane. As is frequently found for endohedral fullerenes that do not obey the IPR, two of the gadolinium ions are positioned near the pentalene units where the pentagons abut. The other gadolinium ion sits below the center of a hexagon on the fullerene surface, a metal ion position that is frequently seen for other endohedral fullerenes, see Figure 2.14.[7]

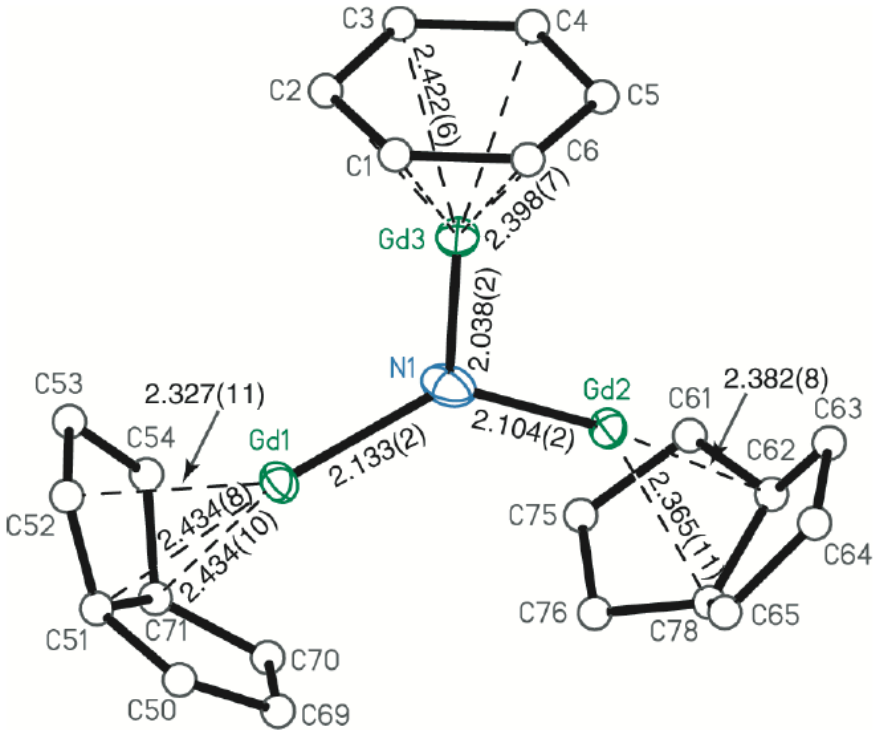


**Figure 2.14**. Drawing of the major position of the $Gd_3N$ unit relative to the closest carbon atoms of the fullerene cage in $Gd_3N@C_2(22010)$-$C_{78}$. The distances are given in Å.

$Gd_3N@C_2(22010)$-$C_{78}$ is the smallest of the six $Gd_3N$-containing EMFs that have been synthesized and isolated in this study. Interestingly, from the $Gd_3N@C_{2n}$ family

$Gd_3N@I_h$-$C_{80}$ follows the IPR and possesses a pyramidalized gadolinium nitride cluster where the nitrogen atom is away from the $Gd_3$ plane by 0.522 Å.[3] In contrast $Gd_3N@C_2$(22010)-$C_{78}$ does not obey the IPR but contains a planar $Gd_3N$ unit. The ability of the $C_2$(22010)-$C_{78}$ cage to accommodate a planar $Gd_3N$ unit must provide a significant driving force for the formation of this particular cage isomer. If a $Gd_3N$ unit were placed inside an $D_{3h}$(5)-$C_{78}$ cage, the nitrogen atom would need to be *ca.* 0.55 Å out of the $Gd_3$ plane in order to accommodate the average Gd-N distance of 2.091 Å found in $Gd_3N@C_2$(22010)-$C_{78}$.

Metal ions play a role in determining the distribution of sizes of the fullerene cages that are formed during the arcing process. For metallic nitride EMFs, larger metal ions favor the formation of larger cages and determine also the specific templating of a given family of metallic nitride EMFs (an analysis of the different template stages in metallic nitride EMFs is given in the next Chapter). Thus, with scandium, a family of four $Sc_3N$-containing endohedrals are produced: $Sc_3N@C_{68}$, $Sc_3N@C_{70}$, and two isomers of $Sc_3N@C_{80}$ with $Sc_3N@I_h$-$C_{80}$ as the most abundant compound in the family.[24] In the case of gadolinium, six endohedrals are mainly formed: $Gd_3N@C_{78}$, $Gd_3N@C_{80}$, $Gd_3N@C_{82}$, $Gd_3N@C_{84}$, $Gd_3N@C_{86}$, and $Gd_3N@C_{88}$.[6]

Usually, for a particular carbon-cage size, the nature of the encapsulated metal ion has not been found to affect the cage geometry.[7] For instance, the major isomers found for $Gd_3N@C_{84}$, $Tb_3N@C_{84}$ and $Tm_3N@C_{84}$ all use the $C_s$(51365)-$C_{84}$ fullerene cage regardless of the fact that there are twenty-four IPR and 51,568 non-IPR isomers available for a $C_{84}$ cage. [7-8] Likewise, the predominant isomer for endohedrals of the

$M_3N@C_{80}$ type uses the $I_h$-$C_{80}$ fullerene cage to encapsulate different metallic nitride clusters including: homometallic groups such as $Sc_3N$,[24] $Lu_3N$,[25] $Gd_3N$,[3] $Tb_3N$,[26] $Tm_3N$,[27] $Dy_3N$,[28] as well as heterometallic clusters such as $ErSc_2N$,[29] $CeSc_2N$,[30] $GdSc_2N$,[31] $Gd_2ScN$,[30] $TbSc_2N$.[31] The less abundant isomer of the $M_3N@C_{80}$ class utilizes the $D_{5h}$-$C_{80}$ cage to encapsulate $Sc_3N$,[32] $Tb_3N$,[27] and $Tm_3N$ units.[27] The major isomers of Ca@$C_{3v}$-$C_{94}$ and Tm@$C_{3v}$-$C_{94}$ have been shown to use the $C_{3v}$-$C_{94}$ cage.[33] Finally, despite the wide variation in internal composition, the endohedrals - $La_2@C_{78}$, $Ce_2@C_{78}$, $Sc_3N@C_{78}$, and $Ti_2C_2@C_{78}$ - all utilize the same $D_{3h}(5)$-$C_{78}$ cage.[7]

The situation with $Gd_3N@C_2(22010)$-$C_{78}$ is clearly different. Despite the similarity in internal composition, unique cages are found for $Gd_3N@C_2(22010)$-$C_{78}$ and $Sc_3N@D_{3h}(5)$-$C_{78}$. The ability of the $C_2(22010)$-$C_{78}$ cage to accommodate a planar $Gd_3N$ unit appears to be a major factor in the stabilization of this particular fullerene cage.

**An Egg-Shapped Fullerene: Non-Isolated Pentagon Structure of $Gd_3N@C_s(51365)$-$C_{84}$[34]**

The fullerene cage containing 84 carbon atoms possesses twenty-four IPR and 51,568 non-IPR structures that could in principle encapsulate a metallic moiety.[8] Figure 2.15 shows the 24 possible IPR structures of the $C_{84}$ fullerene cage. In 2005, Poblet and co-workers predicted by DFT calculations that none of the 24 IPR structures of $C_{84}$ would be suitable to encapsulate a metallic nitride cluster.[35] Their calculations were based on the assumption of a six-fold electron transfer between the metallic nitride cluster and the fullerene cage. In other words, the bonding in metallic nitride EMFs is widely described by the ionic model $M_3N^{6+}@C_{2n}^{6-}$ (see the Introduction and Chapter 4 sections for further

analysis of the ionic model in EMFs). In this model the ability of the fullerene cage to accept six electrons determines its capacity to encapsulate the metallic nitride cluster. Therefore only empty fullerene isomers with a large (LUMO-3)-(LUMO-4) energy gap can encapsulate and stabilize the metallic nitride unit.[35]

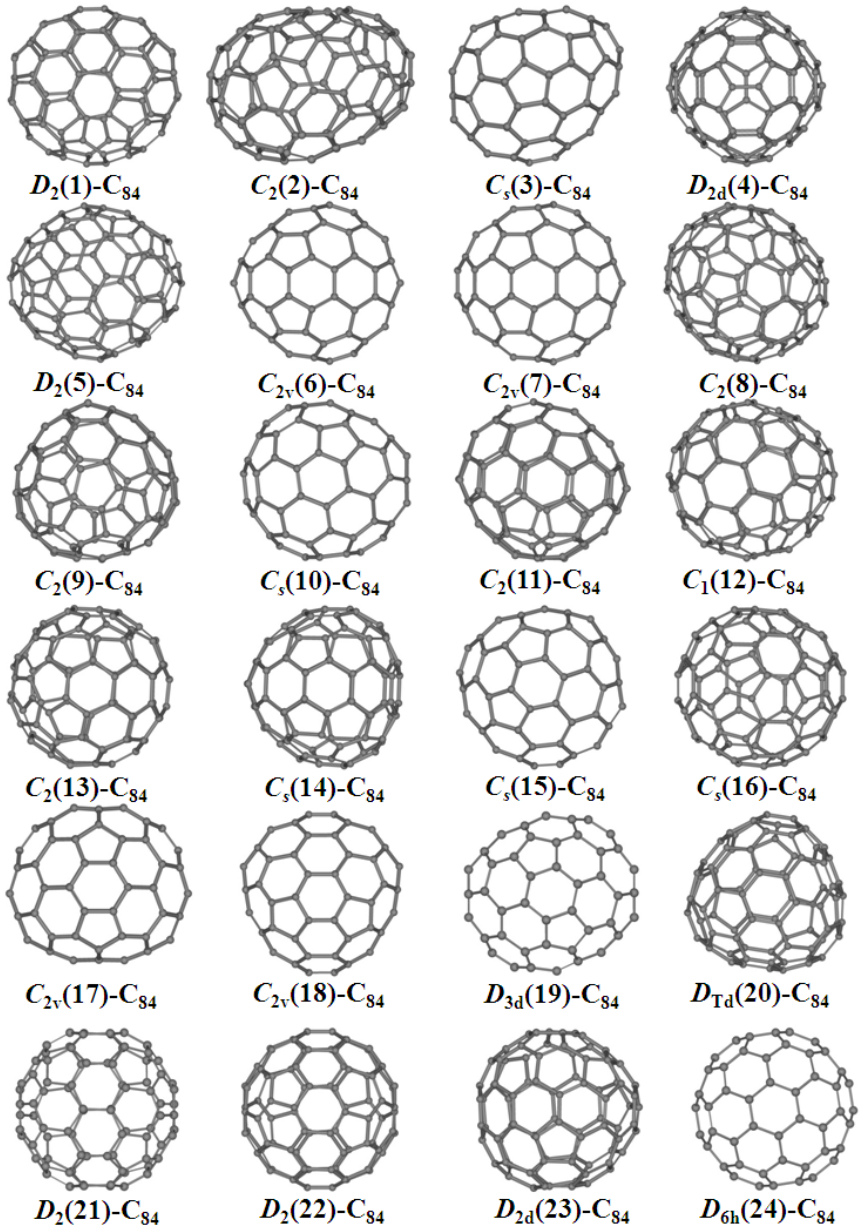


**Figure 2.15.** IPR fullerene isomers of $C_{84}$.

The structure of $Tb_3N@C_s(51365)\text{-}C_{84}$, the more abundant of the two isomers of $Tb_3N@C_{84}$, was determined in 2006 and found to violate the IPR.[36] While there are 24 IPR isomeric structures available for a $C_{84}$ cage, the second eluting isomer of $Tb_3N@C_{84}$ adopts one of the 51,568 isomeric structures that do not conform to the IPR. It utilizes the non-IPR structure No. 51,365 with $C_s$ symmetry.[8] This cage has a single site where two pentagons abut. With such a large number of isomeric $C_{84}$ cages as possible hosts for metallic nitride units, it remained to be determined whether other metals would select the same cage structure in forming analogs of $Tb_3N@C_s(51365)\text{-}C_{84}$.

Black blocks of $Gd_3N@C_s(51365)\text{-}C_{84} \bullet Ni^{II}(OEP) \bullet 2(C_6H_6)$ were obtained by diffusion of a benzene solution of $Gd_3N@C_s(51365)\text{-}C_{84}$ into a benzene solution of $Ni^{II}(OEP)$ and utilized for the crystal structure determination by X-ray diffraction.[37] Figure 2.16 shows a drawing of the $Gd_3N@C_s(51365)\text{-}C_{84}$ compound and its relative relationship with the porphyrin. The fullerene cage does not obey the IPR; there is one pentagon-pentagon contact, which is highlighted in red.

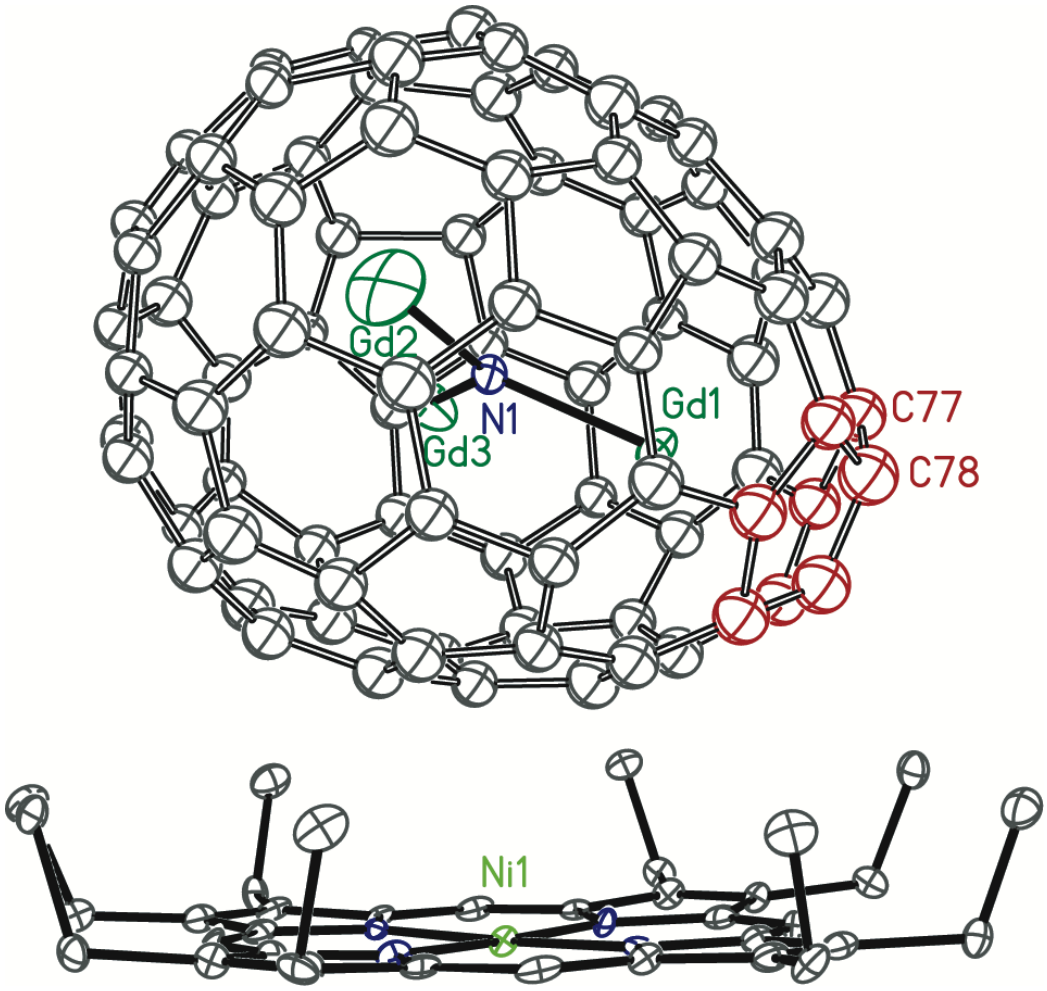


**Figure 2.16**. A view of the structure of $Gd_3N@C_s(51365)$-$C_{84}$·Ni(OEP)·$2C_6H_6$ with 30% thermal contours. The pair of fused pentagons is highlighted in red. Only the major site of the $Gd_3$ is shown and the benzene molecules are omitted for clarity.

The fullerene cage in $Gd_3N@C_s(51365)$-$C_{84}$ has the same $C_s$ structure and utilizes the same cage isomer (non-IPR isomer No. 51365) as found originally for $Tb_3N@C_s(51365)$-$C_{84}$.[36] Noteworthy, the same non-IPR cage is formed under different experimental conditions using different metal oxide precursors, different packing materials inside the graphite rods and different arc-discharge generators. The occurrence

of the same cage structure in these different molecules suggests that it is the carbon cage and the number of electrons transferred to it by the metals inside, rather than the specific metals trapped inside, that determine which of the multitude of structures available for a cage of 84 carbon atoms is actually utilized, as noted in recent computational studies.[22, 35] The carbon atoms in $Gd_3N@C_s(51365)$-$C_{84}$•Ni(OEP)•2 $C_6H_6$ display the same type of cage disorder as previously found for $Tb_3N@C_s(51365)$-$C_{84}$ • Ni(OEP) • 2 $C_6H_6$. The 64 atoms of the cage closest to the fused pentagon pair are well behaved, but the 20 carbon atoms at the opposite end are found in two sets of positions that are related by a 180 ° rotation of the cage.

The metal ions inside the cage also display disorder. The major sites of $Gd_3N@C_s(51365)$-$C_{84}$•Ni(OEP)•2 $C_6H_6$ involve Gd1 with 0.85 occupancy, Gd2 with occupancy of 0.38 and Gd3 with occupancy of 0.51. There are eight other Gd sites with occupancies ranging from 0.29 to 0.05. In the major sites, the $Gd_3N$ units are planar with the sum of the Gd-Gd-Gd angles equal to 359.7 °. Figure 2.17 shows the dimensions of the $M_3N$ (M=Tm, Gd and Tb) units in the three $M_3N@C_s(51365)$-$C_{84}$ and the interactions between one of the metal atoms of the $M_3N$ unit with carbon atoms of the pair of abutting pentagons. In all three cases the M-N distances and the M-C distances are similar.

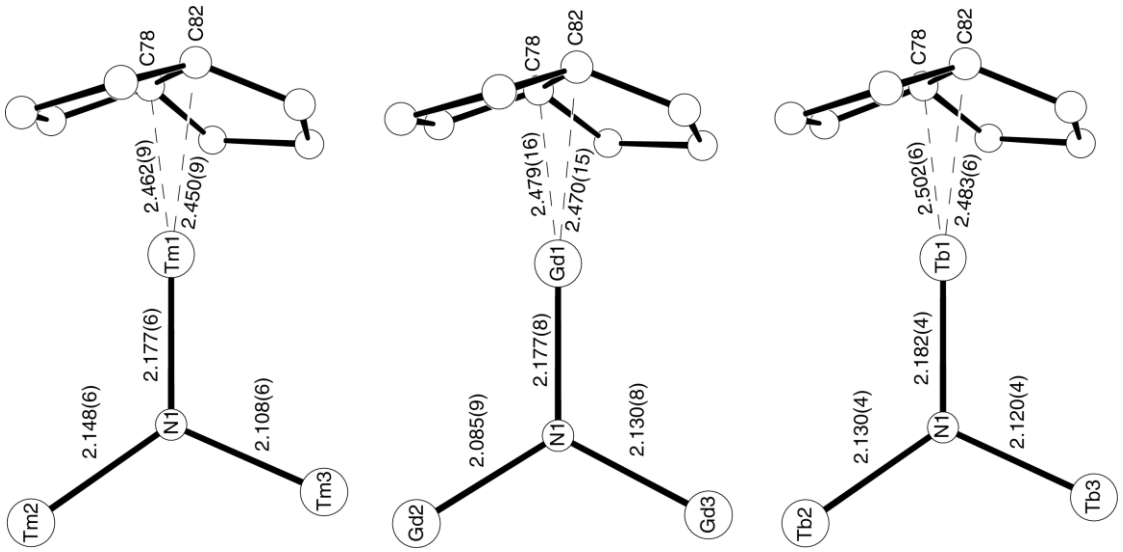


**Figure 2.17**. Views showing the locations of the $M_3N$ units relative to the fused pentagon system in $Tm_3N@C_s(51365)$-$C_{84}$, $Gd_3N@C_s(51365)$-$C_{84}$ and $Tb_3N@C_s(51365)$-$C_{84}$. Values are given in Å.

These results highlight the fact that the metal ions in the non-IPR cages are associated with the fused pentagons. Theoretical calculations indicate that the charge transferred from the $M_3N$ cluster to the carbon cage is mainly localized in the fused pentagon moiety.[38] Thus, the antiaromatic fused pentagon moiety becomes more aromatic in character. This charge distribution may explain the experimental observations that fused pentagon pairs are always associated with the presence of a metal ion in the pentalene fold of endohedral fullerenes that do not obey the IPR.

**Is the Isolated Pentagon Rule Merely a Suggestion for Endohedral Fullerenes? The Structure of a Second Egg-Shapped Endohedral Fullerene-$Gd_3N@C_s(39663)$-$C_{82}$[39]**

The $C_{82}$ fullerene cage has played an important role in the development of endohedral metallofullerene chemistry. The first experimental evidence of encapsulation

of metals inside the $C_{82}$ fullerene cage and its particular stability was obtained in 1991 when Smalley and co-workers observed that La@$C_{82}$, unlike La@$C_{60}$ and La@$C_{74}$, had better solubility in organic solvents and higher stability.[40] Subsequently, the number of endohedral metallofullerenes with $C_{82}$ carbon cages has become particularly large especially in the case of metallofullerenes encapsulating one or two metals.[7, 41] Figure 18 shows the nine isomers of the $C_{82}$ fullerene cage that obey the IPR (three $C_2$ isomers, three $C_s$ isomers, two $C_{3v}$ isomers, and one $C_{2v}$ isomer). It has been established that the major and minor isomers of La@$C_{82}$ have IPR-obeying cage structures with $C_{2v}$[42] and $C_s$[43] symmetry respectively, and the $C_{2v}$ structure appears to be preferred for a number of other endohedrals of the M@$C_{82}$ type.[44] The structures of two of the three known isomers of $Er_2$@$C_{82}$ have been crystallographically characterized and shown to have the IPR-obeying structures $Er_2@C_s(6)$-$C_{82}$[45] and $Er_2@C_{3v}(8)$-$C_{82}$.[46]

It is important to emphasize that even though $Tm_3N$@$C_{82}$[47] and $Dy_3N$@$C_{82}$[48] were synthesized and isolated prior to our work, no structural studies on metallic nitrides encapsulated inside the $C_{82}$ fullerene cage had been reported. Popov and Dunch performed a systematic and detailed study for the most stable isomers of $M_3N$@$C_{82}$ based on DFT calculations of empty cages in the hexaanionic state ($C_{2n}^{6-}$).[22] They suggested that none of the 9 IPR-obeying fullerene cages would encapsulate a metallic nitride. Similarly to the $C_{84}$ fullerene cage case, the most probable fullerene cage encapsulating a metallic nitride cluster would be a non-IPR. The authors proposed two possible structures $C_{2v}(39707)$-$C_{82}$ and $C_s(39663)$-$C_{82}$ with HOMO-LUMO gaps of 1.32 and 1.51 eV

respectively.[22] X-ray data of our $Gd_3N@C_{82}$ compound confirmed later the non-IPR structure.[39]

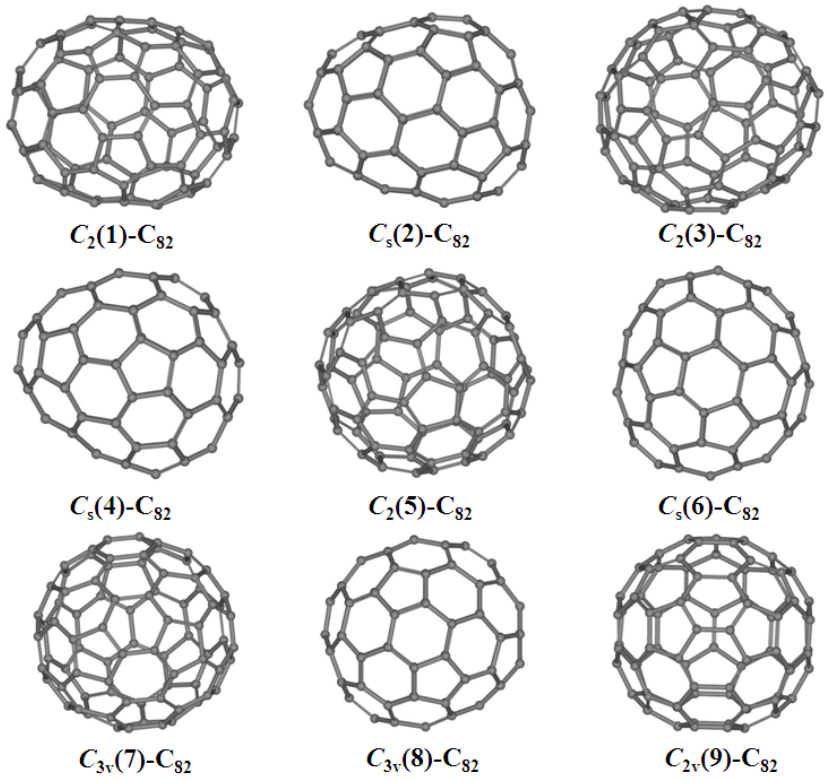


**Figure 2.18**. IPR fullerene isomers of $C_{82}$.

Black parallelepipeds of $Gd_3N@C_s(39663)$-$C_{82}$•$Ni^{II}$(OEP)•2($C_6H_6$) were obtained by slow diffusion of a benzene solution of the endohedral metallofullerene into a benzene solution of $Ni^{II}$(OEP) and utilized in the crystal structure determination.[49]

Figure 2.19 shows a drawing of the egg-shaped $Gd_3N@C_s(39663)$-$C_{82}$ compound, which is nestled within the eight ethyl groups of the $Ni^{II}$(OEP) structure. The carbon cage in $Gd_3N@C_s(39663)$-$C_{82}$ does not obey the IPR. The fused pentagon pair is highlighted in Figure 2.19 in purple. For a $C_{82}$ cage there are nine isomers that conform to the IPR

and 39,709 isomeric structures that do not conform to the IPR.[8] The structure found here is one of the two previously predicted to be stable for a $C_{82}$ cage bearing a $6^-$ charge.[22]

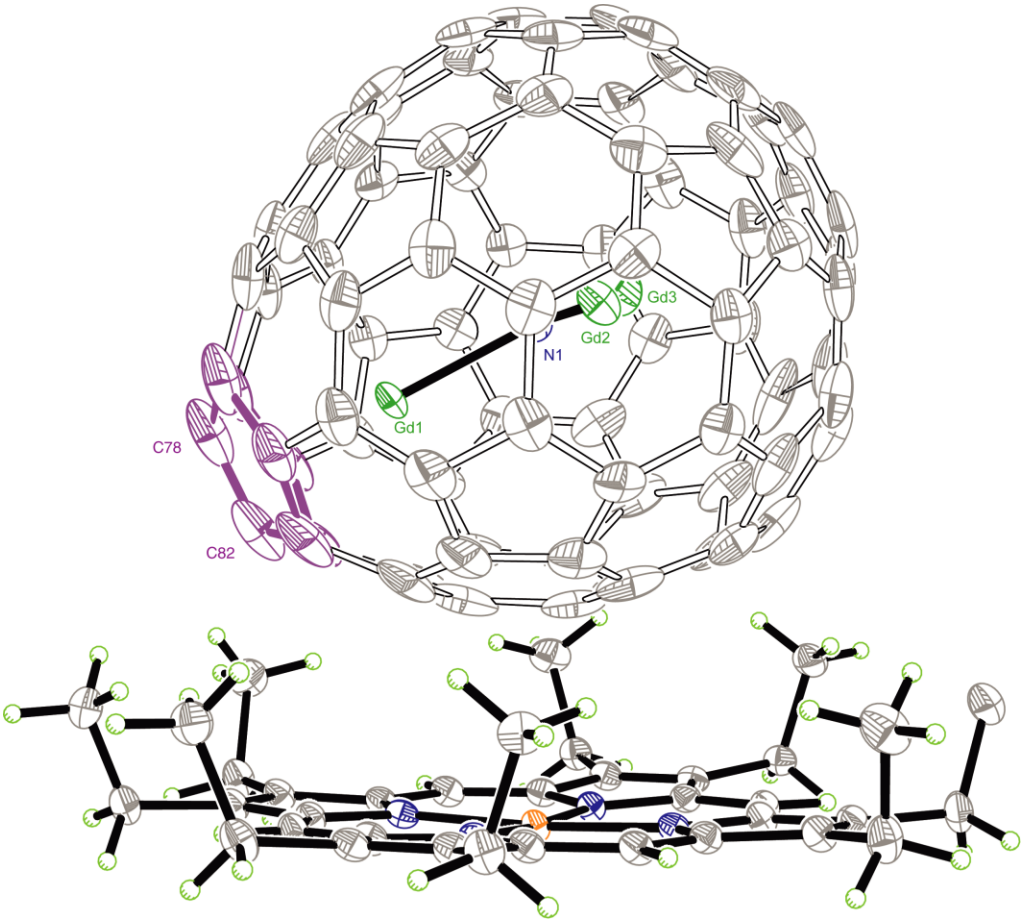


**Figure 2.19**. A view of the structure $Gd_3N@C_s(39663)$-$C_{82}$•$Ni^{II}$(OEP)•2($C_6H_6$) with 30% thermal contours. The pair of fused pentagons is highlighted in purple. Only the major site for the $Gd_3$ group is shown. For clarity the benzene molecules have been omitted.

The fullerene cage in $Gd_3N@C_s(39663)$-$C_{82}$ closely resembles the cage found for the most prevalent isomer of $M_3N@C_{84}$, which is $M_3N@C_s(51365)$-$C_{84}$ (M = Gd, Tb, Tm).[34, 36] A comparison of the shapes of these two fullerenes is presented in Figure 20.

Both cages have an egg shape with mirror symmetry and a single location where two pentagons abut. In both cases the mirror plane of the fullerene is positioned perpendicular to the C-C bond that connects the two pentagonal rings. There is some disorder in the structure. Gd1, Gd2, and Gd3 constitute the major site for this group with 0.84, 0.67, and 0.70 fractional occupancy, respectively. The Gd-N distances are 2.152(5), 2.094(5), and 2.077(5) Å for Gd1, Gd2, and Gd3, respectively. The $Gd_3N$ unit is planar at the major site. The sum of the three Gd-N-Gd angles is 359.6.° There are an additional 16 Gd sites with occupancies ranging from 0.09 to 0.02. The carbon cage also displays disorder with two orientations for the cage.

Gd1 is situated within the fold of the pentalene unit formed by the fused pentagon pair. Within that unit the Gd-C distances are shortest at the fold (Gd1-C78, 2.476(10), Gd1-C82, 2.484(10) Å) and longer for the four adjacent carbon atoms, which range from 2.486(10) to 2.554(10) Å. The Gd1-C78 and Gd1-C82 distances are comparable to the Gd-C distances (2.470(15) and 2.479(16) in $Gd_3N@C_s(51365)\text{-}C_{84}$.[34] The positioning of Gd1 near the fused pentagon pair is similar to that of the Gd, Tb and Tm ions in $M_3N@C_s(51365)\text{-}C_{84}$ and to the scandium ions within the three pentalene units of $Sc_3N@D_{3h}(6140)\text{-}C_{68}$.[34, 36] For comparison, there is a significant body of data available for coordination of organometallic groups to the inner face of pentalene and substituted pentalenes.[50]

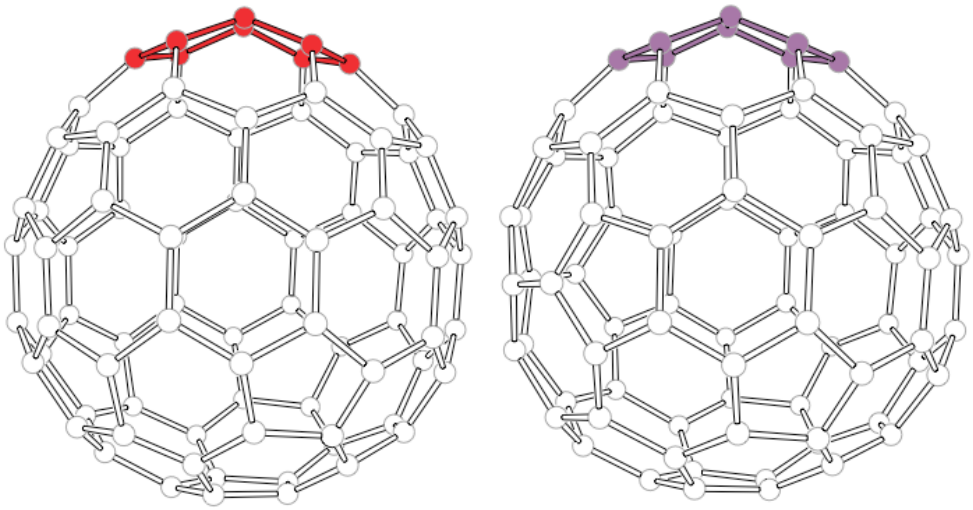

**Figure 2.20**. Comparison of the structures of the fullerene cage in $Gd_3N@C_s(51365)$-$C_{84}$ (left side with the fused pentagon pair highlighted in red) and $Gd_3N@C_s(39663)$-$C_{82}$ (right side with the fused pentagon highlighted in purple). The noncrystallographic mirror plane in each case lies parallel to the page.

The encapsulation of metals and metallic clusters inside fullerene cages certainly has made possible the synthesis of non-IPR endohedral metallofullerenes. The first reports of metallofullerenes with carbon cages containing adjacent pentagon-pentagon rings were those of $Sc_2@C_{66}$[51] and $Sc_3N@D_3(6140)$-$C_{68}$.[52] Other examples are $Sc_2C_2@C_{2v}(6073)$-$C_{68}$, $Sc_3N@C_{2v}(7854)$-$C_{70}$, $La_2@D_2(10611)C_{72}$, $La@C_{72}$, $DySc_2N@C_s(17490)$-$C_{76}$, $Gd_3N@C_2(22010)$-$C_{78}$, $Gd_3N@C_s(39663)$-$C_{82}$, and $M_3N@C_s(52365)$-$C_{84}$ (M=Gd, Tb, Tm).[34, 36, 39, 53-57] On the other hand, spectroscopy along with DFT calculations strongly suggested that $Ce_2@C_{72}$ possesses a non-IPR carbon cage of $D_2$ symmetry as in the case of $La_2@C_{72}$ .[58] It is interesting to note that as the size of the fullerene increases the number of fused pentagon systems decreases, for

instance, $Sc_3N@D_3(6140)$-$C_{68}$ has three fused pentagon systems while $Gd_3N@C_s(39663)$-$C_{82}$, and $M_3N@C_s(52365)$-$C_{84}$ (M=Gd, Tb, Tm) have only one.

It should also be noted that the IPR is justified for the uncharged carbon cages where the number of π-electrons coincides with the number of carbon atoms.[8] The 6-fold electron transfer from the metal(s) or metallic nitride cluster to the fullerene cage allows a change in the hybridization state of the carbons in the pentalene unit. For instance, neutral pentalene (Figure 2.21 on top) has been known for a long time to be a rather unstable molecule.[50] It can be stabilized in its 10-π-electron dianionic form (Figure 2.21, bottom) or by complexation to transition or rare-earth metals.[50] Therefore, complexation is believed to provide additional stabilization to the aromatic dianion in the same way as it does for the aromatic cyclopentadienyl monoanion.

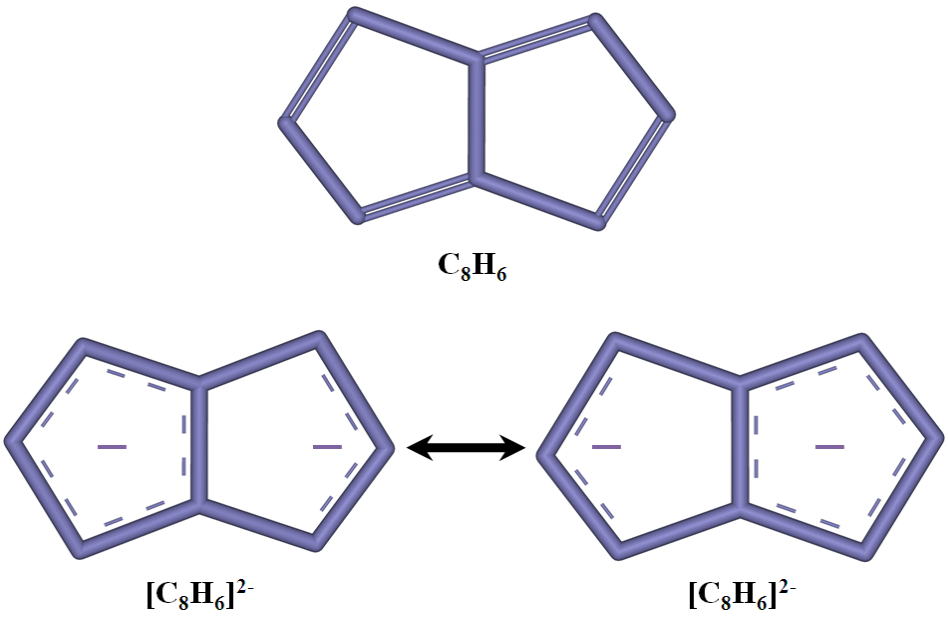


**Figure 2.21**. Neutral pentalene (top) and its stabilized aromatic 10-π-electron dianion form (bottom).

Pentagon-pentagon systems may also be stabilized by the change of the hybridization of the carbon atoms in the pentagon/pentagon junctions to the C($sp^3$) state, which can be exemplified by the isolation of the stable $C_{50}Cl_{10}$[60] or $C_{64}H_4$[61] non-IPR fullerenes. Based on the stabilization of the pentalene dianion one may conceive that the 6-fold electron transfer to the fullerene can stabilize up to three different fused pentagon systems. This reasoning agrees with the fact that no metallofullerenes containing more than three violations of the IPR have been reported to date.[7] On the other hand, the influence of the 6-fold charging of the fullerene should be decreased with the growth of the fullerene size, and therefore its stabilizing role is smaller for the larger fullerenes. With the increase of the cage size a more uniform distribution of the pentagon-induced strain over the fullerene is possible, and hence, localization of such a strain in pentagon adjacencies should become more unfavorable than that for the smaller cages.

**The Structure of $Gd_3N@D_3$-$C_{86}$ as Determined by Single Crystal X-ray Diffraction**

For a cage comprised of 86 carbon atoms there are nineteen isomers that obey the IPR, corresponding to six isomers of $C_1$ symmetry, six of $C_2$ symmetry, three of $C_s$ symmetry, two of $C_{2v}$ symmetry, one of $C_3$ symmetry and one with $D_3$ symmetry (see figure 2.22).[8] In the hexaanionic state the isomer with $D_3$ symmetry is found to be the most stable and the one with the largest HOMO-LUMO gap (1.51 eV), thus strongly suggesting that $D_3(19)$-$C_{86}$ is the most suitable fullerene able to encapsulate a metallic nitride cluster. [35, 22]

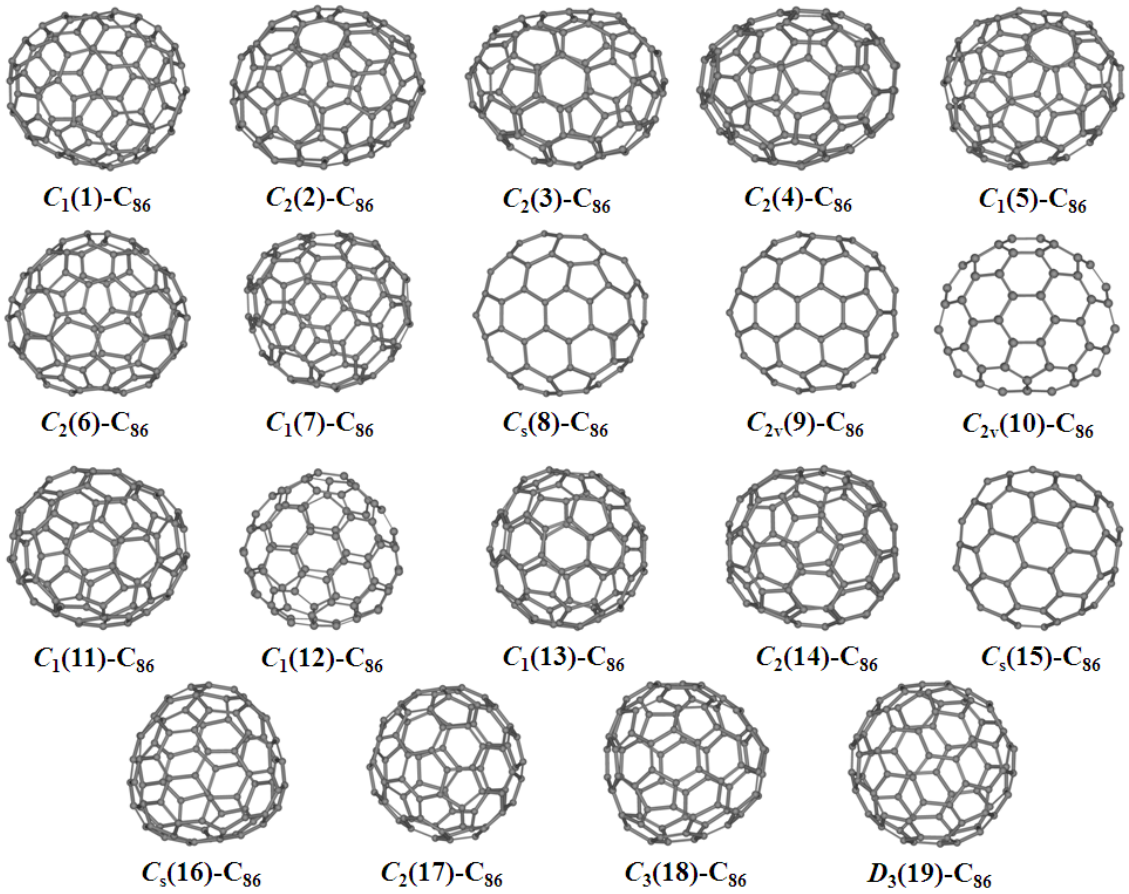


**Figure 2.22**. IPR fullerene isomers of $C_{86}$.

Black parallelepipeds of $Gd_3N@D_3$-$C_{86}$ • $Ni^{II}$(OEP) • $2C_6H_6$ were obtained by diffusion of a benzene solution of the endohedral fullerene into a benzene solution of $Ni^{II}$(OEP) and utilized in the crystal structure determination. The crystals were removed from the glass tubes in which they were grown together with a small amount of mother liquor and immediately coated with hydrocarbon oil on the microscope slide. Suitable crystals were mounted on glass fibers with silicone grease and placed in the cold dinitrogen stream of a Bruker ApexII diffractometer with graphite-monochromated Mo Kα radiation at 90(2) K.[62]

These crystals are isostructural with those of $Tb_3N@D_3$-$C_{86}$ • $Ni^{II}$(OEP) • $2C_6H_6$, whose structure was reported previously.[26] As seen in Figure 2.23, which shows the endohedral fullerene and its relationship to the nickel porphyrin, $Gd_3N@D_3$-$C_{86}$ has a flattened, chiral carbon cage. Unlike the recently encountered situations with $Gd_3N@C_2$(22010)-$C_{78}$, $Gd_3N@C_s$(39663)-$C_{82}$ and $Gd_3N@C_s$(51365)-$C_{84}$[10, 34, 39] where the carbon cage does not obey the IPR, the carbon cage in $Gd_3N@D_3$-$C_{86}$ does obey the IPR.

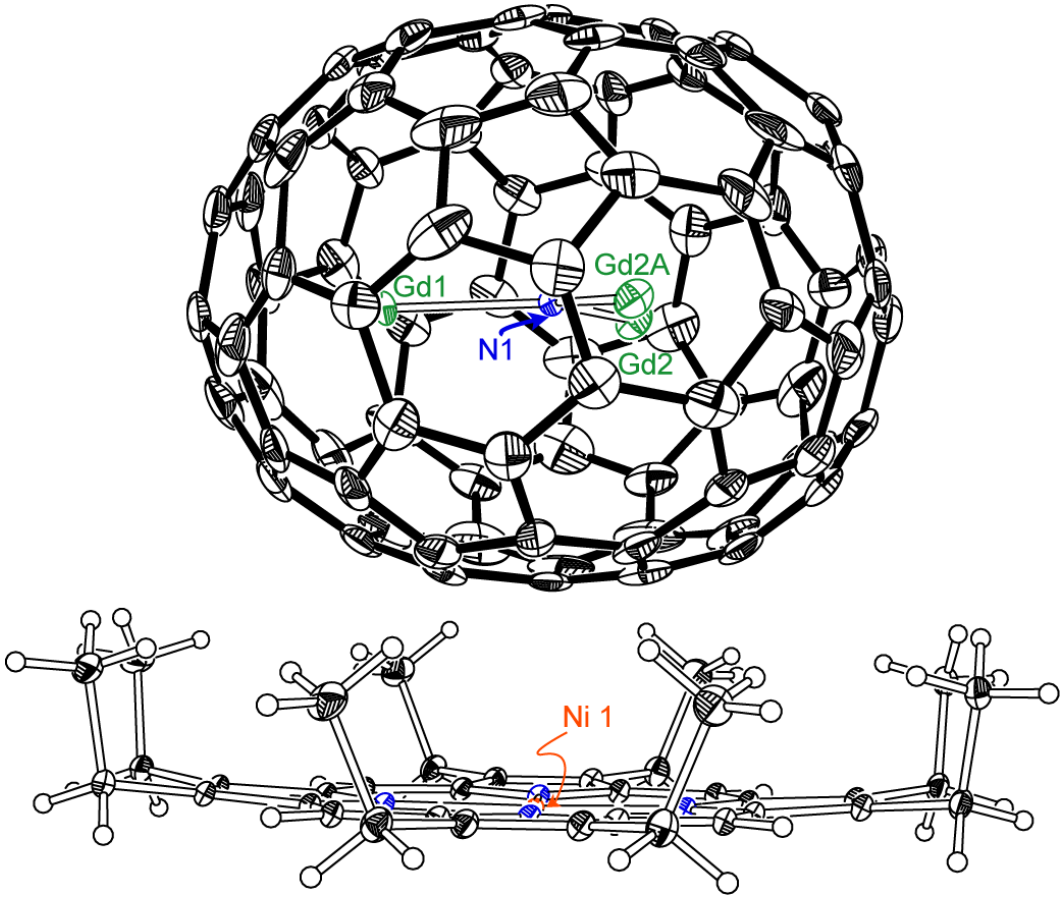


**Figure 2.23**. A drawing of $Gd_3N@D_3$-$C_{86}$ • $Ni^{II}$(OEP) • $2C_6H_6$ with 30% thermal contours. Only one orientation of the fullerene cage and the major sites for the gadolinium ions are shown.

Figure 2.24 shows a view of the endohedral fullerene looking down the three-fold axis. There are two equally populated orientations of the carbon cage that are related by a crystallographic mirror plane. Inside the cage, there is one nitrogen atom site, which is located on a mirror plane, and several sites for the gadolinium atoms. The major $Gd_3$ unit has 0.674(5) occupancy and involves Gd1, which is situated on a mirror plane, Gd2, and Gd2A. Alternate $Gd_3$ units consist of Gd3, Gd4A, Gd5, with 0.163(2) fractional occupancy and Gd3, Gd4B, Gd5 which have 0.163(2) fractional occupancy.

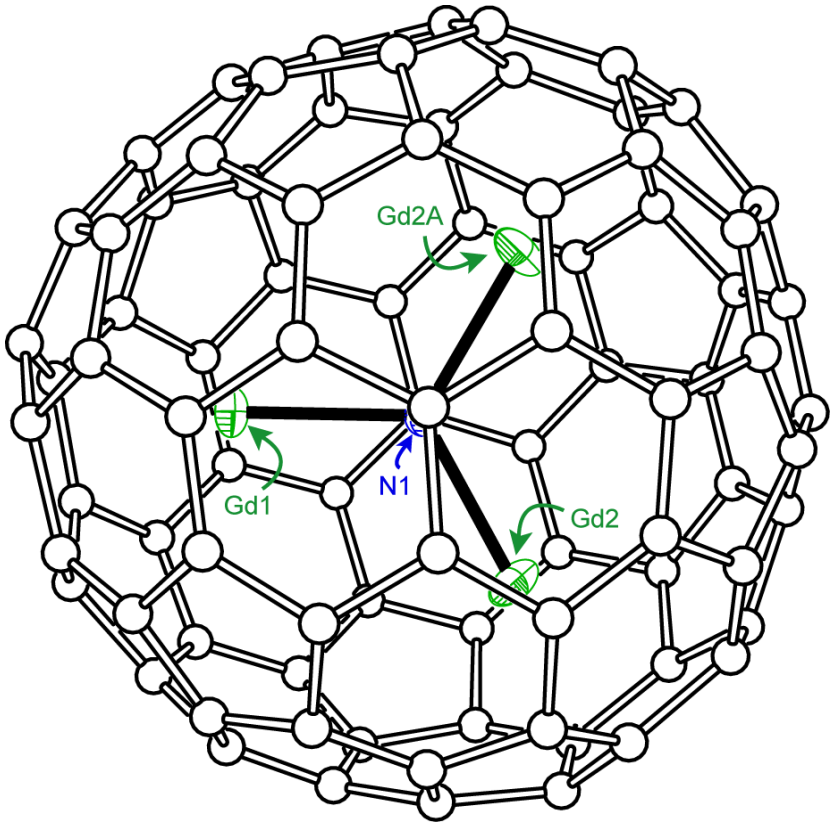


**Figure 2.24**. A drawing of $Gd_3N@D_3$-$C_{86}$ looking down the three-fold axis in crystalline $Gd_3N@D_3$-$C_{86}$ • $Ni^{II}$(OEP) • $2C_6H_6$. Only the major sites for the gadolinium ions are shown.

The $Gd_3N$ unit is planar in the major and minor sites. For the major site, the sum of the Gd-N-Gd angles is 359.46 °. In the major site, the $Gd_3N$ plane lies parallel to the plane of the porphyrin. The closest contact between the nickel atom of the porphyrin and the cage is the non-bonded Ni1···C86 distance of 2.954(5) Å. The Gd-N distances in the major site are: Gd1-N1, 2.168(3) Å and Gd2-N1, 2.1538(14) Å. It appears that, generally, the Gd-N distances increase in length as the fullerene cage size increases. Thus, in $Gd_3N@C_s$(51365)-$C_{84}$ the Gd-N distances are 2.177(8), 2.130(8), and 2.085(9) Å, while in $Gd_3N@C_s$(39663)-$C_{82}$ they are 2.152(5), 2.094(5), and 2.077(5) Å. In these two non-IPR endohedral fullerenes, the longest Gd-N distances are those that involve a gadolinium ion that resides near the fused pentagon system. In $Gd_3N@I_h$-$C_{80}$, which has a pyramidalized $Gd_3N$ unit, the Gd1-N distances are 2.117(5), 2.085(4), and 2.038(8) Å.[3]

## Redox Properties of the $Gd_3N@C_{2n}$ Family: Remarkably Low HOMO-LUMO Gap and Unusual Electrochemical Reversibility of $Gd_3N@C_{88}$ [6, 10, 63]

Cyclic voltammetry (CV) and Osteryoung Square Wave Voltammetry (OSWV) of the gadolinium nitride EMF family was performed in *o*-dichlorobenzene containing 0.05 M of $NBu_4PF_6$ as supporting electrolyte, using a 3 mm diameter glassy carbon disk as the working electrode. Ferrocene was added at the end of the experiments and used as an internal reference for measuring the potentials. The concentrations of the EMFs solutions in dichlorobenzene were all $10^{-4}$ M. A BAS-100B potentiostat controlled by a PC was used for all electrochemical experiments.

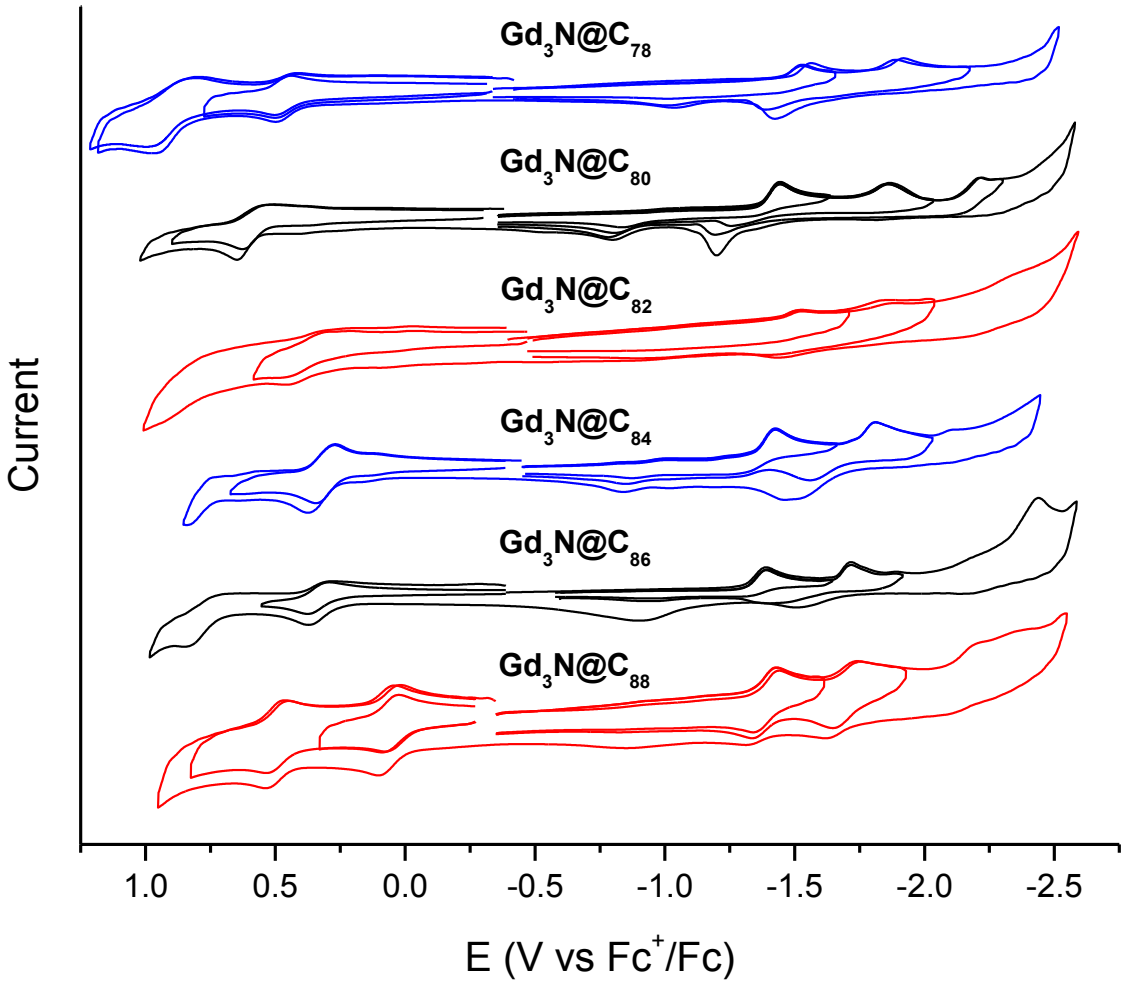


**Figure 2.25**. Cyclic voltammograms of $Gd_3N@C_{2n}$ ($39 \leq n \leq 44$) compounds obtained in *o*-DCB + 0.05 M $(nBu)_4NPF_6$ (scan rate 0.1 $Vs^{-1}$).

Figure 2.25 shows the CVs of the gadolinium nitride EMF family and Table 2.1 contains their redox potentials. The smallest member of the family, $Gd_3N@C_2$(22010)-$C_{78}$, exhibits two oxidation processes, the first being reversible and the second quasireversible. This compound also exhibits two irreversible one-electron reductions

$Gd_3N@D_3$-$C_{86}$ and the two non-IPR metallic nitride EMFs $Gd_3N@C_s$(39663)-$C_{82}$ and $Gd_3N@C_s$(51365)-$C_{84}$ showed three irreversible reductions and one reversible

oxidation process, a behavior qualitatively similar to that of the IPR-obeying $Gd_3N@I_h$-$C_{80}$. In contrast, for $Gd_3N@C_{88}$, both reductions and oxidations are reversible. Noteworthy, changing the cage size does not affect significantly the reduction potential of these compounds, which displayed very similar first reduction potentials (see table 2.1), but dramatically influenced their oxidation ability. These results strongly suggest that the HOMO of the metallic nitride EMFs are cage-centered (this concept will be further developed in chapter 4). A significant lowering of the electrochemical bandgap is observed when increasing the cage-size, from $C_{80}$ to $C_{88}$ resulting in a remarkable low HOMO-LUMO gap in $Gd_3N@C_{88}$.

**Table 2.1**. Redox potentials (in V vs $Fc^+/Fc$) of $Gd_3N@C_{2n}$ ($39 \leq n \leq 44$) compounds obtained In *o*-DCB + 0.05 M $(nBu)_4NPF_6$ (scan rate 0.1 $Vs^{-1}$).

| Compound | $Ep_c$ $red_1$ | $Ep_c$ $red_2$ | $E_{1/2}$ $ox_1$ | $E_{1/2}$ $ox_2$ | $\Delta E_{gap}$ |
|---|---|---|---|---|---|
| $Gd_3N@C_{78}$ | -1.53 | -1.89 | 0.47 | 1.00 ($E_p$) | 2.00 |
| $Gd_3N@C_{80}$ | -1.44 | -1.86 | 0.58 | | 2.02 |
| $Gd_3N@C_{82}$ | -1.53 | -1.87 | 0.38 | | 1.91 |
| $Gd_3N@C_{84}$ | -1.37 | -1.76 | 0.32 | | 1.69 |
| $Gd_3N@C_{86}$ | -1.39 | -1.72 | 0.33 | | 1.72 |
| $Gd_3N@C_{88}$ | -1.43 | -1.74 | 0.06 | 0.49 | 1.49 |

As mentioned earlier, two other gadolinium containing EMFs were isolated by HPLC. According to high resolution mass spectrometry these two compounds correspond to $Gd_2C_{90}$ and $Gd_2C_{92}$, and preliminary attempts to solve their crystal structure have been unsuccessful but suggest that these compounds could be metal carbide structures in which a $Gd_2C_2$ unit is encapsulated inside $C_{88}$ and $C_{90}$ fullerene cages respectively. Figure 2.26 shows the CVs of these two compounds, and it is observed that $Gd_2C_{90}$ and $Gd_2C_{92}$

exhibit at least six reductive events where the first three are reversible while the others are irreversible. In the anodic scan $Gd_2C_{90}$ exhibits three reversible oxidations while $Gd_2C_{92}$ shows only two. Remarkably, this behavior is quite different to the electrochemical properties of metallic nitride EMFs and even metal carbide EMFs with smaller carbon cages such as $Sc_2C_2@C_{82}$ and $Sc_3C_2@_{80}$ where up to three irreversible reductions and one irreversible oxidation event are observed.[7]

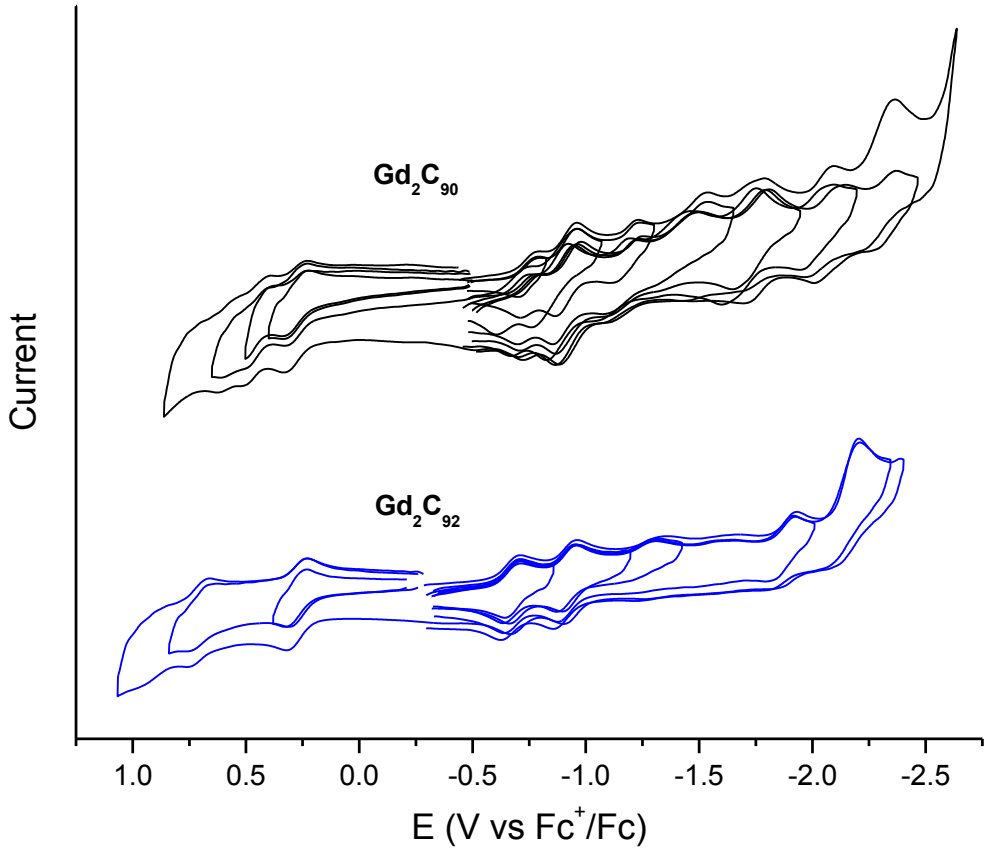


**Figure 2.26**. Cyclic voltammograms of $Gd_2C_{90}$ and $Gd_2C_{92}$ compounds obtained In *o*-DCB + 0.05 M $(nBu)_4NPF_6$ (scan rate 0.1 $Vs^{-1}$).

Interestingly, the OSWV of $Gd_2C_{92}$ (see Figure 2.27) exhibits six well behaved reduction peaks and two oxidation processes. Noteworthy, neither the CV nor the OSWV seems to show the presence of any isomeric impurity in the sample.

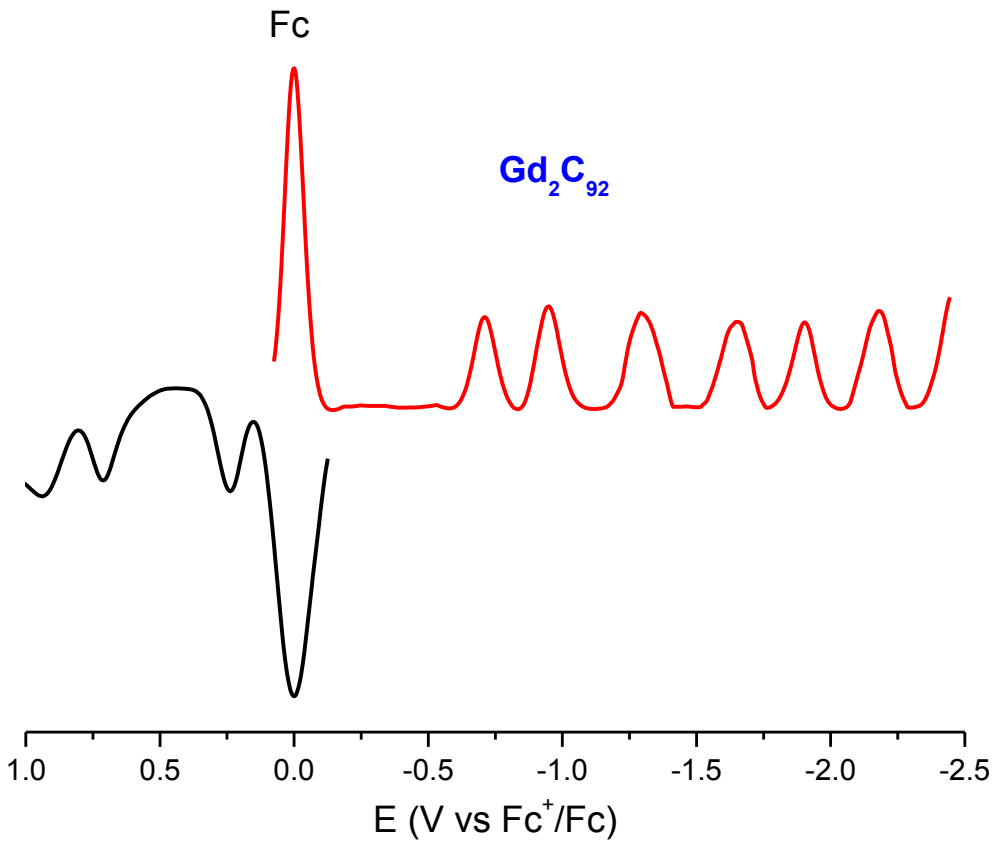


**Figure 2.27**. Osteryoung Square Wave Voltammetry of $Gd_2C_{92}$ obtained In *o*-DCB + 0.05 M $(nBu)_4NPF_6$ (scan rate 0.1 $Vs^{-1}$).

The $Gd_3N@C_{2n}$ represents the largest EMF family that have been isolated and characterized by X-ray and electrochemistry. Interestingly this is also the only family of EMFs with the most number of exceptions of the IPR. Electrochemical properties of $Gd_3N@C_{2n}$, in general, show similar reductive properties and a considerable decrease in

the first oxidation potential associated with an increase in the fullerene size. On the other hand, compounds $Gd_2C_{90}$ and $Gd_2C_{92}$ exhibit a rich electrochemistry with at least six reductive processes. Their very low HOMO-LUMO gaps enable them to be of potential use in many fields such as molecular electronics, photovoltaics and medical uses. X-ray characterization of their structures is still pending at the time this thesis is being written, but it is likely that they will be available in the near future.

## References and Notes


[1] Vlaardingerbroek, M.T.; den Boer, J.A. *Magnetic Resonance Imaging. Theory and Practice*, Springer Verlag, (Germany), **1996**.

[2] Cacheris, W.P.; Quay, S.C.; Rocklage, S.M. *Magn. Reson. Imaging*, **1990**, 8, 467-481.

[3] Stevenson, S.; Phillips, J.P.; Reid, J.E.; Olmstead, M.M; Rath. S.P.; Balch, A. *Chem. Commun*. **2004**, *24*, 2814-2815.

[4] Krause, M.; Dunsch, L. *Angew. Chem. Int. Ed*. **2005**, *44*, 1557-1560.

[5] Ge, Z.; Duchamp, J.C.; Cai, T.; Gibson, H.W.; Dorn, H.C. *J. Am. Chem. Soc*. **2005**, 127, 16292-16298.

[6] Chaur, M.N.; Melin, F.; Elliot, B.; Athans, J.A.; Walker, K.; Holloway, B.C.; Echegoyen, L. *J. Am. Chem. Soc*. **2007**, 129, 14826-14829.

[7] Chaur, M.N.; Melin, F.; Ortiz, A.L.; Echegoyen, L. *Angew. Chem. Int. Ed.* **2009**, 48, 7514-7538.

[8] Fowler, P.W.; Monolopoulos, D.E. *An Atlas of Fullerenes*, Clarendon Press, Oxford, 1995.

[9] Kroto, H.W. *Nature* **1987**, 329, 529-531.

[10] Beavers, C.M.; Chaur, M.N.; Olmstead, M.M.; Echegoyen, L.; Balch, A.L. *J. Am. Chem. Soc*. **2009**,

[11] Diederich, F.; Whetten, R. L.; Thilgen, C.; Ettl, R.; Chao, I.; Alvarez, M. M. *Science* **1991**, *254*, 1768−1770.

[12] Kikuchi, K.; Nakahara, N.; Wakabayashi, T.; Suzuki, S.; Shiromaru, H.; Miyake, Y.; Saito, K.; Ikemoto, I.; Kainosho, M.; Achiba, Y. *Nature* **1992**, *357*, 142−145.

[13] Taylor, R.; Langley, G. J.; Dennis, T. J. S.; Kroto, H. W.; Walton, D. R. M. *J. Chem. Soc., Chem. Commun.* **1992**, 1043−1044.

[14] Shustova, N. B.; Kuvychko, I. K.; Bolskar, R. D.; Seppelt, K.; Strauss, S. H.; Popov, A. A.; Boltalina, O. V. *J. Am. Chem. Soc.*, **2006**, *128*, 15793-15798.

[15] Olmstead, M. M.; de Bettencourt-Dias, A.; Duchamp, J. C.; Stevenson, S.; Marcui, D.; Dorn, H. C.; Balch, A. L. *Angew. Chem., Int. Ed.* **2001**, *40*, 1223-1225.

[16] Cao, B.; Wakahara, T.; Tsuchiya, T.; Kondo, M.; Maeda, Y.; Rahman,G. M. A. Akasaka,T.; Kobayashi, K.; Nagase, S.; Yamamoto, K. *J. Am. Chem. Soc.*, **2004**, *126*, 9164-9165.

[17] Yamada, M.; Wakahara, T.; Tsuchiya, T.; Maeda, Y.; Kako, M.; Akasaka, T.; Yoza, K.; Horn, E.; Mizorogi, N.; Nagase, S. *Chem. Commun.*, **2008**, 558-560.

[18] Cao, B.; Hasegawa, M.; Okada, K.; Tomiyama, T.; Okazaki, T.; Suenaga, K.; Shinohara, H. *J. Am. Chem. Soc.*, **2001**, *123*, 9679–9680.

[19] Yumura, T.; Sato, Y.; Suenaga, K.; Iijima S. *J. Phys. Chem*. B **2005**, *109*, 20251-20255.

[20] Otani, M.; Susumu Okada, S.; Oshiyama, A. *Chem. Phys. Lett*. **2007**, *438*, 274-278.

[21] Popov, A. A.; Krause, M.; Yang, S.; J. Wong, J.; Dunsch L. *J. Phys. Chem. B*, **2007**, 111, 3363-3369.

[22] Popov, A. A.; Dunsch, L. *J. Am. Chem. Soc*. **2007**, *129*, 11835-11849.

[23] A black block of dimensions 0.110 x 0.090 x 0.085 mm was mounted in the 90(2) K nitrogen cold stream provided by an Oxford Cryostream low temperature apparatus on the goniometer head of a Bruker D8 diffractometer equipped with an ApexII CCD detector, on beamline 11.3.1 at the Advanced Light Source in Berkeley, CA. Diffraction data were collected using synchrotron radiation monochromated with silicon(111) to a wavelength of 0.77490 Å. An approximate full sphere of data to $2\theta$=103° was collected using 0.3° ω scans. A multi-scan absorption correction was applied using the program SADABS-2008/1. A total of 567829 reflections were collected, of which 63384 were unique [R(int) = 0.0658] and 47323 were observed [I>2σ (I)]. The structure was solved by direct methods (SHELXS) and refined by full-matrix least-squares on $F^2$ (SHELXL97) using 3528 parameters.

The fullerene cage is chiral; two orientations of each enantiomer are present within the structure. The fullerene cage of one enantiomer was first identified and determined to have $C_2$ symmetry. Symmetry related geometric restraints were applied on related 1-2 and 1-3 distances, and the occupancy was decreased to allow the identification of a second orientation, which had the opposite enantiomeric geometry. This process was repeated and allowed the identification of four cage orientations. All four of the cages were kept isotropic with thermal parameter similarity restraints, while the cage occupancies were refined and summed to one.

Once the occupancies had converged, the cage carbon atoms of the major site were refined anisotropically, while the carbon atoms of the other three cages remained isotropic. The cage occupancies refined to 0.402(2), 0.232(3), 0.181(3) and 0.184(3). Due to the high level of overlap, refining the major cage anisotropically without the similarity restraints was not possible. Evidence for more, but decidedly minor, orientations of the cages are visible in the difference map, but these were not modelled.

The cage contents, $Gd_3N$, are also highly disordered, although the nitrogen atom position is unique. The trigonal planar unit $Gd_3N$ appears to rotate about the 2-fold axis of the fullerene, giving a spherical region of density that corresponds to one Gd and a toroidal region that corresponds to the other two. To accurately refine the Gd sites occupancies, the occupancies of the sites within the toroidal region were summed to 2, and the occupancies of the spherical region were summed to 1. Once the occupancies had converged, they were fixed at those values. Twenty-five Gd sites were refined. Only Gd1, Gd2 and Gd3 were identifiable as a viable $Gd_3N$ set; this set corresponds primarily to the major cage. The occupancies of Gd1, Gd2 and Gd3 were 0.36, 0.23, and 0.25 respectively. The difference in their occupancies is due to the other possible combinations of Gd sites that correspond to other cage orientations, some of which have not been modelled. Only Gd sites with occupancies greater than 5% were refined anisotropically.

The hydrogen atoms were generated geometrically and refined as riding atoms with C-H distances = 0.95- 0.99 Å and $U_{iso}(H)$ = 1.2 times $U_{eq}(C)$ for CH and $CH_2$ groups

and $U_{iso}(H)$ = 1.5 times $U_{eq}(C)$ for $CH_3$ groups. The maximum and minimum peaks in the final difference Fourier map were 4.874 and -2.795 eÅ$^{-3}$.

Crystal data: $C_{123}H_{53}N_5NiGd$, Mw = 2131.16 amu, monoclinic, C*2/c*, *a* = 24.9897(6) Å, *b* = 15.0876(4) Å, *c* = 39.2517(10) Å, β = 94.2080(10)°, V = 14759.4(6) Å$^3$, T = 90(2) K, Z = 8, R1 [I>2σ (I)] = 0.0960, *w*$R_2$ (all data) = 0.3026, GOF (on $F^2$) = 1.017.

[24] Stevenson, S.; Rice, G.; Glass, T.; Harich, K.; Cromer, F.; Jordan, M. R.; Craft, J.; Hadju, E.; Bible, R.; Olmstead, M. M.; Maitra, K.; Fisher, A. J.; Balch, A. L.; Dorn, H. C. *Nature*, **1999**, *401*, 55-57.

[25] Stevenson, S.; Lee, H. M.; Olmstead, M. M.; Kozikowski, C.; Stevenson, P.; Balch, A. L. *Chem. Eur. J.*, **2002**, *8*, 4528-4535.

[26] Zuo, T.; Beavers, C. M.; Duchamp, J. C.; Campbell, A.; Dorn, H. C.; Olmstead, M. M.; Balch, A. L. *J. Am. Chem. Soc*. **2007**, *129*, 2035-2043.

[27] Zuo, T.; Olmstead, M. M.; Beavers, C. M.; Balch, A. L.; Wang, G.; Yee, G. T.; Shu, C.; Xu, L.; Elliot, B.; Echegoyen, L.; Duchamp, J. C.; Dorn, H. C. *Inorg. Chem.*, **2008**, *47*, 5234-5244.

[28] Yang, S.; Troyanov, S. I.; Popov, A. A.; Krause, M.; Dunsch, L. *J. Am. Chem. Soc.*, **2006**, *128*, 16733-16739.

[29] Olmstead, M. M.; de Bettencourt-Dias, A.; Duchamp, J. C.; Stevenson, S.; Dorn, H. C.; Balch, A. L. *J. Am. Chem. Soc.*, **2000**, *122*, 12220-12226.

[30] Wang, X.; Zuo, T.; Olmstead, M. M.; Duchamp, J. C.; Glass, T. E.; Cromer, T. E.; Balch, A. L.; H. C. Dorn, H. C. *J. Am. Chem. Soc.*, **2006**, *128*, 8884-8889.

[31] Stevenson, S.; Chancellor, C. J.; Lee, H. M.; Olmstead, M. M.; Balch, A. L. *Inorg. Chem*., **2008**, *47*, 1420-1427.

[32] Cai, T.; Xu, L.; Anderson, M. R.; Ge, Z.; Zuo, T.; Wang, X.; Olmstead, M. M.; Balch, A. L.; Gibson, H. W.; Dorn, H. C. *J. Am. Chem. Soc*., **2006**, *128*, 8581-8589.

[33] Che, Y.; Yang, H.; Wang, Z.; Jin, H.; Liu, Z.; Lu, C.; Zuo, T.; Dorn, H. C.; Beavers, C. M.; Olmstead, M. M.; Balch, A. L. *Inorg. Chem*. **2009**, *48*, 6004-6010.

[34] Zuo, T., Walker, K., Olmstead, M. M., Melin, F., Holloway, B. C., Echegoyen, L., Dorn, H. C., Chaur, M. N., Chancellor, C. J., Beavers, C. M., Balch, A. L., Athans, A. J. *Chem. Commun.* **2008**, 1067.

[35] J. M. Campanera, C. Bo and J. M. Poblet, *Angew. Chem. Int. Ed*., 2005, **44**, 7230.

[36] Beavers, C.M.; Zuo, T.; Duchamp, J.C.; Harich, K.; Dorn, H.C.; Olmstead, M.M.; Balch, A. *J. Am. Chem. Soc*. **2006**, *128*, 11352-11353.

[37] $Gd_3N@C_s$(51365)-$C_{84}$ • Ni(OEP) • 2benzene, black blocks of $C_{132}H_{56}Gd_3N_5Ni$, M = 2242.28, triclinic, space group $P\bar{1}$, $a$ = 14.6344(11) Å, $b$ = 15.0158(11) Å, $c$ = 19.7975(14) Å, α = 85.319(2) °, β = 89.353(2) °, γ = 62.328(2) °, V = 3838.2(5) $Å^3$ at 90(2) K, μ(Mo-Kα) = 2.872 $mm^{-1}$, Z = 2. Refinement of 13632 reflections, 988 parameters, and 49 restraints yielded wR2 = 0.261 for all data and a conventional $R_1$ = 0.090 based on 8125 reflections with I > 2σ($I$).

[38] Park, S.S.; Liu, D.; Hagelberg, F. *J. Phys. Chem. A,* 2005, **109**, 8865.

[39] Mercado, B.C.; Beavers, C.M.; Olmstead, M.M.; Chaur, M.N.; Walker, K.; Holloway, B.C.; Echegoyen, L.; Balch, A.L. *J. Am. Chem. Soc*. **2008**, 130, 7854-7855.

[40] Chai, Y.; Guo, T.; Jin, C.; Haufler, R. E.; Felipe Chibante, L. P.; Fure, J.; Wang, L.; Alford, J. M.; Smalley, R. E. *J. Phys. Chem.* **1991**, *95*, 7564.

[41] Shinohara, H. in *Fullerenes; Chemistry, Physics and Technology*, Kadish, K. M.; Ruoff, R. eds. John Wiley and Sons, N. Y. **2000**, p. 357.

[42] (a) Akasaka, T.; Wakahara, T.; Nagase, S.; Kobayashi, K.; Waelchli, M.; Yamamoto, K.; Kondo, M.; Shirakura, S.; Okubo, S.; Maeda, Y.; Kato, T.; Kako, M.; Nakadaira, Y.; Nagahata, R.; Gao, X.; Van Caemelbecke, E.; Kadish, K. M. *J. Am. Chem. Soc.* **2000***, 122*, 9316. (b) Feng, L.; Tsuchiya, T.; Wakahara, T.; Nakahodo, T.; Piao, Q.; Maeda, Y.; Akasaka, T.; Kato, T.; Yoza, K.; Horn, E.; Mizorogi, N.; Nagase, S. *J. Am. Chem. Soc.* **2006**, *128*, 5990.

[43] Akasaka, T.; Wakahara, T.; Nagase, S.; Kobayashi, K.; Waelchli, M.; Yamamoto, K.; Kondo, M.; Shirakura, S.; Maeda, Y.; Kato, T.; Kako, M.; Nakadaira, Y.; Gao, X.; Van Caemelbecke, E.; Kadish, K. M. *J. Phys. Chem. B*. **2001**; *105*, 2971.

[44] Feng, L.; Wakahara, T.; Tsuchiya, T.; Maeda, Y.; Lian, Y.; Akasaka, T.; Mizorogi, N.; Kobayashi, K.; Nagase, S. Kadish, K. M. *Chem. Phys. Lett*. **2005**; *405*, 274.

[45] Olmstead, M. M.; de Bettencourt-Dias, A.; Stevenson, S.; Dorn, H. C.; Balch, A. L. *J. Am. Chem. Soc.* **2002***, 124*, 4172.

[46] Olmstead, M. M.; Lee, H. M.; Stevenson, S.; Dorn, H. C.; Balch, A. L. *Chem. Commun.* **2002**, 2688.

[47] Krause, M.; Wong, J.; Dunsch, L.; *Chem. Eur. J.* **2005**, 11, 706-711.

[48] Yang, S.; Dunsch, L.; *J. Phys. Chem. B* **2005**, 109, 12320-12328.

[49] Crystal data for $C_{82}NGd_3 \bullet C_{36}H_{44}N_4Ni \bullet 2(C_6H_6)$, black parallelepiped, triclinic, space group *P1bar*, $a$ = 14.6044(17) Å, $b$ = 14.9475(17) Å, $c$ = 19.842(2) Å, α = 85.636(2) °, δ = 88.649(2) °, γ = 61.500(1) °, $V$ = 3795.2(7) Å$^3$, $Z$ = 2, $D_c$ = 1.941 Mg/m$^3$, $T$ = 150(2) K; R1 = 0.0629, wR2 = 0.1555 for all data; conventional R1 = 0.1007 computed for 19622 observed data ($I > 2\sigma(I)$) with 123 restraints and 1401 parameters.

[50] Summerscales, O. T.; J. G. N. Cloke, *Coord. Chem. Revs*. **2006**, *250*, 1122.

[51] Wang, C.R.; Kai, T.; Tomiyama, T.; Yoshida, T.; Kobayashi, Y.; Nishibori, E.; Takata, M.; Sakata, M.; Shinohara, H. *Nature*, **2000**, 408, 426-427.

[52] S. Stevenson, P.W. Fowler, T. Heine, J.C. Duchamp, G. Rice, T. Glass, K. Harich, E. Hajdu, R. Bible, H.C. Dorn, *Nature* **2000**, 408, 427-428.

[53] T. Wakatsugu, H. Nikawa, T. Kikuchi, T. Nakahodo, G.M.A. Rahman, T. Tsuchiya, Y. Maeda, T. Akasaka, K. Yoza, E. Horn, K. Yamamoto, N. Mizorogi, Z. Slanina, S. Nagase. *J. Am. Chem. Soc.* **2006**, 128, 14228-14229.

[54] Shi, Z.Q.; Wu, X.; Wang, C.R.; Lu, X.; Shinohara, H. *Angew. Chem. Int. Ed*. **2006**, 45, 2107-2111.

[55] Yang, S.; Popov, A.A.; Dunsch, L. *Angew. Chem. Int. Ed*. **2007**, 46, 1256-1259.

[56] Yang, S.; Popov, A.A.; Dunsch, L. *J. Phys. Chem. B* **2007**, 111, 13659-13663.

[57] Kato, H.; Taninaka, A.; Sugai, T.; Shinohara, H. *J. Am. Chem. Soc*. **2003**, 125, 7782-7783.

[58] Yamada, M.; Wakahara, T.; Tsuchiya, T.; Maeda, Y.; Akasaka, T.; Mizorogi, M.; Nagase, S. *J. Phys. Chem. A* **2008**, 112, 7627-7631.

[59] a) Lu, X.; Nikawa, H.; Nakahodo, T.; Tsuchiya, T.; Ishitsuka, M.O.; Maeda, Y.; Akasaka, T.; Toki, M.; Sawa, H.; Slanina, Z.;Mizorogi, N.; Nagase. S. *J. Am. Chem. Soc*. **2008**, 130, 9129-9136. b) Lu, X.; Nikawa, H.; Tsuchiya, T.; Maeda, Y.; Ishitsuka, M.O.; Akasaka, T.; Toki, M.; Sawa, H.; Slanina, Z.; Mizorogi, N.; Nagase. S. *Angew. Chem. Int. Ed*. **2008**, 47, 8642-8645.

[60] Xie, S. Y.; Gao, F.; Lu, X.; Huang, R. B.; Wang, C. R.; Zhang, X.; Liu, M. L.; Deng, S. L.; Zheng, L. S. *Science* **2004**, *304*, 699.

[61] Wang, C. R.; Shi, Z. Q.; Wan, L. J.; Lu, X.; Dunsch, L.; Shu, C. Y.; Tang, Y. L.; Shinohara, H. *J. Am. Chem. Soc.* **2006**, *128* (20), 6605-6610.

[62] The structure was solved by direct methods and refined using all data (based on $F^2$) using the software of SHELXS97 and SHELXL97. A semi-empirical method utilizing equivalents was employed to correct for absorption. Hydrogen atoms were located in a difference map, added geometrically, and refined with a riding model.

The asymmetric unit consists of 86 carbon atoms in general positions at half occupancy that represent the fullerene , one-half of the nickel porphyrin, and two half molecules of benzene. The nickel porphyrin resides on a mirror plane that bisects N2, Ni and N4. One of the benzene molecules resides in a general position that is disordered with respect to a crystallographic mirror plane, while the other benzene molecule resides on a mirror plane. The enantiomer of the fullerene cage at equal occupancy is produced by reflection through the mirror plane.

Crystal data for $C_{86}NGd_3 \bullet C_{36}H_{44}N_4Ni \bullet 2(C_6H_6)$, black parallelepiped, triclinic, space group C2/m, $a$ = 25.2056(8) Å, $b$ = 15.4634(5) Å, $c$ = 19.9594(6) Å, β = 92.520(2) °, $V$ = 7771.9(4) Å$^3$, $Z$ = 4, $D_c$ = 1.937 Mg/m$^3$, $T$ = 90(2) K; R1 = 0.071, wR2 = 0.173 for all data; conventional R1 = 0.061 computed for 15037 observed data ($I > 2\sigma(I)$) with 1046 parameters and 1083 restraints.

[63] Chaur, M. N.; Athans, A.J.; Echegoyen, L. *Tetrahedron* **2008**, 64, 11387-11393.

CHAPTER THREE

# THE LARGER METALLIC NITRIDE ENDOHEDRAL FULLERENES

As mentioned in the introductory chapter the field of trimetallic nitride endohedral fullerenes began in 1999 with the discovery of $Sc_3N@C_{80}$ by Dorn and coworkers.[1] They vaporized graphite rods packed with scandium oxide in a Krätschmer–Huffman arc reactor under a mixture of nitrogen and helium. Later, Dunsch and coworkers showed that the same compound can be obtained in higher yields under a mixture of helium and ammonia.[2] Scandium is the smallest metal that has been shown to form a trimetallic nitride cluster inside a fullerene. The conditions described by Dunsch et al. afford mainly $Sc_3N@C_{80}$ in high yields, as compared to mono-, di-, or tri-EMFs,[3] along with small amounts of $Sc_3N@C_{68}$ and $Sc_3N@C_{78}$ (Figure 1, top HPLC trace). Over the years, the family of trimetallic nitride endohedral fullerenes has been considerably expanded with the encapsulation of a new Group 3 metal (Y),[2] lanthanides (Er,[1] Ho,[2,8] Lu,[4] Tm,[5] Gd,[6,7] Dy,[9] Tb[8, 10]), and mixed metal clusters.[1, 11] Upon increasing the size of the encapsulated metal (from Sc to Gd), the yield of cluster fullerenes usually decreases, and a distribution of molecules is obtained, with cages as large as $C_{88}$. However, the $C_{80}$ cage, however, remains the most abundant. For instance, the $Y_3N@C_{2n}$ family consists mainly of $Y_3N@C_{80}$ along with small amounts of $Y_3N@C_{82}$, $Y_3N@C_{84}$, $Y_3N@C_{86}$, and $Y_3N@C_{88}$ (Figure 3.1, bottom trace; for MALDI data, see Figure 3.2). For the compounds for which the $C_{80}$ is the most abundant product, dysprosium gives the largest distribution of molecules reported to date, where the smallest cage produced is $C_{76}$ and the largest is $C_{98}$.[9] In the case of $Gd_3N$, which was the largest cluster encapsulated

until the work reported herein, $C_{78}$ was the smallest carbon cage obtained, and the relative abundance of the bigger cages ($C_{82}$, $C_{84}$, $C_{86}$, and $C_{88}$) is higher than that obtained with the other metals.[7]

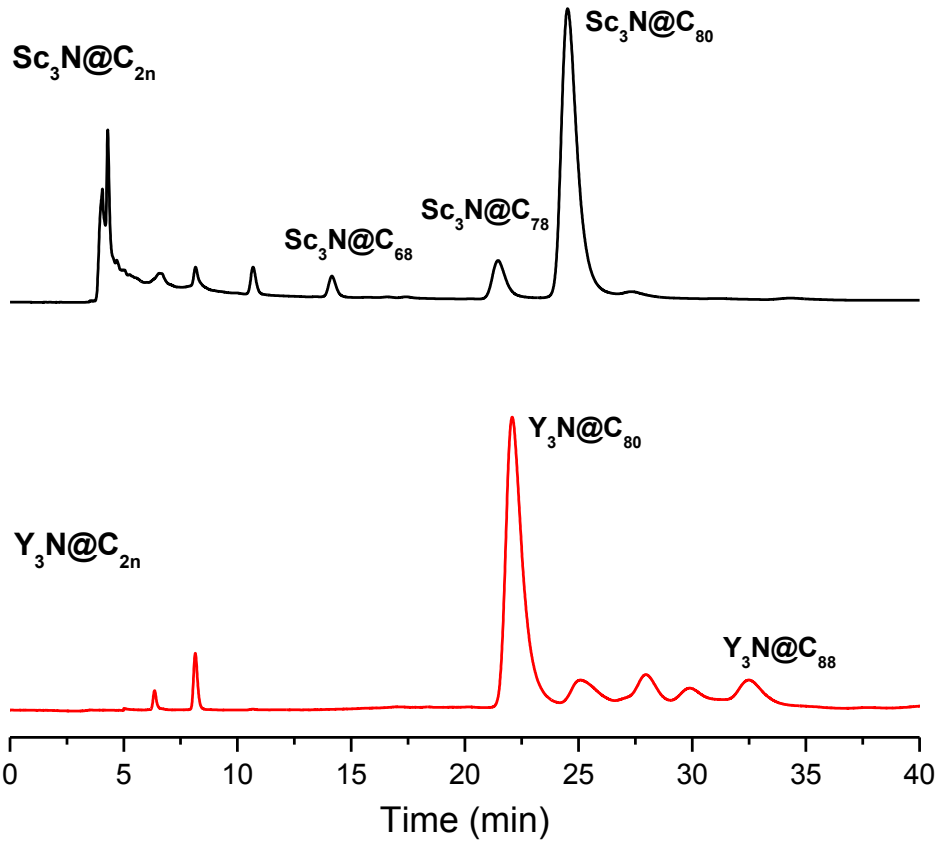


**Figure 3.1**. HPLC chromatograms of the $Sc_3N@C_{2n}$ and $Y_3N@C_{2n}$ EMFs. Buckyprep-M column, mobile phase toluene, flow rate 4.0 mL/min. A UV detector was utilized, monitoring at 370 nm.

Calculations and experimental observations have given insight into the exceptionally high abundance of the $C_{80}$ cage, which is preferentially observed even with clusters as large as $Gd_3N$. Poblet and co-workers linked this stability to a large HOMO–LUMO gap and have calculated that among all fullerenes that satisfy the isolated

pentagon rule (IPR) from $C_{60}$ to $C_{84}$, $C_{80}$ :7 ($I_h$) and $C_{80}$:6 ($D_{5h}$) provide the largest HOMO–LUMO gap after encapsulating a metallic nitride cluster.[12] Raman and IR spectroscopy studies have also shown that a mutual stabilization of the cluster and the $C_{80}$ cage through cluster–cage charge transfer could explain the high abundance of this cage.[7, 13] However, the stabilization of cages bigger than $C_{80}$ with clusters larger than $Gd_3N$ cannot be ruled out. No reports of the encapsulation of larger clusters, such as $La_3N$, inside fullerene cages had appeared in the literature until our group started the search for the synthesis of larger fullerene cages.

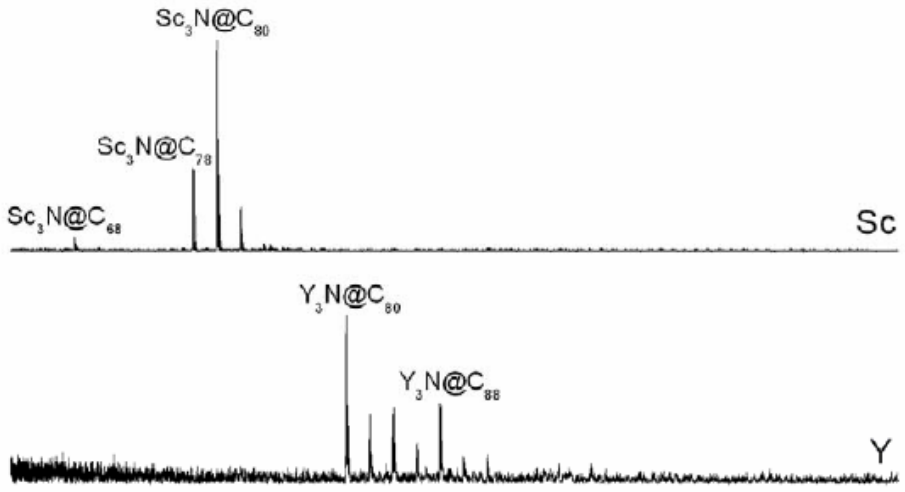


**Figure 3.2**. MALDI-TOF MS of the $Sc_3N@C_{2n}$ and $Y_3N@C_{2n}$ EMFs.

In this chapter we will present three breakthroughs in the field of metallic nitride EMF research, the introduction of $Nd_3N@C_{88}$, the most abundant member of the $Nd_3N@C_{2n}$ family and the first metallic nitride cluster that prefers to be encapsulated in a fullerene cage larger than $C_{80}$. Then we will see that not only $Nd_3N$ clusters are preferentially encapsulated inside the $C_{88}$ cage but also other larger clusters such as $Pr_3N$

and $Ce_3N$. Finally the synthesis of $La_3N@C_{2n}$ metallofullerenes will show that besides the $C_{80}$ and $C_{88}$ template there are at least two more templated cages, $C_{96}$ and $C_{104}$.

## The Large $Nd_3N@C_{2n}$ ($40 \leq n \leq 49$) Clusterfullerene Family: First Preferential Templating of a $C_{88}$ Cage by a Trimetallic Nitride Cluster [14]

This section reports the preparation of $Nd_3N@C_{2n}$ ($40 \leq n \leq 49$) and the predominance of the larger $C_{88}$ cage. These endohedral fullerenes were obtained by arc burning of high purity graphite rods containing neodymium oxide under a mixture of ammonia (20 mbar) and helium (200 mbar). Rods containing 10% $Nd_2O_3$ seemed to give the best yield (0.2 mg per rod) of $Nd_3N@C_{2n}$ in the soluble extract of the soot. The new family of cluster fullerenes was characterized by mass spectrometry and HPLC. The most abundant species ($Nd_3N@C_{88}$) was also studied by UV/Visible/NIR spectroscopy and electrochemistry.

### Identification and Isolation

MALDI-TOF mass spectrometry analysis of the crude mixture of $Nd_3N@C_{2n}$ reveals the presence of at least ten different compounds in this family (Figure 3.3), with cages ranging from $C_{80}$ to $C_{98}$ and the highest peak corresponding to $Nd_3N@C_{88}$. The mass spectrum also shows very low amounts of $Nd_3N@C_{80}$ and $Nd_3N@C_{82}$ EMFs.

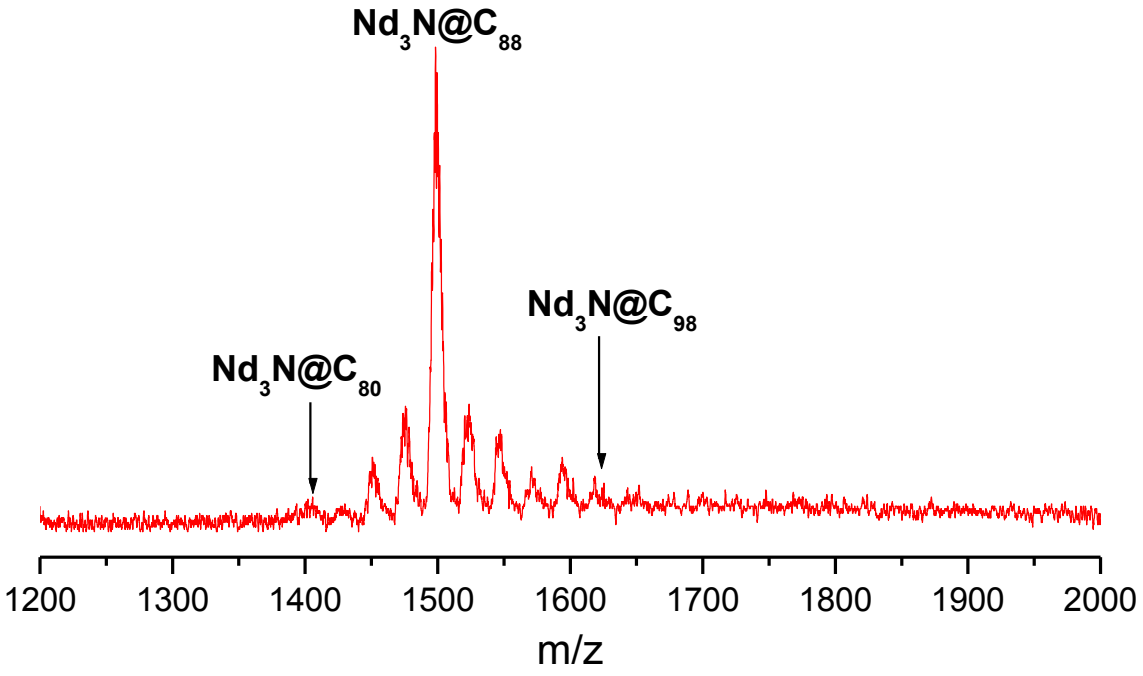


**Figure 3.3**. MALDI-TOF MS of the crude mixture of $Nd_3N@C_{2n}$ EMF family.

On the other hand, five distinct peaks in the range 20–40 min can be seen in the HPLC trace (Figure 3.4). The identity of the peaks observed in the HPLC trace was established by MALDI-TOF mass spectrometry analysis after isolation. The compound with a retention time of 24 min (fraction1) can be identified as $Nd_3N@C_{80}$. Its retention time is comparable to that of $Sc_3N@C_{80}$ (24.7 min). The second peak in the HPLC trace (retention time 27.1 min, fraction 2) corresponds to $Nd_3N@C_{84}$. The fourth and highest peak (retention time 31.6 min, fraction 4) corresponds to $Nd_3N@C_{88}$. Its retention time is close to that of $Y_3N@C_{88}$ (32.7 min). Both the HPLC trace and MALDI-TOF spectra show that it is the most abundant species in the soluble extract of the arced soot. The amount of material collected after isolation of each fraction confirmed that $Nd_3N@C_{88}$ is the most abundant species.

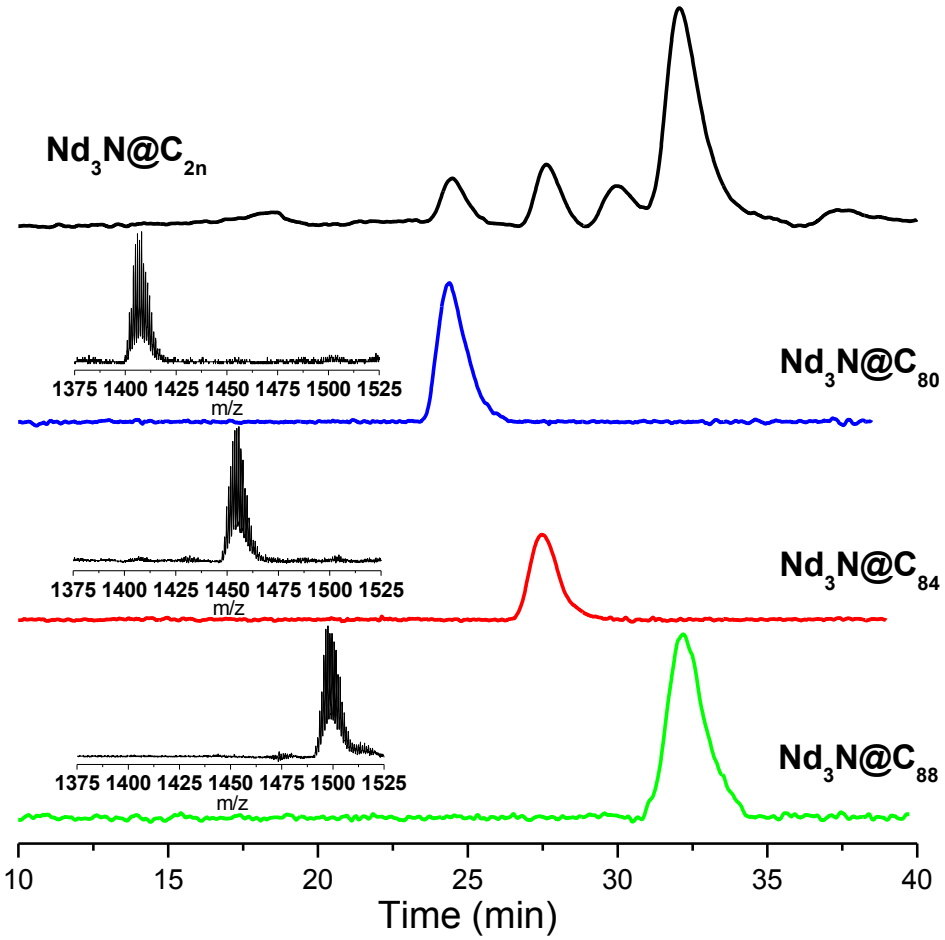


**Figure 3.4**. HPLC chromatograms and MALDI-TOF MS of the $Nd_3N@C_{2n}$ mixture and isolated fractions. Buckyprep-M column, mobile phase toluene, flow rate 4.0 mL/min, detection 370 nm.

A sample of $Nd_3N@C_{88}$ was also deposited on a TEM grid and submitted to an energy dispersive spectroscopy (EDS) analysis. The spectrum shows the characteristic peaks of neodymium (Figure 3.5). The compound corresponding to the third peak in the HPLC trace was more difficult to isolate in pure form, owing to the close proximity of its retention time to the most abundant species. It can be tentatively assigned as $Nd_3N@C_{86}$.

The fifth peak of the HPLC trace (retention time 36 min) has not been characterized, owing to its very low intensity.

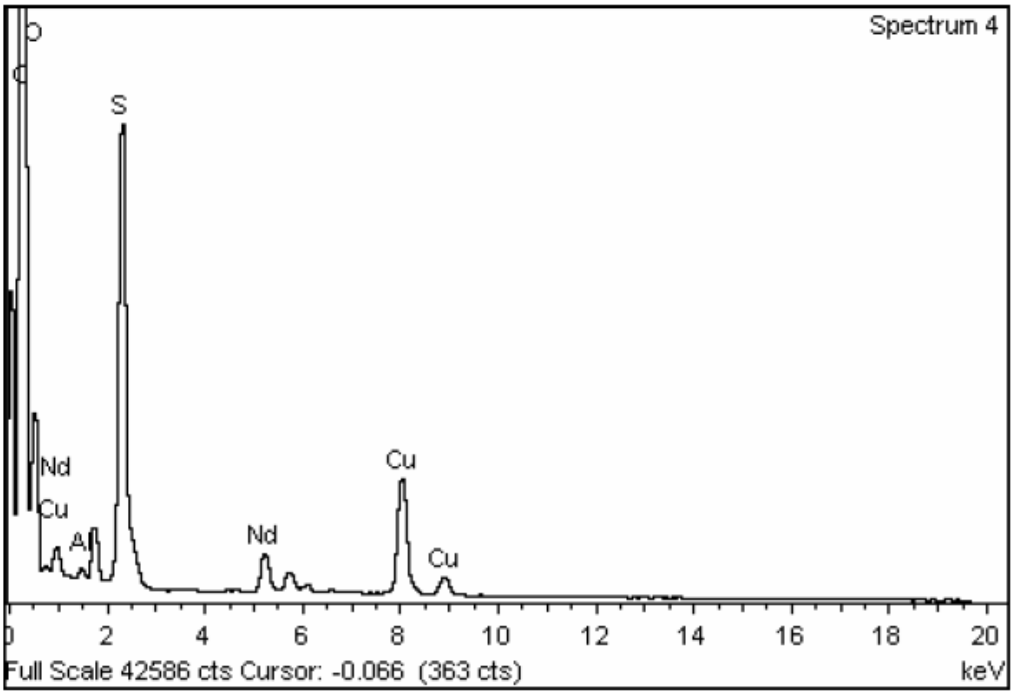


**Figure 3.5**. Energy Dispersive Spectroscopy (EDS) spectrum of the $Nd_3N@C_{88}$ fraction after HPLC. Copper and aluminium are coming from the grid and sample holder. Sulfur and oxygen are probably coming from the solvents used to manipulate the samples (ether, carbon disulfide).

Although neodymium is only slightly larger than gadolinium (Table 3.1), these studies show that the cage-size distributions of $Gd_3N@C_{2n}$ and $Nd_3N@C_{2n}$ are dramatically different. $C_{88}$ is the most abundant species (relative yield 30–40% as established by HPLC) in the case of neodymium, whereas the $C_{80}$ cage is still predominant for gadolinium (relative yield 35–40%).[7] However, the relative abundance of the other cages encapsulating these two clusters (the smaller cages $C_{80}$, $C_{84}$, and $C_{86}$

for neodymium and the bigger cages $C_{82}$, $C_{84}$, $C_{86}$, and $C_{88}$ for gadolinium) is far from negligible. It appears that the cluster $Gd_3N$ is the upper threshold for stabilization of the $C_{80}$ cage and that, similarly, the $Nd_3N$ cluster is the lower threshold for stabilization of the $C_{88}$ cage. Interestingly, the yield of $Nd_3N@C_{2n}$ (0.2 mg per rod) was found to be higher than those of $Y_3N@C_{2n}$ and $Gd_3N@C_{2n}$ and slightly less than that of $Sc_3N@C_{80}$ (0.3 mg per rod). The possibility to accommodate the $Nd_3N$ cluster in bigger cages than the $Gd_3N$ cluster apparently results in higher yields.

**Table 3.1**. Size of the metallic ion $M^{3+}$ (octahedral coordination) [15] and of the cluster $M_3N$ for some group III and lanthanides elements.

| Metal M | Sc | Y | Dy | Gd | Nd | La |
|---|---|---|---|---|---|---|
| $r(M^{3+})$ Å | 0.75 | 0.90 | 0.91 | 0.94 | 0.98 | 1.05 |
| $d(M_3N)$ Å[a] | 3.00 | 3.60 | 3.64 | 3.76 | 3.92 | 4.20 |

[a] Calculated using the formula commonly used in the literature $d(M_3N)=4\ r(M^{3+})$[7b]

Owing to its relatively high yield, $Nd_3N@C_{88}$ could be easily isolated in high purity (greater than 95%, see Figure 3.4) and in amounts allowing characterization by UV/Vis/NIR spectroscopy (see Figure 3.6) and electrochemistry (Figure 3.7). The $Nd_3N@C_{88}$ spectrum shares some common characteristics with another metallic nitride cluster encapsulated in a $C_{88}$ cage (Table 3.2). The band gap obtained from the spectral onset is comparable to that of $Dy_3N@C_{88}$ [9] and is significantly lower than that usually obtained for the trimetallic nitride clusters encapsulated in $C_{80}$ cages. $Nd_3N@C_{88}$ also exhibits two absorptions in the NIR region; such behavior was previously observed only

for the $C_{88}$ cage in the $Dy_3N@C_{2n}$ family. These spectral similarities suggest that these two metallic nitride EMFs may share a fullerene cage of the same symmetry.

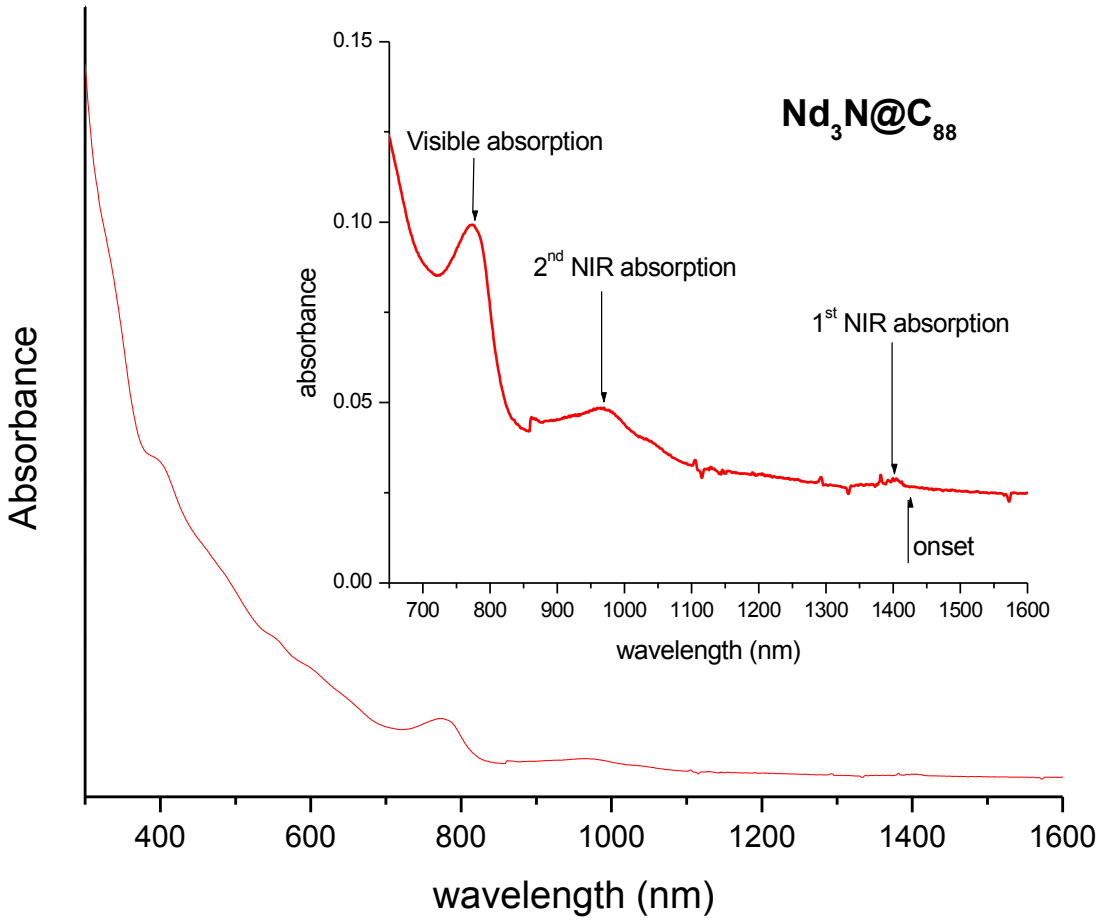


**Figure 3.6**. UV/Vis-NIR spectrum of $Nd_3N@C_{88}$ dissolved in toluene.

**Table 3.2**. Comparison of the spectral characteristics of $Dy_3N@C_{88}$ and $Nd_3N@C_{88}$.

| EMF | Onset (nm) | Band-gap[a] (eV) | UV-Vis-NIR peaks (nm) |
|---|---|---|---|
| $Dy_3N@C_{88}$ | 1548 | 0.80 | 345, 733, 1045, 1462 |
| $Nd_3N@C_{88}$ | 1500 | 0.83 | 390,770,965,1400 |

[a] Calculated from the onset using a published formula: band-gap (eV)≈1240/onset (nm)[8]

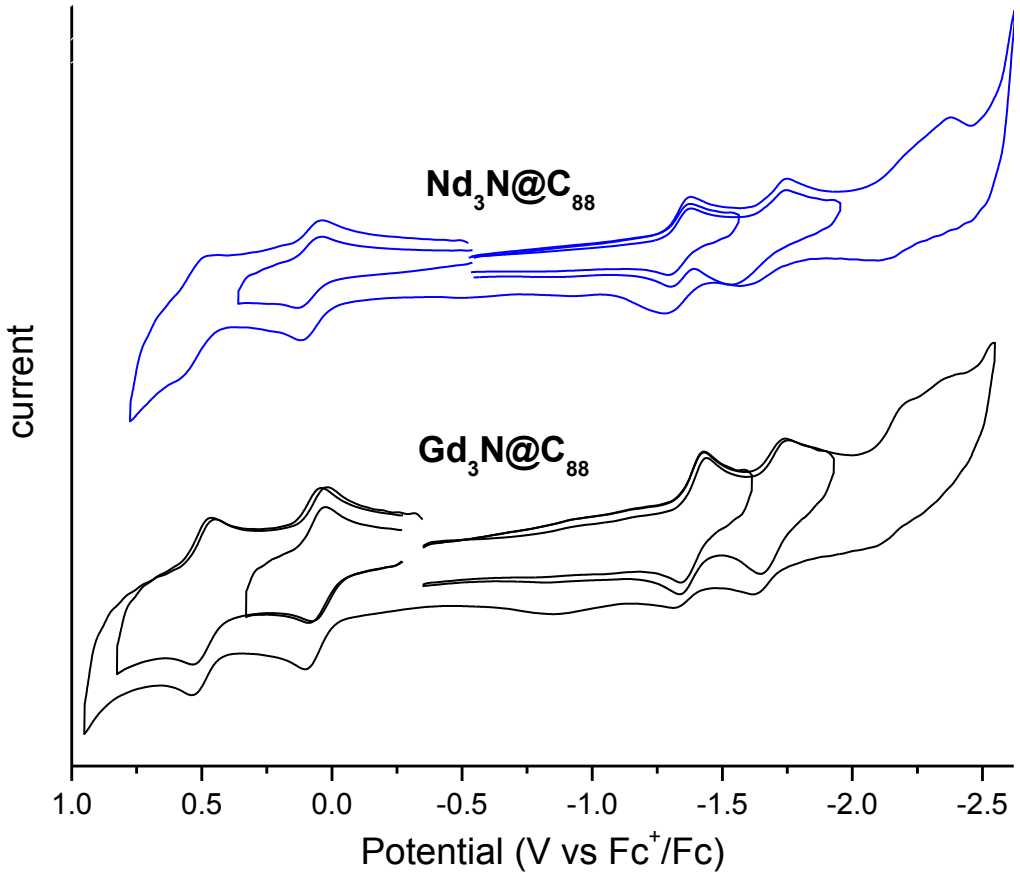


**Figure 3.7**. Cyclic voltammograms of $Nd_3N@C_{88}$ and $Gd_3N@C_{88}$ compounds obtained in *o*-DCB + 0.05 M $(nBu)_4NPF_6$ (scan rate 0.1 $Vs^{-1}$)

The cyclic voltammogram of $Nd_3N@C_{88}$ shows three cathodic waves; the first is monoelectronic and reversible, while the second is monoelectronic and quasireversible. The third wave is less well defined and could be multielectronic. Anodically, the compound showed two waves; the first was monoelectronic and reversible, but the second was not very well defined. The redox behavior of $Nd_3N@C_{88}$ is significantly different from that of the reported nonderivatized $M_3N@C_{80}$ species, which always exhibit irreversible reduction steps in *o*-DCB and very similar to that of $Gd_3N@C_{88}$.[16, 7a]

The electrochemical HOMO–LUMO gap obtained for $Nd_3N@C_{88}$ (1.40 V) is also significantly smaller than that usually obtained for $M_3N@C_{80}$ (see Table 3.3).[16]

**Table 3.3**. Redox potentials (in V vs $Fc^+/Fc$) of $C_{60}$, $Sc_3N@C_{80}$ (reference 16a), $Dy_3N@C_{80}$ (reference 16b), $Nd_3N@C_{88}$ and $Gd_3N@C_{88}$ (reference 7a) compounds obtained In *o*-DCB + 0.05 M $(nBu)_4NPF_6$ (scan rate 0.1 $Vs^{-1}$).

| **Compound** | **$Ep_c$ $red_1$** | **$E_{1/2}$ $ox_1$** | **$\Delta E_{gap}$** |
|---|---|---|---|
| $C_{60}$ | $E_{1/2=}$-1.18 | 1.33 | 2.51 |
| $Sc_3N@C_{80}$ | -1.26 | 0.59 | 1.88 |
| $Dy_3N@C_{80}$ | -1.37 | 0.70 | 2.11 |
| $Nd_3N@C_{88}$ | $E_{1/2}$=-1.37 | 0.07 | 1.40 |
| $Gd_3N@C_{88}$ | $E_{1/2}$=-1.43 | 0.06 | 1.49 |

The new $Nd_3N@C_{2n}$ family of metallic nitride EMFs shows very interesting features and gives answers to several questions concerning the influence of the size of the encapsulated cluster on the yield of endohedral fullerenes and the cage-size distribution. The limit of stability of the $C_{80}$ cage is now reached, since the cluster $Nd_3N$ prefers to be encapsulated in the small-band-gap $C_{88}$ cage. Interestingly, the transition between the predominance of the $C_{80}$ cage, which is still observed for $Gd_3N$, and the predominance of the $C_{88}$ cage, which is observed for the first time with $Nd_3N$, comes with an increase in the yield of production.

## New $M_3N@C_{2n}$ Endohedral Metallofullerene Families (M=Nd, Pr, Ce and $40 \leq n \leq 53$): Expanding the Preferential Templating of the $C_{88}$ Cage and Approaching the $C_{96}$ Cage[17]

Two additional new families of metallic nitride EMFs, based on cerium and praseodymium were synthesized by vaporizing packed graphite rods in a conventional Krätschmer-Huffman arc reactor. Each of these families of metallofullerenes was identified and characterized by mass spectroscopy, HPLC, UV/Vis-NIR spectroscopy, and cyclic voltammetry. The mass spectra and HPLC chromatograms show that these larger metallic clusters are preferentially encapsulated by a $C_{88}$ cage. When the size of the cluster is increased, the $C_{96}$ cage is progressively favored over the predominant $C_{88}$ cage. It is also observed that the smaller cages ($C_{80}$-$C_{86}$) almost disappear on going from neodymium to cerium endohedral metallofullerenes. The UV/Vis-NIR spectra and cyclic voltammograms confirm the low HOMO-LUMO gap and reversible electrochemistry of these $M_3N@C_{88}$ metallofullerenes.

Until recently, all of the isolated EMFs had a common characteristic, that is, the preferential templating of $C_{80}$ cages. This is favored for most metallic clusters owing to an electronic stabilization between the metallic cluster and the fullerene cage,[12] which gives $M_3N@C_{80}$ (M=metal) as the most abundant species in the fullerene soot after the arcing process. In the previous section we reported the $Nd_3N@C_{2n}$ EMF family[14] that showed for the first time preferential templating of a larger cage ($C_{88}$), which was probably the result of both the size and the electronic stabilization of the cluster. This result prompted the question of whether a $C_{88}$ cage is the maximum size limit for

metallofullerenes or if larger clusters would favor still larger cages, and if so, which cages would those be?

**Synthesis and identification of the $M_3N@C_{2n}$ (M= Nd, Pr, and Ce) endohedral metallofullerene families**

Graphite rods were packed with a mixture of the corresponding metal oxide and graphite powder and then burned in a $He/NH_3$ atmosphere. For the synthesis of $Nd_3N@C_{2n}$ ($40 \leq n \leq 50$) and $Pr_3N@C_{2n}$ ($40 \leq n \leq 52$), a 1:1 graphite/metal oxide mixture gave the highest yield of metallofullerenes (0.2 mg of fullerenes per rod for Nd and 0.4 mg of fullerenes per rod for Pr). For $Ce_3N@C_{2n}$ ($43 \leq n \leq 53$), the maximum yield of fullerenes (0.1 mg of fullerenes per rod) was obtained when the graphite rods were packed with a 3:1 mixture of graphite powder and cerium oxide.

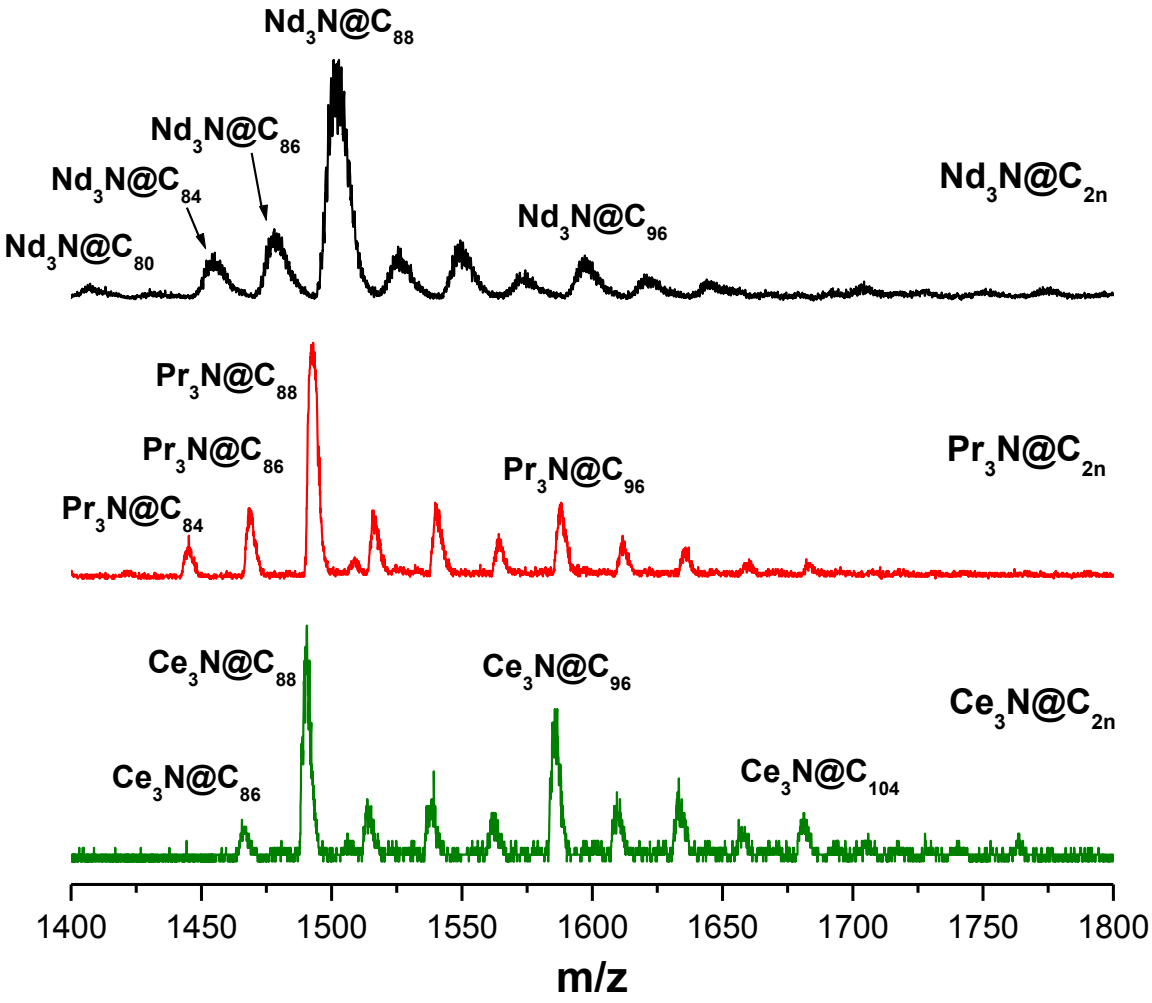


**Figure 3.8**. MALDI-TOF mass spectra of the $Nd_3N@C_{2n}$ (top), $Pr_3N@C_{2n}$ (middle) and $Ce_3N@C_{2n}$ (bottom) EMFs families.

Figure 3.8 shows the mass spectra and Figure 3.9 the HPLC chromatograms of the $Nd_3N@C_{2n}$, $Pr_3N@C_{2n}$, and $Ce_3N@C_{2n}$ families. From the mass spectra it is evident that a wider range of EMF sizes was obtained as the size of the metal in the cluster was increased (Figure 3.8) and metallofullerenes with cages as large as $C_{104}$ were formed (Figure 3.8, bottom). Both the Nd and Pr species gave a very low amount of the $C_{80}$

metallofullerene, and no $C_{82}$ metallofullerene was observed. In the case of $Ce_3N@C_{2n}$, only a small amount of the $C_{86}$ metallofullerene was formed.

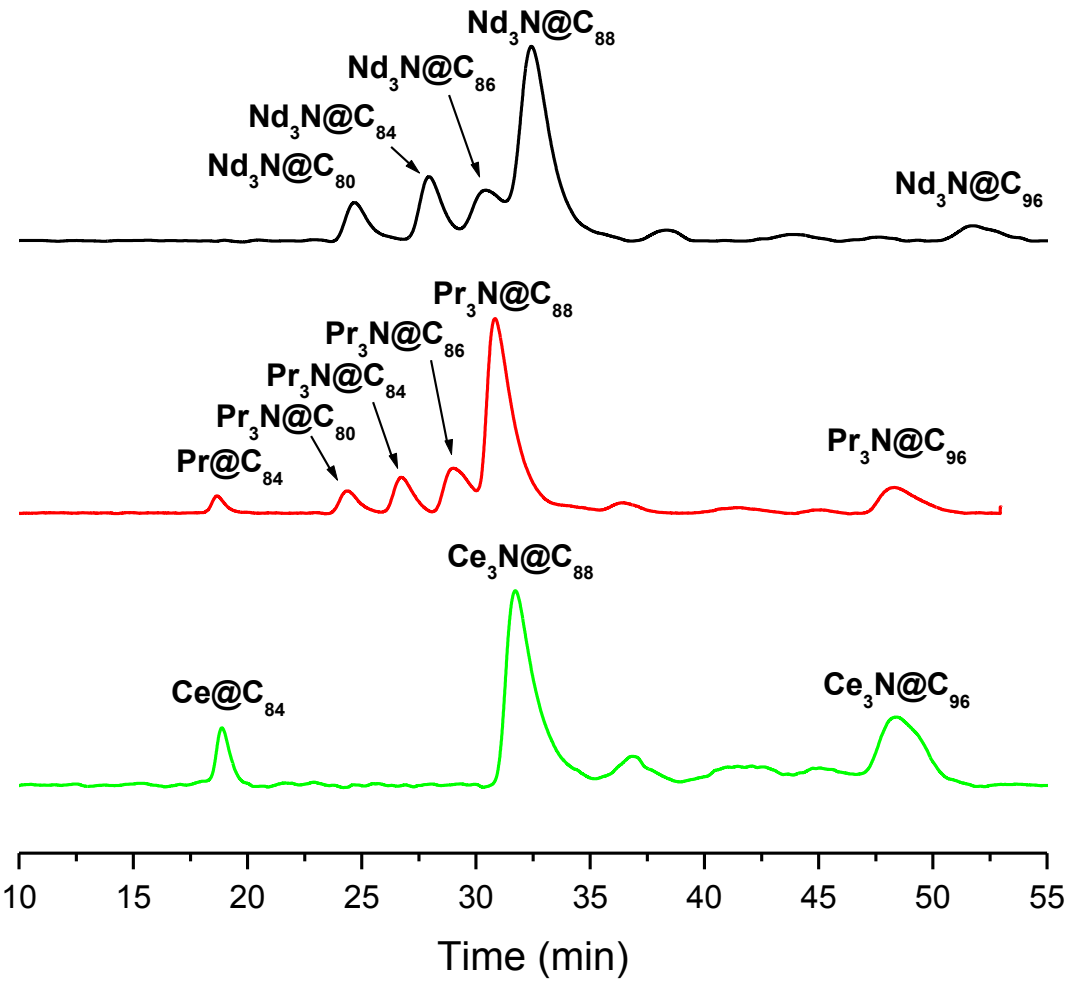


**Figure 3.9**. HPLC chromatograms of $Nd_3N@C_{2n}$ (top), $Pr_3N@C_{2n}$ (middle) and $Ce_3N@C_{2n}$ (bottom). Eluent: Toluene, Flow rate: 4.0 mL/min, Buckyprep-M column, detection wavelength: 372 nm.

The mass spectra and HPLC chromatograms also show the formation of two monometallofullerenes under these arcing conditions, $Pr@C_{84}$ (Figure 3.9, middle trace)

and $Ce@C_{84}$ (Figure 3.9, bottom trace) The yields of these monometallofullerenes were favored as the metal size was increased; for Ce, a relatively high abundance of this species was observed in the chromatogram, but for Nd no $Nd@C_{84}$ was observed. The identity of each chromatography peak was established by mass spectrometry and the products were isolated using a one-stage HPLC separation. The purity was checked by two-stage HPLC using a liner combination of a Buckyprep-M and a Buckyprep column. No further purification was necessary.

The $Nd_3N@C_{2n}$ ($40 \leq n \leq 50$) EMF family shows four main fractions in the HPLC chromatogram identified as $Nd_3N@C_{80}$, $Nd_3N@C_{84}$, $Nd_3N@C_{86}$, and $Nd_3N@C_{88}$ (Figure 3.10). Higher metallofullerenes were observed in the HPLC chromatogram but in very low yields and in poor isomeric purity. Interesting, the amount of $Nd_3N@C_{82}$ eluted in the HPLC is considerably lower than other metallic nitride EMFs within the neodymium family. It is noteworthy that the retention times of each of these metallic nitride EMFs follow the same tendency observed in the $Gd_3N@C_{2n}$ family.

The isolation of $Nd_3N@C_{80}$ and $Nd_3N@C_{84}$ required only one stage of chromatographic separation using the Buckyprep-M column while the separation of the fractions containing $Nd_3N@C_{86}$ and $Nd_3N@C_{88}$ required two chromatographic stages using the same Buckyprep-M column. As mentioned before, the purity of each sample was checked by passing the samples throughout different chromatography columns such as Buckyprep and Buckyclutcher. A linear combination of two columns was also used to verify the purity of the compounds.

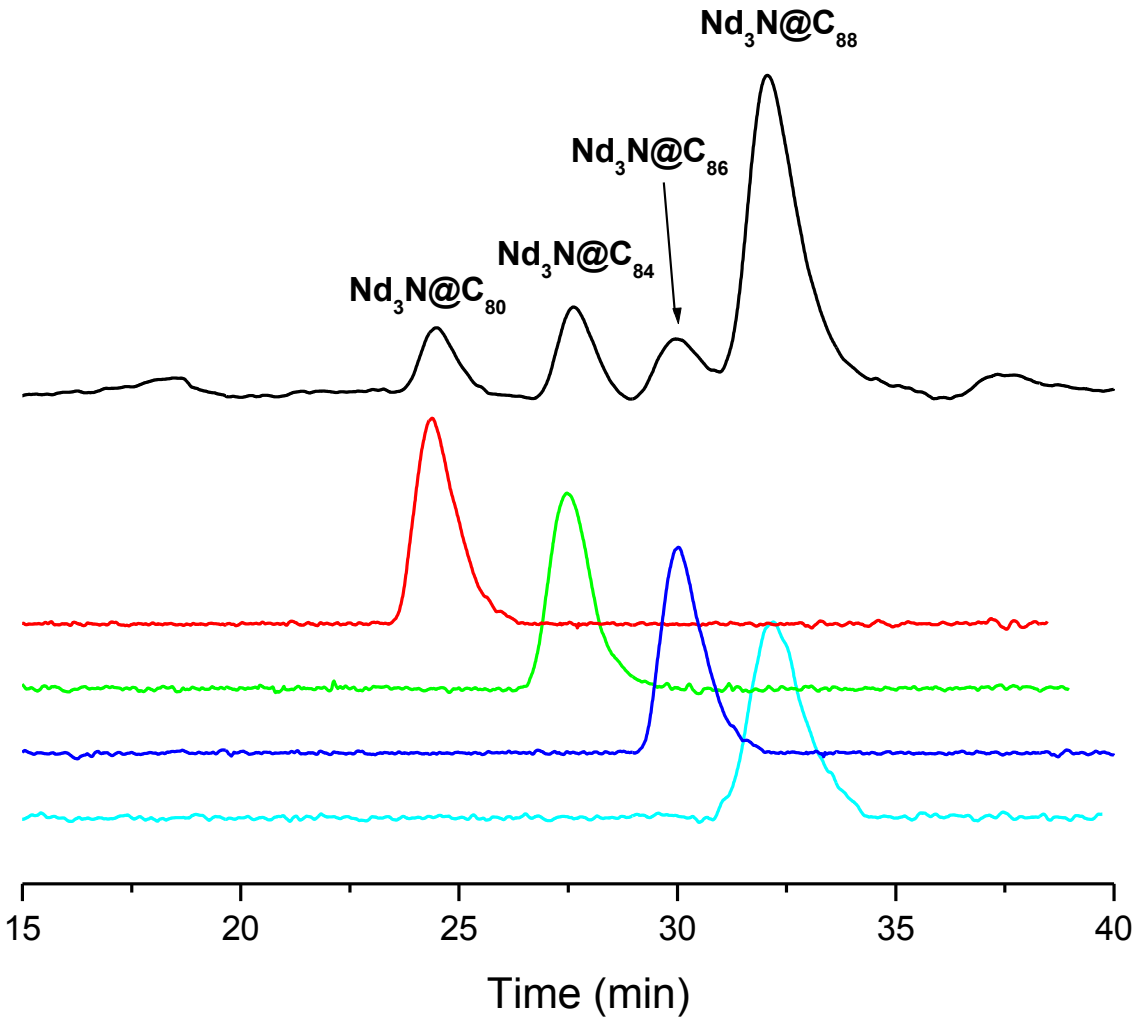


**Figure 3.10**. HPLC chromatograms of the $Nd_3N@C_{2n}$ mixture and isolated fractions. Buckyprep-M column, mobile phase toluene, flow rate 4.0 mL/min, detection 370 nm.

Figures 3.11-3.14 show the MALDI-TOF mass spectra of each of the isolated compounds from the $Nd_3N@C_{2n}$ family. It can be observed that the experimental and the calculated spectra match quite well.

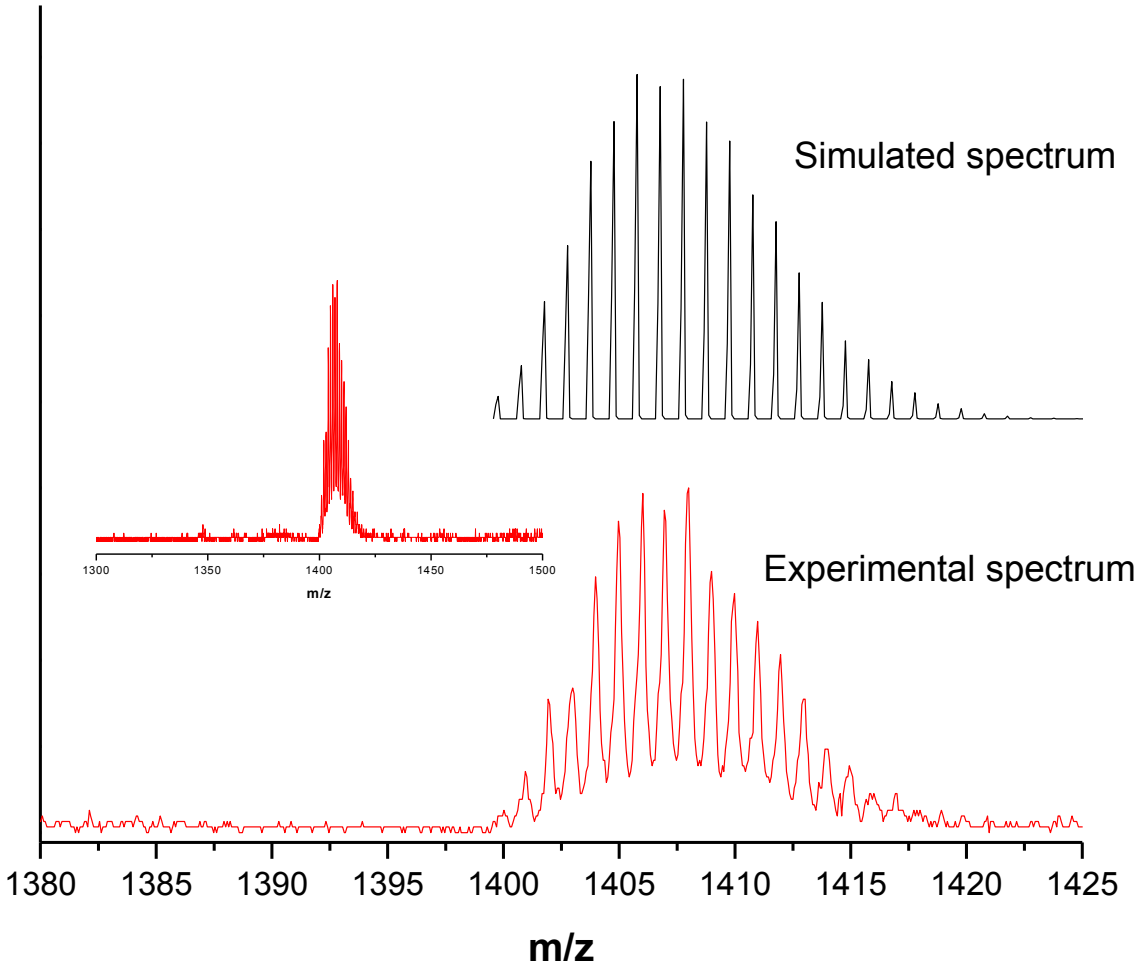


**Figure 3.11**. MALDI-TOF mass spectrum of the purified sample of $Nd_3N@C_{80}$. (Inset) Expansions of the calculated and experimental spectra for $Nd_3N@C_{80}$.

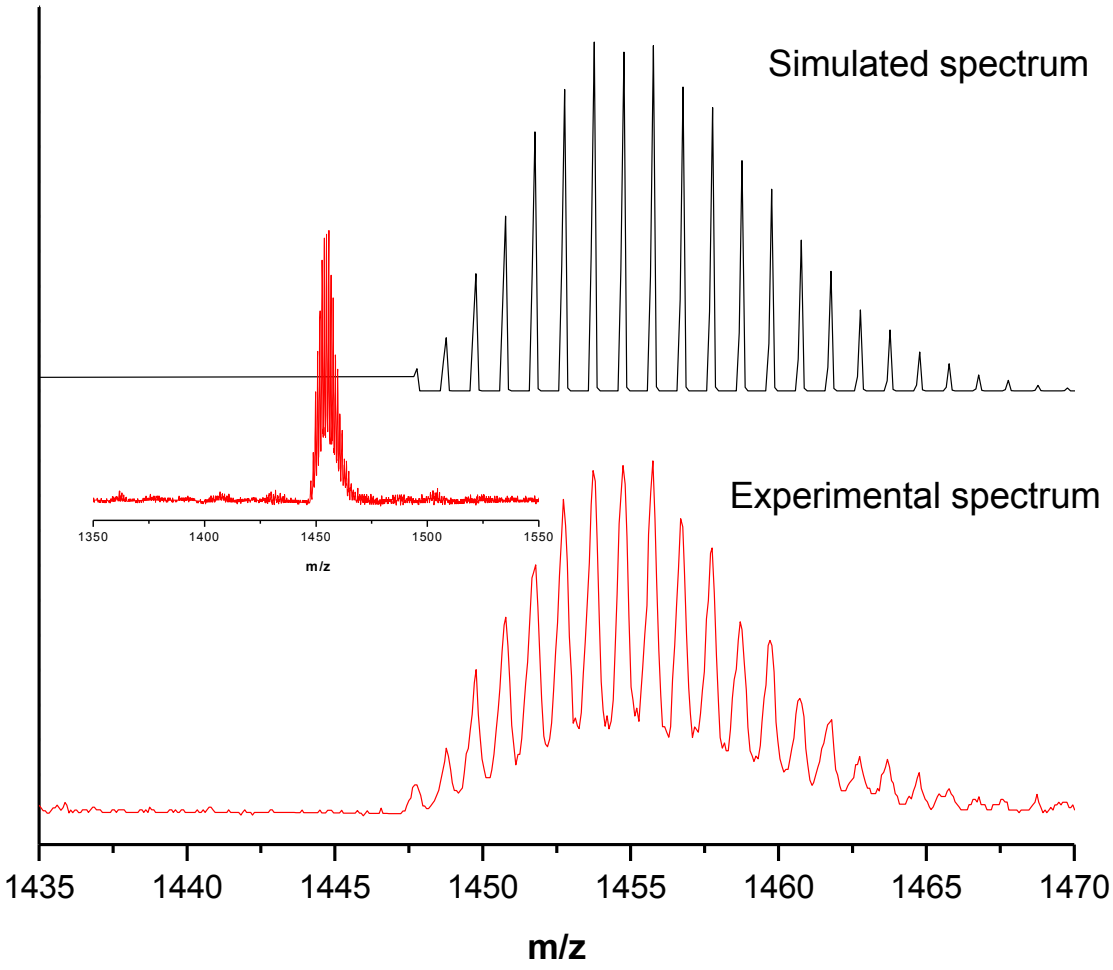


**Figure 3.12**. MALDI-TOF mass spectrum of the purified sample of $Nd_3N@C_{84}$. (Inset) Expansions of the calculated and experimental spectra for $Nd_3N@C_{84}$.

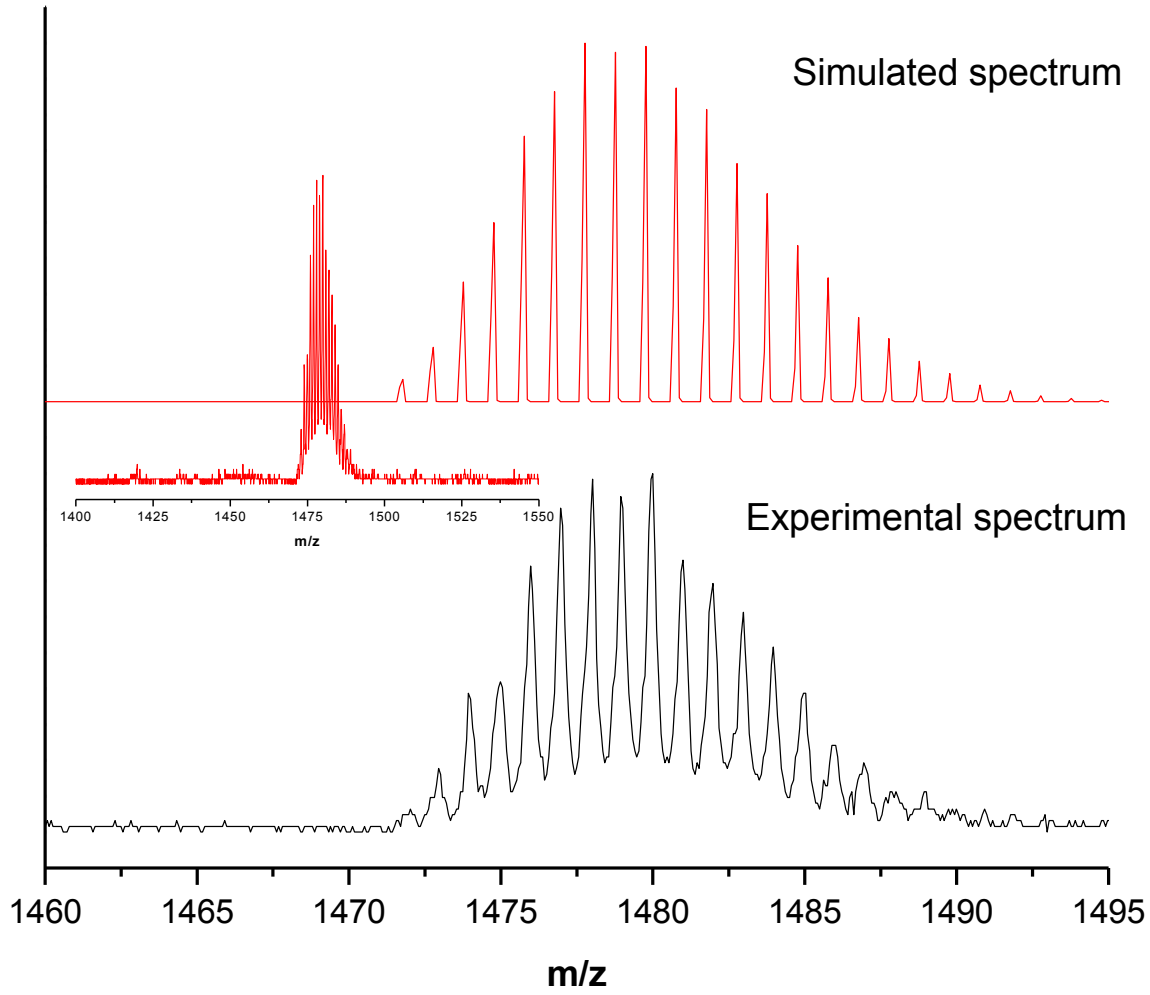


**Figure 3.13**. MALDI-TOF mass spectrum of the purified sample of $Nd_3N@C_{86}$. (Inset) Expansions of the calculated and experimental spectra for $Nd_3N@C_{86}$.

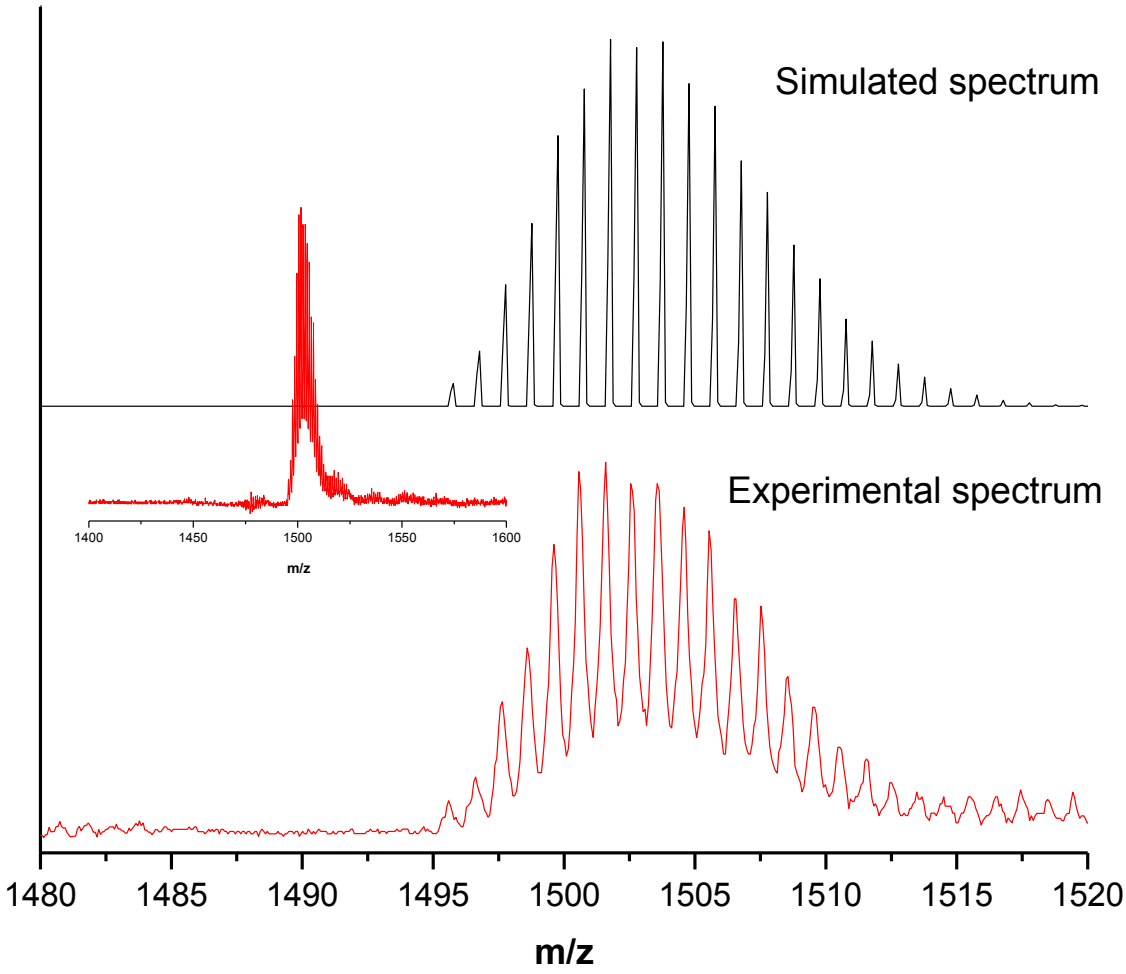


**Figure 3.14**. MALDI-TOF mass spectrum of the purified sample of $Nd_3N@C_{88}$. (Inset) Expansions of the calculated and experimental spectra for $Nd_3N@C_{88}$.

$Pr_3N@C_{2n}$ ($40 \leq n \leq 52$) shows a wider cage-size distribution than its Nd counterpart, containing a significant amount of $Pr_3N@C_{96}$ and a lower concentration of metallofullerenes with cages smaller than $C_{88}$. $Pr_3N@C_{80}$ is produced in very low amounts. The next two peaks were identified as $Pr_3N@C_{84}$ and $Pr_3N@C_{86}$, respectively (Figure 3.15).

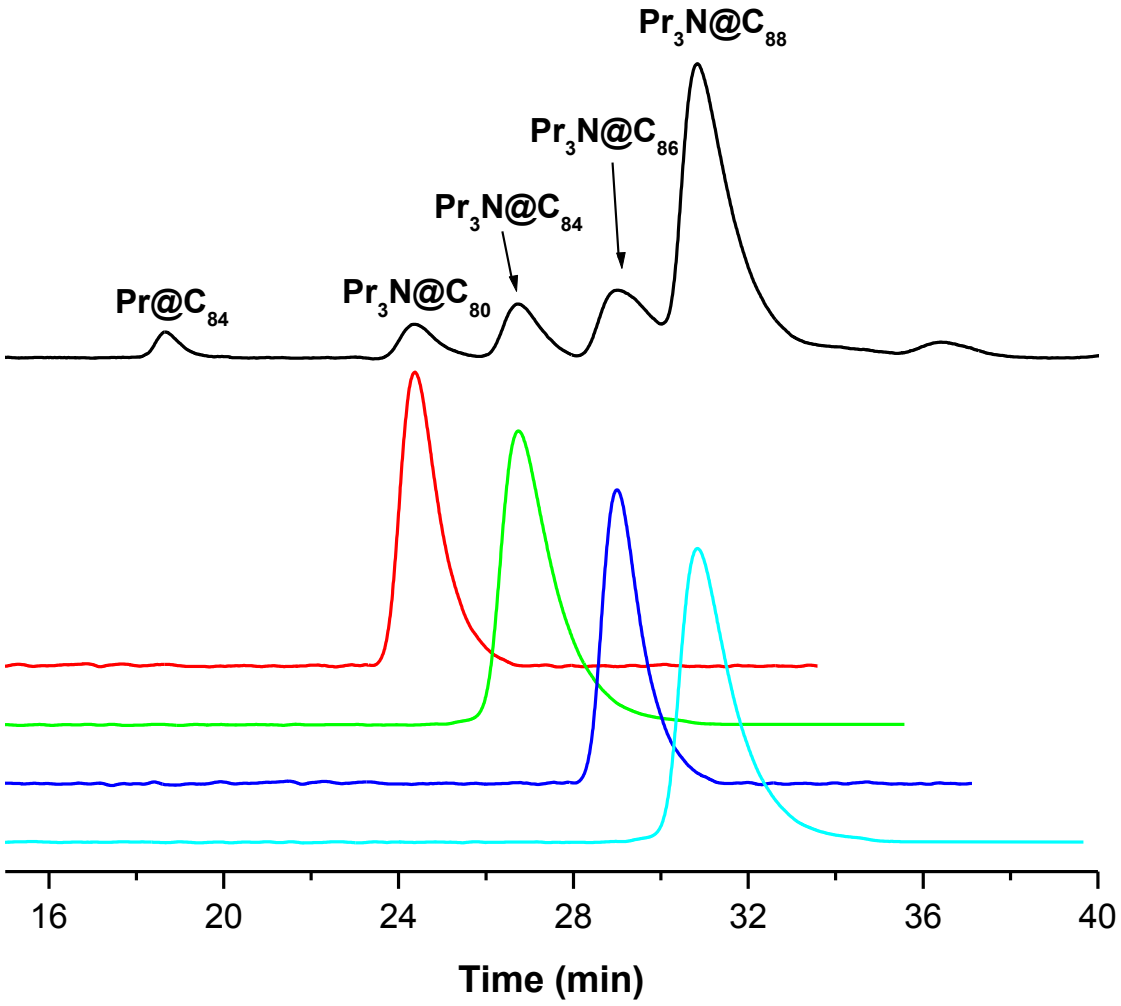


**Figure 3.15**. HPLC chromatograms of the $Pr_3N@C_{2n}$ mixture and isolated fractions. Buckyprep-M column, mobile phase toluene, flow rate 4.0 mL/min, detection 370 nm.

The HPLC chromatogram of the $Pr_3N@C_{2n}$ EMF family shows no peak for $Pr_3N@C_{82}$ similarly to the $Nd_3N@C_{2n}$ EMF family. The isolated fractions corresponded to $Pr_3N@C_{80}$, $Pr_3N@C_{84}$, $Pr_3N@C_{86}$ and $Pr_3N@C_{88}$. Each of these fractions was identify by MALDI-TOF MS (Figures 3.16-3.19).

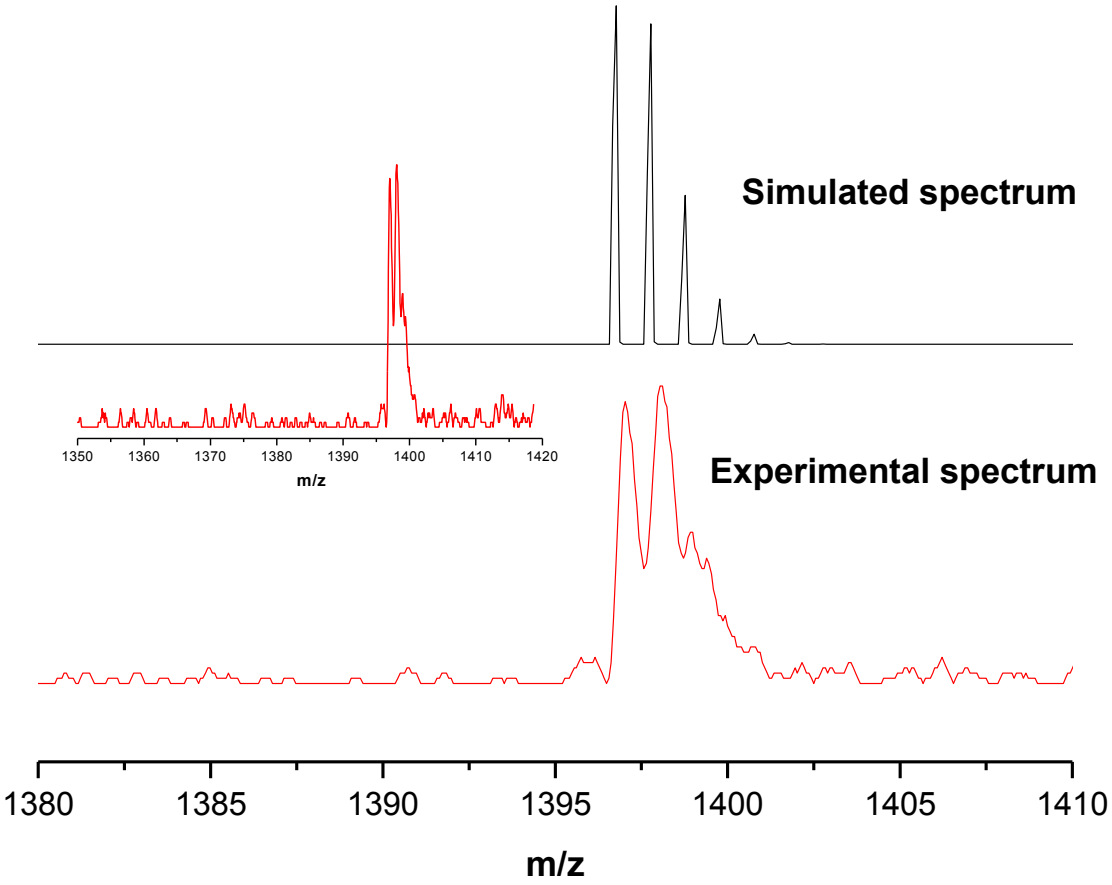


**Figure 3.16**. MALDI-TOF mass spectrum of the purified sample of $Pr_3N@C_{80}$. (Inset) Expansions of the calculated and experimental spectra for $Pr_3N@C_{80}$.

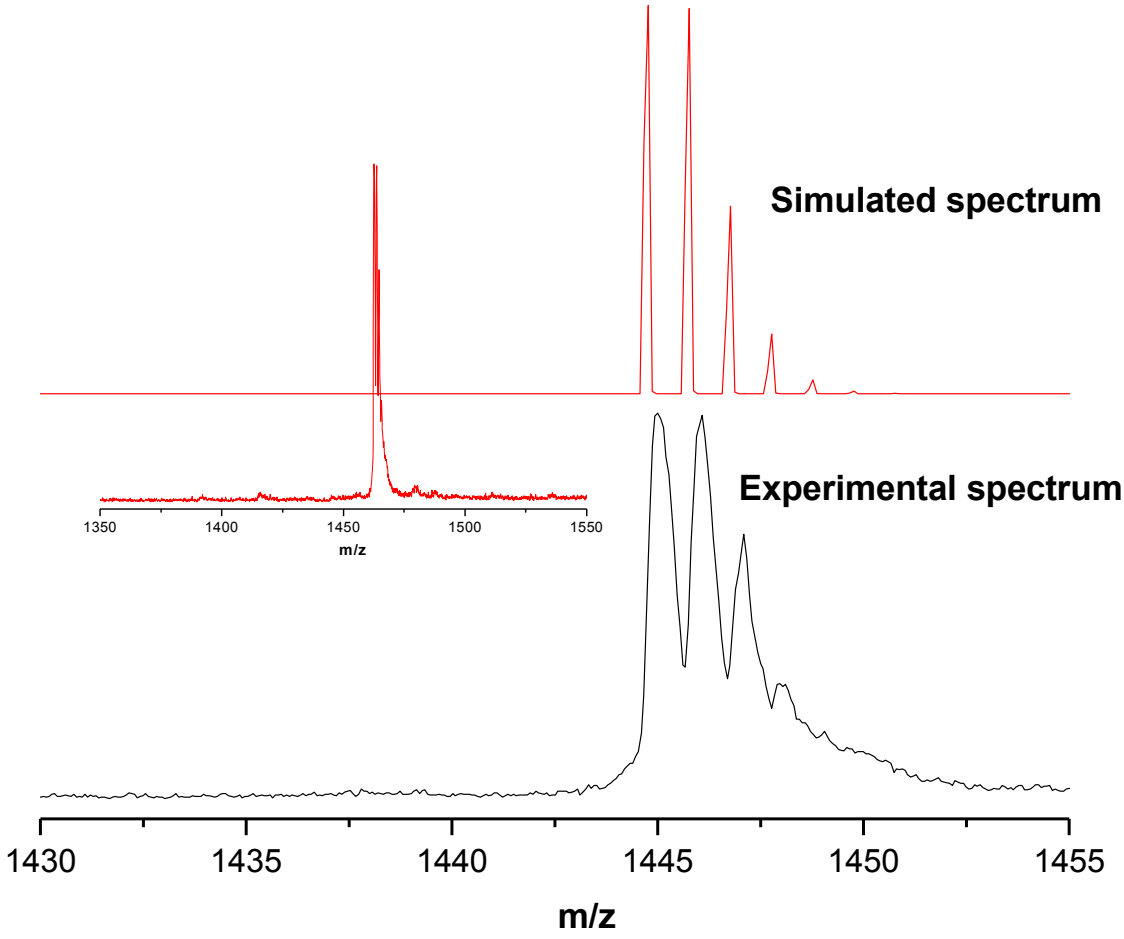


**Figure 3.17**. MALDI-TOF mass spectrum of the purified sample of $Pr_3N@C_{84}$. (Inset) Expansions of the calculated and experimental spectra for $Pr_3N@C_{84}$.

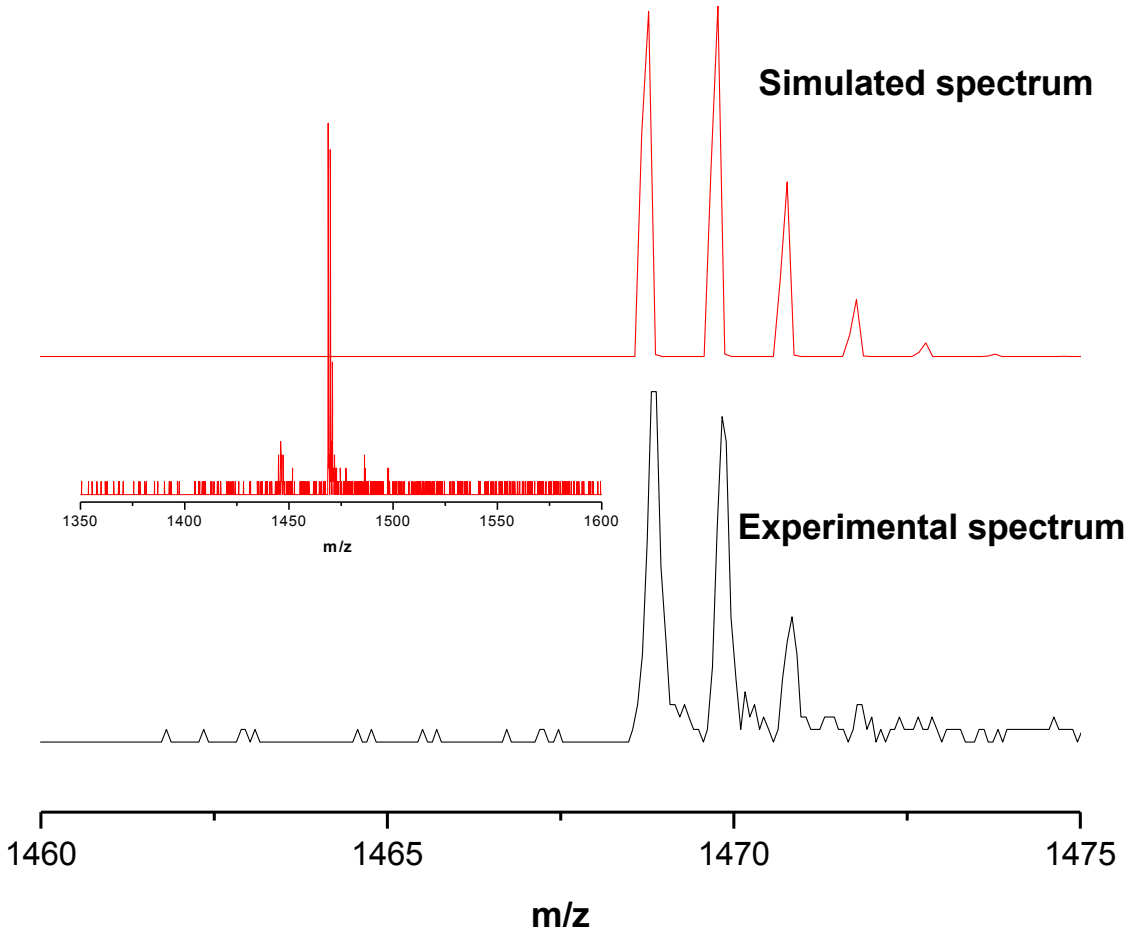


**Figure 3.18**. MALDI-TOF mass spectrum of the purified sample of $Pr_3N@C_{86}$. (Inset) Expansions of the calculated and experimental spectra for $Pr_3N@C_{86}$.

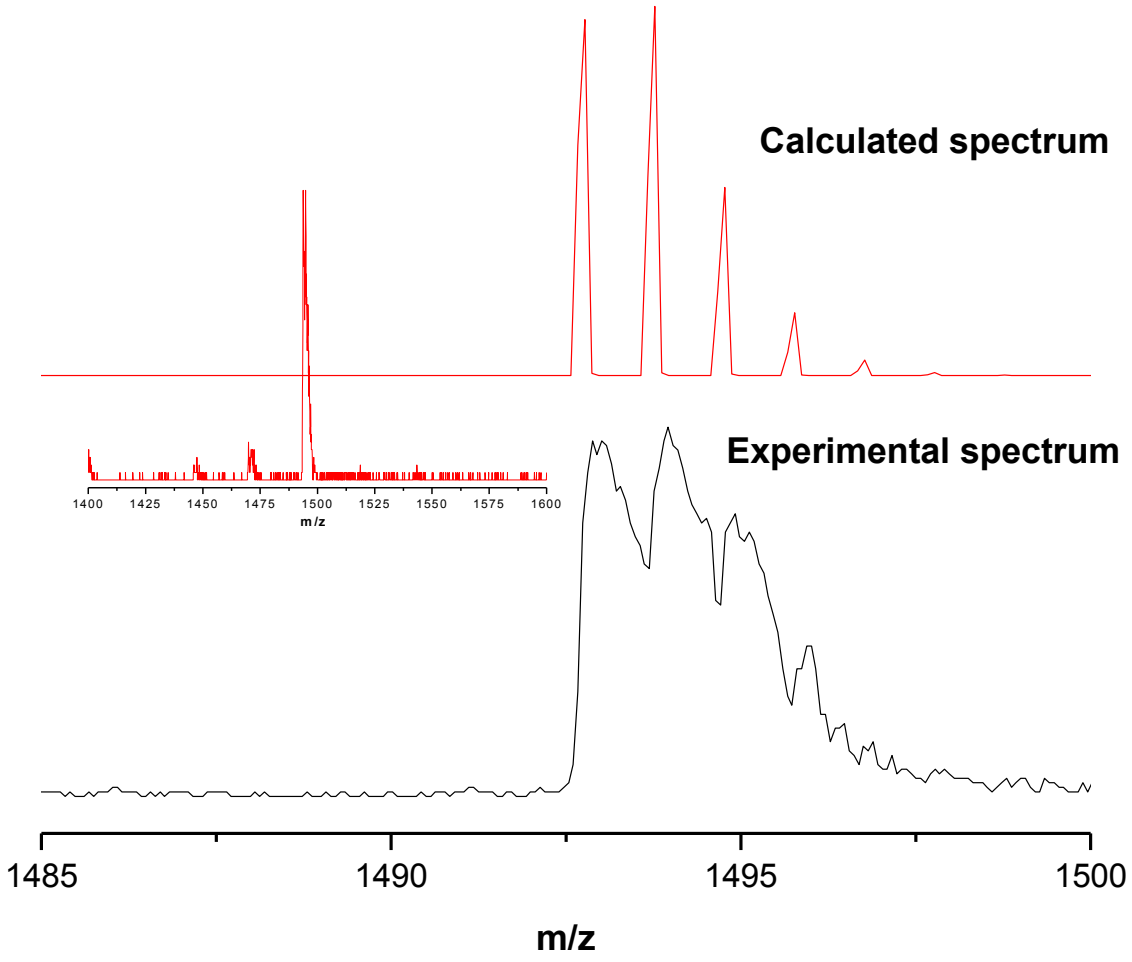


**Figure 3.19**. MALDI-TOF mass spectrum of the purified sample of $Pr_3N@C_{88}$. (Inset) Expansions of the calculated and experimental spectra for $Pr_3N@C_{88}$.

A sample of $Pr_3N@C_{88}$ was also deposited on a TEM grid and submitted to an energy dispersive spectroscopy (EDS) analysis. The spectrum shows the characteristic peaks of praseodymium (Figure 3.20).

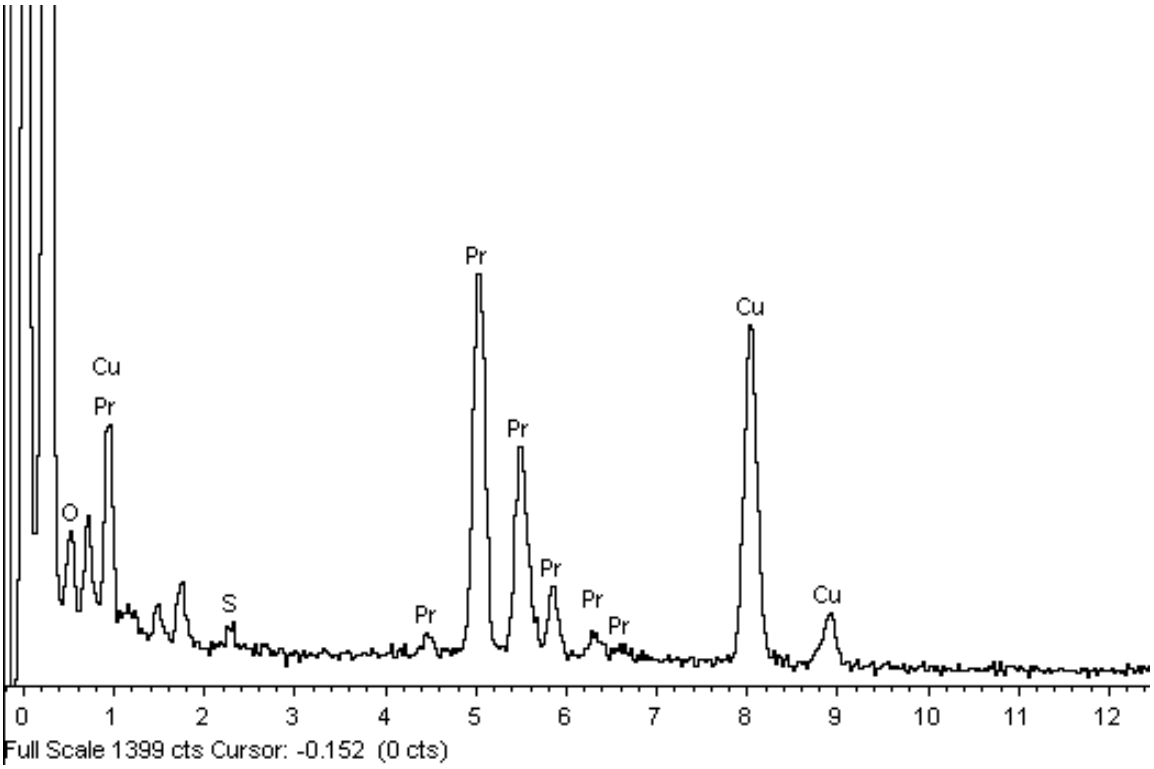


**Figure 3.20**. Energy Dispersive Spectroscopy (EDS) spectrum of the $Pr_3N@C_{88}$ fraction after HPLC. Copper is coming from the grid. Sulfur and oxygen are probably coming from the solvents used to manipulate the samples (ether, carbon disulfide).

The $Ce_3N@C_{2n}$ ($43 \leq n \leq 53$) EMF family mainly contained metallofullerenes larger than $Ce_3N@C_{86}$, in which $Ce_3N@C_{88}$ and $Ce_3N@C_{96}$ were the most abundant species (Figure 3.21). The other peaks were identified as $Ce_3N@C_{90}$, $Ce_3N@C_{92}$, and $Ce_3N@C_{94}$, respectively; however, their isomeric purity is probably low because as the cage size increases, the number of possible isomeric structures also increases dramatically.[18] For example, there are 187 possible isomers that follow the isolated pentagon rule (IPR) for $C_{96}$, which explains why the purification process is a major issue in metallofullerene research. However, recent computational work has shown that the

number of isomeric IPR cages with an electronic structure that can accept the transfer of six electrons from the cluster is actually quite low,[19] but the presence of multiple isomers still cannot be ruled out.

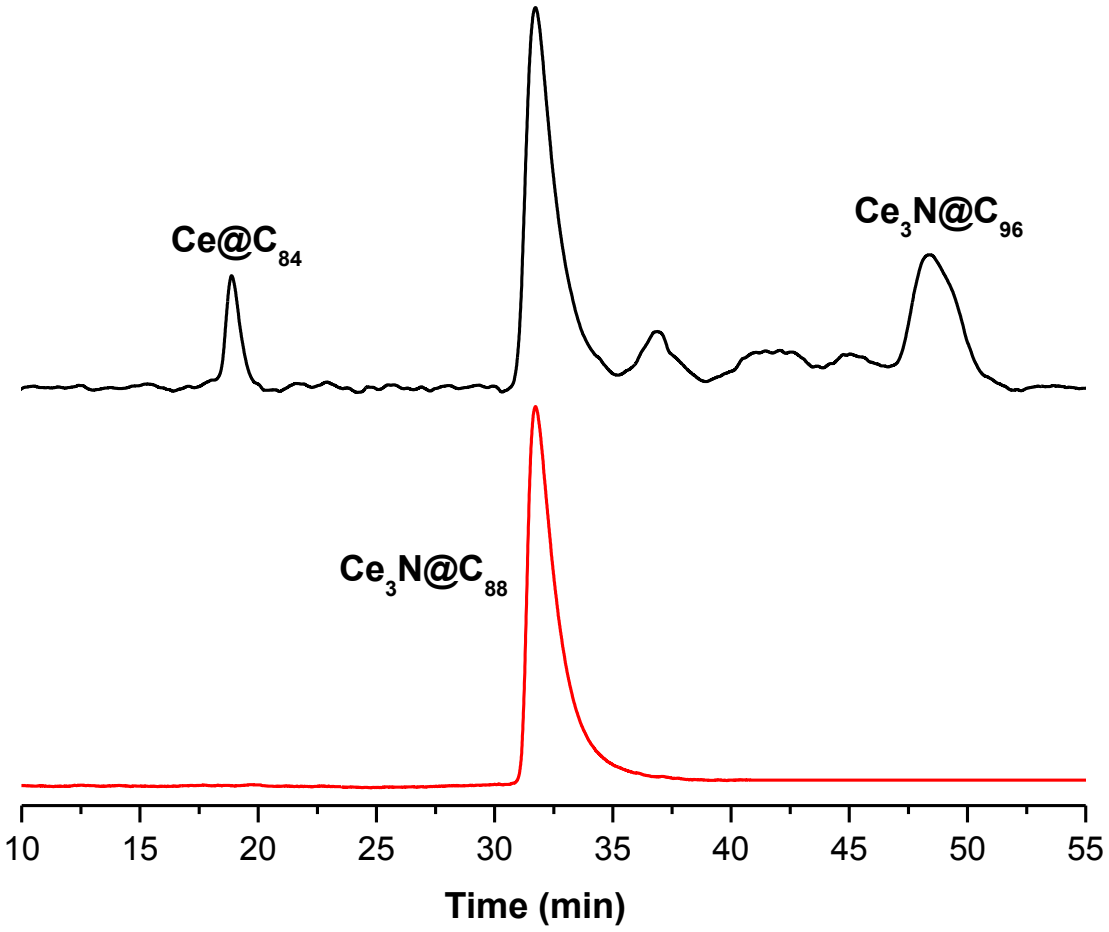


**Figure 3.21**. HPLC chromatograms of the $Ce_3N@C_{2n}$ mixture and isolated $Ce_3N@C_{88}$. Buckyprep-M column, mobile phase toluene, flow rate 4.0 mL/min, detection 370 nm.

MALDI-TOF MS of the isolated sample from the $Ce_3N@C_{2n}$ mixture confirmed the identity of this compound as $Ce_3N@C_{88}$ (Figure 3.22). A sample of $Ce_3N@C_{88}$ was also deposited on a TEM grid and submitted to an energy dispersive spectroscopy (EDS) analysis. The spectrum shows the characteristic peaks of praseodymium (Figure 3.23).

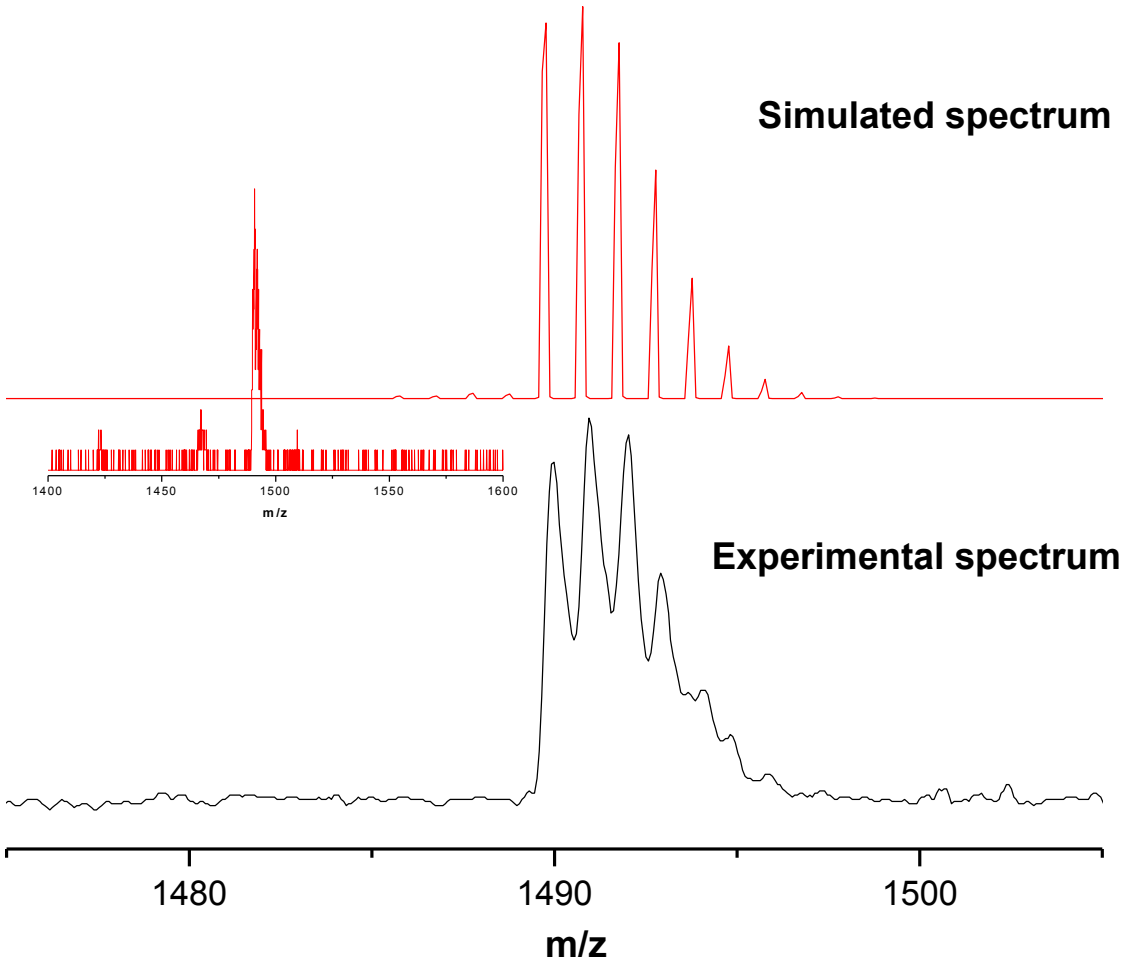


**Figure 3.22**. MALDI-TOF mass spectrum of the purified sample of $Ce_3N@C_{88}$. (Inset) Expansions of the calculated and experimental spectra for $Ce_3N@C_{88}$.

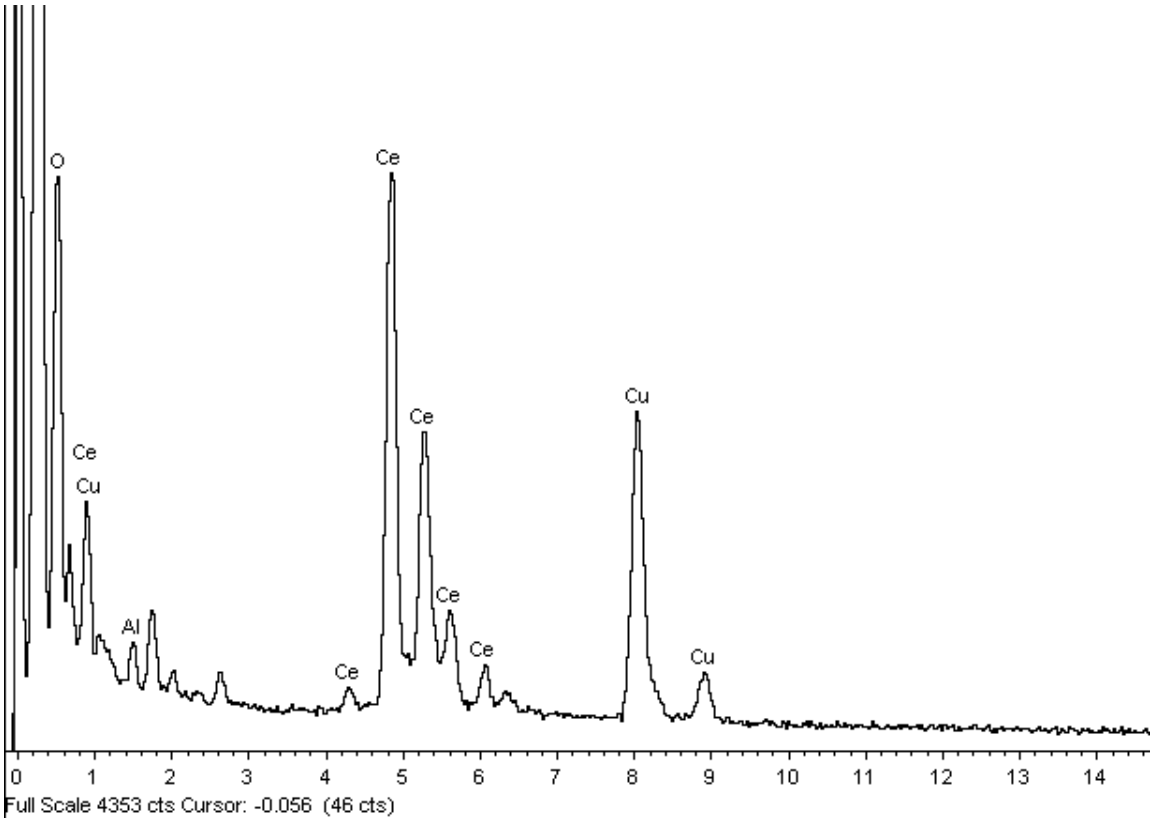


**Figure 3.23**. Energy Dispersive Spectroscopy (EDS) spectrum of the $Pr_3N@C_{88}$ fraction after HPLC. Copper and aluminium are coming from the grid and sample holder. Sulfur and oxygen are probably coming from the solvents used to manipulate the samples (ether, carbon disulfide).

**UV-vis-NIR spectra of the isolated Nd, Pr, and Ce-based endohedral metallofullerenes**

It has been demonstrated that the electronic absorptions of metallofullerenes are due to π-π* transitions of the fullerene cage.[2-3] It is also known that the spectral onset in the UV/Vis-NIR spectrum can be used to calculate the optical band gap.[2] Usually, 1.0 eV is used to differentiate between small and large band gap fullerenes,[2] so

metallofullerenes with an optical band gap larger than 1.0 eV are considered to be large band gap EMFs, which determines their reactivity and stability to some degree.

The isolated EMFs were dissolved in toluene and their UV/Vis-NIR spectra were recorded. Figure 3.24 shows the electronic spectra of the isolated products of the $Nd_3N$ and $Pr_3N$ EMF families. The corresponding absorption peaks, spectral onsets, and optical band gaps are listed in Table 3.4.

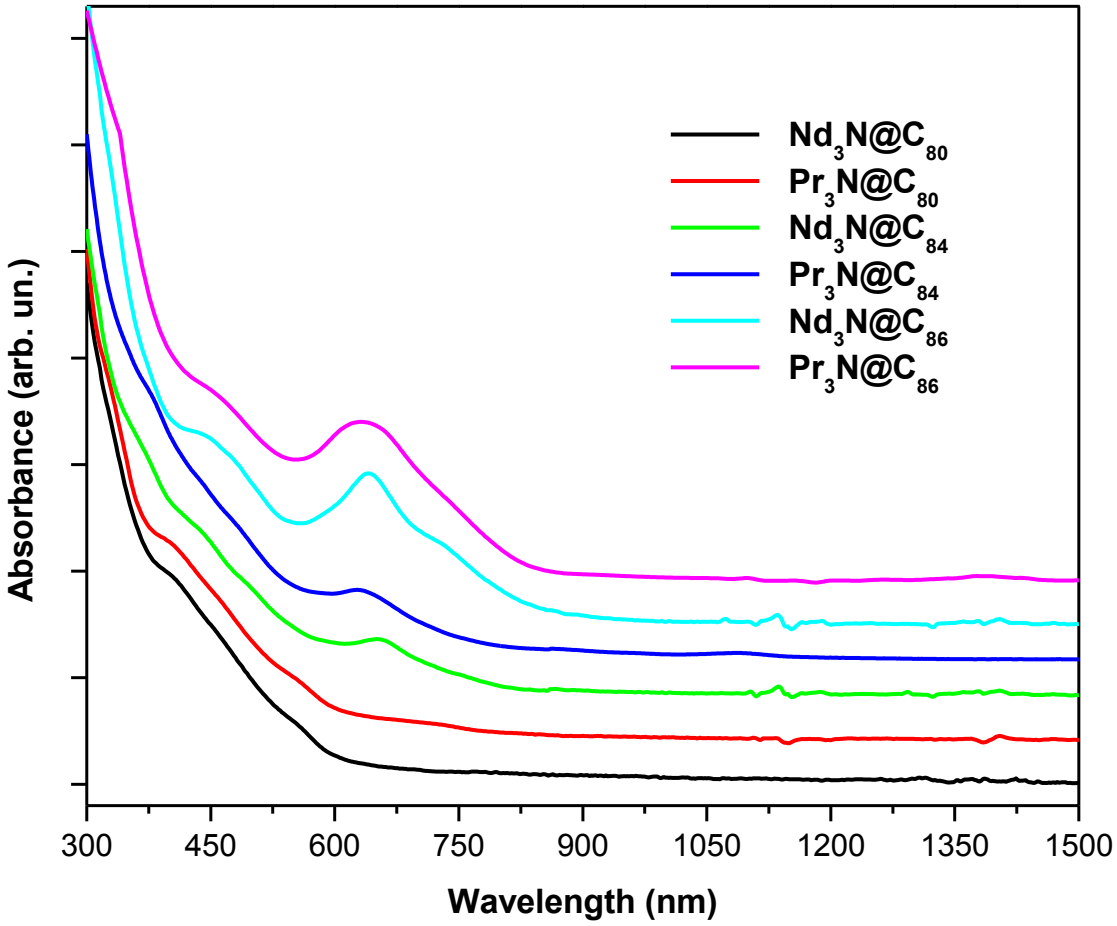


**Figure 3.24**. UV-vis-NIR spectra of the $Nd_3N@C_{2n}$ and $Pr_3N@C_{2n}$ endohedral metallofullerenes dissolved in toluene.

**Table 3.4**. Characteristic UV-vis-NIR absorptions and absorption onset of some $M_3N@C_{2n}$ (n = 40, 42, and 44).

| EMF | Onset (nm) | Band-gap (eV)[a] | UV-vis-NIR absorptions peaks (nm) |
|---|---|---|---|
| $Nd_3N@C_{80}$ | 800 | 1.55 | 404, 560, 721 |
| $Pr_3N@C_{80}$ | 820 | 1.51 | 404, 555, 728 |
| $Nd_3N@C_{84}$ | 1041 | 1.19 | 358, 441, 655 |
| $Pr_3N@C_{84}$ | 1342 | 0.92 | 380, 488, 627, 1086 |
| $Nd_3N@C_{86}$ | 1194 | 1.04 | 338, 445, 641, 739 |
| $Pr_3N@C_{86}$ | 1479 | 0.84 | 335, 461, 636, 744, 1389 |
| $Nd_3N@C_{88}$ | 1420 | 0.87 | 390, 770, 965 |
| $Pr_3N@C_{88}$ | 1445 | 0.86 | 395, 491, 775, 955 |
| $Ce_3N@C_{88}$ | 1442 | 0.86 | 395, 481, 769, 949 |

[a] Band-gap calculated from the spectral onset (bandgap (eV) ≈ 1240/onset (nm) [9])

$Nd_3N@C_{80}$ and $Pr_3N@C_{80}$ both have a strong visible absorption at λ = 404 nm. Two other peaks were also observed in the same region, and all of these absorptions correlate well with the peaks observed for the $M_3N@C_{80}$ ($I_h$; M=Gd, Dy, Tm) counterparts, which suggests that they have similar electronic and structural properties. The HOMO-LUMO gaps were calculated to be 1.5 eV for $Nd_3N@C_{80}$ and 1.51 eV for $Pr_3N@C_{80}$. These values fall within the range of 1.50 to 1.60 eV that is usually calculated for metallofullerenes with the general formula $M_3N@C_{80}$ (M=Sc, Tb, Ho, Y, Er, Tm, Dy, Gd).[2, 7, 9, 20]

The spectrum of $Nd_3N@C_{84}$ shows a relatively smaller spectral onset and thus a higher optical band gap than $Pr_3N@C_{84}$ and other isolated $M_3N@C_{84}$ (M = Dy, Tb, Gd)

metallofullerenes, and it can, therefore, be classified as a large-band gap metallofullerene. However, its absorption peaks resemble those observed for $Pr_3N@C_{84}$ and $Gd_3N@C_{84}$[7a] with the exception of the NIR absorption, which is not present in the spectrum of $Nd_3N@C_{84}$. On the other hand, $Pr_3N@C_{84}$ has a band gap that is closer to that of $Gd_3N@C_{84}$, and some very close absorptions as well, such as the UV absorption at $\lambda$ = 380 nm, two visible absorptions at $\lambda$ = 488 and 627 nm, and finally a NIR absorption at $\lambda$ = 1086 nm.

$Nd_3N@C_{86}$ and $Pr_3N@C_{86}$ have very similar electronic spectra, but $Pr_3N@C_{86}$ has an additional absorption in the NIR region and its spectral onset is located at around $\lambda$ = 1479 nm, which results in the same optical band gap as that reported for $Dy_3N@C_{86}$.[9]

The UV/Vis-NIR spectra of $Nd_3N@C_{88}$, $Pr_3N@C_{88}$, and $Ce_3N@C_{88}$ are quite similar, which suggests that these metallic nitride EMFs share the same fullerene structure. A very strong absorption located between $\lambda$ = 769 and 775 nm and NIR absorptions at around $\lambda$ = 949 and 965 nm were found for all three metallofullerenes. $Nd_3N@C_{88}$ has an optical band gap of 0.87 eV, whereas for $Pr_3N@C_{88}$ and $Ce_3N@C_{88}$ the band gap is 0.86 eV (Figure 3.25 and Table 3.4).

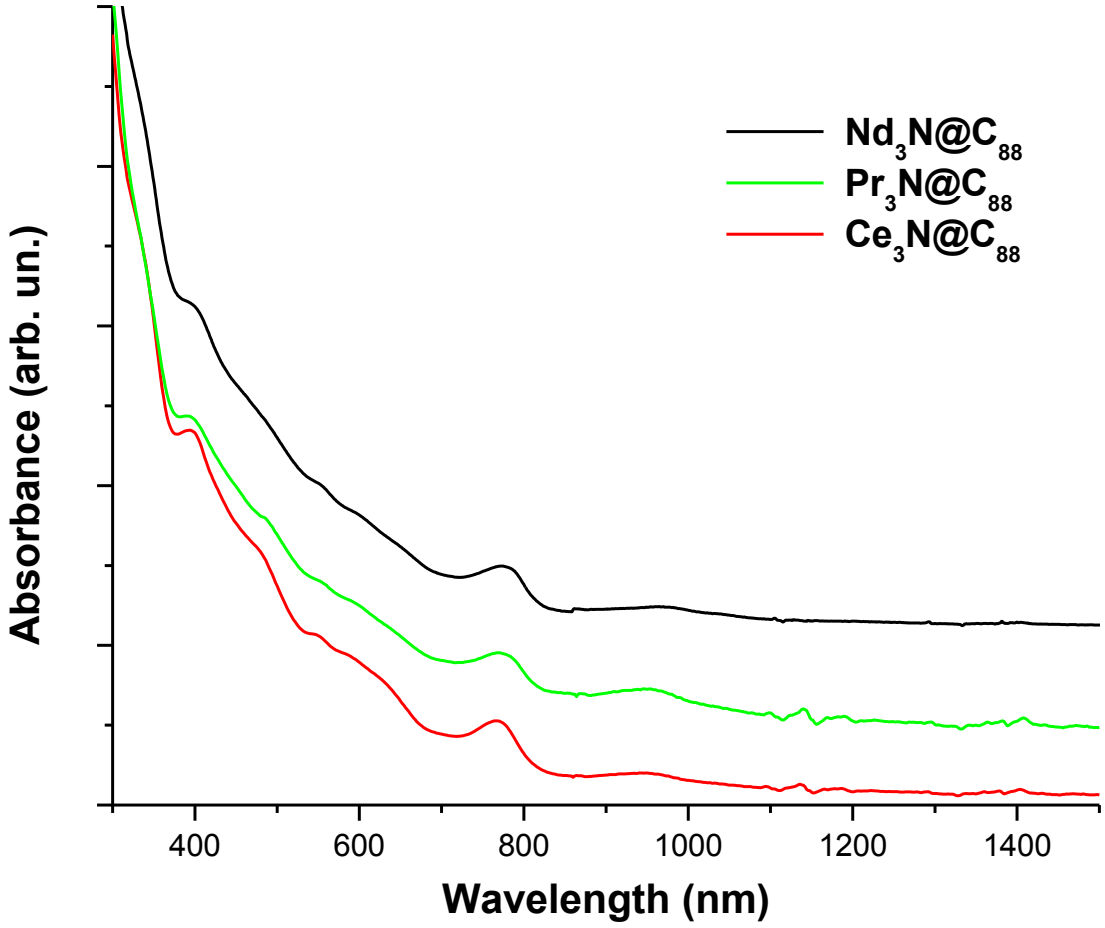


**Figure 3.25**. UV-vis-NIR spectra of the $Nd_3N@C_{88}$, $Pr_3N@C_{88}$, and $Ce_3N@C_{88}$ endohedral metallofullerenes dissolved in toluene.

**Electrochemical studies of the Nd, Pr, and Ce endohedral metallofullerene families**

Figure 3.26 and Table 3.5 show the redox behavior of both $Pr_3N@C_{88}$ and $Ce_3N@C_{88}$, which was very similar to that of $Nd_3N@C_{88}$[14] and $Gd_3N@C_{88}$[7a] (see Figure 3.26). All of these EMFs show three reduction steps; the first is monoelectronic and reversible (peak to peak separation = 60 mV), the second is monoelectronic and quasi-reversible (peak to peak separation = 120-200 mV), and the third is less clearly defined and probably multielectronic.

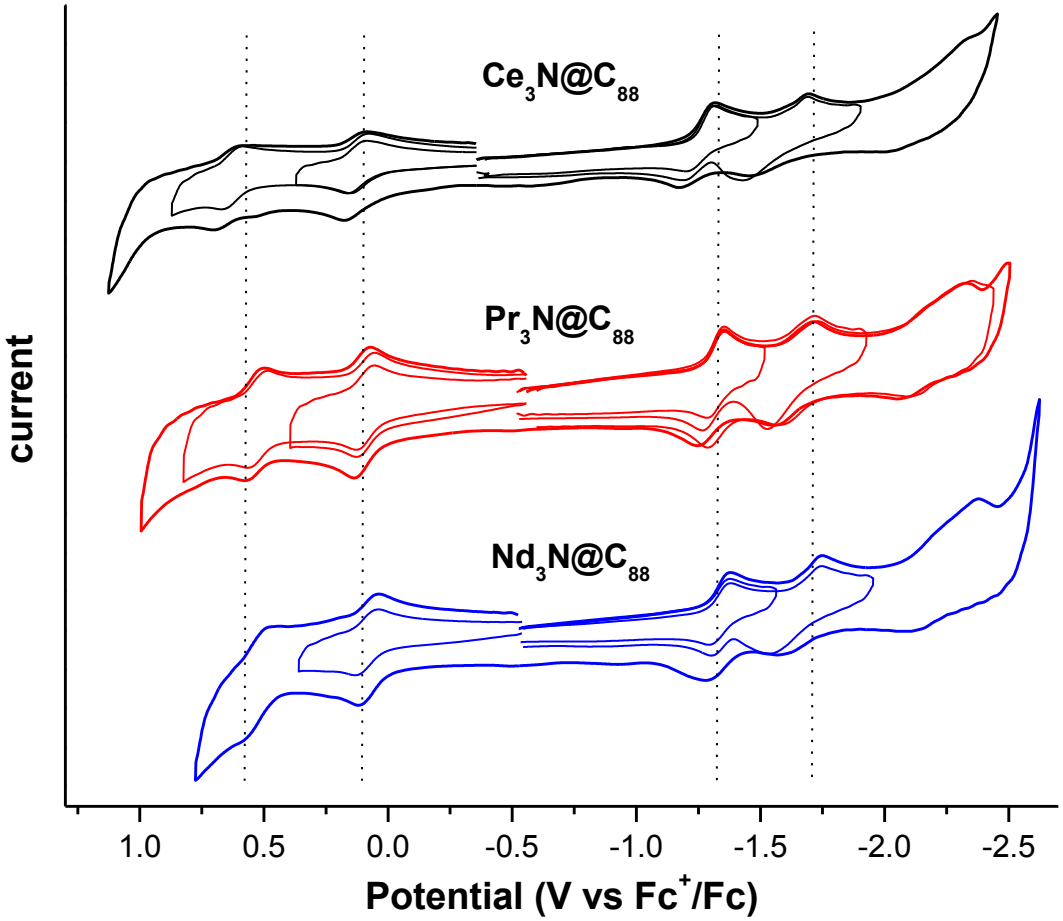


**Figure 3.26**. Cyclic voltammograms of $Ce_3N@C_{88}$, $Pr_3N@C_{88}$, and $Nd_3N@C_{88}$ in 0.05 M $NBu_4PF_6$/*o*-DCB with ferrocene as internal standard, scan rate 0.1 $Vs^{-1}$.

These compounds also show two reversible, monoelectronic oxidation steps. This behavior appears to be characteristic of the $C_{88}$ EMFs. We note that $Ce_3N@C_{88}$, $Pr_3N@C_{88}$, and $Nd_3N@C_{88}$ also have very similar electrochemical HOMO-LUMO gaps, which is probably a consequence of their similar structures and the similar electronic properties of the encapsulated metals (see the electronegativity values of the three metals in Table 3.5). The same trend was observed for the calculated optical band gaps, which were very similar (Figure 3.25 and Table 3.4).

**Table 3.5**. Half wave potentials vs $Fc^+/Fc$ of the first reduction and the first oxidation steps of $Ce_3N@C_{88}$, $Pr_3N@C_{88}$ and $Nd_3N@C_{88}$.

| EMF | $\chi$[a] | Redox potential | | |
|---|---|---|---|---|
| | | $E_{1/2,red(1)}$ | $E_{1/2,\ ox(1)}$ | $\Delta E_{gap}$ |
| $Nd_3N@C_{88}$ | 1.14 | -1.33 | 0.07 | 1.40 |
| $Pr_3N@C_{88}$ | 1.13 | -1.31 | 0.09 | 1.40 |
| $Ce_3N@C_{88}$ | 1.12 | -1.30 | 0.08 | 1.38 |

[a] Pauling electronegativity of the metal. [15]

As expected, $Nd_3N@C_{80}$ and $Pr_3N@C_{80}$ exhibited redox behavior that was comparable to that of previously described $Sc_3N@C_{80}$, $Er_3N@C_{80}$, $Y_3N@C_{80}$, $Dy_3N@C_{80}$, $Tm_3N@C_{80}$, and $Gd_3N@C_{80}$ (see Figures 3.27 and 3.28 and Table 3.6).[7a, 16, 20] One reversible oxidation step and at least two irreversible reduction steps were observed.

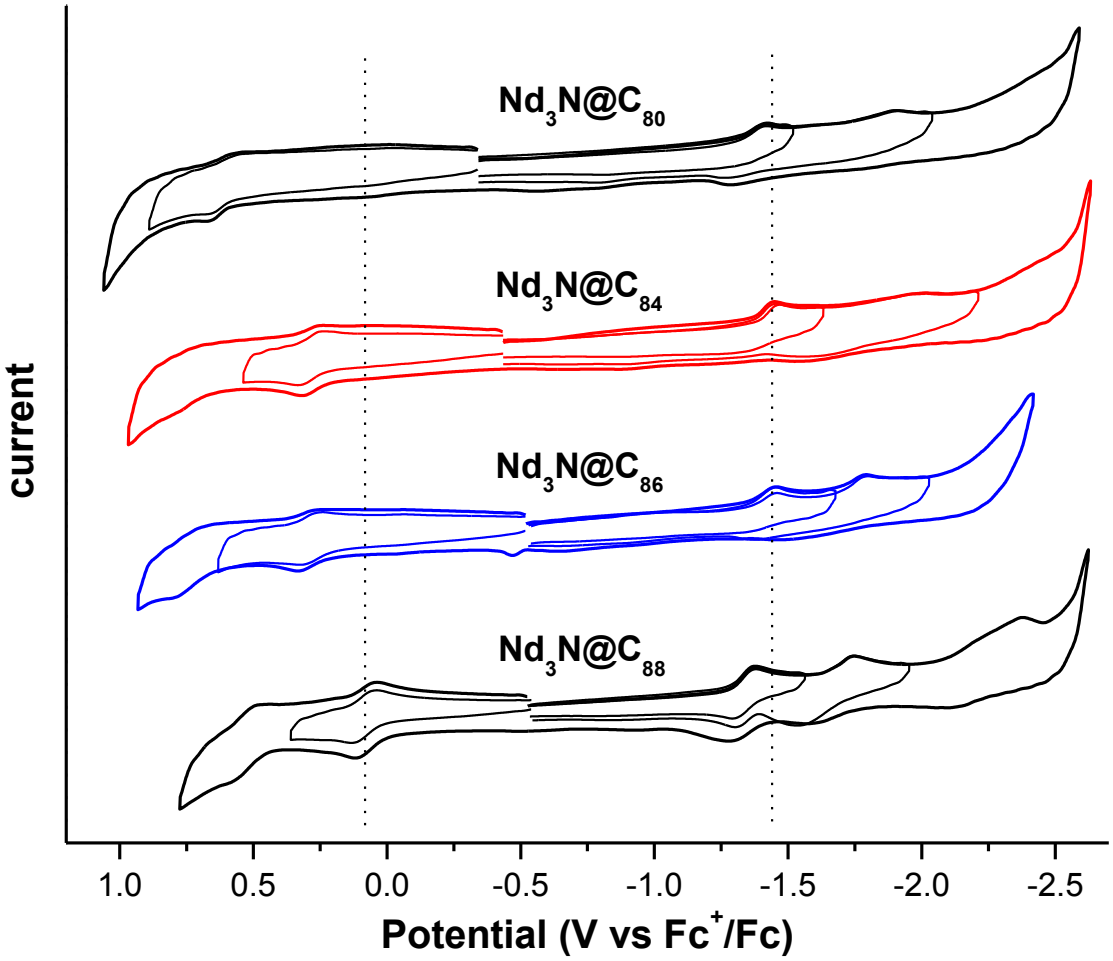


**Figure 3.27**. Cyclic voltammograms of the $Nd_3N@C_{2n}$ family in 0.05 M $NBu_4PF_6$/*o*-DCB with ferrocene as internal standard, scan rate 0.1 $Vs^{-1}$.

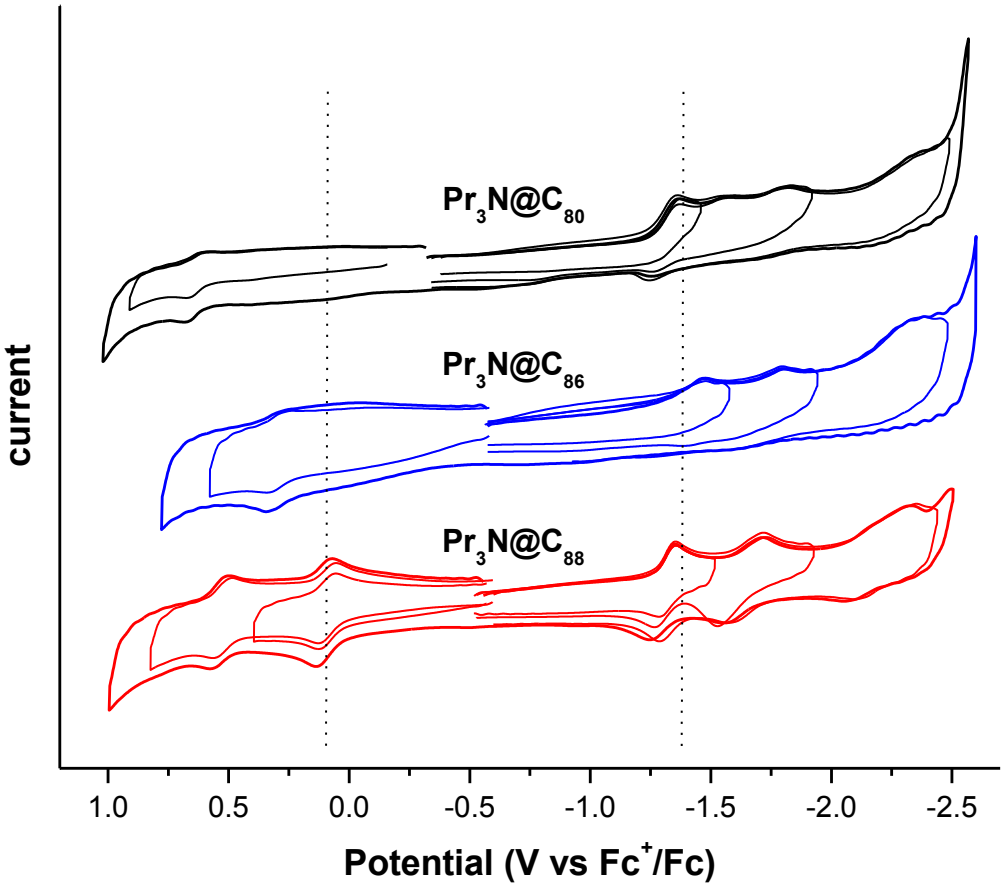


**Figure 3.28**. Cyclic voltammograms of $Pr_3N@C_{80}$, $Pr_3N@C_{86}$ and $Pr_3N@C_{88}$ in 0.05 M $NBu_4PF_6$/*o*-DCB with ferrocene as internal standard, scan rate 0.1 $Vs^{-1}$.

**Table 3.6**. Cathodic peak potentials vs $Fc^+/Fc$ of the first reduction step and half wave potential of the other cluster fullerenes isolated, based on Nd and Pr metals.

| **EMF** | $E_{p,red(1)}$ **(V)** | $E_{1/2,\,ox(1)}$ **(V)** | $E_{1/2,\,ox(1)} - E_{p,\,red(1)}$ **(V)** |
|---|---|---|---|
| $Nd_3N@C_{80}$ | -1.42 | 0.63 | 2.05 |
| $Pr_3N@C_{80}$ | -1.41 | 0.59 | 2.00 |
| $Nd_3N@C_{84}$ | -1.44 | 0.31 | 1.75 |
| $Nd_3N@C_{86}$ | -1.46 | 0.36 | 1.82 |
| $Pr_3N@C_{86}$ | -1.48 | 0.31 | 1.78 |

The first reduction process in Nd and Pr metallic nitride EMFs was cathodically shifted compared with that of triscandium nitride EMFs and was similar to that of the metallic nitride EMFs of gadolinium, which is reasonable since they have similar electronegativity values (Pr, Nd, and Gd (1.13-1.20)) while Sc has a higher value (1.36). $Nd_3N@C_{84}$ also showed at least two irreversible reduction steps and a reversible oxidation step, which were also previously observed for $Gd_3N@C_{84}$. We also reported the electrochemical behavior of $C_{86}$ metallic nitride EMFs for the first time. Interestingly, the electrochemistry of $Nd_3N@C_{86}$ and $Pr_3N@C_{86}$ is qualitatively very similar to that of $Nd_3N@C_{84}$, $Nd_3N@C_{80}$, and $Pr_3N@C_{80}$ since these compounds also showed irreversible reduction and reversible oxidation behavior.

The electrochemical HOMO-LUMO gaps for these new metallic nitride EMF families follow the trends previously reported for the $Gd_3N@C_{2n}$ family.[7a] A large gap was recorded for the $C_{80}$ cage and a smaller one for the $C_{88}$ cage. The cluster fullerenes encapsulated in $C_{84}$ and $C_{86}$ cages appear to have similar HOMO-LUMO gaps, which are intermediate between those of $C_{80}$ and $C_{88}$.

### Lanthanum Nitride Endohedral Fullerenes $La_3N@C_{2n}$ ($43 \leq n \leq 55$): Preferential Formation of $La_3N@C_{96}$[21]

While the trimetallic nitrides of Sc, Y and the lanthanides between Gd and Lu preferentially template $C_{80}$ cages, $M_3N@C_{80}$, and while those of Ce, Pr and Nd preferentially template the $C_{88}$ cage, $M_3N@C_{88}$, in this section we shall see that the largest metallic nitride cluster, $La_3N$, preferentially leads to the formation of $La_3N@C_{96}$ and to a lesser extent the $La_3N@C_{88}$. This is the first time that $La_3N$ has been successfully

encapsulated inside fullerene cages. $La_3N@C_{2n}$ EMFs were synthesized by arcing packed graphite rods in a modified Krätschmer-Huffman arc reactor, extracted from the collected soot and identified by mass spectroscopy. They were isolated and purified by High Performance Liquid Chromatography (HPLC). Different arcing conditions were studied to maximize fullerene production, and results showed that yields have a high $La_2O_3$/C dependence. Relatively high yields were obtained when a 1:5 ratio was used. Three main fractions, $La_3N@C_{88}$, $La_3N@C_{92}$, and $La_3N@C_{96}$, were characterized by UV/Vis-NIR and cyclic voltammetry. Unlike other trimetallic nitride metallofullerenes of the same carbon cage size, $La_3N@C_{88}$ exhibits a higher HOMO-LUMO gap and irreversible reduction and oxidation steps.

**Synthesis of $La_3N@C_{2n}$ ($43 \leq n \leq 55$) Endohedral Fullerenes**

The synthesis of $La_3N@C_{2n}$ metallofullerenes was accomplished by using the reactive gas atmosphere method. Graphite rods were packed with different $La_2O_3$/C mass ratios, annealed for 12 h at 1000 °C, and vaporized in a modified Krätschmer-Huffman arc reactor under a mixture of ammonia (20 mbar) and helium (200 mbar).

When the rods were packed with 1:1 up to 1:3 ratios of $La_2O_3$/C, the fullerene yield was very low; however, when the ratio was changed to 1:4, the yield increased (Figure 3.29). As anticipated, the $C_{96}$ cage is preferentially templated by the $La_3N$ cluster. From the MALDI-TOF mass spectrum, a large carbon cage distribution was observed, with cages as large as $C_{104}$ and as small as $C_{86}$. These results demonstrate that the synthesis and isolation of large fullerene cages is possible by increasing the size of the

metallic cluster encapsulated, and that metallic clusters larger than $Ce_3N$ are preferentially encapsulated inside $C_{96}$ carbon cages.

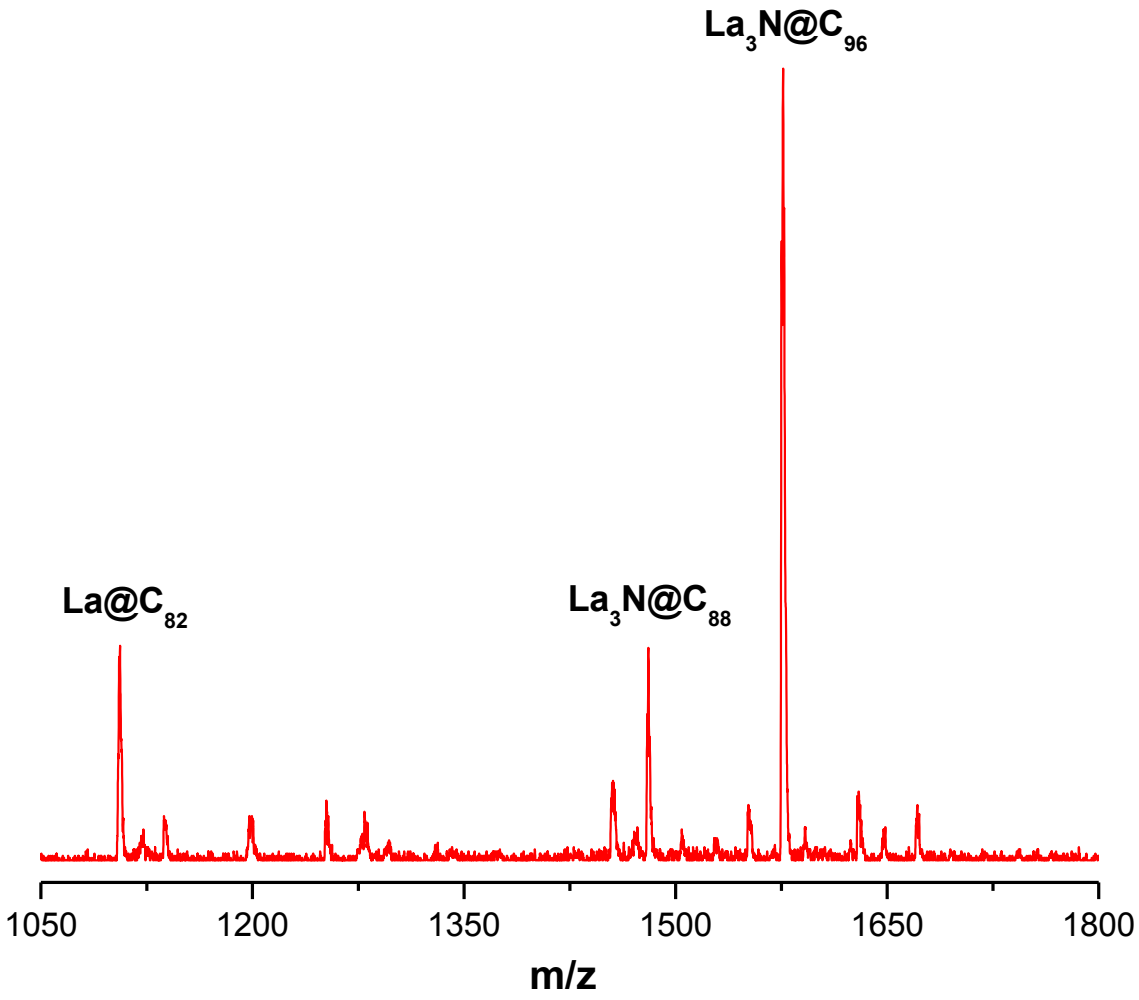


**Figure 3.29**. MALDI-TOF mass spectrum of the $La_3N@C_{2n}$ clusterfullerene family using a $La_2O_3$/C 1:4 ratio.

Even though the mass spectrum showed that $La_3N@C_{2n}$ metallofullerenes are formed during the arcing process, the total fullerene yield still remained low. When the $La_2O_3$/C ratio was increased to 1:5, a significant increase in fullerene yield was obtained

(~0.1 mg per every five burned rods). Other $La_2O_3$/C ratios were tried, but in those cases the packed material was unstable, under arcing conditions.

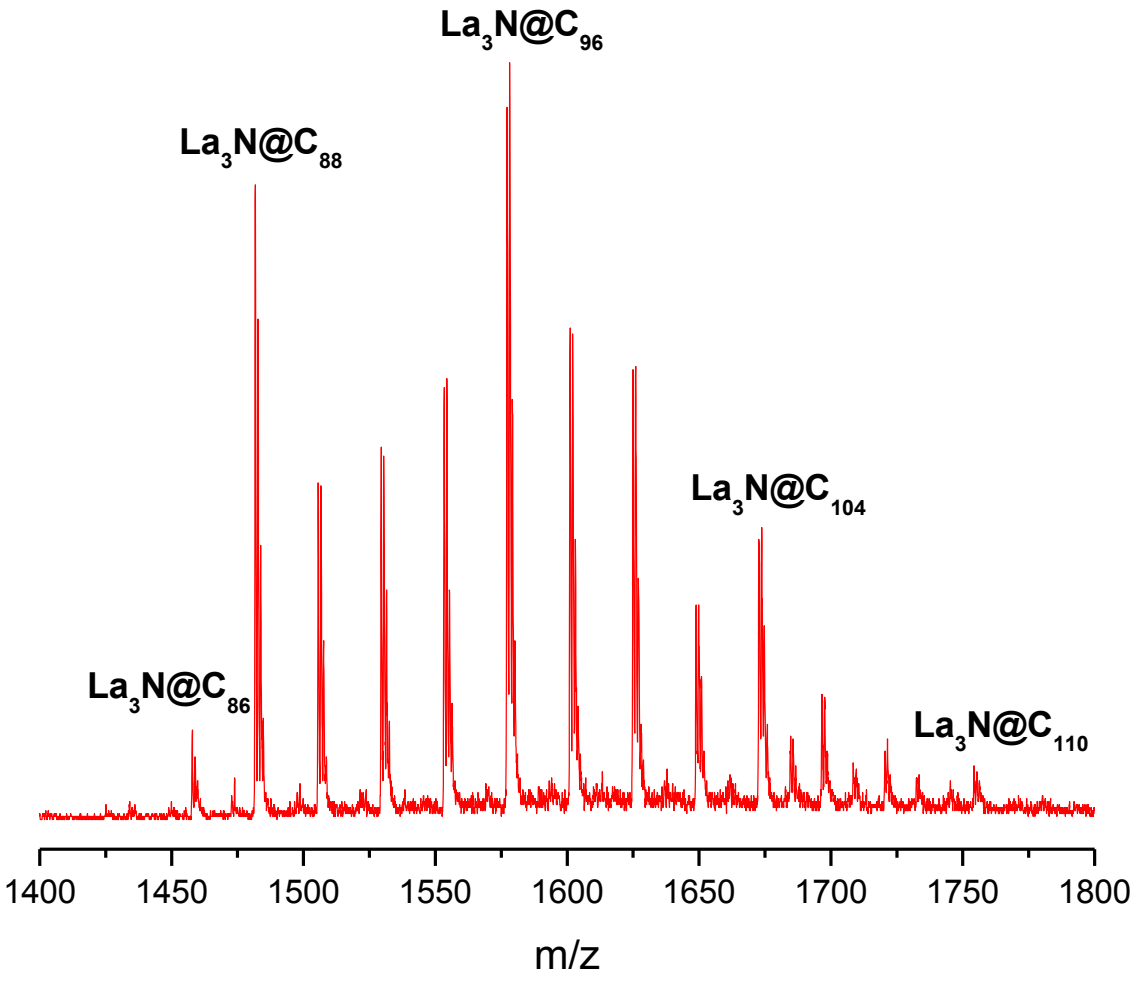


**Figure 3.30**. Mass spectrum of the $La_3N@C_{2n}$ clusterfullerene family using a $La_2O_3$/C 1:5 ratio (top trace).

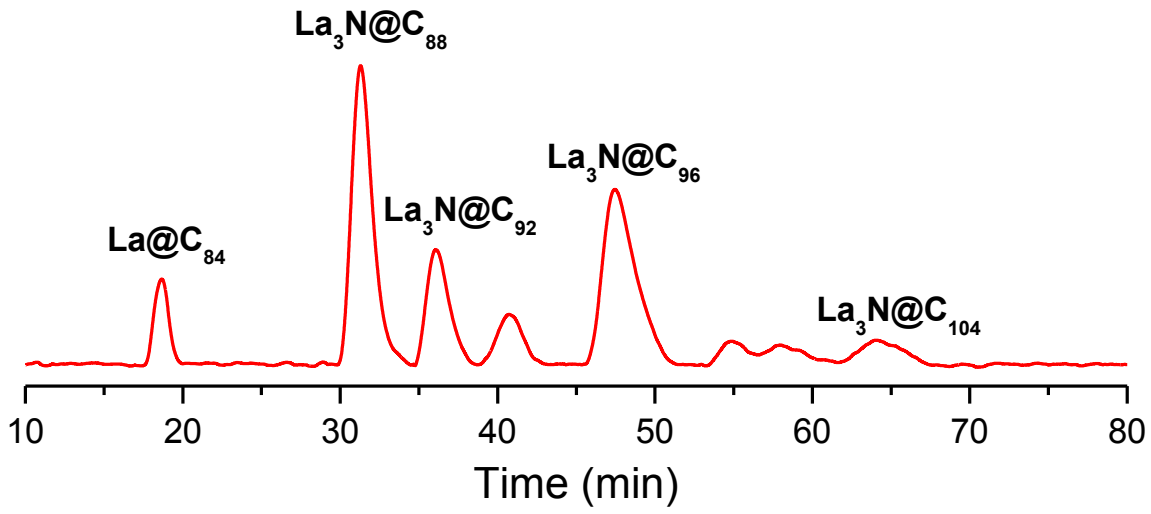


**Figure 3.31**. HPLC chromatogram of the $La_3N@C_{2n}$ metallofullerene family. Buckyprep-M column, mobile phase toluene, flow rate 4.0 mL/min, detection 370 nm.

Figure 3.30 shows the MALDI-TOF mass spectrum and Figure 3.31 the HPLC trace of the $La_3N@C_{2n}$ clusterfullerene family extracted from the soot produced using a 1:5 $La_2O_3$/C ratio. Note that as this ratio increases from 1:4 to 1:5 the mass distribution changes dramatically, but $La_3N@C_{96}$ still remains as one of the major products. A significant increase in the $La_3N@C_{88}$ yield is also observed. Another noteworthy point is that a wider carbon-cage distribution of $La_3N@C_{2n}$ cluster fullerenes is formed, with cages ranging from $C_{86}$ to $C_{110}$, making this family of metallofullerenes the largest in terms of cluster and carbon-cage sizes.

The fact that the metallofullerene yield decreases when the size of the metallic cluster increases suggests that the cluster size plays the most important role in terms of carbon-cage distribution, abundance, and preference for a given fullerene template.[14, 17] For example, $Sc_3N@C_{2n}$ ($r_{Sc}^{3+}$=0.745 Å) preferentially templates the $C_{80}$ cage, producing

the highest fullerene yield, whereas $Gd_3N@C_{2n}$ ($r_{Gd}^{3+}$=0.938 Å) continues to prefer the $C_{80}$ cage but produces the lowest yield.

Metallic clusters larger than $Gd_3N$ such as $Nd_3N$, $Pr_3N$ and $Ce_3N$ are preferentially encapsulated inside a $C_{88}$ cage, and the fullerene yield increases in the order $Ce_3N@C_{2n}$ ($r_{Ce}^{3+}$=1.010 Å) < $Pr_3N@C_{2n}$ ($r_{Pr}^{3+}$=0.997 Å) < $Nd_3N@C_{2n}$ ($r_{Nd}^{3+}$=0.983 Å).[15] Since metallic nitride endohedral fullerenes appear in larger abundance templating the $C_{80}$ rather than the $C_{88}$ cage (with the exception of $Gd_3N@C_{2n}$), it was not surprising to find that $La_3N@C_{2n}$ ($r_{La}^{3+}$=1.045 Å) produces the lowest fullerene yield among all the metallic nitride endohedral fullerenes under the same preparation conditions. Also, it should be noted that under our arcing conditions, $Eu_3N@C_{2n}$ and $Sm_3N@C_{2n}$ are not formed. As suggested by Gu and co-workers, this is likely due to product yields being associated with thermal properties of the caged metals, such as boiling points.[22] Current work in our group is underway to understand this dependence and to try to bypass the problems to obtain those novel EMFs.

**Isolation and Purification of the $La_3N@C_{2n}$ Endohedral Fullerenes**

Using our optimized conditions, we were able to isolate and purify $La_3N@C_{88}$, $La_3N@C_{92}$ and $La_3N@C_{96}$. The identity and purity of these three metallofullerenes were established by their HPLC chromatograms, mass spectra and SEM/EDS analysis. The much lower yield of the other fractions prevented their isolation (see Figures 3.32-3.35).

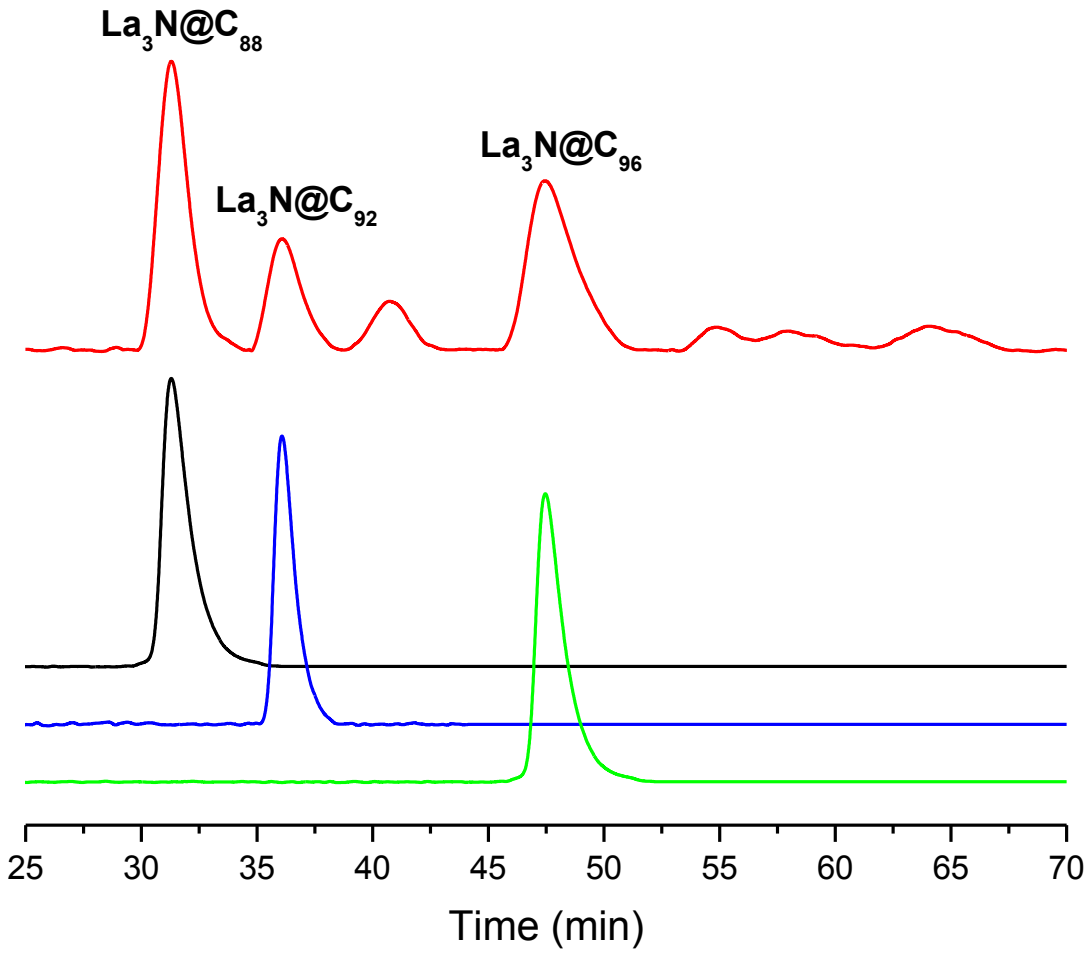


**Figure 3.32**. HPLC chromatogram of the $La_3N@C_{2n}$ clusterfullerene family and isolated fractions. Buckyprep-M column; toluene flow rate = 4.00 mL/min; detection at 372 nm.

Using a semipreparative Buckyprep-M column the three main fractions were isolated in considerably high purity. The purity was checked by HPLC injections using both Buckyprep-M and Buckyprep columns, followed by MALDI-TOF mass analysis in both positive and negative ion modes.

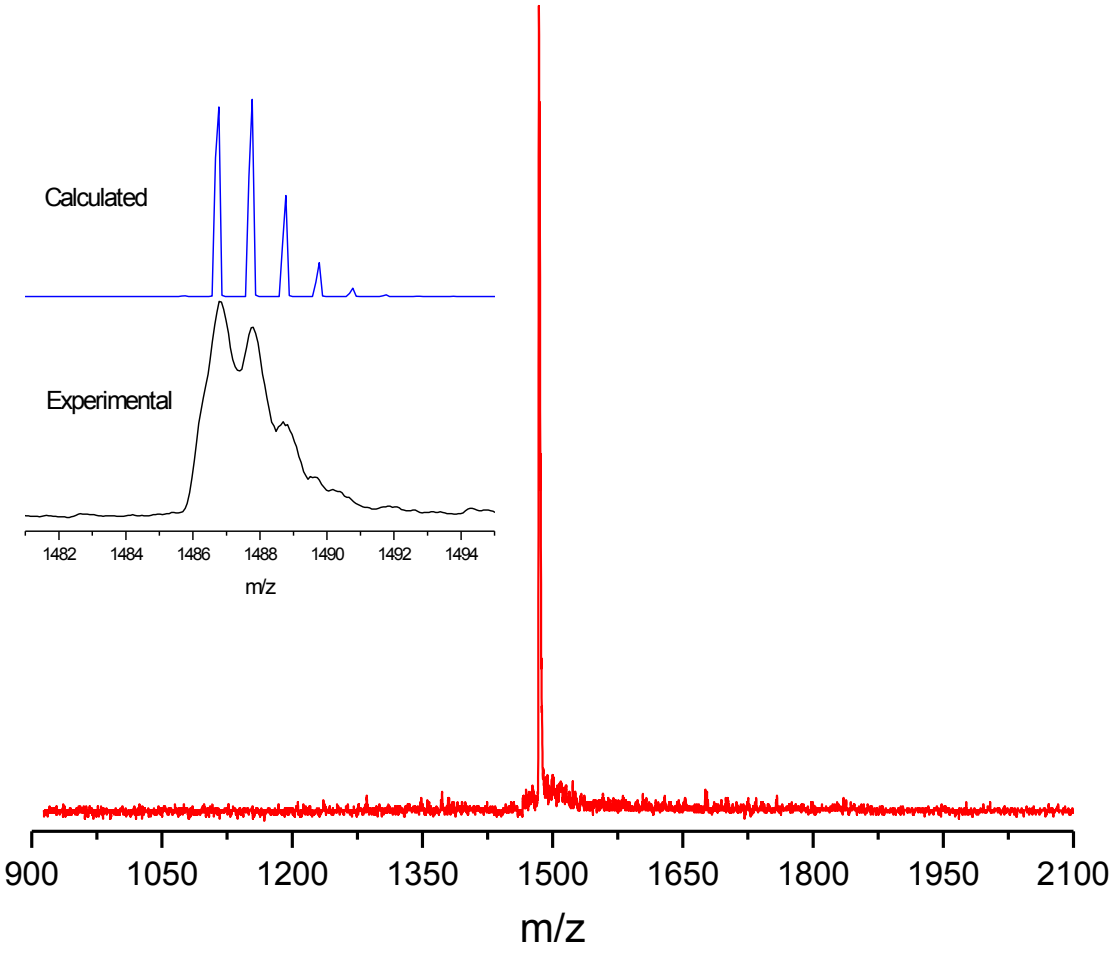


**Figure 3.33**. MALDI-TOF mass spectrum of the isolated sample of $La_3N@C_{88}$. (Inset) Expansions of the calculated and experimental spectra for $La_3N@C_{88}$.

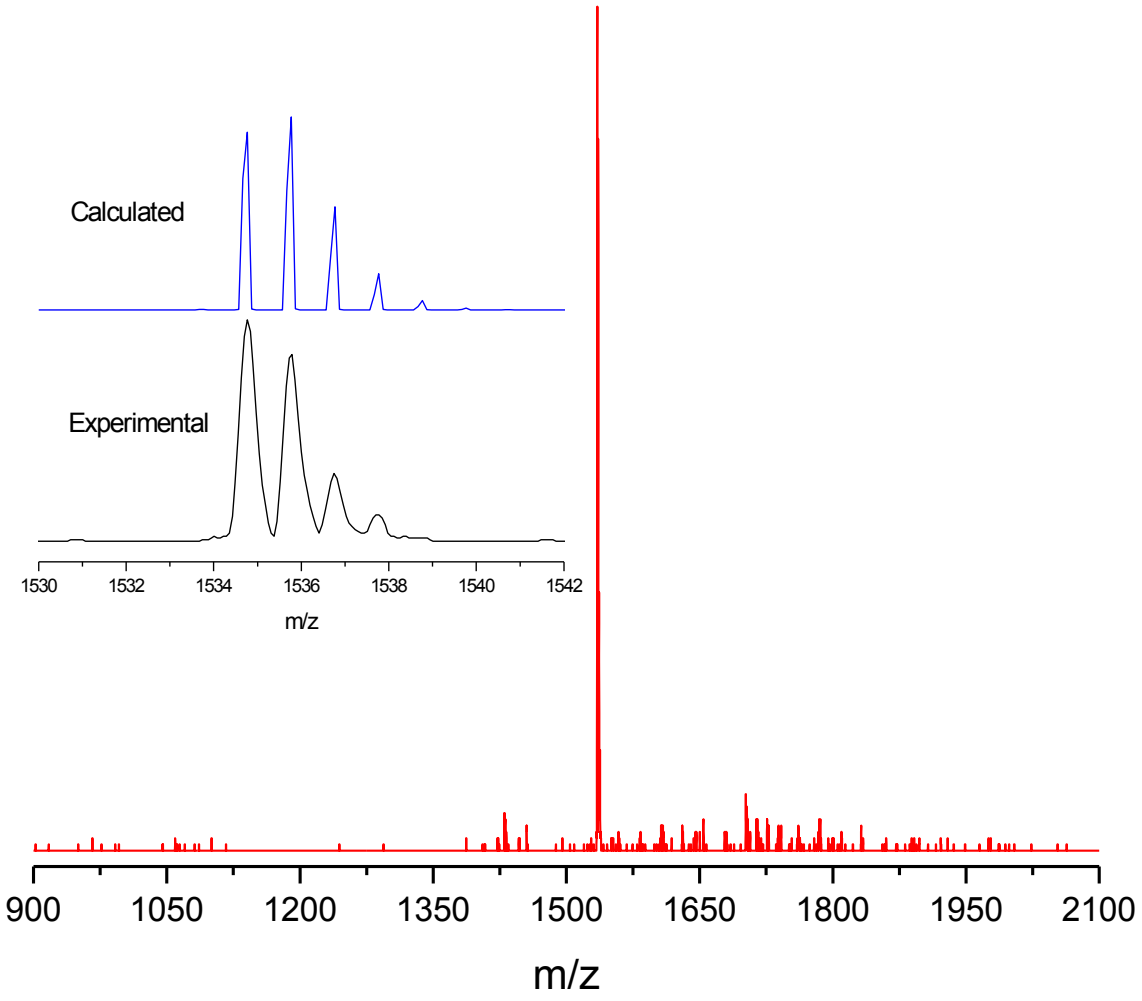


**Figure 3.34**. MALDI-TOF mass spectrum of the isolated sample of $La_3N@C_{92}$. (Inset) Expansions of the calculated and experimental spectra for $La_3N@C_{92}$.

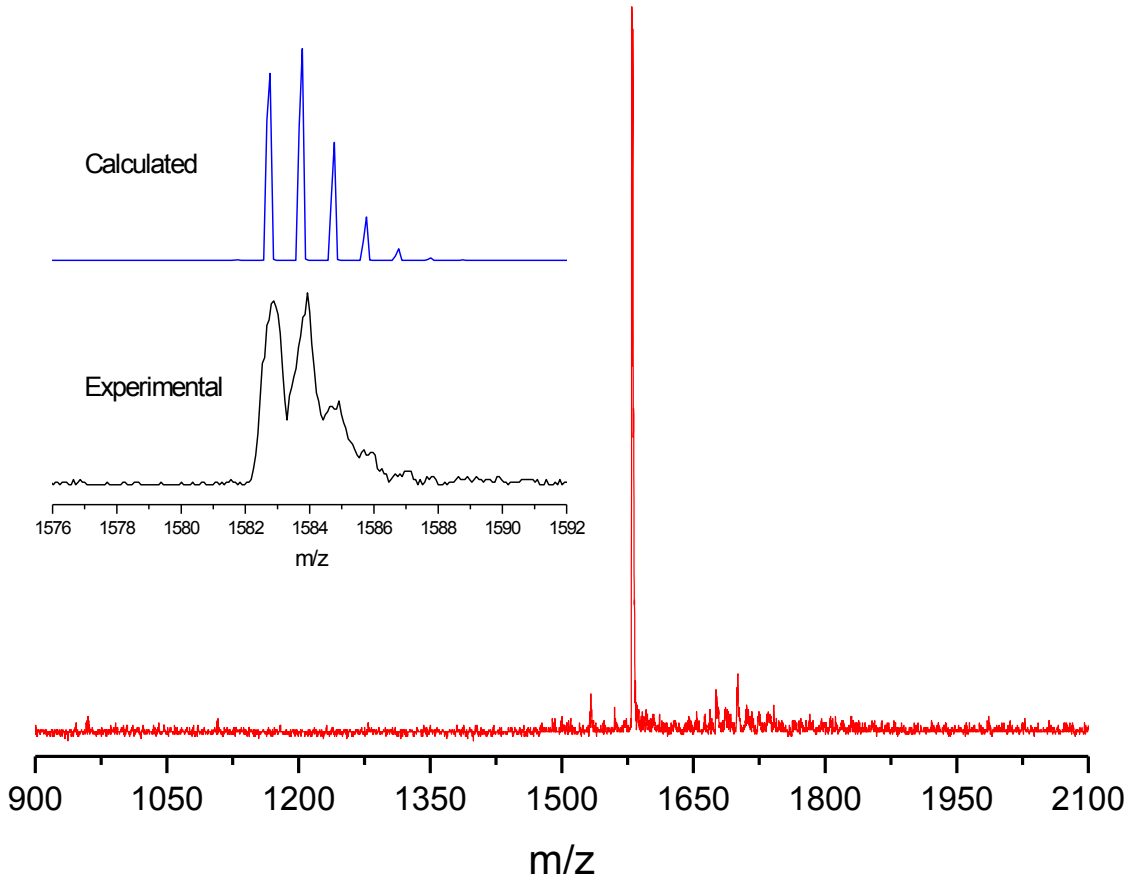


**Figure 3.35**. MALDI-TOF mass spectrum of the isolated sample of $La_3N@C_{96}$. (Inset) Expansions of the calculated and experimental spectra for $La_3N@C_{96}$.

A closer look at the positive ion mode MALDI TOF MS (Figures 3.33-3.35) of these metallofullerenes shows an excellent agreement between the calculated and experimental isotopic distributions, confirming their chemical identities. Furthermore, samples of $La_3N@C_{2n}$ (n = 44, 46 and 48) were deposited on TEM grids and submitted to energy dispersive spectroscopy (EDS) analysis (Figure 3.36), which showed the characteristic peaks of lanthanum, giving further proof of the nature of these endohedral fullerenes.

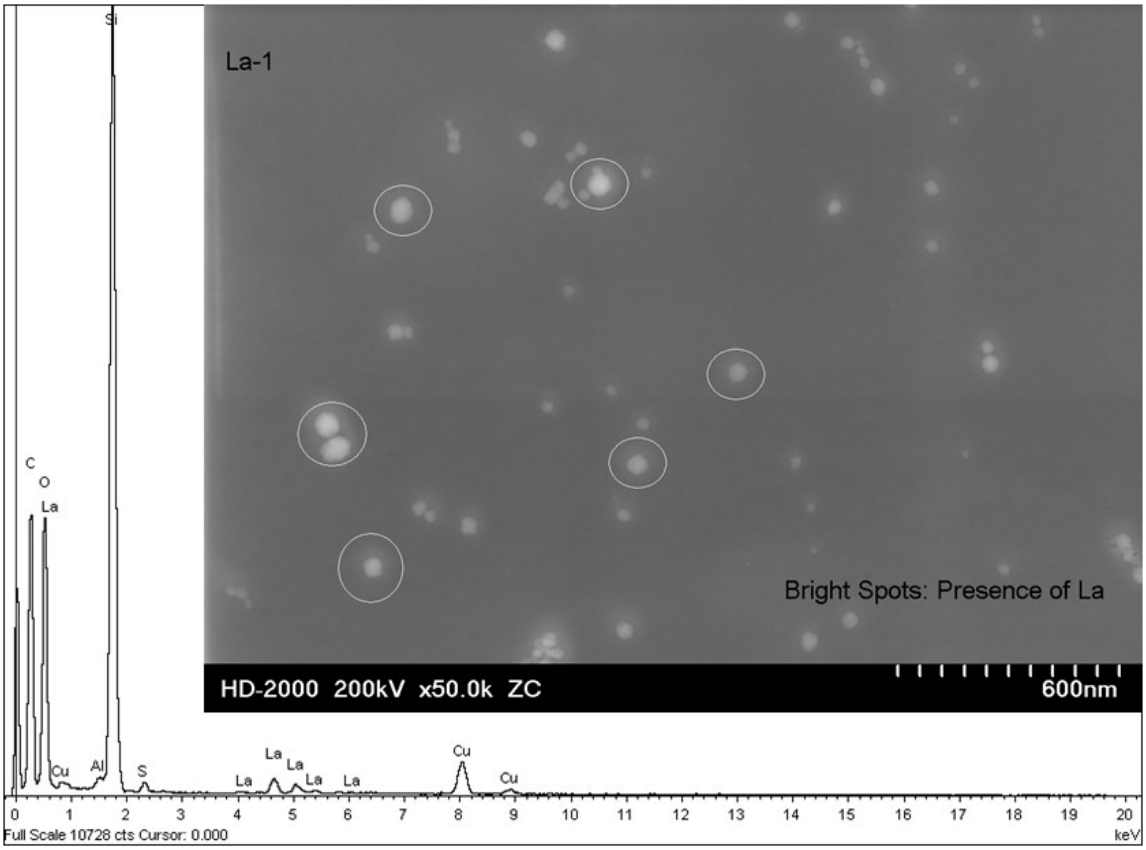


**Figure 3.36**. SEM/EDS of $La_3N@C_{88}$. Copper and aluminium come from the grid and sample holder. Sulfur and oxygen probably come from the solvents used to manipulate the samples (ether and carbon disulfide). And Si comes as an impurity after passing the sample through a silica column (in a Pasteur pipette) after electrochemical analysis.

From the HPLC chromatogram and the amounts of metallofullerenes collected, it was observed that $La_3N@C_{96}$ corresponds to 36% of the extracted metallofullerenes while $La_3N@C_{88}$ represents 33%.

It is important to note from the mass spectrum and HPLC chromatograms (Figure 3.30-3.31) that beyond $La_3N@C_{96}$, the yield decreases until $La_3N@C_{104}$, where an appreciable increase is observed. Such a yield distribution suggests that if larger metallic

nitride clusters could be formed the expected templated fullerene would be the $C_{104}$ cage. An interesting finding is that the preferentially templated fullerene cages seem to increase in size exactly by eight carbons as the size of the metallic nitride increases from $C_{80}$ to $C_{88}$ to $C_{96}$ and then $C_{104}$. The nature of this stabilization phenomenon remains uncertain and calculations are currently underway in order to understand this discrete increase.

**Electrochemical Studies of $La_3N@C_{2n}$ Endohedral Fullerenes**

The redox properties of metallic nitride endohedral fullerenes ranging from $C_{80}$ to $C_{88}$ cages have shown a progressive decrease of the HOMO-LUMO gaps as the size of the carbon cage increases, and irreversible reductions that become reversible when the carbon cage reaches the $C_{88}$ size.[7a, 14, 17] However, from $C_{88}$ to $C_{96}$ this straightforward tendency is not observed (Figure 3.37).

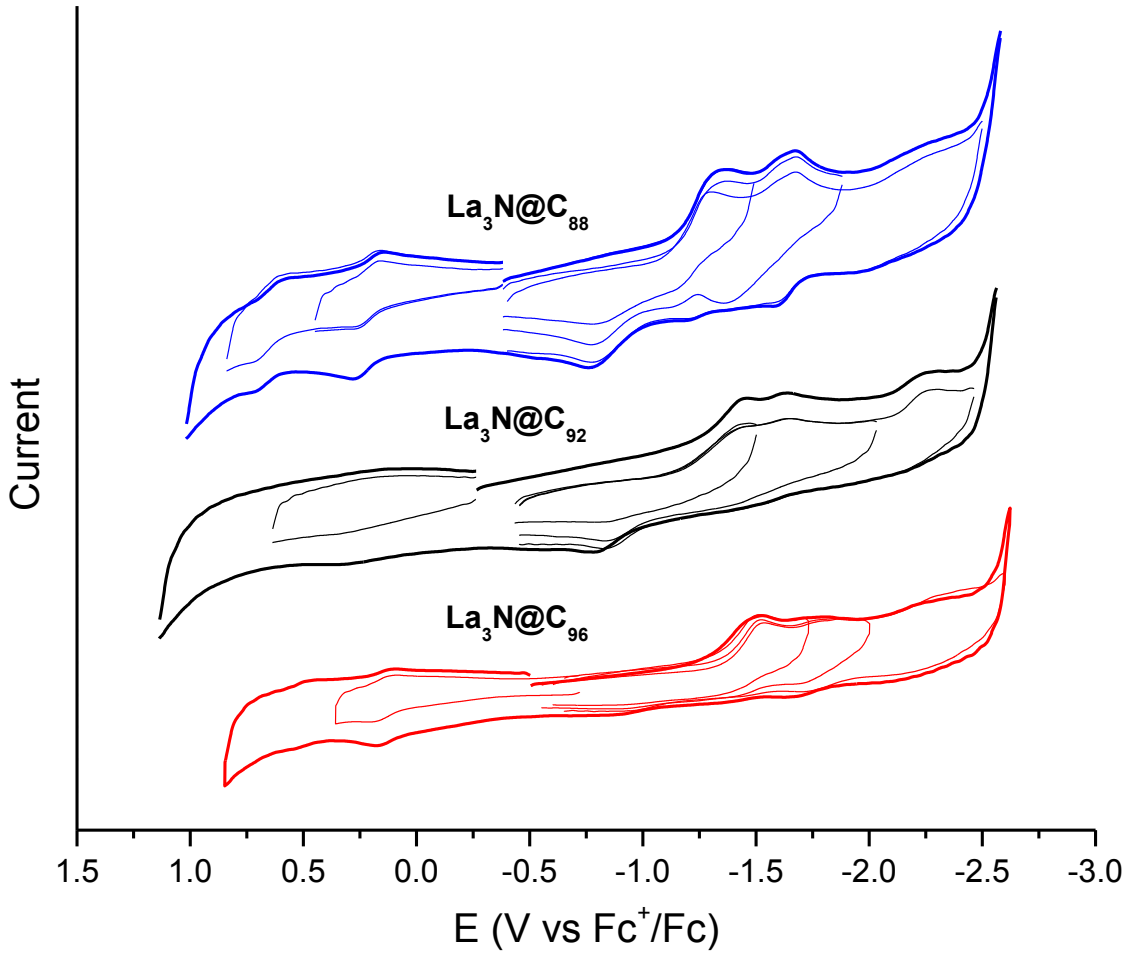


**Figure 3.37**. Cyclic voltammograms of $La_3N@C_{88}$, $La_3N@C_{92}$, and $La_3N@C_{96}$ in 0.05 M $NBu_4PF_6$/*o*-DCB with ferrocene as internal standard. Scan rate = 0.1 $Vs^{-1}$.

$La_3N@C_{2n}$ (n = 44, 46 and 48) metallofullerenes exhibit three irreversible reduction and two irreversible oxidation steps. Their electrochemical HOMO-LUMO gaps are 1.57, 1.80, and 1.68 V respectively for $La_3N@C_{88}$, $La_3N@C_{92}$ and $La_3N@C_{96}$ (Table 3.7).

**Table 3.7**. Half wave potentials vs $Fc^{+}/Fc$ of the reduction and oxidation steps of $La_3N@C_{88}$, $La_3N@C_{92}$ and $La_3N@C_{96}$.

| EMF | $E_p$ red$_1$ | $E_p$ red$_2$ | $E_{1/2}$ ox$_1$ | $E_{1/2}$ ox$_2$ | $\Delta E_{gap}$ |
|---|---|---|---|---|---|
| $La_3N@C_{88}$ | -1.36 | -1.67 | 0.21 | 0.66 | 1.57 |
| $La_3N@C_{92}$ | -1.44 | -1.64 | 0.36 | | 1.80 |
| $La_3N@C_{96}$ | -1.54 | -1.77 | 0.14 | 0.53 | 1.68 |

A very interesting finding is that with the exception of $La_3N@C_{88}$, the electrochemistry of all the $M_3N@C_{88}$ (M = Gd, Nd, Pr and Ce) metallofullerenes studied by our group have shown two reversible oxidations (the first one at very low potentials ≈ 0.06-0.08 V), a reversible first reduction, a second quasi-reversible reduction and what is likely a multielectronic third reduction step.[7a, 14, 17] Those metallofullerenes also have very low HOMO-LUMO gaps (~1.38-1.46 V). Nevertheless, $La_3N@C_{88}$ seems to behave differently (Figure 3.38 and Table 3.8), exhibiting two irreversible oxidation and reduction steps. Additionally, it has a slightly larger HOMO-LUMO gap of 1.57 V. Increasing the scan rates (100 $mVs^{-1}$ to 2 $Vs^{-1}$) did not improve the reversibility of the reduction waves.

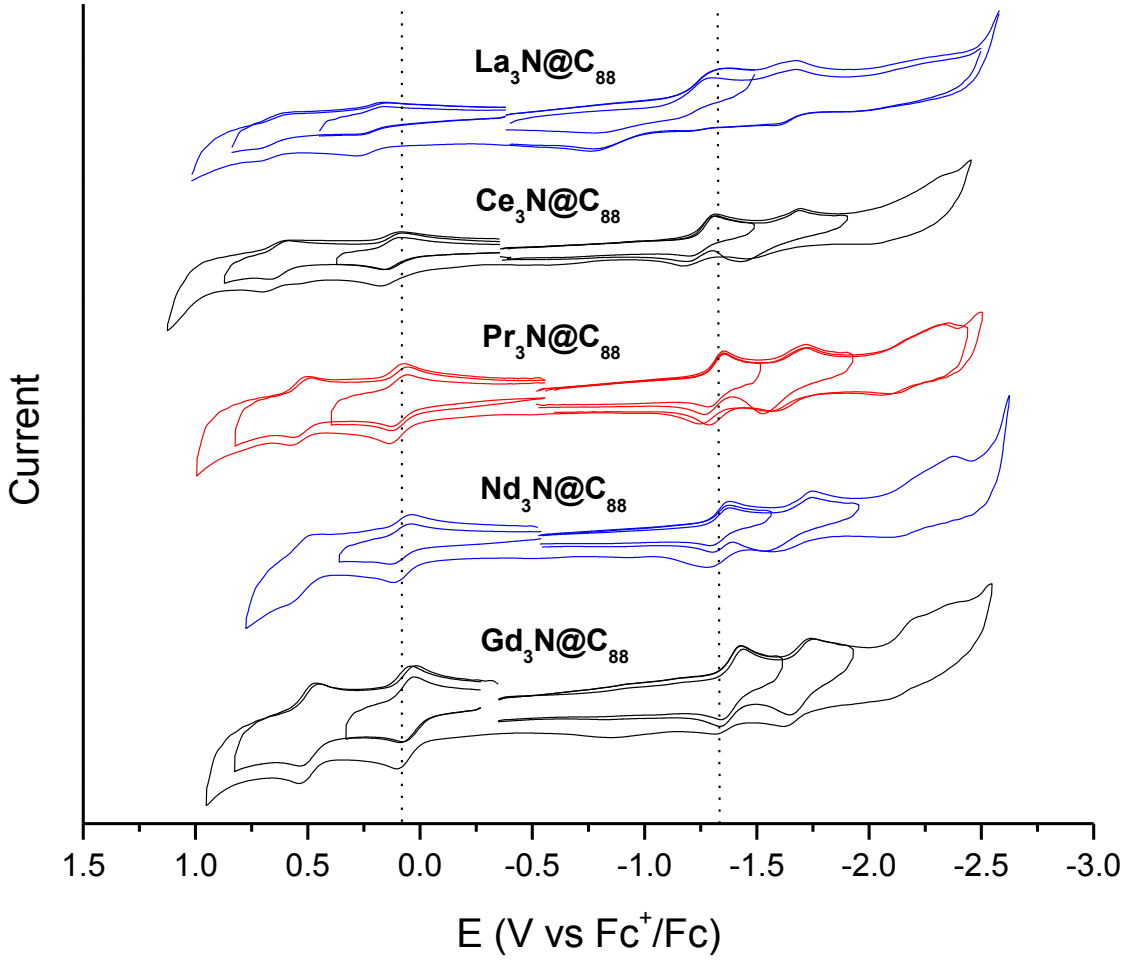


**Figure 3.38**. Cyclic voltammograms of $M_3N@C_{88}$ (M=La, Ce, Pr, Nd and Gd) in 0.05 M $NBu_4PF_6$/*o*-DCB with ferrocene as internal standard. Scan rate = 0.1 $Vs^{-1}$.

**Table 3.8**. Half wave potentials vs $Fc^+/Fc$ of the reduction and oxidation steps of several $M_3N@C_{88}$ metallofulerenes.

| EMF | Electronegativity | $E_{1/2}$ red$_1$ | $E_{1/2}$ ox$_1$ | $\Delta E_{gap}$ |
|---|---|---|---|---|
| **$Gd_3N@C_{88}$** | 1.20 | -1.40 | 0.06 | 1.46 |
| **$Nd_3N@C_{88}$** | 1.14 | -1.33 | 0.07 | 1.40 |
| **$Pr_3N@C_{88}$** | 1.13 | -1.31 | 0.09 | 1.40 |

| | | | | |
|---|---|---|---|---|
| **$Ce_3N@C_{88}$** | 1.12 | -1.30 | 0.08 | 1.38 |
| **$La_3N@C_{88}$** | 1.10 | $E_p$=-1.36 | $E_p$=0.21 | 1.57 |

[a] Pauling electronegativity. [15]

Due to the low yield of $M_3N@C_{92}$ (M = Pr and Ce) metallofullerenes, we were unable to isolate these for electrochemical studies and to compare to $La_3N@C_{92}$. However, samples of $Pr_3N@C_{96}$ and $Ce_3N@C_{96}$ were synthesized, isolated, and purified as reported earlier.[17]

Figure 3.39 shows the cyclic voltammograms of the $M_3N@C_{96}$ (M=Pr, Ce and La) metallofullerenes. These compounds exhibit similar redox behavior, with two reversible oxidations and two irreversible reductions; a third, possibly multielectronic, irreversible reduction is also observed. Their electrochemical HOMO-LUMO gaps also have similar values (Table 3.9).

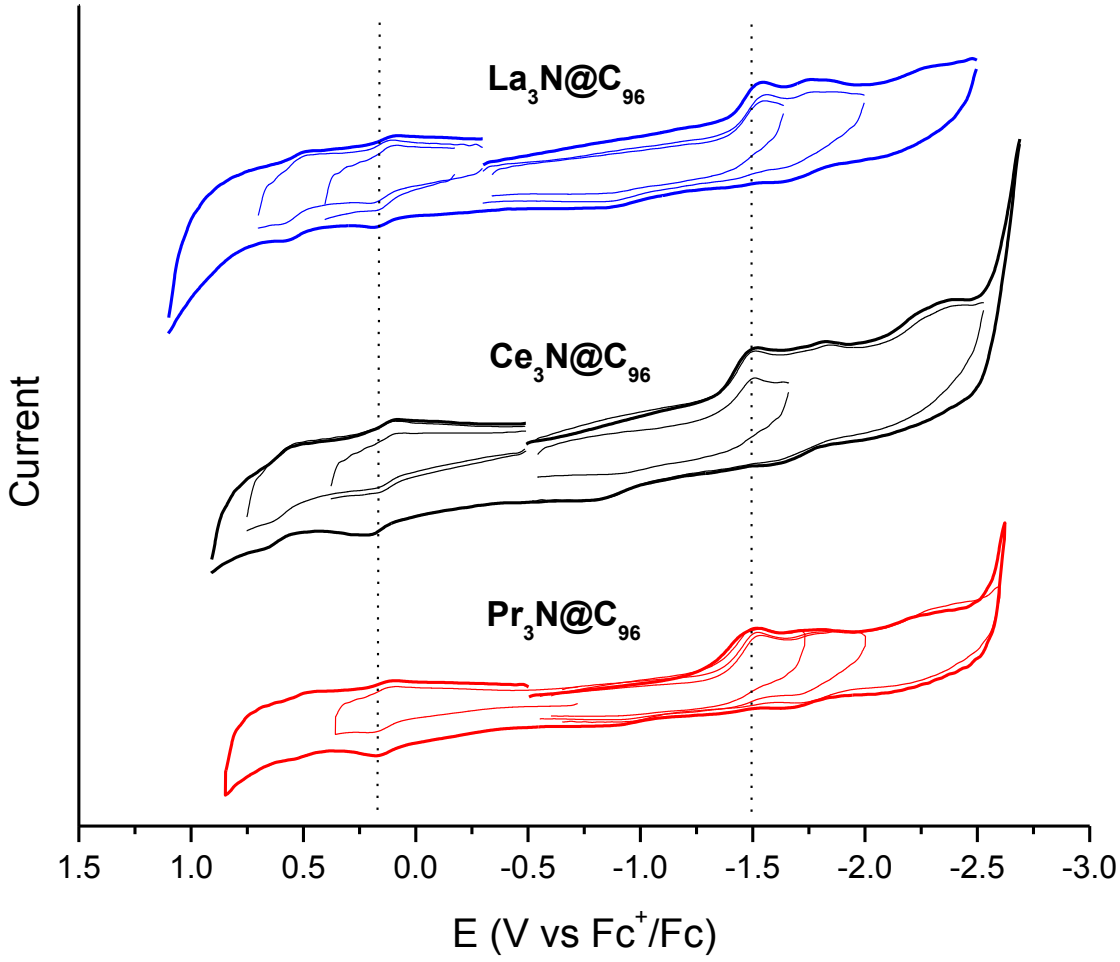


**Figure 3.39**. Cyclic voltammograms of $La_3N@C_{96}$, $Ce_3N@C_{96}$ and $Pr_3N@C_{96}$ in 0.05 M $NBu_4PF_6$/*o*-DCB with ferrocene as internal standard. Scan rate = 0.1 $Vs^{-1}$.

**Table 3.9**. Half wave potentials vs $Fc^+/Fc$ of the reduction and oxidation steps of $Pr_3N@C_{96}$, $Ce_3N@C_{96}$ and $La_3N@C_{96}$.

| EMF | $r(M^{3+})$ Å | $E_p$ red$_1$ | $E_p$ red$_2$ | $E_{1/2}$ ox$_1$ | $E_{1/2}$ ox$_2$ | $\Delta E_{gap}$ |
|---|---|---|---|---|---|---|
| **$Pr_3N@C_{96}$** | 0.997 | -1.51 | -1.86 | 0.14 | 0.53 | 1.65 |
| **$Ce_3N@C_{96}$** | 1.010 | -1.38 | -1.68 | 0.30 | 0.74 | 1.68 |
| **$La_3N@C_{96}$** | 1.045 | -1.54 | -1.77 | 0.14 | 0.53 | 1.68 |

All metallofullerenes of the same cage-size and different metallic nitride cluster have shown similar redox behavior and HOMO-LUMO gaps, suggesting that the carbon cage symmetry is probably the same for each size. $La_3N@C_{88}$ is an exception, which may be an indication that the cage symmetry is different or that due to the cluster size the interactions between the cluster and the carbon cage are stronger for this metallofullerene. X-ray data are necessary to confirm this suggestion.

**UV/Vis-NIR Studies of $La_3N@C_{2n}$ Endohedral Fullerenes**

UV/Vis-NIR studies have proven to be very useful in metallofullerene research because they give insight about the symmetry of the fullerene cage and their optical HOMO-LUMO gaps, since absorptions of these compounds are mainly due to $\pi$-$\pi^*$ transitions.[2-3] Samples of $La_3N@C_{2n}$ (n = 44, 46 and 48) were dissolved in toluene and their UV/Vis-NIR spectra were recorded using a Perkin-Elmer Lambda 950 spectrophotometer. Figure 3.40 shows the superimposed spectra of the isolated $La_3N$ endohedral fullerene fractions while table 3.10 lists absorption values and optical onset of these metallofullerenes.

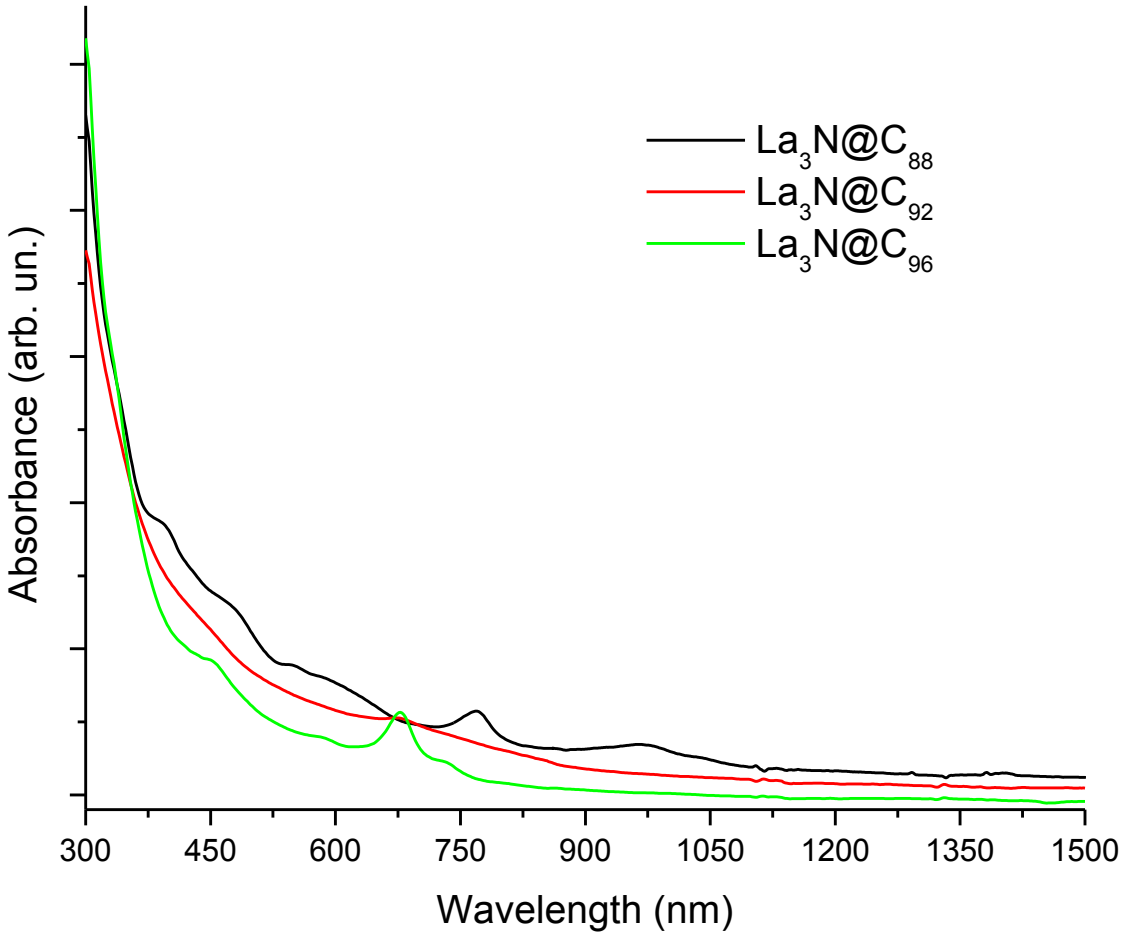


**Figure 3.40**. UV-vis-NIR spectra of $La_3N@C_{88}$, $La_3N@C_{92}$, and $La_3N@C_{96}$ dissolved in toluene.

$La_3N@C_{88}$ exhibits absorptions at 395, 479, 602, 768 and 965 nm. Except for the absorption at 602 nm, these values are in the same range as those found for other $M_3N@C_{88}$ (M=Nd, Pr and Ce) metallofullerenes.[17] However, the spectral onset of $La_3N@C_{88}$ is located around 1330 nm, which results in an optical gap of ~0.93 V, higher than the optical gaps reported for the same cage-size counterparts, in agreement with the electrochemical band gaps for all these metallofullerenes.

Unlike what was observed by electrochemistry, where the electrochemical gaps differed significantly, the optical gaps of $La_3N@C_{92}$ and $La_3N@C_{96}$ exhibit similar values (1.08 and 1.09 V, respectively) with absorptions exclusively in the UV/Vis region (see Table 3.10).

**Table 3.10**. Characteristic UV-vis-NIR absorptions and absorption onset of some $La_3N@C_{2n}$ (n = 44, 46, and 48).

| EMF | Onset (nm) | Band-gap (eV)[a] | UV-vis-NIR absorptions peaks (nm) |
|---|---|---|---|
| $La_3N@C_{88}$ | 1330 | 0.93 | 395, 479, 602, 768, 965 |
| $La_3N@C_{92}$ | 1147 | 1.08 | 342, 449, 674 |
| $La_3N@C_{96}$ | 1136 | 1.09 | 450, 583, 677, 733 |

[a] Band-gap calculated from the spectral onset (bandgap (eV) ≈ 1240/onset (nm) [8])

## Experimental Section

High purity graphite rods (6 mm diameter) purchased from POCO were core-drilled (4 mm diameter) and packed with (3/1), (1/1), and (1/1) mixtures of graphite powder and $CeO_2$ (cerium oxide), $Pr_6O_{11}$ (praseodymium oxide) and $Nd_2O_3$ (neodymium oxide), respectively. For the synthesis of the $La_3N@C_{2n}$ family the rods were packed with different ratios. The rods were annealed at 1000 °C for 12 hours and then vaporized in a Krätschmer-Huffman arc reactor under a mixture of ammonia (20 mbar) and helium (200 mbar) using an arc current of 85A. The soot collected from the arc reactor for each packed rod was extracted with $CS_2$ in a sonicator for about two hours. After removal of the solvent, the crude mixtures were washed with ether and acetone until the solution was

no longer colored. The solids were dissolved in toluene and separated by HPLC using a semipreparative 10 mm x 250 mm Buckyprep-M column with a flow rate of 4 mL of toluene per minute. MALDI-TOF mass spectrometry was carried out using a Bruker Omni Flex. For the EDS analysis, the samples were deposited on TEM grids and the spectra were taken on a HD-2000 STEM, equipped with an Oxford EDS system. Cyclic voltammetry was carried out in a one-compartment cell connected to a BAS 100B workstation in a solution of *o*-DCB containing 0.05 M $NBu_4PF_6$. A 2 mm diameter glassy carbon disk was used as the working electrode and a platinum wire served as a counter electrode. Ferrocene was added to the solution at the end of each experiment as internal standard and all the electrochemical potentials were referenced to its redox couple.

## Conclusions

The $Nd_3N@C_{2n}$ ($40 \leq n \leq 50$), $Pr_3N@C_{2n}$ ($40 \leq n \leq 52$), and $Ce_3N@C_{2n}$ ($43 \leq n \leq 53$) endohedral metallofullerene families were successfully synthesized, isolated, and characterized by mass spectroscopy, HPLC, UV-vis-NIR and cyclic voltammetry. These are the isolated endohedral metallofullerenes with the largest clusters encapsulated to date. These three families of metallofullerenes exhibit the same preferential templating for the $C_{88}$ cage. When the ionic radii of the metal forming the cluster is increased another tendency appears, a progressive and significant increase in the yield of the $M_3N@C_{96}$ metallofullerene, suggesting preferential templating for larger endohedral metallofullerenes. The electronic properties of these new endohedral compounds were studied obtaining smaller optical gaps as the size of the cage is increased. Metallofullerenes of the same cage size showed similar absorptions and close bandgap

values suggesting similar structures. The electrochemical properties were investigated by cyclic voltammetry and showed reversible reductions for the $C_{88}$ cage compounds and irreversible reductions for the smaller cages. The oxidation steps are easier for the larger cages.

$La_3N$ represents the largest metallic nitride cluster encapsulated to date inside a fullerene cage, with preference for the $C_{96}$ cage. This represents the first example of this cage being preferentially formed. The electrochemical properties of this family showed that $La_3N@C_{88}$ exhibits irreversible oxidation and reduction steps, unlike other $M_3N@C_{88}$ metallofullerenes. In general $La_3N@C_{92}$ and $La_3N@C_{96}$ exhibit similar electrochemistry, UV/Vis-NIR absorptions and HOMO-LUMO gaps.

## References


[1] Stevenson, S.; Rice, G.; Glass, T.; Harich, K.; Cromer, F.; Jordan, M. R.; Craft, J.; Hadju, E.; Bible, R.; Olmstead, M. M.; Maitra, K.; Fisher, A. J.; Balch, A. L.; Dorn, H. C. *Nature*, **1999**, *401*, 55-57.

[2] Dunsch, L.; Yang, S. *Small* **2007**, 3, 1298-1320.

[3] Shinohara, H. *Rep. Prog. Phys*. **2000**, 63, 843-892.

[4] Stevenson, S.; Lee, H. M.; Olmstead, M. M.; Kozikowski, C.; Stevenson, P.; Balch, A. L. *Chem. Eur. J.*, **2002**, *8*, 4528-4535.

[5] Krause, M.; Wong, J.; Dunsch, L. *Chem. Eur. J*. **2005**, 11, 706-711.

[6] Stevenson, S.; Phillips, J.P.; Reid, J.E.; Olmstead, M.M.; Rath, S.P.; Balch, A.L. *Chem. Commun*. **2004**, 2814-2815.

[7] a) Chaur, M.N.; Melin, F.; Elliot, B.; Athans, J.A.; Walker, K.; Holloway, B.C.; Echegoyen, L. *J. Am. Chem. Soc*. **2007**, 129, 14826-14829. b) Krause, M.; Dunsch, L. *Angew. Chem. Int. Ed*. **2005**, *44*, 1557-1560.

[8] Wolf, M.; Muller, K.H.; Skourski, Y.; Eckert, D.; Georgi, P.; Krause, M.; Dunsch, L. *Angew. Chem. Int. Ed*. **2005**, 44, 3306-3309.

[9] Yang, S.; Dunsch, L.; *J. Phys. Chem. B* **2005**, 109, 12320-12328.

[10] Zuo, T.; Beavers, C. M.; Duchamp, J. C.; Campbell, A.; Dorn, H. C.; Olmstead, M. M.; Balch, A. L. *J. Am. Chem. Soc*. **2007**, *129*, 2035-2043.

[11] a) Stevenson, S.; Fowler, P.W.; Heine, T.; Duchamp, J.C.; Rice, G.; Glass, T.; Harich, K.; Hajdu, E.; Bible, R; Dorn, H.C. *Nature* **2000**, 408, 427-428. b) Olmstead, M. M.; de Bettencourt-Dias, A.; Duchamp, J. C.; Stevenson, S.; Dorn, H. C.; Balch,

A. L. *J. Am. Chem. Soc.*, **2000**, *122*, 12220-12226. c) Yang, S.; Kalbac, M.; Popov, A.; Dunsch, L. *ChemPhysChem* **2006**, 7, 1990-1995.

[12] Campanera, J.M.; Bo, C.; Poblet, J.M. *Angew. Chem. Int. Ed*., **2005**, 44, 7230-7233.

[13] Krause, M.; Kuzmany, H.; Georgi, P.; Dunsch, L.; Vietze, K.; Seifert, G. *J. Chem. Phys*. **2001**, 115, 6596-6605.

[14] Frederic, M.; Chaur, M.N.; Engmann, S.; Elliott, B.; Kumbhar, A.; Athans, A.J.; Echegoyen, L. *Angew. Chem. Int. Ed*. **2007**, 46, 9032-9035.

[15] CRC *Handbook of Chemistry and Physics*, 81st ed. (Ed.: D.R. Lide), CRC, New York City, **2000**.

[16] a) Cardona, C.M.; Elliott, B.; Echegoyen, L. *J. Am. Chem. Soc*. **2006**, 128, 6480-6485. b) Yang, S.; Zalibera, M.; Rapta, P.; Dunsch, L. *Chem. Eur. J*. **2006**, 12, 7848-7855. c) Zhang, L.; Chen, N.; Fan, L.; Wang, C.; Yang, S. *J. Electroanal. Chem*. **2007**, 608, 15-21.

[17] Chaur, M.N.; Melin, F.; Elliott, B.; Kumbhar, A.; Athans, A.J.; Echegoyen, L. *Chem. Eur. J*. **2008**, 14, 4594-4599.

[18] Fowler, P.W.; Manolopoulos, D.E. in *An Atlas of Fullerenes*, Clarendon, Oxford, **1995**.

[19] Popov, A.A.; Dunsch, L. *J. Am. Chem. Soc.* **2007**, 129, 11835-11849. b) Valencia, R.; Rodriguez-Fortea, A.; Poblet, J.M. *Chem. Commun.* **2007**, 4161-4163.

[20] Chaur, M.N.; Melin, F.; Ortiz, A.L.; Echegoyen, L. *Angew. Chem. Int. Ed.* **2009**, 48, 7514-7538.

[21] Chaur, M.N.; Melin, F.; Ashby, J.; Elliott, B.; Kumbhar, A.; Rao, A.M.; Echegoyen, L. *Chem. Eur. J.* **2008**, 14, 8213-8219.

[22] Lian, Y.; Shi, Z.; Zhou, X.; He, X.; Gu, Z. *Chem. Matter*. **2001**, 13, 39-42.

.

CHAPTER FOUR

# ELECTRONIC STRUCTURES AND REDOX PROPERTIES OF METALLIC NITRIDE ENDOHEDRAL METALLOFULLERENES

As of today the most abundant metallic nitride EMF is $Sc_3N@C_{80}$.[1] Its high abundance is largely attributed to its electronic structure which is $(Sc^{3+})_3N^{3-}@C_{80}^{6-}$.DFT calculations have shown that the stability of the $I_h$ (7)-$C_{80}$ isomer increases markedly when six electrons are transferred to the cage. As a result, the $I_h$ isomer becomes the most stable structure for $C_{80}^{6-}$. Seven isomeric structures of $C_{80}$ (with symmetries and numbering: $D_{5d}$(1)-$C_{80}$, $D_2$(2)-$C_{80}$, $C_{2v}$(3)-$C_{80}$, $D_3$(4)-$C_{80}$, $C_{2v}$(5)-$C_{80}$, $D_{5h}$(6)-$C_{80}$ and $I_h$(7)-$C_{80}$) fulfill the Isolated Pentagon Rule (IPR).[2] From these seven isomers only two empty cage isomers, $D_2$(2)-$C_{80}$ and $D_{5d}$(1)-$C_{80}$, have been isolated[3] and theoretical calculations have shown that the $I_h$(7)-$C_{80}$ structure is the least stable isomer overall.[4] However, metallic nitrides encapsulated inside the $C_{80}$ fullerene cage have only been found with cages of $I_h$ and $D_{5h}$ symmetry.[5] Calculations have also shown that the encapsulation of a metallic nitride inside a fullerene cage is accompanied by a significant charge transfer from the encapsulated moiety to the fullerene. Poblet and co-workers have rationalized the stabilization of metallic nitrides inside fullerene cages thought what they called the ionic model.[6-7]

In the ionic model a total of six electrons go from the highest occupied nitride orbitals to the lowest unoccupied cage orbitals. This formal electron transfer is accompanied by a large binding energy for the encapsulation process.[6] Poblet and co-

workers first reported the electronic structures of the $Sc_3N@C_{2n}$ (2n=68, 78 and 80) family. In this particular case the three fullerene cages ($D_3$-(6140)-$C_{68}$, $D_{3h}$(5)-$C_{78}$, and $I_h$(7)-$C_{80}$) have four very low-lying LUMOs accompanied with a large energy separation between the LUMO+3 and LUMO+4 (Figure 4.1).[6] On the other hand, the metallic nitride unit has three HOMOs that are relatively high in energy. Consequently, the cage orbitals can easily accommodate six electrons that stem from the three destabilized orbitals. Moreover, the electronic structure of the empty fullerenes suggests that it acquires, presumably, a considerable HOMO-LUMO gap after a transfer of six electrons, thus giving stability to the final complex. The final HOMO-LUMO gap of the metallic nitride EMFs can be estimated from the gap between LUMO+3 and LUMO+4 of the free cages. The calculated and estimated values are 1.27/1.17 eV for $Sc_3N@C_{68}$, 1.24/1.16 eV for $Sc_3N@C_{78}$, and 1.18/1.93 eV for $Sc_3N@C_{80}$.[7] The main conclusion that can be drawn from this observation is that the final HOMO-LUMO gaps can be predicted by simply checking the molecular-orbital energies of the free fullerene cage. In principle, only the free isomers with a large (LUMO+3)-(LUMO+4) gap will be predisposed to encapsulate metallic nitride units regardless of its metallic nature.[7]

Poblet calculated the (LUMO+3)-(LUMO+4) gaps for all the IPR isomers from $C_{60}$ to $C_{84}$.[7] He observed that the (LUMO+3)-(LUMO+4) gaps for all IPR cages were smaller than 1 eV, except for $C_{60}$, $D_3$-(6140)-$C_{68}$, $D_{3h}$(5)-$C_{78}$, and $I_h$(7)-$C_{80}$ isomers, see Figure 4.2. $C_{60}$ was rejected because its cavity measured through the cage radius, 3.551 Å, is not big enough to encapsulate a four-atom unit. In the other fullerene cages the cavity is not a limitation for the encapsulation of the metallic nitride unit. Based on these

results Poblet proposed that none $C_{82}$ and $C_{84}$ fullerenes that obey the IPR were able to encapsulate a trimetallic nitride unit.[7] These observations were later demonstrated experimentally by Echegoyen and co-workers when they reported that $Gd_3N@C_{82}$ and $Gd_3N@C_{84}$ are EMFs that do not obey the IPR.[5]

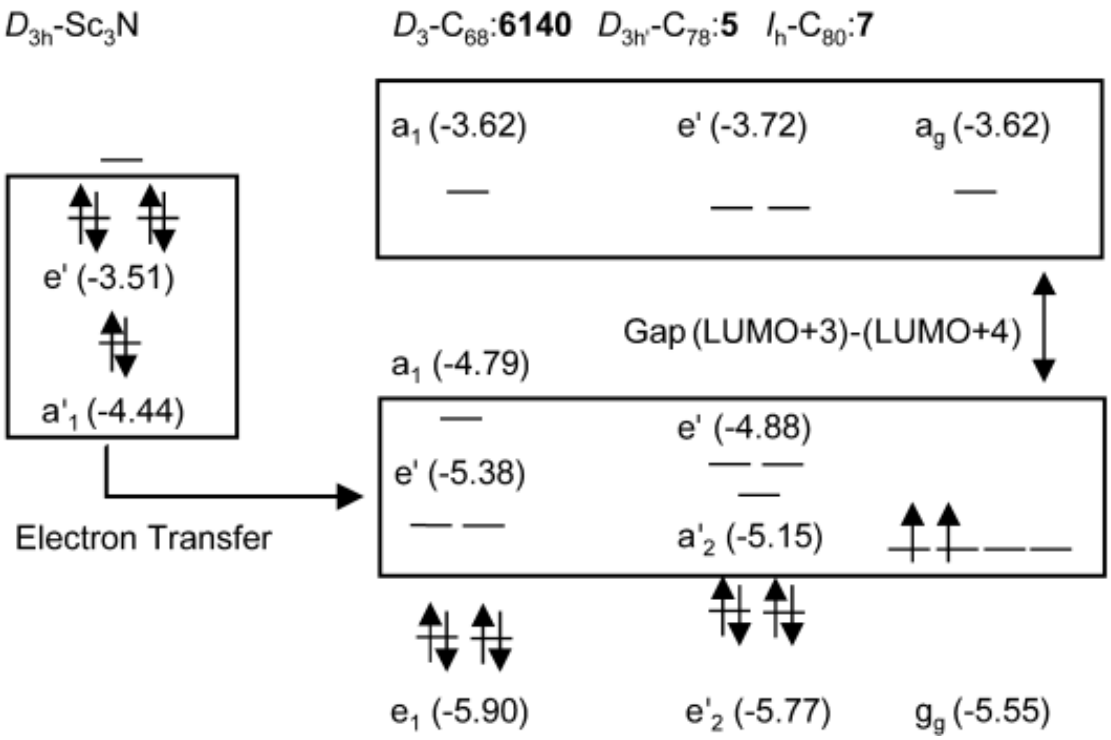


**Figure 4.1**. Representation of the ionic bond between the metallic nitride unit and the fullerene cages $D_3$-(6140)-$C_{68}$, $D_{3h}$(5)-$C_{78}$, and $I_h$(7)-$C_{80}$. There is a formal transfer of six electrons from the three highest occupied orbitals of the metallic nitride cluster to the three lowest unoccupied orbitals of the fullerene cages. Consequently, the $M_3N@C_{2n}$ (2n=68, 78, and 80) EMFs are described as $Sc_3N^{6+}@C_{2n}^{6-}$ with a relatively large HOMO-LUMO gap nearly equal to the (LUMO+3)-(LUMO+4) found in the free cages: The (LUMO+3)-(LUMO+4) rule. Reproduced with permission from reference 7. Copyright Wiley-VCH Verlag GmbH & Co. KGaA.

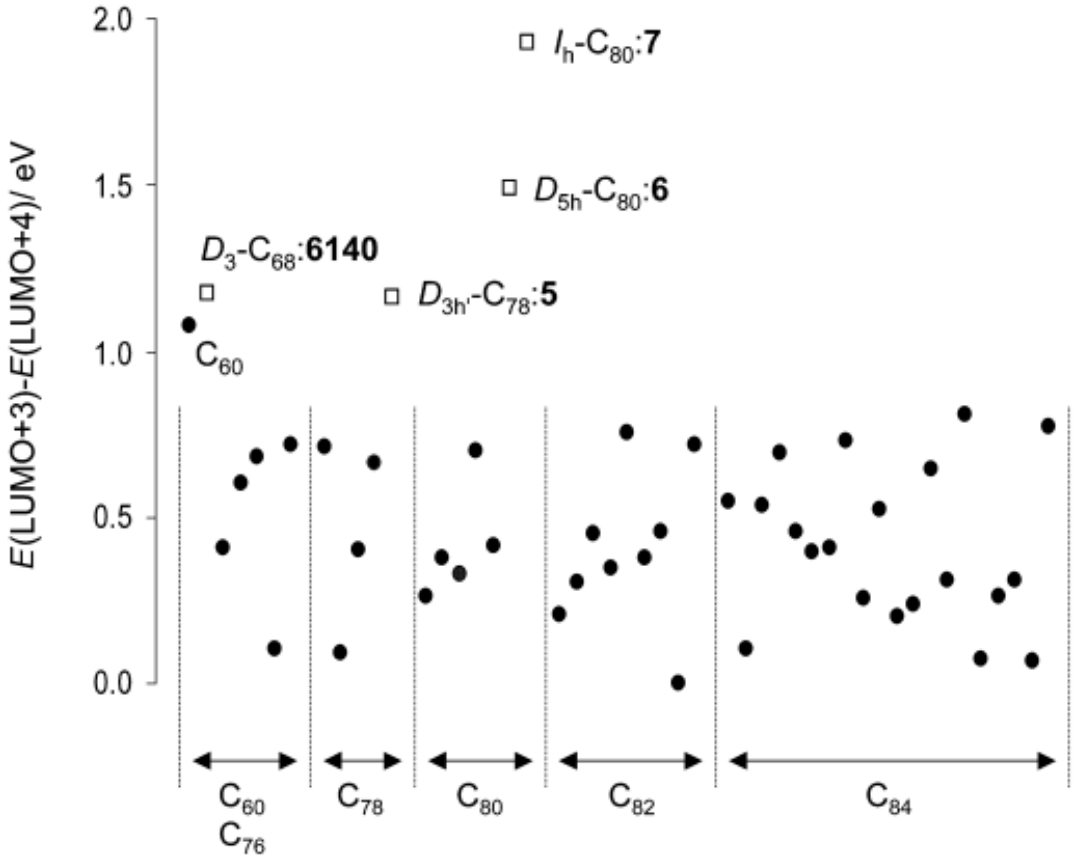


**Figure 4.2**. The (LUMO+3)-(LUMO+4) gap for all IPR isomers from $C_{60}$ to $C_{84}$ and also the non-IPR $D_3$-$C_{68}$:**6140**. Only isomers with the gap larger than 1 eV have been capable of encapsulating TNT units. Reproduced with permission from reference 7. Copyright Wiley-VCH Verlag GmbH & Co. KGaA.

**Trimetallic Nitride Endohedral Fullerenes: The First Experimental Evidence for the $M_3N^{6+}@C_{2n}^{6-}$ model [8]**

As just mentioned Poblet and co-workers based on the electron-transfer model, rationalized the occurrence of the most abundant species of metallic nitride EMFs that have been experimentally characterized, they were also able to predict the cage isomers

for systems that have yet to be prepared.[7, 9] Popov and Dunsch performed a systematic and detailed study for the most stable isomers of $M_3N@C_{2n}$ (M=Sc, Y; $34 \leq n \leq 49$) based on the relative energies of the empty fullerenes in their hexaanionic state. In most of the cases, the cage structures predicted by both groups coincide.[10]

In this section we report the synthesis, electrochemistry, and theoretical characterization of the large metallic nitride EMFs $M_3N@C_{2n}$ family (M=La, Ce, and Pr; n=46 and 48). The combined electrochemical and computational analyses (DFT calculations were carry out by Prof. Josep Maria Poblet at Spain) of the series from $M_3N@C_{80}$ to $M_3N@C_{96}$, that have been extensively and exclusively studied by our group (see Chapters 1-3), allow us to verify the ionic model $M_3N^{6+}@C_{2n}^{6-}$ for metallic nitride EMFs.

**Experimental section**

Graphite rods (6 mm diameter) purchased from POCO were core-drilled (4 mm diameter) and packed with (3:1), (1:1), and (1:5) mixtures of graphite powder and $CeO_2$ (cerium oxide), $Pr_6O_{11}$ (praseodymium oxide), and $La_2O_3$ (lanthanum oxide), respectively. The rods were annealed at 1000 °C for 12 h and then vaporized in a modified Krätschmer-Huffman reactor under a mixture of ammonia (20 mbar) and helium (200 mbar) using an arc current of 85 A. The soot collected from the arc reactor for each packed rod was extracted with $CS_2$ in a sonicator for about two hours. After removal of the solvent, the crude mixtures were washed with diethyl ether and acetone until the washings were no longer colored. The solids were dissolved in toluene and

separated by HPLC using a semipreparative 10 mm×250 mm Buckyprep-M column with a flow rate of 4.0 mL of toluene per minute. Isolated samples were then passed through a linear combination of Buckyprep and Buckyprep-M columns with a flow rate of 2.0 mL of toluene per minute without any further sign of isomeric separation. MALDI-TOF mass spectrometry was carried out using a Bruker Omni Flex. For the EDS analysis, the samples were deposited on TEM grids and the spectra were taken on a HD-2000 STEM, equipped with an Oxford EDS system. Cyclic voltammetry was carried out in a one-compartment cell connected to a BAS 100B workstation in a solution of *o*-DCB containing 0.05 M $NBu_4PF_6$. A 2 mm diameter glassy carbon disk was used as the working electrode. Ferrocene was added to the solution at the end of each experiment as internal standard and all the electrochemical potentials were referenced to its redox couple. The calculations were carried out by using DFT methodology with the ADF 2004 program.[11-12] The exchange-correlation functionals of Becke[13] and Perdew[14] were used. Relativistic corrections were included by means of the ZORA formalism. TZP basis sets were employed to describe the valence electrons of C, N, and metal atoms. The calculations for predicting the electrochemical gaps were performed in the presence of a continuous model solvent by means of the conductor-like screening model (COSMO) implemented in the ADF code.

**Electrochemistry of the larger metallic nitride EMFs**

The larger metallic nitride EMFs were purified, isolated, and identified using HPLC, mass spectrometry, and energy dispersive spectroscopy as described in the last

chapter. Electrochemical studies were conducted in a 0.05 M solution of $NBu_4PF_6$ in *o*-dichlorobenzene (*o*-DCB). A 2 mm diameter glassy carbon disk was used as the working electrode. Ferrocene was added at the end of the experiments for internal reference of the potentials.

Figure 4.3 shows the cyclic voltammograms (CVs) and the Osteryoung square-wave voltametry (OSWV, anodic part) of $M_3N@C_{92}$ (M=La, Ce, and Pr) metallofullerenes. These compounds exhibit two irreversible reduction steps and a likely multielectronic third reduction. $M_3N@C_{92}$ metallofullerenes also show a monoelectronic reversible oxidation step and a second oxidation that is not well defined.

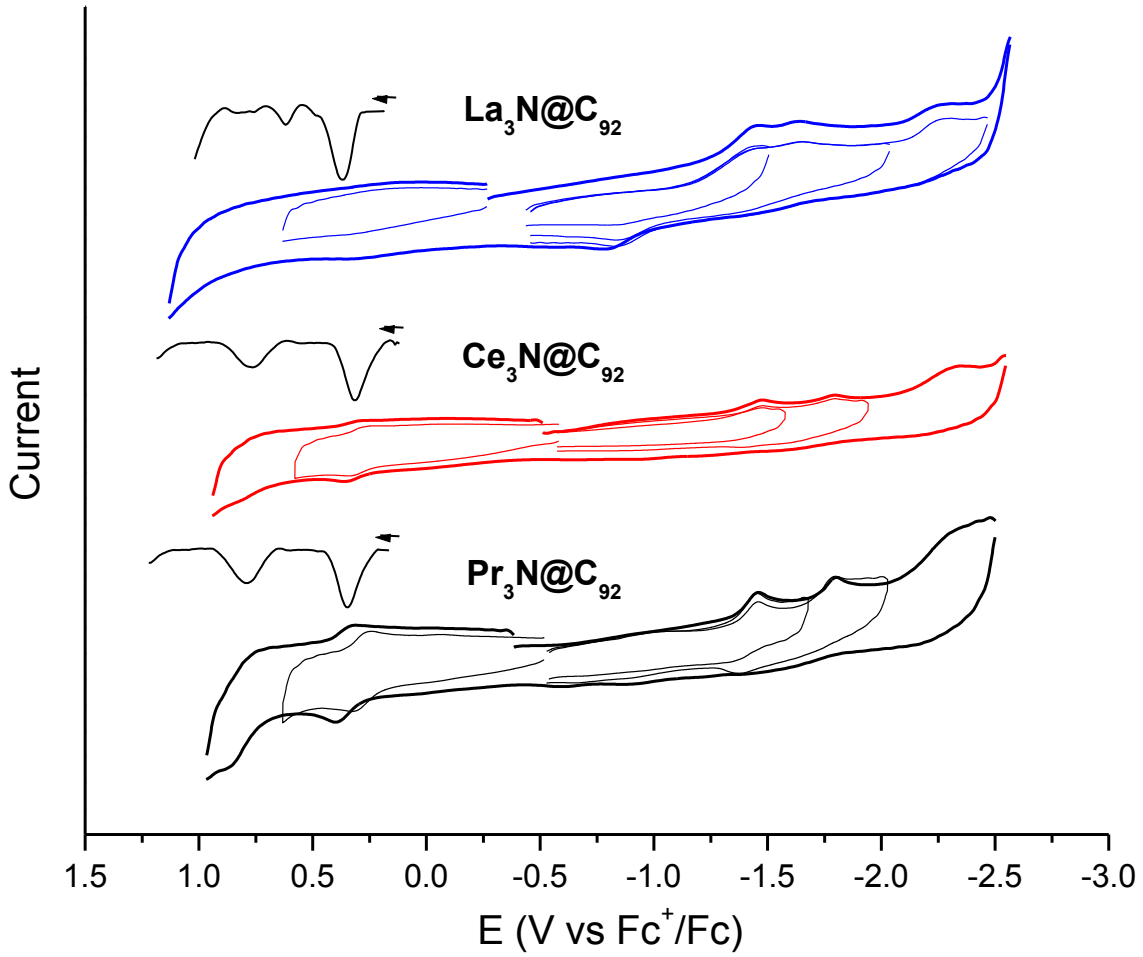


**Figure 4.3**. Cyclic voltammograms and Osteryoung square-wave voltammetry (OSWV) of $La_3N@C_{92}$, $Ce_3N@C_{92}$, and $Pr_3N@C_{92}$ in 0.05 M $NBu_4PF_6$/*o*-DCB with ferrocene as internal standard and a scan rate of 0.1 $Vs^{-1}$.

$M_3N@C_{96}$ (M=La, Ce, and Pr) metallofullerenes exhibit at least two irreversible reduction steps and two reversible oxidations (Figure 4.4). It is interesting that regardless of the encapsulated cluster, metallofullerenes exhibit similar redox behavior for a specific carbon cage symmetry and size and similar electrochemical gaps (Table 4.1). This behavior has been largely observed for all the EMFs studied so far.[5]

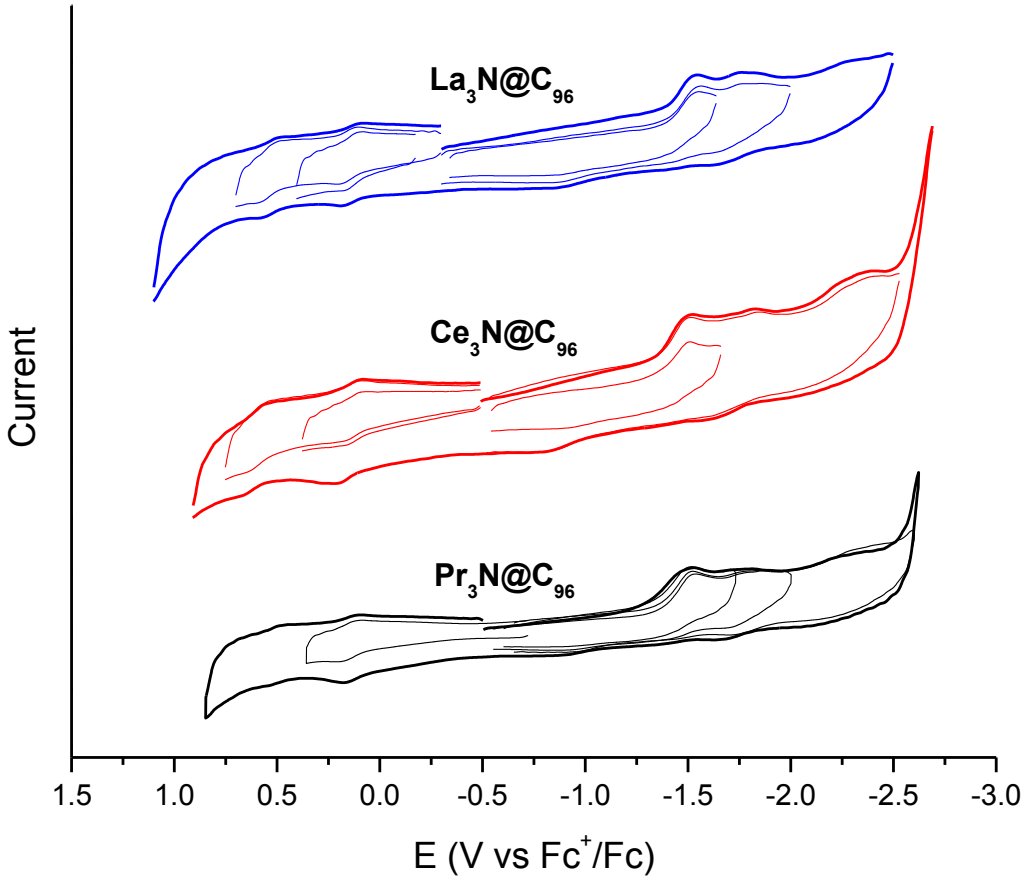


**Figure 4.4**. Cyclic voltammograms of $La_3N@C_{96}$, $Ce_3N@C_{96}$, and $Pr_3N@C_{96}$ in 0.05 M $NBu_4PF_6$/*o*-DCB with ferrocene as internal standard and a scan rate of 0.1 $Vs^{-1}$.

**Table 4.1**. Half wave potentials vs $Fc^+/Fc$ of the reduction and oxidation steps of $M_3N@C_{92}$ and $M_3N@C_{96}$ (M=La, Ce and Pr) EMFs.

| EMF | $E_p$ red$_1$ | $E_p$ red$_2$ | $E_{1/2}$ ox$_1$ | $E_{1/2}$ ox$_2$ | $\Delta E_{gap}$ |
|---|---|---|---|---|---|
| $La_3N@C_{92}$ | -1.44 | -1.64 | 0.36 | | 1.80 |
| $La_3N@C_{96}$ | -1.54 | -1.77 | 0.14 | 0.53 | 1.68 |
| $Ce_3N@C_{92}$ | -1.48 | | 0.32 | | 1.80 |
| $Ce_3N@C_{96}$ | -1.50 | -1.84 | 0.18 | 0.67 | 1.68 |
| $Pr_3N@C_{92}$ | -1.46 | | 0.35 | | 1.81 |
| $Pr_3N@C_{96}$ | -1.51 | -1.86 | 0.14 | 0.53 | 1.65 |

DFT calculations were carried out for $La_3N@C_{92}$ and $La_3N@C_{96}$ to understand the electronic and electrochemical properties of these metallic nitride EMFs. The calculations for these EMFs were performed without symmetry restrictions. In the case of $La_3N@C_{96}$ we have assumed that the fullerene cage corresponds to isomer **186** (see Figure 4.5) of symmetry $D_2$, which shows the highest gap between LUMO-4 and LUMO-3 for the free cage.[9] The same isomer was proposed by Popov and Dunsch for the $Y_3N$ cluster inside the $C_{96}$ cage.[10] The endohedral structure was optimized for several orientations of the metallic nitride unit inside the cage and it was found that the cluster may adopt some orientations with similar energies (within less than 2 kcal/mol). Figure 4.5b shows the representation of one of the most stable orientations. As suggested by the low dependence of the electrochemical properties on the nature of the encapsulated metal, the participation of the metal nitride in the HOMO and LUMO is almost negligible. Based on the electronic structure of the free fullerene cage, Poblet and co-workers [9] proposed isomer **86** of $C_{92}$ (see Figure 4.5) with symmetry *T* as the most suitable isomer to encapsulate a metallic nitride cluster. Nevertheless, Popov and Dunsch found isomer **85** ($Y_3N@C_{92}$) with $D_3$ symmetry to be more stable than isomer **86** by about 14 kcal/mol when the internal cluster is $Y_3N$ [10]. If the metal is lanthanum, the difference in the stability between the two isomers is 7.7 kcal/mol, isomer **85** again being the most stable species.

a) b)

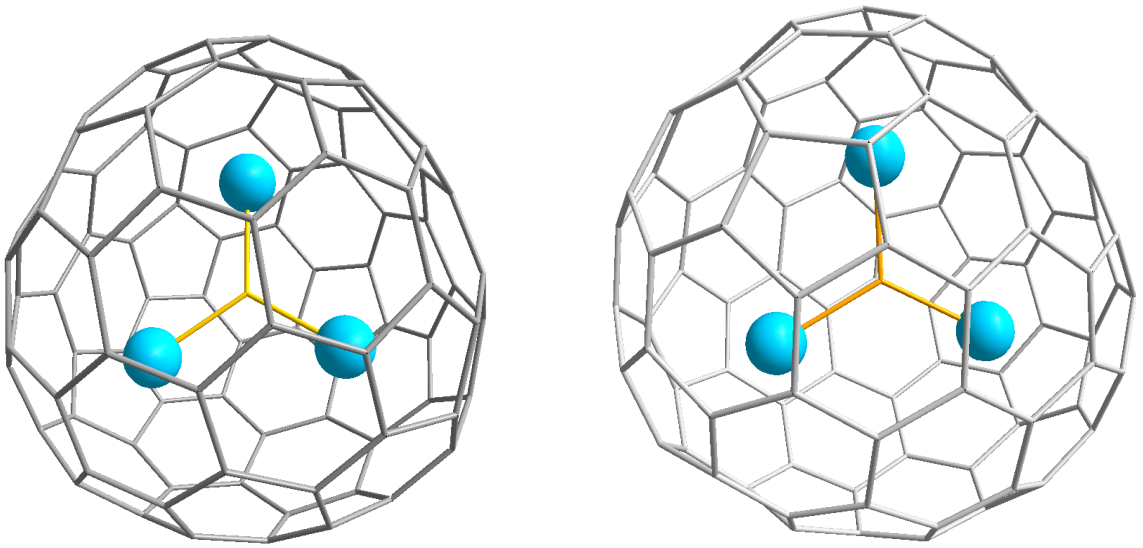

**Figure 4.5**. Structures for left) $La_3N@C_{92}$ (isomer **86**) and right) $La_3N@C_{96}$ (isomer **186**).

To verify the structures proposed for the $C_{92}$ and $C_{96}$ hosts the electrochemical gaps (EG) were computed as the difference between the electron affinities and ionization potentials in solution (Table 4.2). This procedure has been used by Poblet's group in polyoxoanions with reasonable agreement between theory and experiments (see Ref. 15 for more details). Using *o*-DCB as solvent, the EG for $C_{92}$:**86** was computed to be 1.75 V, which is in very good agreement with the experimental value of 1.80 V. In contrast, the computed EG for $C_{92}$:**85** is only 1.08 V. This extremely low gap, which derives from the high electron affinity (EA) and low ionization potential (IP) of isomer **85**, excludes it as the host cage for $C_{92}$. The oxidation potentials (Figures 4.3-4.4, and Table 4.1) for $La_3N@C_{92}$ (+0.36 V) and $La_3N@C_{96}$ (+0.14 V) show that the compound with the $C_{96}$ cage is easier to oxidize than that with the $C_{92}$ cage. $C_{92}$:**85** would not be compatible with

this behavior, because its IP is lower than the IP computed for $C_{96}$:**186** by 0.25 eV, which is derived from the high energy of the HOMO in $La_3N@C_{92}$ (isomer **85**). However, the IP computed for $C_{92}$:**86** perfectly matches the electrochemical data available. Its IP is higher than that of the compound with the $C_{96}$ cage by 0.16 eV, a value that is very close to the experimental difference of 0.22 V.

**Table 4.2**. Relative stability (ΔE), ionization potential (IP), electron affinity (EA), electrochemical (EG) and HOMO-LUMO (H-L) gap computed for $La_3N@C_{92}$ and $La_3N@C_{96}$.[a)]

| | **ΔE** | **IP** [b)] | **EA** [b)] | **EG** [b)] | **H-L** |
|---|---|---|---|---|---|
| 92: **85** | 0.0 | 4.42 | 3.34 | 1.08 | 0.70 |
| 92: **86** | 7.7 | 4.83 | 3.09 | 1.75 | 1.37 |
| 96:**186** | - | 4.67 | 3.15 | 1.53 | 1.16 |

a) Relative stabilities in kcal $mol^{-1}$, IP, EA and H-L gap in eV and EG in V; b) values computed in *o*-DCB media. For experimental values of EG see Table 4.1.

We can also compare this result with other cages. For instance, the first oxidation peak for $La_3N@C_{92}$ appears at approximately the same potential as the one for $Sc_3N@C_{80}$ ($D_{5h}$), the difference is less than 20 mV.[16] Consistently the difference in the computed IPs is also very small (40 meV). Therefore, although $C_{92}$:**85** is computed to be somewhat more stable than $C_{92}$:**86** we assume that $C_{92}$:**86** is the host cage observed for $La_3N@C_{92}$. Popov and Dunsch have suggested that $C_{92}$:**85** could be kinetically unstable.[10] A 3D representation of $La_3N@C_{92}$ (isomer **86**) and $La_3N@C_{96}$ (isomer **186**) is given in Figure 4.5. Table 4.3 shows the relative energies of several orientational isomers of $La_3N@C_{92}$

(**85**), $La_3N@C_{92}$ (**86**) $La_3N@C_{96}$ (**186**) and Figures 4.6-4.8 show the 3D representations of these orientational isomers.

**Table 4.3**. Relative energy (in kcal/mol) for several orientational isomers of $La_3N@C_{92}$ (**85**), $La_3N@C_{92}$ (**86**) and $La_3N@C_{96}$ (**186**).

| Isomer | $La_3N@C_{92}$ (**85**) | $La_3N@C_{92}$ (**86**) | $La_3N@C_{96}$ (**186**) |
|---|---|---|---|
| **1** | +13.4 | +1.3 | +6.4 |
| **2** | +11.1 | +3.0 | +6.2 |
| **3** | 0.0 | +0.1 | 0.0 |
| **4** | +0.9 | 0.0 | +1.4 |

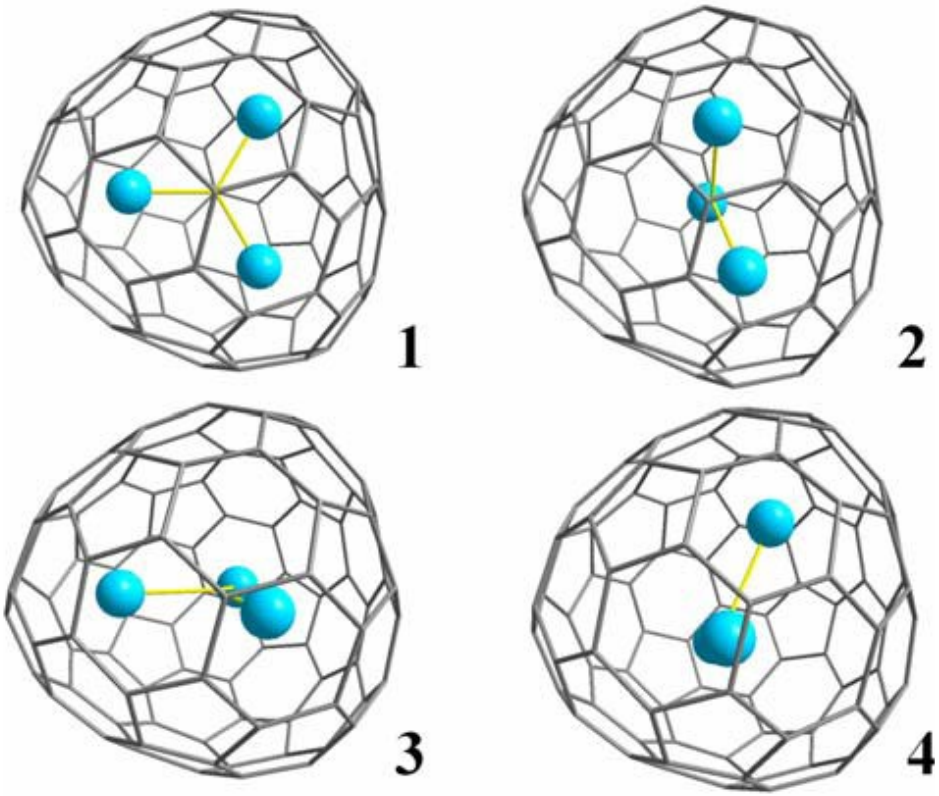


**Figure 4.6**. Orientational isomers of $La_3N@C_{92}$ (**85**).

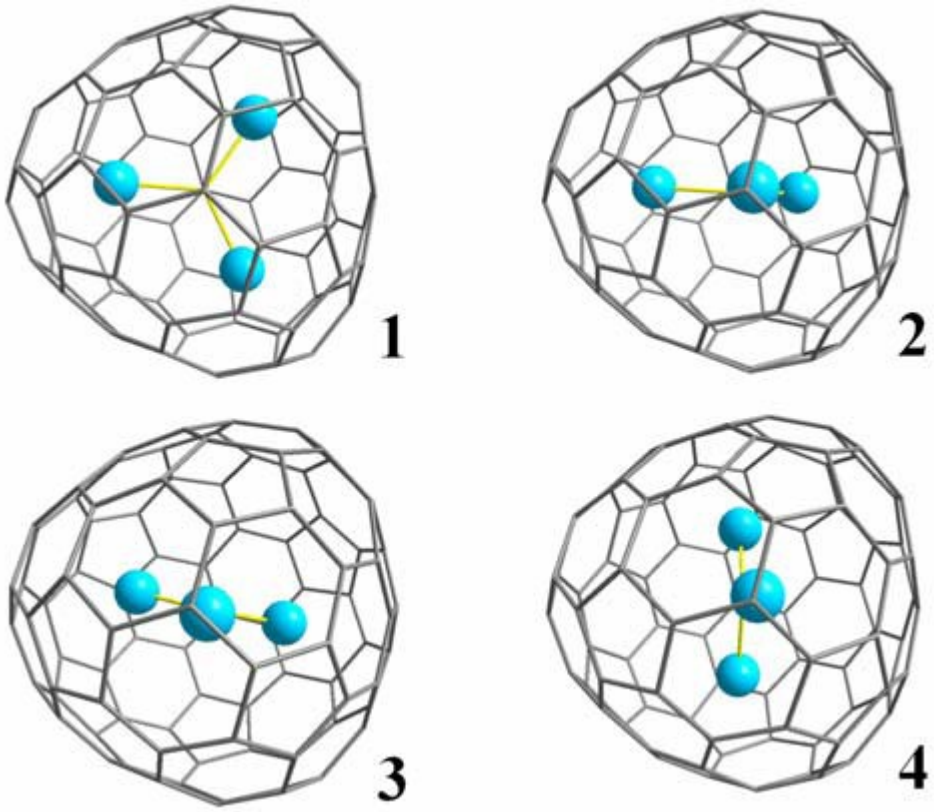


**Figure 4.7**. Orientational isomers of $La_3N@C_{92}$ (**86**).

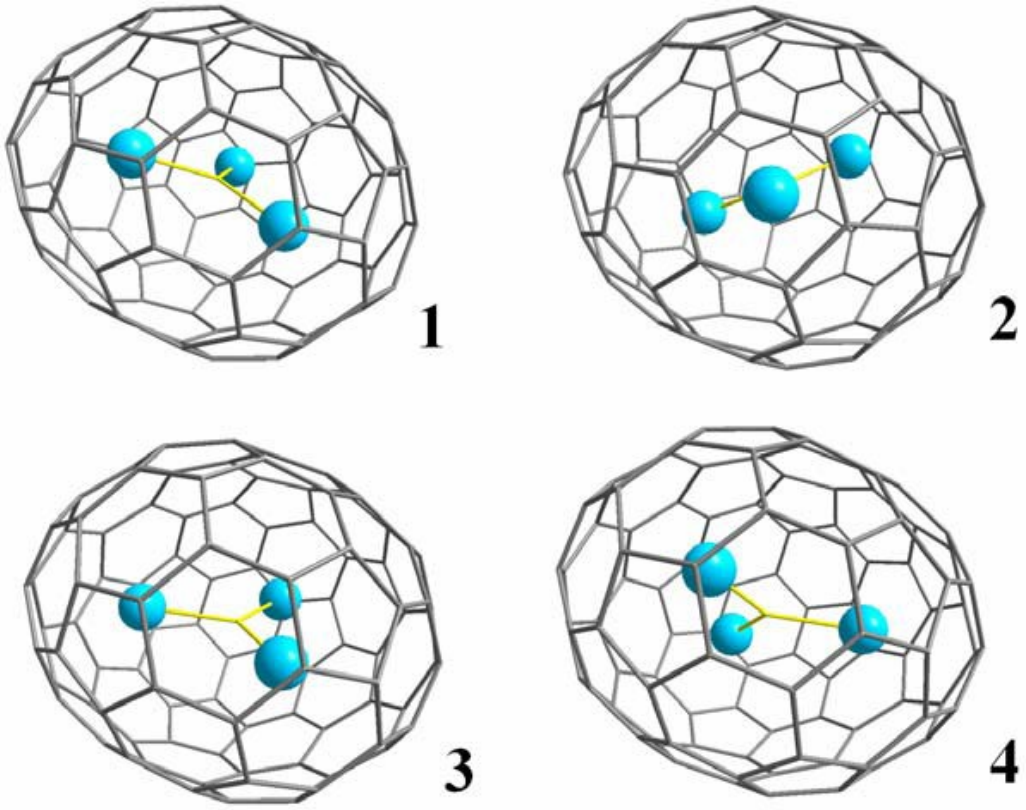


**Figure 4.8**. Orientational isomers of $La_3N@C_{96}$ (**186**).

The electrochemical characterization of the large metallic nitride EMFs $M_3N@C_{2n}$ (n=46 and 48) provides the basis for the comparison of cages between $C_{80}$ and $C_{96}$. From the values compiled in Table 4.4 the following can be concluded: the difference between the first oxidation peak and the first reduction peak for metallic nitride EMFs does not depend on the encapsulated metal nor does it correlate with the fullerene size. With the exception of $Sc_3N@C_{80}$, the HOMO and LUMO of metallic nitride EMFs are primarily cage orbitals, therefore the first oxidation and first reduction involve orbitals without (or very low) contribution from the metal. The ionic model for metallic nitride EMFs assumes that six electrons are transferred from the metallic nitride

cluster to the fullerene cage thus filling the three lowest unoccupied orbitals of the cage.[6] In this model it would be expected that the EG of the endohedral fullerene should correlate with the electronic structure of the carbon cage.

**Table 4.4**. Electrochemical gaps for several MNEFs.[a]

| M | $C_{80}$ | $C_{84}$ | $C_{86}$ | $C_{88}$ | $C_{92}$ | $C_{96}$ |
|---|---|---|---|---|---|---|
| Sc | 1.85 | | | | | |
| Y | 2.05 | | | | | |
| Ce | | | | 1.38 | 1.80[b] | 1.68[b] |
| Pr | 2.05 | | 1.78 | 1.40 | 1.81[b] | 1.65[b] |
| Nd | 2.05 | 1.75 | 1.82 | 1.40 | | |
| Gd | 2.02 | 1.69 | | 1.49 | | |
| Lu | 2.04 | | | | | |
| La | | | | | 1.80[b] | 1.68[b] |
| average | 2.04[c] | 1.72 | 1.80 | 1.42 | 1.80 | 1.67 |

[a] Values taken from reference 5; [b] this work; [c] average for all metallic nitride EMFs except for M=Sc.

**Table 4.5**. (LUMO-4)-(LUMO-3) orbital gaps in free carbon cages.

| | **$C_{80}$** | **$C_{84}$** | **$C_{86}$** | **$C_{88}$** | **$C_{92}$** | **$C_{96}$** |
|---|---|---|---|---|---|---|
| IPR isomer | **7** ($I_h$) | 51365 (Cs) [a] | 19 ($D_3$) | 35 ($D_2$) | 86 (T) | 186 ($D_2$) |
| LUMO-4 | -3.59 | -3.77 | -3.57 | -3.88 | -3.63 | -3.86 |
| LUMO-3 | -5.46 | -5.09 | -5.07 | -4.73 | -5.18 | -5.04 |
| Gap[b] | 1.87 | 1.32 | 1.50 | 0.85 | 1.55 | 1.18 |

[a] Non-IPR isomer; [b] Orbital gap (LUMO-4)–(LUMO-3) in eV.

The energy difference between the LUMO-4 and LUMO-3 for a series of free cages is given in Table 4.5. Figure 4.9 shows the correlation between the average EG observed for metallic nitride EMFs and the orbital gap in the free cage. The LUMO-4 changes by less than 0.3 eV, whereas for the LUMO-3 varies by more than twice that

amount, explaining why the first oxidation potential in a CV of a metallic nitride EMF is more sensitive to the cage than the first reduction potential is.[5] The excellent correlation between the electrochemical data and the orbital energies (Figure 4.9) corroborates the importance of the topology of the cage and not its size.

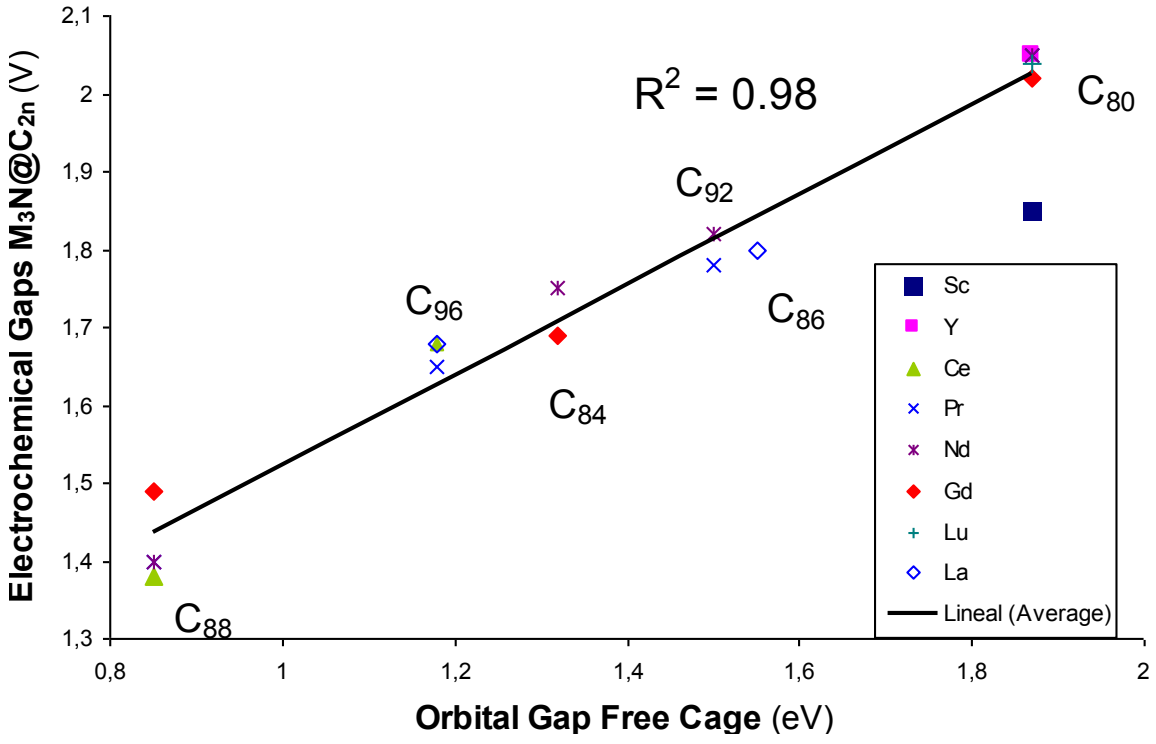


**Figure 4.9**. Correlation between electrochemical gaps and (LUMO-4)-(LUMO-3) orbitals gaps in free carbon cages. Linear regression is calculated using average values for each metal except scandium (see text).

The correlation in Figure 4.9 indicates that the oxidations and reductions occur on the cage. Since the reduction for $Sc_3N@C_{80}$ mainly occurs on the scandium orbitals[6] the correlation coefficient was calculated without taking into account the EG for this metallic

nitride EMF. This correlation also provides direct experimental and theoretical evidence of the six-electron transfer in metallic nitride EMFs for the first time. Such a correlation was not found for the formal transfer of two and four electrons (Figures 4.10-4.11).

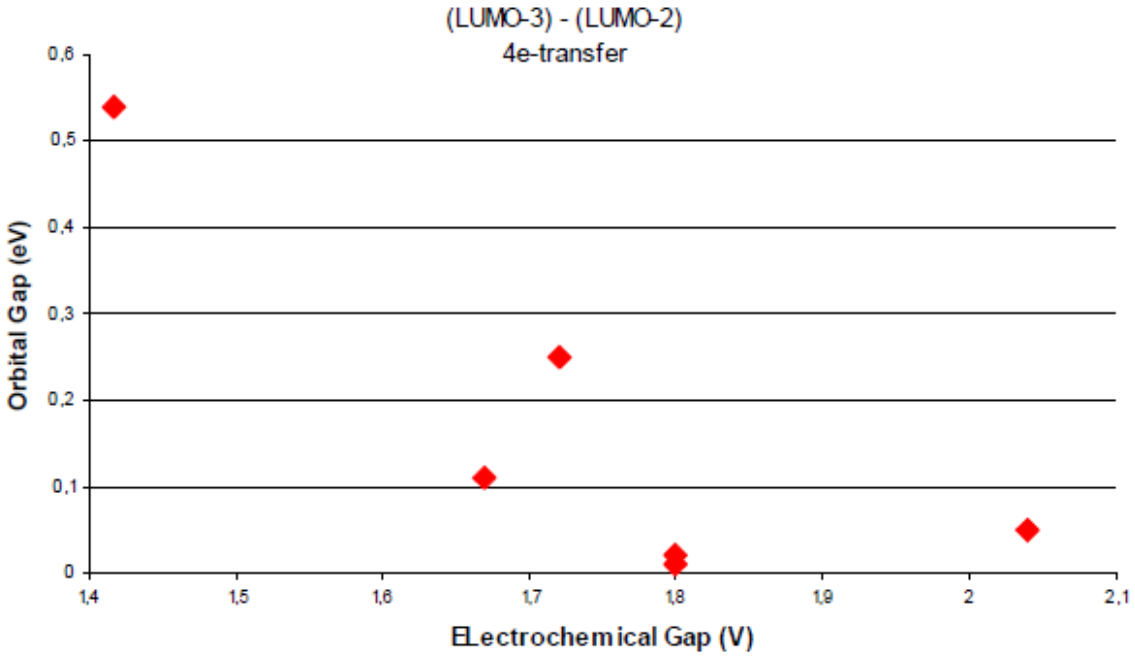


**Figure 4.10**. Correlation between electrochemical gaps and (LUMO-3)-(LUMO-2) orbitals gaps in free carbon cages for a four electron transfer.

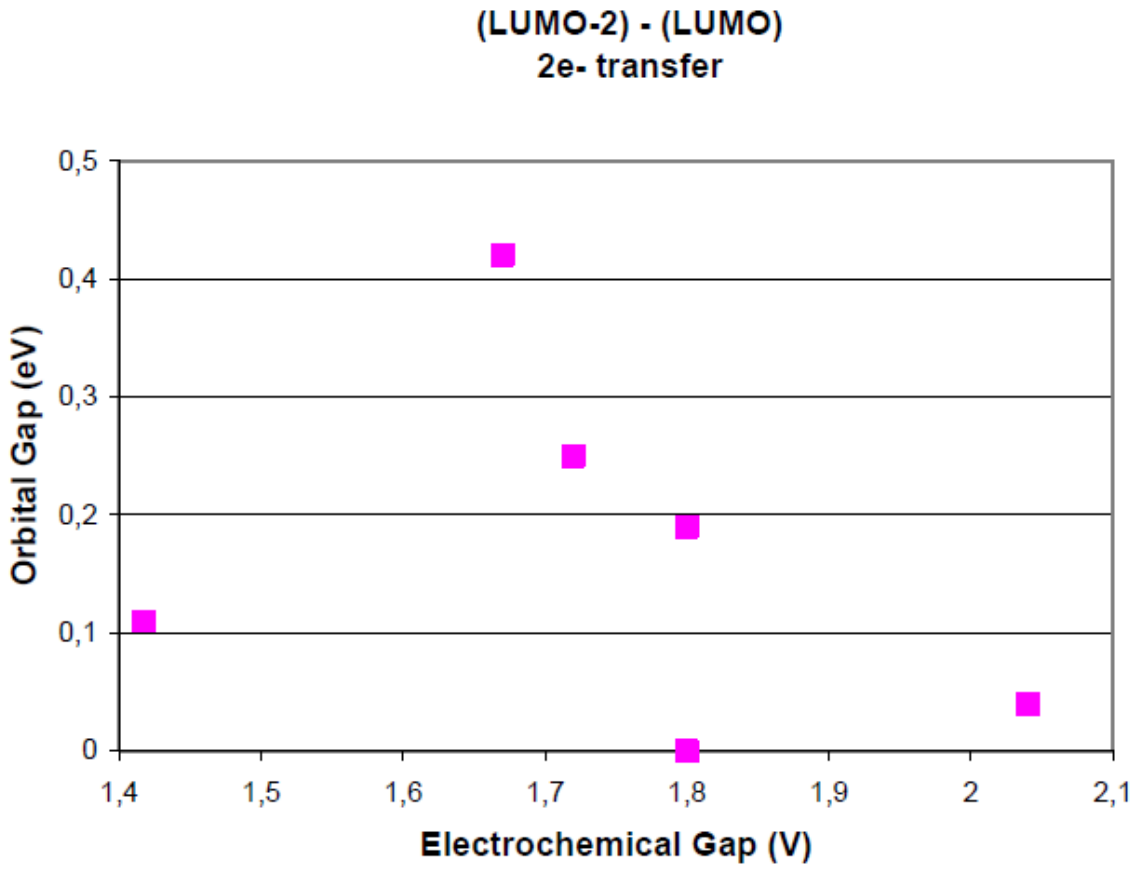


**Figure 4.11**. Correlation between electrochemical gaps and (LUMO-2)-(LUMO) orbitals gaps in free carbon cages for a two electron transfer.

A formal electron transfer of six electrons, however, does not mean that a real transfer of six electrons occurs between the two units. Covalent contributions to the bonding are also present for M = Sc, the most electronegative metal of the series.[10] In addition, the computation of the charge transfer depends significantly on the basis set and on the partition method (Table 4.6). For example, the Mulliken population analysis for $M_3N@C_{2n}$ assigns an electron transfer that ranges between 1 and 2 $e^-$ between the guest and the host, whereas the Multipole Derived Charge method enhances the ionic picture of

the bond, predicting a transfer that may reach up to almost 4 $e^-$ for some metal atoms and fullerene cages (Table 4.6).

**Table 4.6**. Electron charge transfer in $M_3N@C_{2n}$ (2n = 80, 88, 92 and 96).

| | **Milliken** | **MDC-q**[a)] |
|---|---|---|
| $Sc_3N@C_{80}$ (**7**) | 1.29 | 0.92 |
| $Y_3N@C_{80}$ (**7**) | 1.78 | 3.06 |
| $Gd_3N@C_{80}$ (**7**) | 1.12 | 2.36 |
| $Y_3N@C_{88}$ (**35**) | 1.50 | 2.34 |
| $La_3N@C_{88}$ (**35**) | 1.96 | 3.77 |
| $La_3N@C_{92}$ (**86**) | 1.99 | 3.63 |
| $La_3N@C_{92}$ (**85**) | 1.92 | 3.62 |
| $La_3N@C_{96}$ (**186**) | 1.77 | 3.23 |
| $La_3N@C_{96}$ (**187**) | 1.64 | 3.12 |

a) MDC-q: Multipole derived charge method.

## Conclusions

The new trimetallic nitride EMFs based on lanthanum, cerium, and praseodymium represent the largest metallic nitride EMFs isolated and studied to date. Their electrochemical properties together with DFT calculations provide direct evidence for the ionic model in metallic nitride EMFs for cages ranging between $C_{80}$ and $C_{96}$.

The oxidation of all of the $M_3N@C_{2n}$ systems analyzed herein occurs on the carbon cage. The reduction, except for the most electronegative Group 3 atom (Sc), also occurs on the cage (M = Y, Gd, and La).

## References


[1] Stevenson, S.; Rice, G.; Glass, T.; Harich, K.; Cromer, F.; Jordan, M. R.; Craft, J.; Hadju, E.; Bible, R.; Olmstead, M. M.; Maitra, K.; Fisher, A. J.; Balch, A. L.; Dorn, H. C. *Nature*, **1999**, *401*, 55-57.

[2] Fowler, P.W.; Monolopoulos, D.E. *An Atlas of Fullerenes*, Clarendon Press, Oxford, 1995.

[3] a) Hennrich, F.H.; Michel, R.H.; Fischer, A.; Richard S.; Gilb, S.; Kappes, M.M.; Fuchs, D.; Bürk, M.; Kobayashi, K.; Nagase S. *Angew. Chem. Int. Ed. Engl.* **1996**, 35, 1732-35. b) Wang, R.; Sugai, T.; Kai, T.; Tomiyama, T.; Shinohara, H. *Chem. Commun.* **2000**, 557-559.

[4] Kobayashi, K.; Nagase, S.; Akasaka, T. *Chem. Phys. Lett.* **1995**, 245, 230-236.

[5] Chaur, M.N.; Melin, F.; Ortiz, A.L.; Echegoyen, L. *Angew. Chem. Int. Ed.* **2009**, 48, 7514-7538.

[6] Campanera, J.M.; Bo. C.; Olmstead, M.M.; Balch, A.L.; Poblet, J.M. *J. Phys. Chem. A* **2002**, 106, 12356–12364.

[7] Campanera, J.M.; Bo. C.; Poblet, J.M. *Angew. Chem. Int. Ed*. **2005**, 44, 7230-7233.

[8] Chaur, M.N.; Valencia, R.; Rodriguez-Fortea, A.; Poblet, J.M. *Angew. Chem. Int. Ed*. **2009**, 48, 1425-1428.

[9] Valencia, R.; Rodriguez-Fortea, J.M.; Poblet, J.M. *Chem. Commun*. **2007**, 4161-4163.

[10] Popov, A. A.; Dunsch, L. *J. Am. Chem. Soc*. **2007**, *129*, 11835-11849.

[11] ADF 2007.01, Department of Theoretical Chemistry, Vrije Universiteit: Amsterdam, **2007**.

[12] Velde, G.T.; Bickelhaupt, F.M.; Baerends, E.J.; Guerra, C.F.; Van Gisbergen, S.J.; Snijders, J.G.; Ziegler, T. *J. Comput. Chem.* **2001**, 22, 931-967.

[13] Becke, A.D. *Phys. Rev. A* **1988**, 38, 3098.

[14] Perdew, J.P. *Phys. Rev. B* **1986**, 33, 8822.

[15] Fernandez, J.A.; Lopez, X.; Bo, C.; De Graaf, C.; Baerends, E.J.; Poblet, J.M. *J. Am. Chem. Soc.* **2007**, *129*, 12244.

[16] a) Elliott, B.; Yu, L.; Echegoyen, L. *J. Am. Chem. Soc.*, **2005**, 127, 10885–10888; b) Cai, T.; Xu, L.X.; Anderson, M.R.; Ge, Z.X.; Zuo, T.M.; Wang, X.L.; Olmstead, M.; Balch, A.L.; Gibson, H.W.; Dorn, H.C. *J. Am. Chem. Soc.* **2006**, 128, 8581-8589.

.

CHAPTER FIVE

# REACTIVITY OF METALLIC NITRIDE ENDOHEDRAL METALLOFULLERENES

The trimetallic nitride endohedral metallofullerenes have emerged as unique compounds with a wide range of potential applications. Specifically, gadolinium nitride cluster fullerenes have proven to be better contrast agents for magnetic resonance imaging (MRI) than the $Gd^{3+}$-based complexes currently in commercial use.[1, 2] The functionalization of metallic nitride EMFs is a key requirement in order to take full advantage of these compounds for MRI applications. To date many different reactions have been reported for metallic nitride EMFs of general formula $M_3N@C_{80}$, and these have led to completely characterized monoadducts.[2] In the case of $Gd_3N@C_{80}$ derivatives the characterization has been limited to mass spectrometry and HPLC.[2] Nothing is currently known about the reactivity of metallic nitride EMFs with cages larger than $C_{80}$ due to the scarce amounts of the larger metallofullerenes obtained during the arc synthesis. There is therefore great interest to understand how the reactivity of metallic nitride EMFs is influenced by the size of the cage.

The $I_h$-$C_{80}$ fullerene cage has two possible sites for addition reactions, at [5,6] and [6,6] double bonds (Figure 5.1). Previous studies in our group have shown that with $Sc_3N@C_{80}$ [5,6]-adducts are exclusively obtained, whereas $Y_3N@C_{80}$ and $Er_3N@C_{80}$ lead mainly to [6,6]-adducts, which in some cases can be further converted to [5,6]-adducts by heating.[2] More recently, Wang and co-workers have shown that [6,6]-

adducts are also favored in the case of $Gd_3N@C_{80}$.[2] Our group has also reported that the [5,6] and [6,6] derivatives exhibit different electrochemical properties and therefore electrochemistry can be used as a characterization tool to distinguish between the two isomers.[2]

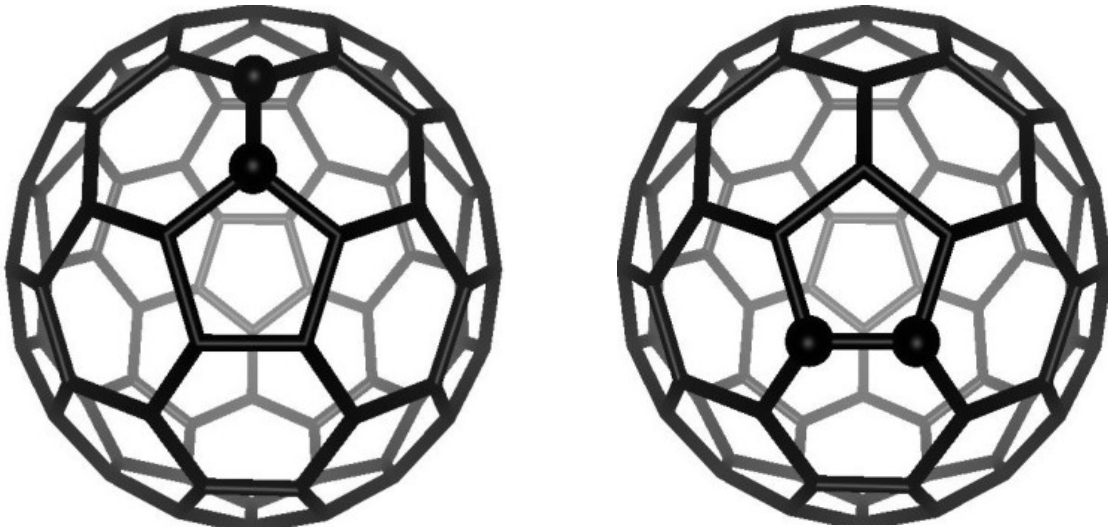

**Figure 5.1**. Possible [1,2] addition sites on the $I_h$-$C_{80}$ carbon cage. Left) the [6,6] ring junction. Right) the [5,6] ring junction.

In this chapter we will see first how the fullerene size affects the reactivity of metallic nitride EMFs towards the [2+1] cycloaddition reaction, better known as a Bingel-Hirsch reaction. Finally, we will discuss the synthesis of water soluble EMFs by the attachment of dendritic units composed of polycarboxylate amide units.

**The influence of cage size on the reactivity of trimetallic nitride metallofullerenes: a mono- and bis-methanoadduct of $Gd_3N@C_{80}$ and a monoadduct of $Gd_3N@C_{84}$[3]**

In this section we report the first reactivity study of higher metallic nitride EMFs. Specifically we compared the reactivity of $Gd_3N@C_{80}$, $Gd_3N@C_{84}$ and $Gd_3N@C_{88}$ in order to see how the cage-size affects the reactivity of the cyclopropanation reaction with bromomalonate (Bingel-Hirsch reaction). This is the first reactivity study of larger cages than $C_{80}$.

Samples of $Gd_3N@C_{2n}$ (2n = 80, 84, and 88) were synthesized, isolated, and purified as described before (for details see Chapter 2).[4] The [2 + 1] cycloaddition of bromodiethylmalonate in the presence of 1,8-diazabicyclo[5.4.0]undec-7-ene (DBU) at room temperature almost instantaneously afforded two highly stable products and several multiadducts of $Gd_3N@C_{80}$ (Figure 5.2). A monoadduct, $Gd_3N@C_{80}C(CO_2Et)_2$, and a bisadduct, $Gd_3N@C_{80}[C(CO_2Et)_2]_2$, were isolated and characterized by HPLC, mass spectrometry, UV-Vis-NIR, and cyclic voltammetry (CV).

The malonate monoadduct was purified from the reaction mixture *via* silica gel column chromatography using $CS_2$–$CHCl_3$ (2:1) as eluent with further purification by HPLC (Buckyprep-M column, see Figure 5.3). Finally the sample was analyzed by a Buckyclutcher column to further check its purity. Figure 5.4 shows the MALDI-TOF mass spectrum of the mono-adduct sample confirming the identity of this compound.

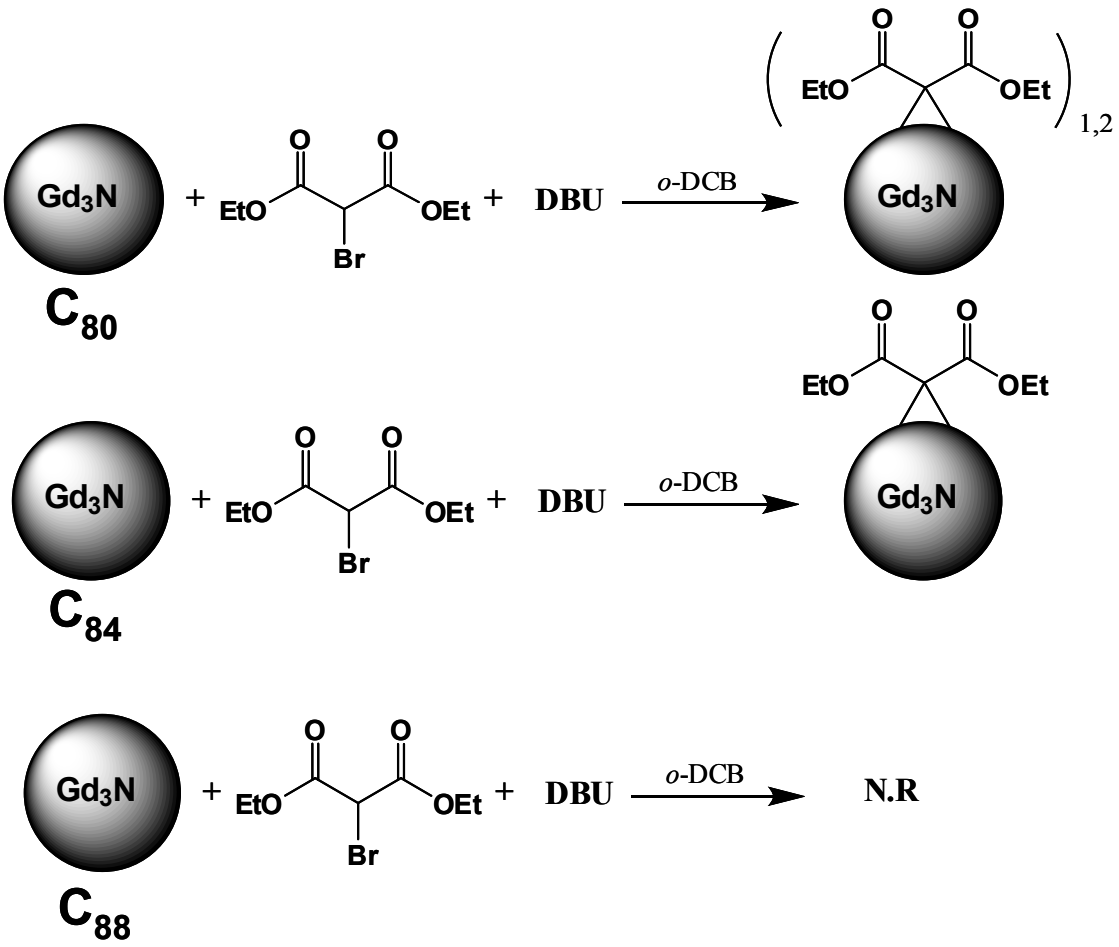


**Figure 5.2**. The [2 + 1] cycloaddition of bromodiethylmalonate in the presence of 1,8-diazabicyclo[5.4.0]undec-7-ene (DBU) with $Gd_3N@C_{2n}$ (2n = 40, 42 and 44) at room temperature.

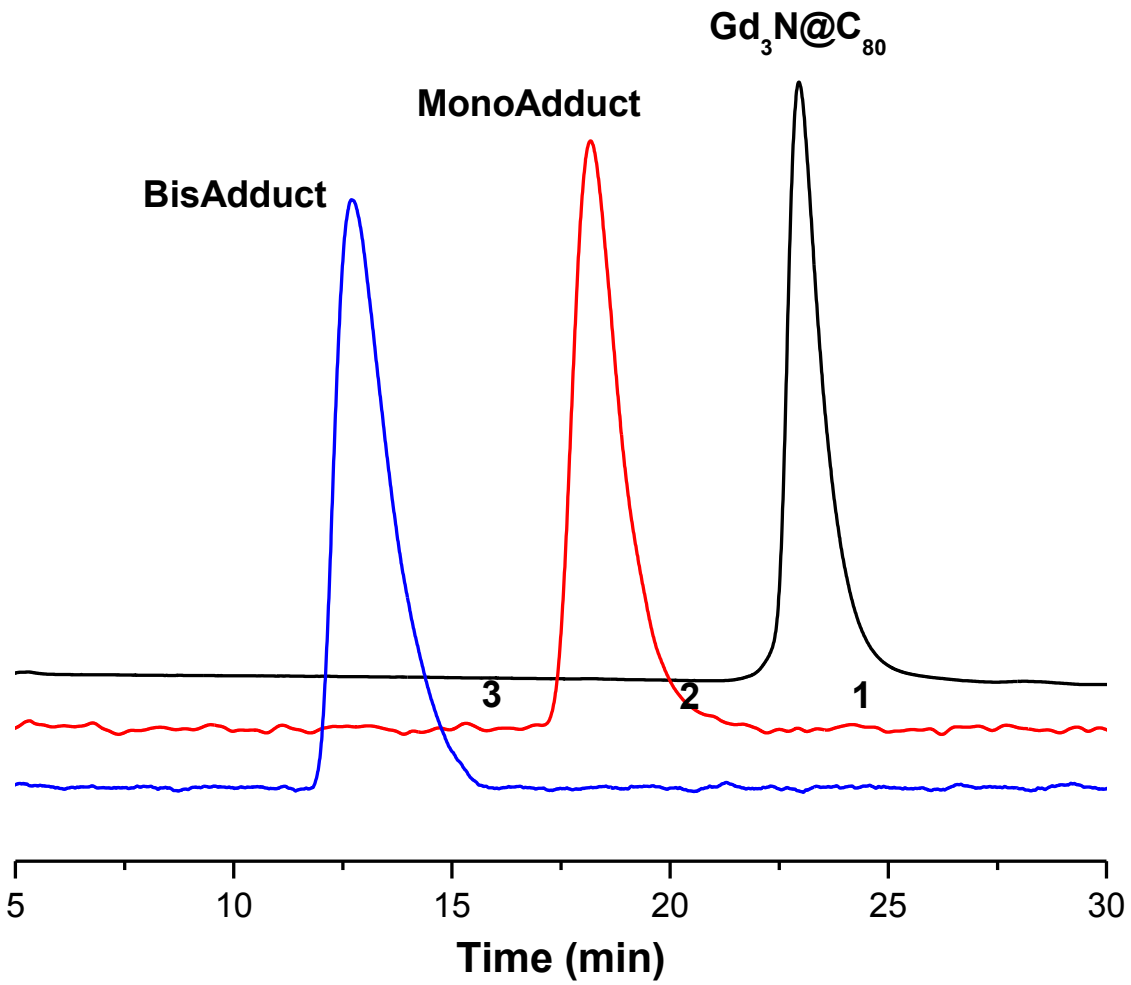


**Figure 5.3**. HPLC chromatograms of $Gd_3N@C_{80}$ before reaction and the isolated adducts (mono-adduct and bis-adduct). Eluent: Toluene, flow rate: 4.0 mL/min, Buckyprep-M column, detection: 372 nm.

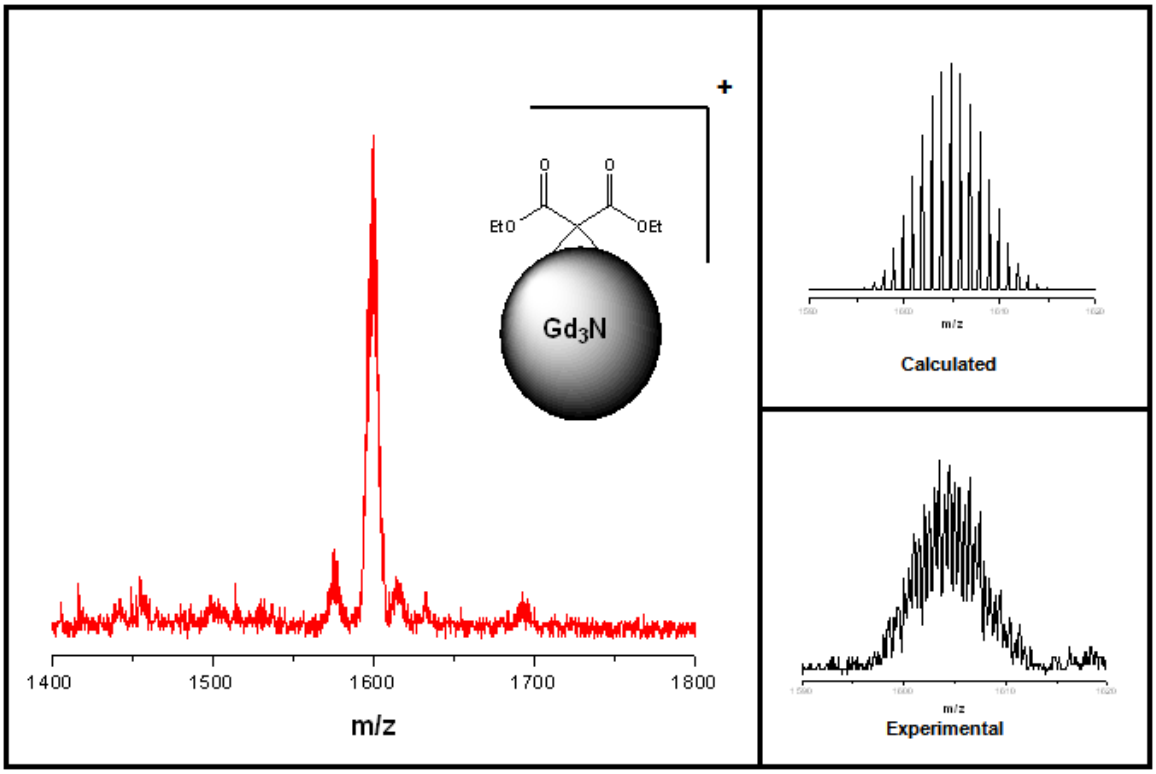


**Figure 5.4**. Simulated and experimental mass spectra of isolated mono-adduct $Gd_3N@C_{80}$-$C(CO_2Et)_2$.

Due to the paramagnetic nature of the gadolinium metallofullerene we were unable to characterize the isolated adducts by NMR spectroscopy. However, HPLC and mass spectrometry reveal that a monoadduct was formed and cyclic voltammetry shows the same redox behavior as other [6,6] Bingel monoadducts reported previously (Figure 11).[5]

After purification through a one stage HPLC Buckyprep-M column, the bisadduct fraction of $Gd_3N@C_{80}$ was analyzed by Buckyclutcher and Buckyprep columns. Finally it was analyzed by a linear combination of Buckyprep and Buckyprep-M columns,

showing in every case a very narrow elution peak, indicating a surprising degree of isomeric purity (Figure 5.3) which is in agreement with a very well defined CV obtained for this product (Figure 5.11). Figure 5 shows the MALDI-TOF mass spectrum of this bis-adduct. At the present time we are not able to establish specifically which regioisomer this compound corresponds to, but we feel confident that it is probably a single regioisomer and not a mixture.

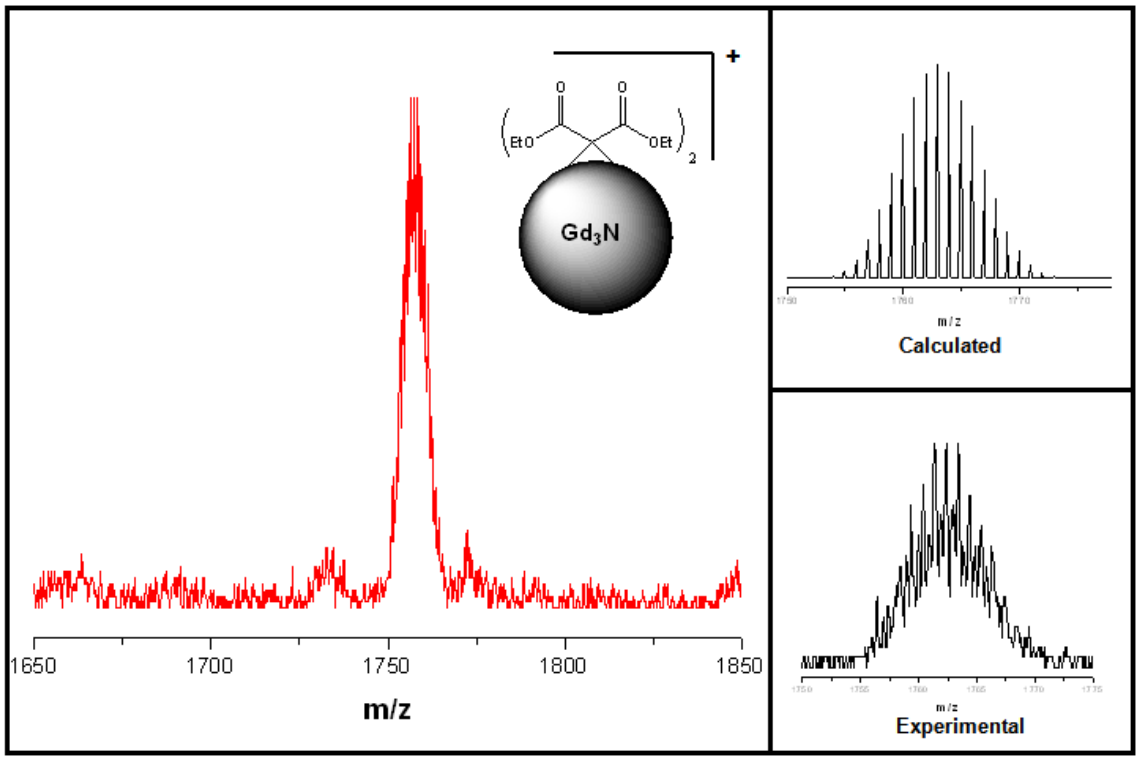


**Figure 5.5**. Simulated and experimental mass spectra of isolated bis-adduct $Gd_3N@C_{80}$-$[C(CO_2Et)_2]_2$.

We recently reported, in collaboration with Balch and Dorn, the X-ray crystal structure of $Gd_3N@C_{84}$, which possesses a non-IPR symmetry with an egg-shape

containing two adjacent pentagon rings at the pointed end.[6] It has been shown that the reactivity of fullerenes is determined by two factors. Bonds with high π orders are preferred as well as pyramidalized bonds. However, calculations suggest and X-ray data confirm that the pyramidalization is the most important factor in the determination of the most reactive sites for the additions.[7-9] For instance, $C_{70}$ presents its most reactive bonds in the poles of the fullerene cage where the pyramidalization is highest.[10] In the case of $M_3N@C_{80}$ (M = Sc, Y and Er) it has been shown that the most pyramidalized C–C bonds are the most reactive ones.[7-9] For example, the $D_{5h}$ isomer possesses greater reactivity than the $I_h$ isomer due to its higher degree of pyramidalization.[7] The $Gd_3N$ unit in $Gd_3N@C_{84}$ is oriented in such a way that one of its metallic ions is oriented toward the two fused pentagons.[6] This orientation makes the antiaromatic fused pentagon moiety more aromatic in character (see Chapter 2). Together with the already large degree of pyramidalization (compared with the other possible addition sites), this may make the [5,5] bond the most reactive double bond in the $C_{84}$ cage.

The reaction of $Gd_3N@C_{84}$ under identical conditions as those described for $Gd_3N@C_{80}$ yielded only one product after 20 min of reaction at room temperature and no multiadducts were observed demonstrating its lower reactivity for the cyclopropanation reaction (see Figure 5.2and 5.6). Due to the paramagnetic character of the metallic cluster it was not possible to use NMR spectroscopy as a characterization technique to prove the site of addition. Interestingly, the cyclopropanation occurs at only one site on the cage, affording a single monoadduct. No further additions were found even after prolonged

reaction times or elevated temperatures. Figure 5.7 shows the MALDI-TOF mass spectrum of this compound confirming its identity.

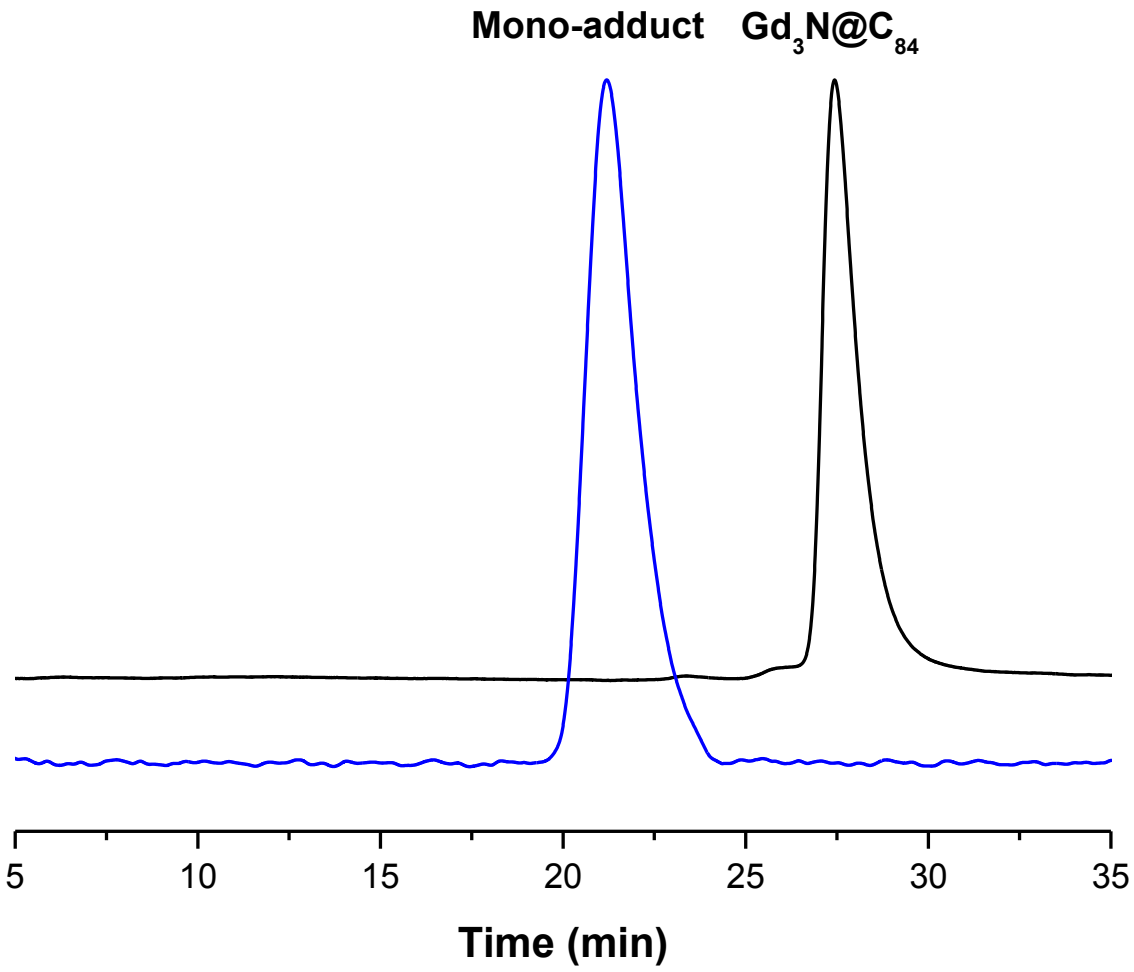


**Figure 5.6**. HPLC chromatograms of $Gd_3N@C_{84}$ before reaction and the isolated adduct. Eluent: Toluene, flow rate: 4.0 mL/min, Buckyprep-M column, detection: 372 nm.

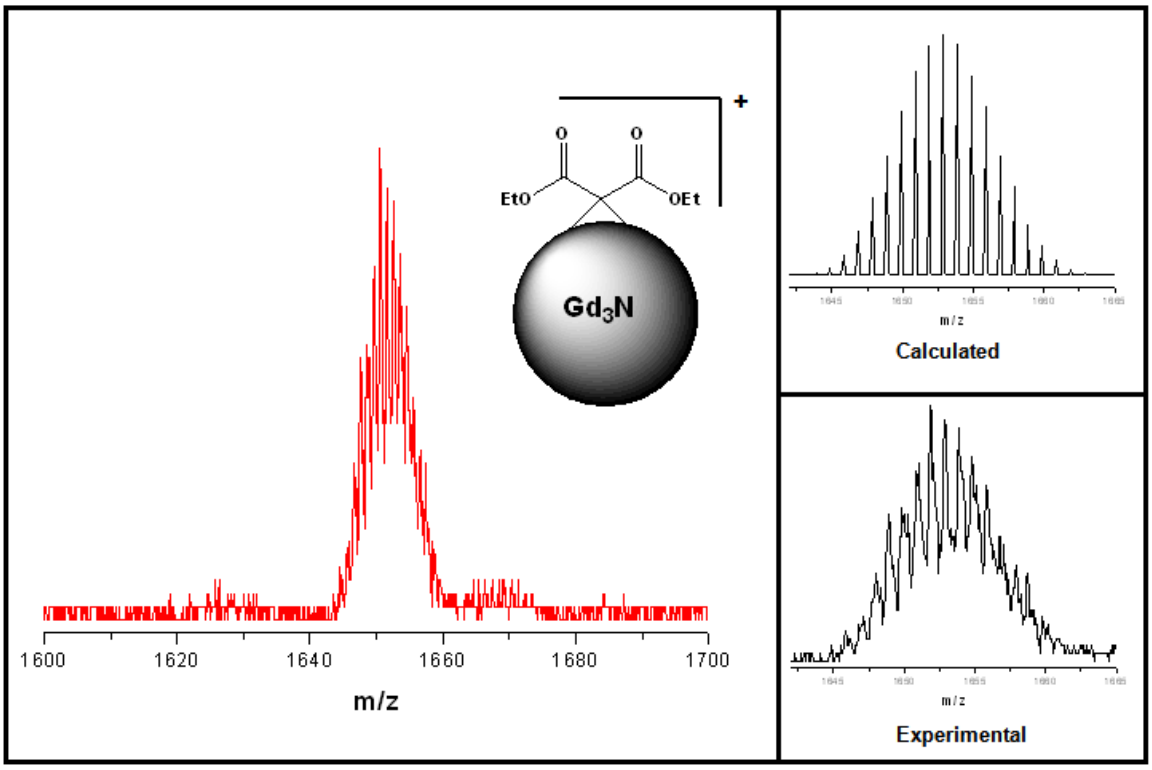


**Figure 5.7**. Simulated and experimental mass spectra of isolated mono-adduct $Gd_3N@C_{84}$-$[C(CO_2Et)_2]_2$.

Perhaps the most surprising result was obtained when $Gd_3N@C_{88}$ was reacted. Despite its low HOMO–LUMO gap,[4] $Gd_3N@C_{88}$ showed no sign of reaction under the same conditions, even after a gradual increase of the temperature (up to 60 °C) and longer reaction time (5 h). This lower reactivity may be attributed to the lower degree of pyramidalization of this larger cage (see Figure 5.2). According to these results $Gd_3N@C_{80}$ appears to be the most reactive metallofullerene in the family whereas $Gd_3N@C_{88}$ is completely unreactive under Bingel-Hirsch reaction conditions. Therefore

there seems to be a gradual decrease in the reactivity of metallofullerenes as the size of the carbon cage increases.

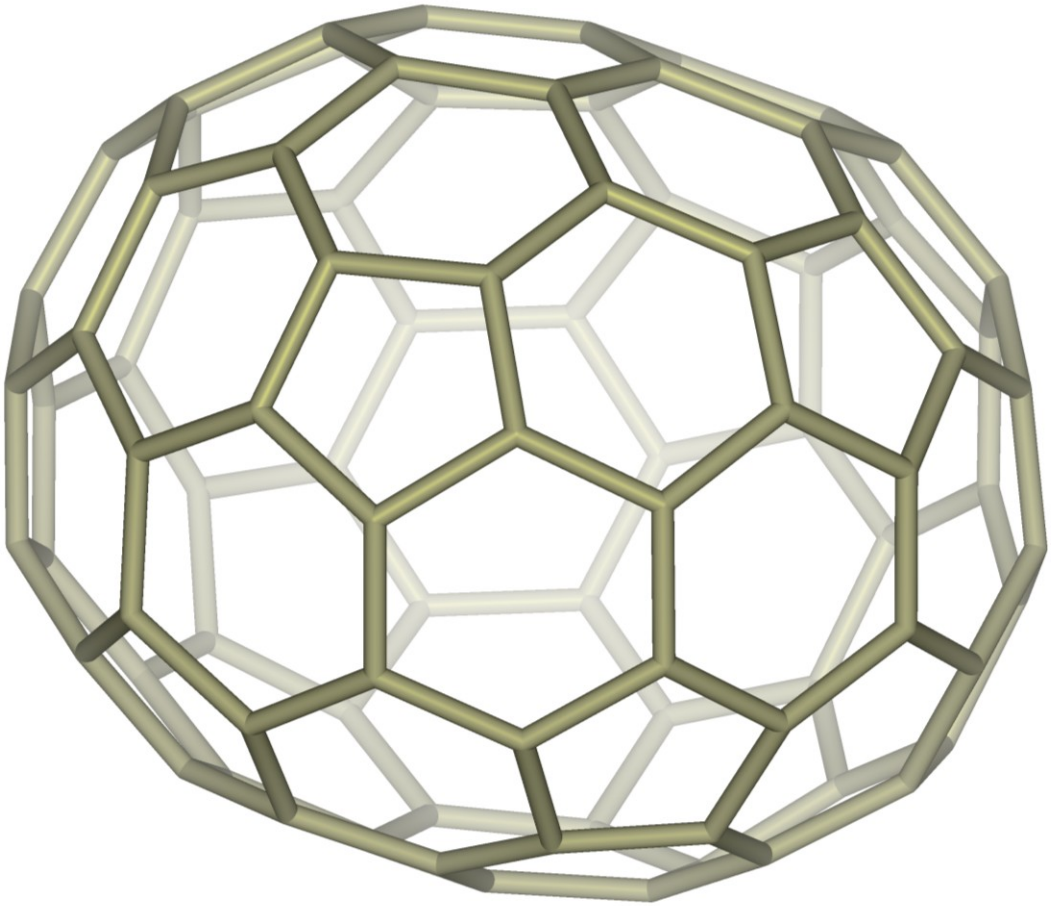

**Figure 5.8**. A drawing of $D_2$-$C_{88}$. The most flattened fullerene in the series of $I_h$-$C_{80}$, $C_s$(51365)-$C_{84}$ and $D_2$-$C_{88}$.

Using DFT level calculations, Dunsch and Popov have shown that the most stable isomer for the $C_{88}^{6-}$ cage is the IPR $D_2$: 81 738,[11] which is separated from other possible isomers by an energy gap of 70.6 kJ mol$^{-1}$, this isomer is the most stable for $Sc_3N@C_{88}$

and $Y_3N@C_{88}$. Therefore $M_3N@C_{88}$ metallofullerenes would have the same $D_2$ symmetry. By X-ray data Dorn, Balch and co-workers[12] showed that $Tb_3N@C_{88}$ possesses the $D_2$ symmetry. Figure 8 shows a drawing of the $D_2$-$C_{88}$ fullerene The $C_{88}$ carbon cage appears to have a flattened shape and that could explain the lack of reactivity for $Gd_3N@C_{88}$ and the highly reactive behavior of the more curved shaped $Gd_3N@C_{80}$. It has been extensively shown that $C_{60}$ and $C_{70}$ are the most reactive fullerenes whereas other fullerenes of larger size such as $C_{80}$ and $C_{82}$ are less reactive under similar reaction conditions.[2]

In addition to characterizing the adducts by HPLC and mass spectroscopy, UV-Vis-NIR spectra of the samples were taken in *o*-DCB. The absorptions of the pristine samples did not seem to change after functionalization (see Figures 5.9-5.10), even when two methano addends were present on the carbon cage, showing that the spherical chromophore is not significantly perturbed and that the derivatives are fulleroids.[2]

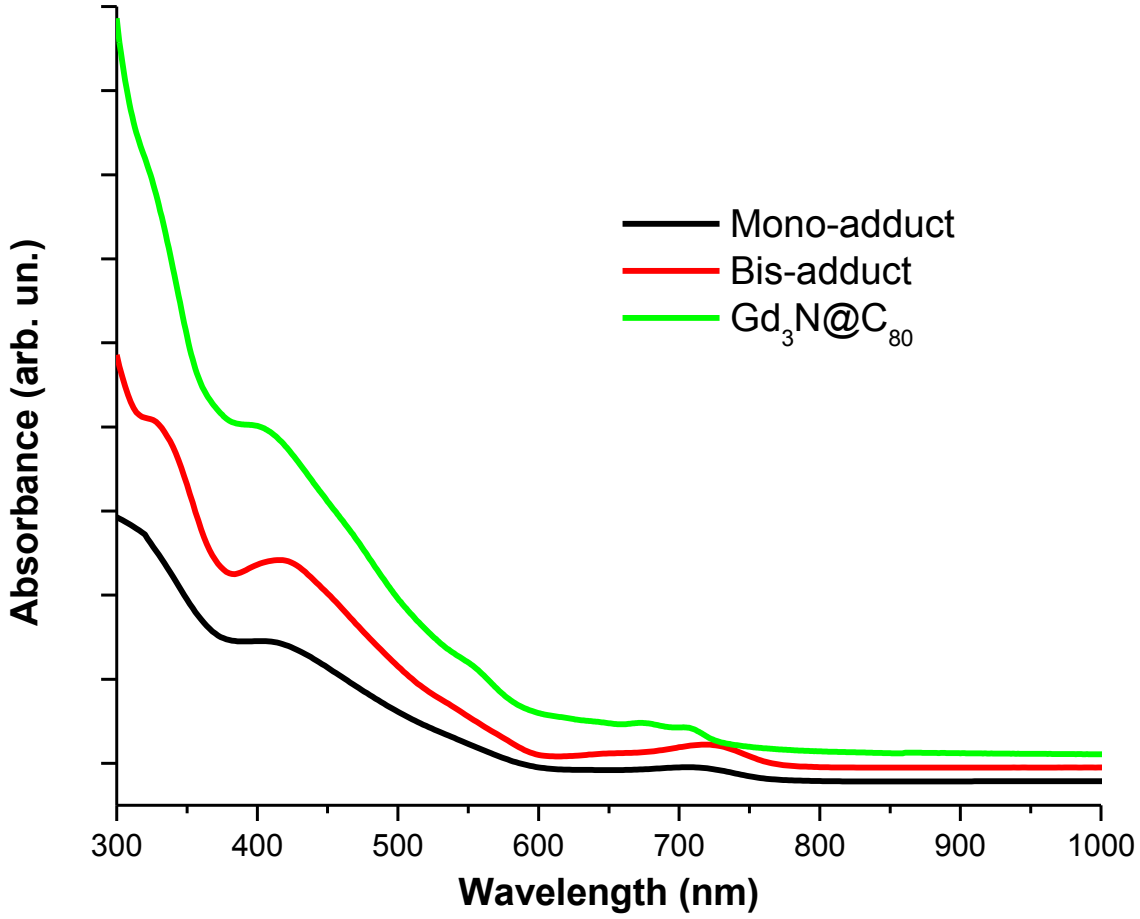


**Figure 5.9**. UV-vis-NIR spectra of pure $Gd_3N@I_h$-$C_{80}$, mono-adduct $Gd_3N@C_{80}$-$C(CO_2Et)_2$ and bis-adduct $Gd_3N@C_{80}$-$[C(CO_2Et)_2]_2$.

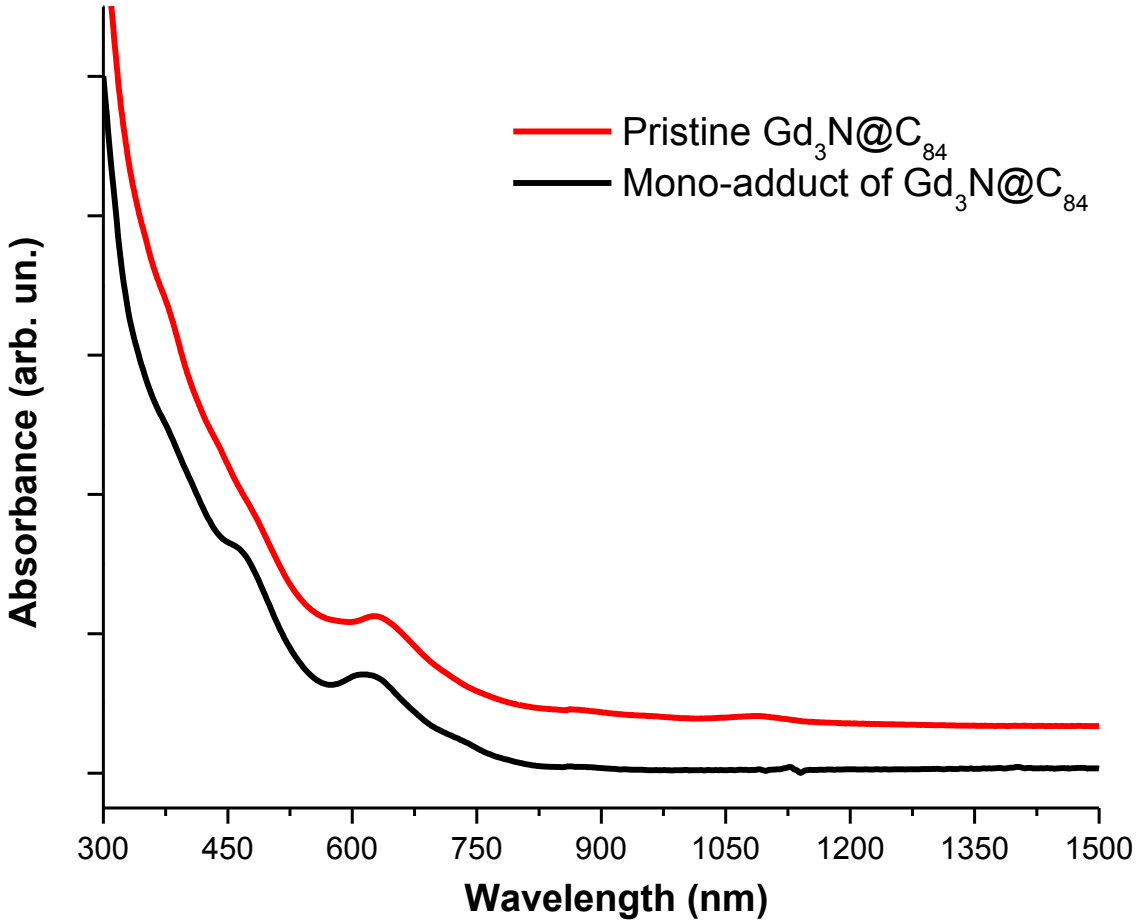


**Figure 5.10**. UV-vis-NIR spectra of pure $Gd_3N@C_{84}$, and mono-adduct $Gd_3N@C_{84}$-$C(CO_2Et)_2$.

The electrochemistry of the $Gd_3N@C_{80}$ and $Gd_3N@C_{84}$ derivatives was carried out in *o*-DCB containing 0.05 M of $NBu_4PF_6$ as supporting electrolyte and using a 2 mm diameter glassy carbon disk as the working electrode. Ferrocene was added at the end of the experiments and used as a reference for measuring the potentials. The same conditions were used for the electrochemical studies of the non-derivatized $Gd_3N@C_{80}$ and $Gd_3N@C_{84}$ reported recently.[4]

The redox behavior of the mono methanofullerene derivatives of $Gd_3N@C_{80}$ (Figure 5.11) is very similar to that of the [6,6]-methanofullerene derivatives of $Y_3N@C_{80}$ and $Er_3N@C_{80}$[2] with irreversible monoelectronic reductive steps and reasonable a reversible monoelectronic oxidative step.

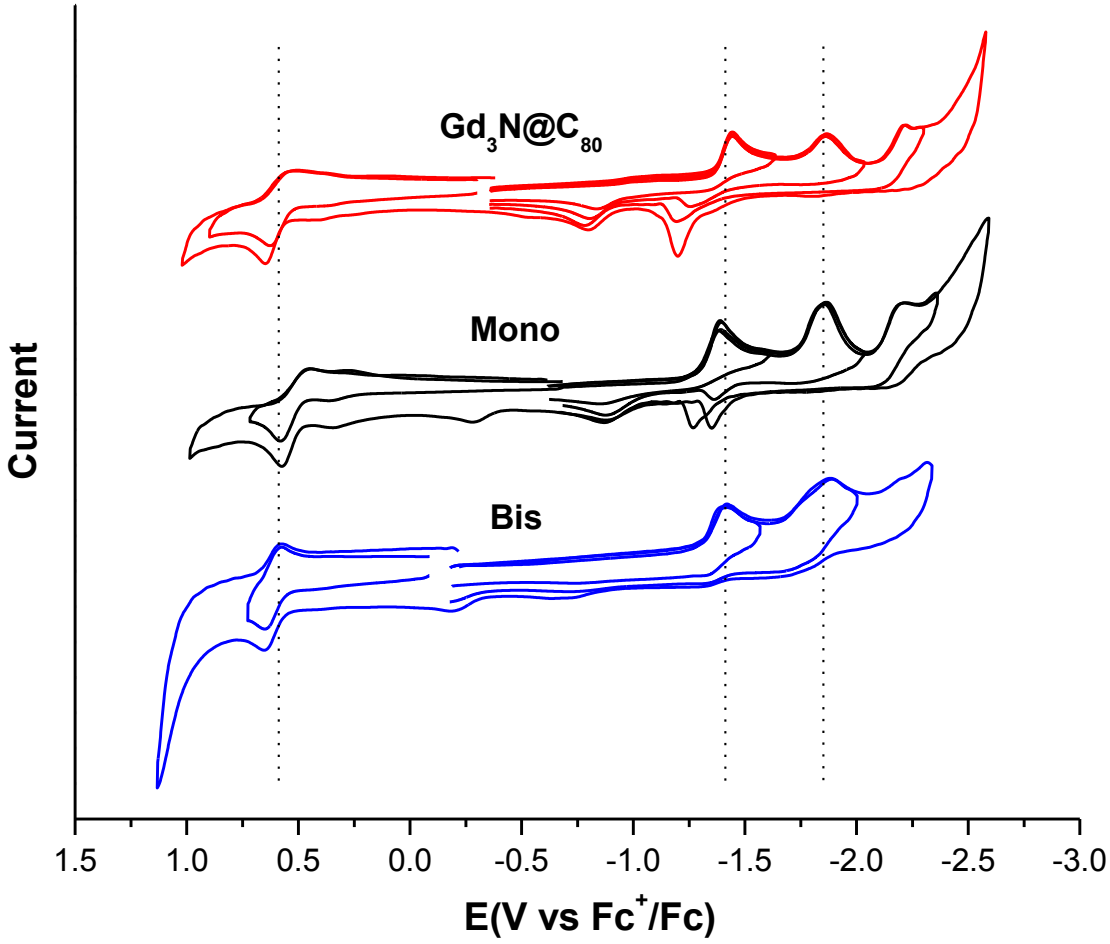


**Figure 5.11**. Cyclic voltammograms of $Gd_3N@C_{80}$ (top), mono-adduct [6,6] $Gd_3N@C_{80}$-$C(CO_2Et)_2$ (middle) and bis-adduct $Gd_3N@C_{80}$-$[C(CO_2Et)_2]_2$ (bottom) compounds obtained in *o*-DCB + 0.05 M $(nBu)_4NPF_6$ (scan rate 0.1 $Vs^{-1}$).

Previous studies with functionalized $Sc_3N@C_{80}$, $Y_3N@C_{80}$, and $Er_3N@C_{80}$ have invariably shown that the electrochemical behavior is highly dependent on the addition site, with [5,6] addends always exhibiting reversible reductive processes and [6,6] addends exhibiting irreversible reductions. Given that the observed electrochemical behavior for the monoadduct of $Gd_3N@C_{80}$ in the present case is essentially identical to that observed for all [6,6] monoadducts of trimetallic nitride endohedrals studied thus far,[2] it seems reasonable to conclude that it is also a [6,6] adduct. In the case of a methano monoadduct on $Y_3N@C_{80}$, it was recently shown to be 'open' at the [6,6] ring junction,[13] a likely possibility for the present example based on the observed similarities.

The bisadduct of $Gd_3N@C_{80}$ exhibits a remarkably simple electrochemical response with well defined peaks (Figure 5.11); two clearly identified irreversible reductive steps and one reversible oxidative step. Based on previous work with bisadduct regioisomers of $C_{60}$, which exhibit very different electrochemical behavior,[14] the observed electrochemical response for this bisadduct indicates a high degree of regioisomeric purity, in agreement with the HPLC observations. Interestingly the addition of one and two methano addends to $Gd_3N@C_{80}$ (Table 5.1) does not systematically shift the reduction potentials cathodically, as observed for $C_{60}$ derivatives.[14]

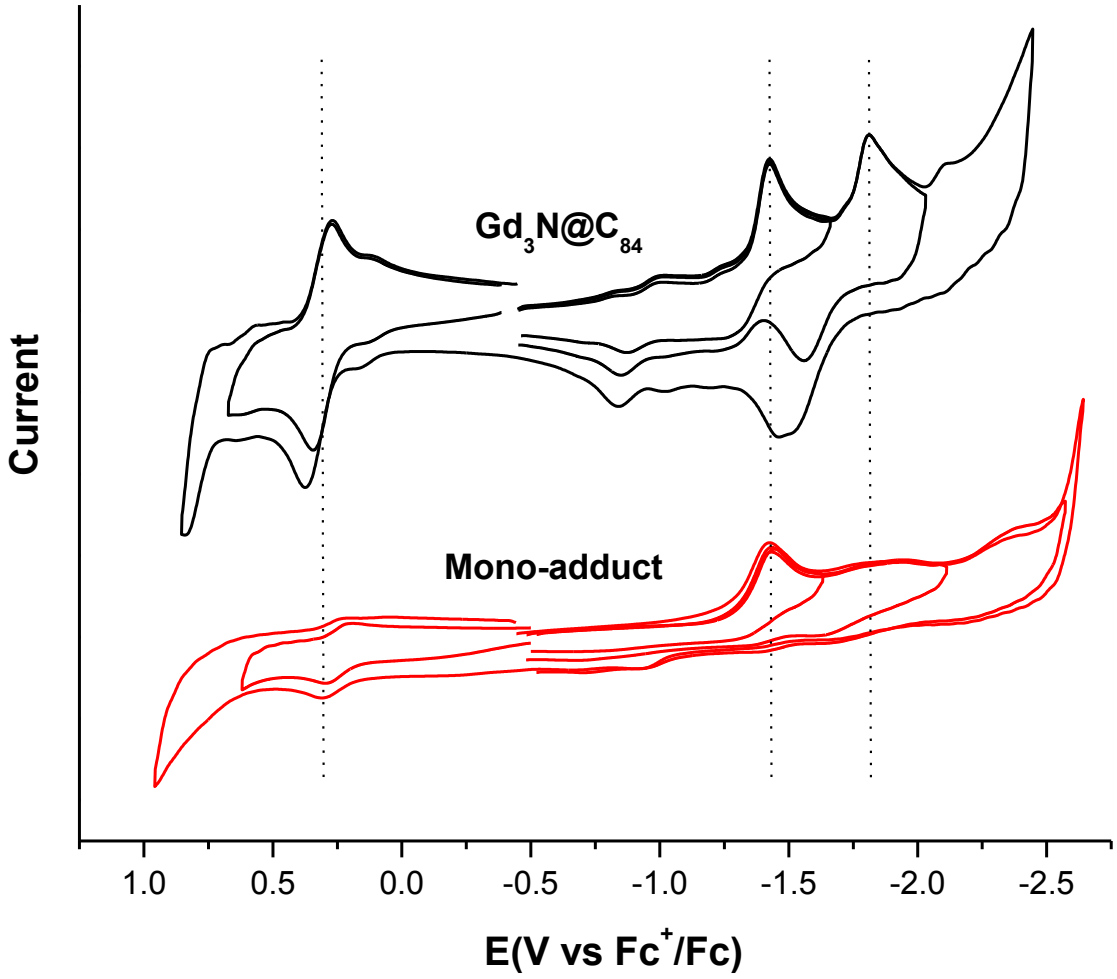


**Figure 5.12**. Cyclic voltammograms of $Gd_3N@C_{84}$ (top) and mono-adduct $Gd_3N@C_{84}$-$C(CO_2Et)_2$ (bottom) compounds obtained in *o*-DCB + 0.05 M $(nBu)_4NPF_6$ (scan rate 0.1 $Vs^{-1}$).

**Table 5.1**. Relevant redox potentials for pristine $Gd_3N@C_{80}$ and $Gd_3N@C_{84}$ and their methano derivatives (V vs $Fc^+/Fc$).

| compound | $E_{1/2}$ $ox_1$ | $E_{pc}$ $red_1$ | $E_{pc}$ $red_2$ | $E_{pc}$ $red_3$ |
|---|---|---|---|---|
| $Gd_3N@C_{80}$ | +0.58 | -1.44 | -1.86 | -2.18 |

| | | | | |
|---|---|---|---|---|
| $Gd_3N@C_{80}$-[C(COOEt)$_2$] | +0.58 | -1.39 | -1.83 | -2.17 |
| $Gd_3N@C_{80}$-[C(COOEt)$_2$]$_2$ | +0.59 | -1.40 | -1.88 | |
| $Gd_3N@C_{84}$ | 0.32 | -1.37 | -1.76 | |
| $Gd_3N@C_{84}$-[C(COOEt)$_2$] | 0.28 | -1.43 | -1.77 | -2.38 |

The CV of the methano derivative of $Gd_3N@C_{84}$ displays irreversible reduction steps and one reversible oxidation step, as in the unfunctionalized parent fullerene (Figure 5.12). Since there are no relevant electrochemical data reported in the literature, it is not possible to assign with confidence the site of addition based on the electrochemical results. Since, as mentioned before, the highly paramagnetic nature of the cluster prevented us from obtaining NMR spectra of these derivatives, the regiochemistry of the second group added to $Gd_3N@C_{80}$ and the addition site on $Gd_3N@C_{84}$ still need to be determined. Further characterization of the monoadducts of $Gd_3N@C_{80}$ and $Gd_3N@C_{84}$ and bisadduct of $Gd_3N@C_{80}$ including X-ray crystallography, is currently underway.

**Synthesis of water soluble metallic nitride endohedral metallofullerenes for MRI applications**

Magnetic resonance imaging (MRI) has evolved into one of the most powerful techniques in diagnostic clinical medicine and biomedical research by enabling the acquisition of high resolution, three-dimensional images of the distribution of water in vivo.[1] The strong expansion of medical MRI has prompted the development of a new class of pharmacological products, called contrast enhancing agents. These agents

catalytically shorten the relaxation time of nearby water molecules, thereby enhancing the contrast with background tissues. In 1999, approximately 30% of all MRI scans used a contrast agent, most of which were based on gadolinium complexes.[14] By now, this number has probably increased to between 50 and 60%. This utility has prompted research on improved Gd-based contrast agents, about which several reviews have recently published. [15]

Gd(III) is highly paramagnetic with seven unpaired electrons and a long electronic relaxation time, making it an excellent candidate as a relaxation agent. However, the very high in vivo toxicity of $[Gd(H_2O)_8]^{3+}$ requires that the metal be complexed by strong organic chelators before it is administered to patients. Current MRI agents require injection of gram quantities of Gd in order to obtain satisfactory contrast in the resulting image.[14, 15] With such large doses required for reasonable image enhancement, current contrast agents are limited to targeting sites where they can be expected to accumulate in high concentrations, such as in the blood stream.[15] Therefore most of the current research on MRI is being addressed to synthesize complexes with larger relaxation times and at the same time that can be able to tight stronger the toxic $Gd^{3+}$ ions.[14]

On the other hand, dendrons are increasingly used as versatile building blocks in organic chemistry in order to design stereochemically defined macromolecules with attractive solubility-, polarity-, amphiphilic-, molecular aggregation-, biological activity-, reactivity-, catalytical- and photochemical properties.[16] Among the various types of

dendritic building blocks 1→3 *C*-branched polyamide dendrimers, developed by Newkome are of special interest due to their high branching multiplicity and bulkiness as well as the high degree of hydrophilicity of their corresponding unprotected polyacids.[17]

In this section of the Chapter we report the synthesis of a dendrimer involving EMFs as a core structure (see Figure 5.13). First we developed a dendrimer containing Newkome type 1 → 3 *C*-branched polyamide dendrons as hydrophilic moieties as shown in Figure 5.14 and 5.15.

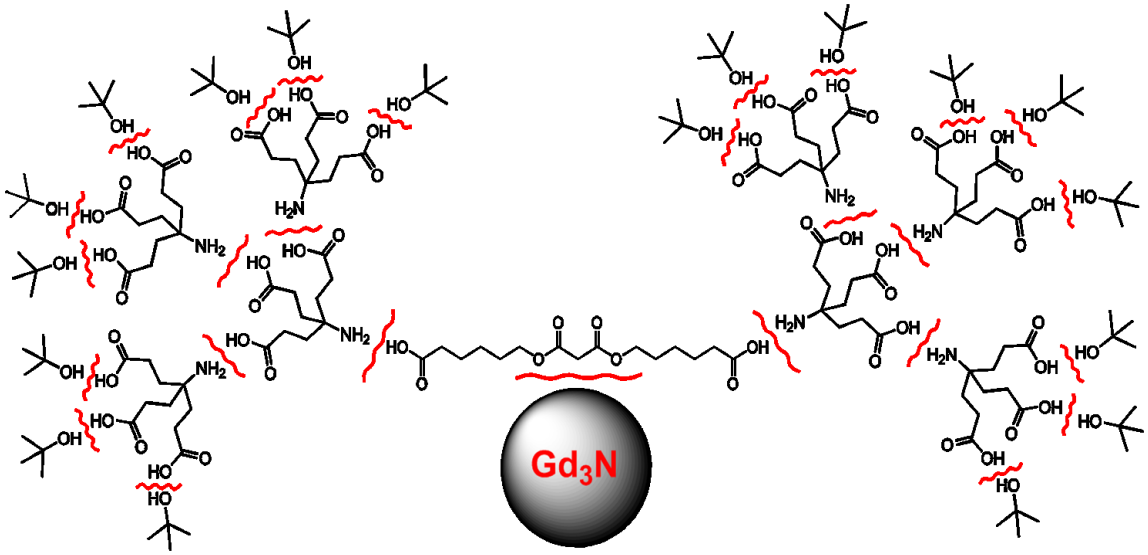


**Figure 5.13**. Building blocks of the dendritic water soluble EMF.

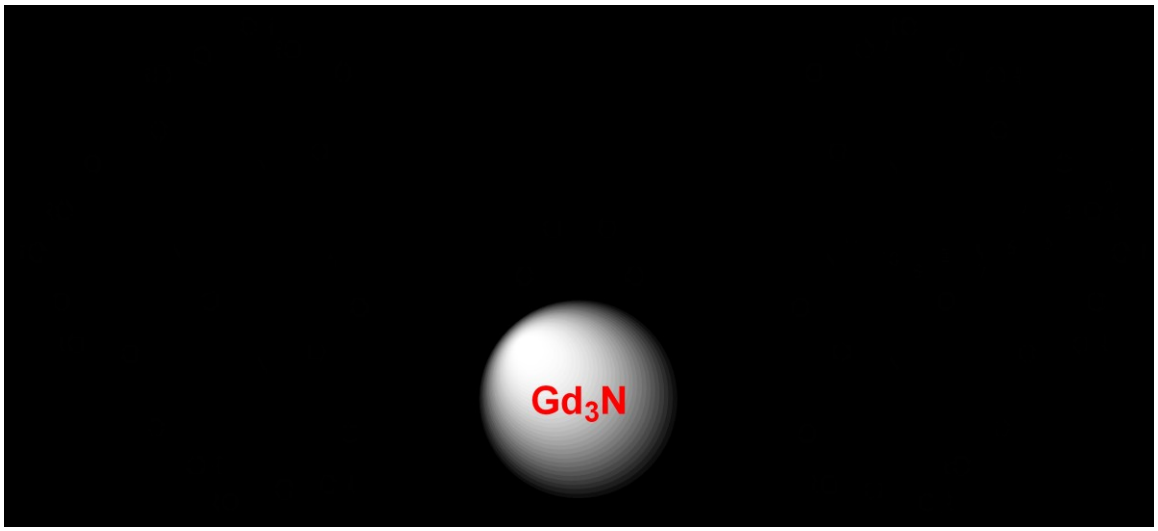


**Figure 5.14**. Proposed water soluble dendritic gadolinium nitride EMF as a potential MRI contrast enhancing agent. R = H.

The water soluble dendritic EMF is composed of two 1 → 3 C-branched polyamides dendrons (compound 5 from Figure 5.15) connected to an adapter molecule (compound 7 from Figure 5.16) that are attached to the fullerene structure *via* a Bingel-Hirsch reaction to finally obtain a highly water soluble EMF that can be potentially used as a MRI contrast enhancing agent.

Figure 5.15 shows the synthetic procedure to obtain the 1 → 3 C-branched polyamide dendron **5**, which is built from the nitroester **1**. Compound **1** was prepared by treatment of nitromethane with slightly more than three equivalents of tert-butyl acrylate in dimethoxyethane (DME). Trace impurities produced during the reaction were removed by recrystallization of the compound in ethanol.

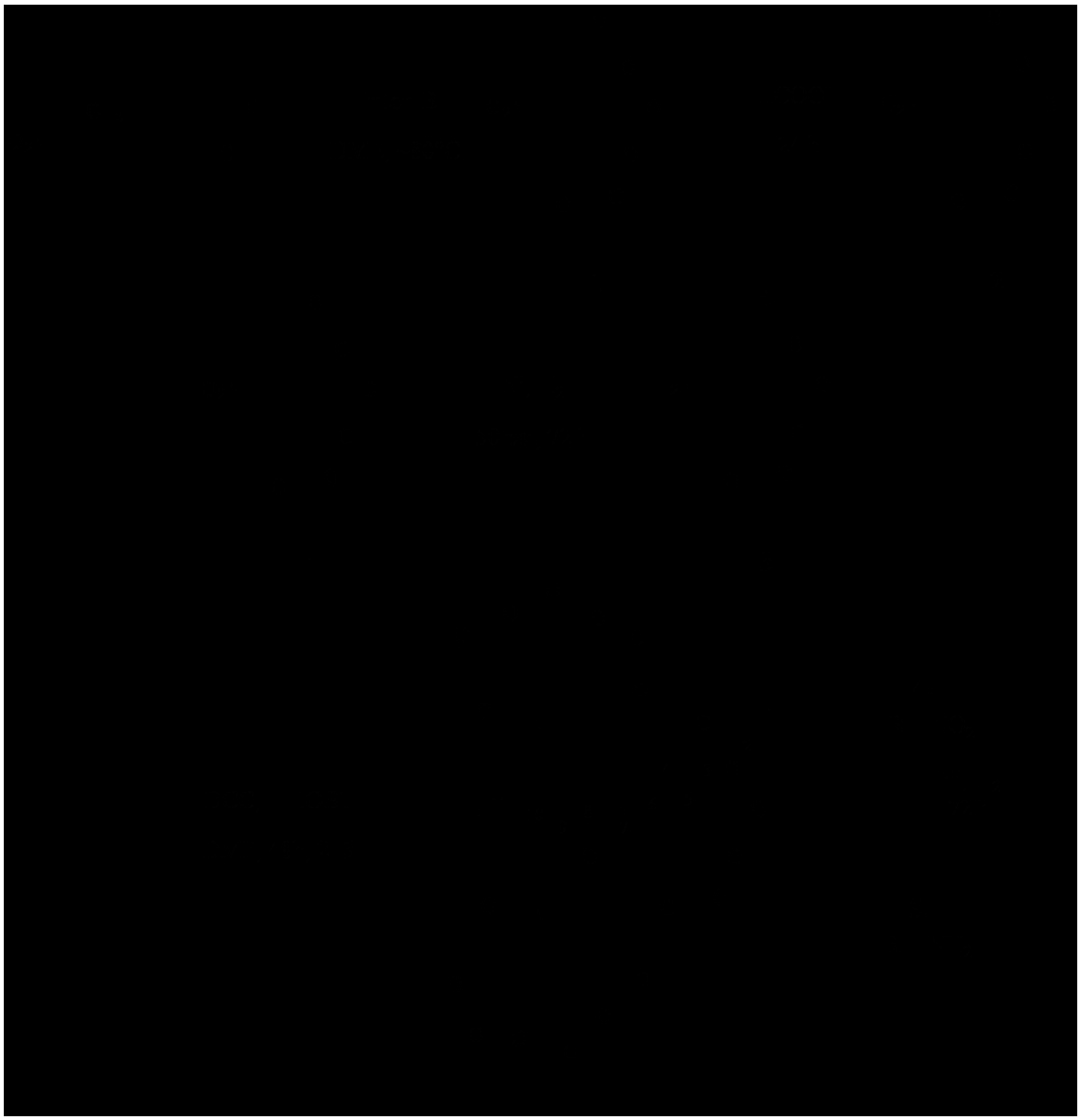

**Figure 5.15**. Synthesis of the Newkome type 1 → 3 *C*-branched polyamide dendron **5**.

The nitroester **1** is also submitted to hydrogenation in ethanol using Raney-Nickel as catalyst to yield the aminotriester **3** in a 94% yield. The nitroester **1** is deprotected as well by stirring the compound in formic acid for 24 hours at room temperature. After removing the formic acid under vacuum the tricarboxylate **2** was obtained in 98% yield.

Compounds **2** and **3** were subjected to a standard amide formation procedure using 1-hydroxy-benzotriazole [HOBT] and dicyclohexylcarbodiimide [DCC] in DMF as condensing agents. The triscarboxamide **4** was isolated in 79% yield after flash chromatography on silica gel (cyclohexane: ethyl acetate 2:1). Finally the second generation amine **5** was obtained by hydrogenation of compound **4** using Raney-Nickel as catalyst to afford the 1 → 3 C-branched polyamide dendron **5** in 84% yield after flash chromatography on silica gel using first cyclohexane: ethyl acetate 1:2 and then cyclohexane : ethyl acetate : methanol 1:2:1 as eluent.

The adapter compound **7** was synthesized from the commercially available compounds tert-butyl 6-hydroxyhexanoate and malonyl chloride which were reacted in pyridine/$CH_2Cl_2$. After stirring the solution for 6 hours the product was purified by flash chromatography using hexane: ethyl acetate 4:1 to obtain compound **6** in 69% yield (see Figure 5.16). This bis-[5-(pentylcarboxyl)] malonate **6** was dried under high vacuum as a yellow oil. This oil was transferred to a crystallizing dish and allowed to solidify under vacuum to give compound **7** in 98% yield.

The second generation polyamide dendron **5** was then subjected to a coupling reaction with the adapter compound **7** using 1-hydroxy-benzotriazole [HOBT] and dicyclohexylcarbodiimide [DCC] in DMF as condensing agents. The amidation reaction of compounds **5** and **7** yielded the didendro malonate **8** which is suitable for the direct nucleophilic [2 + 1] cyclopropanation reaction with fullerenes (see Figure 5.17).

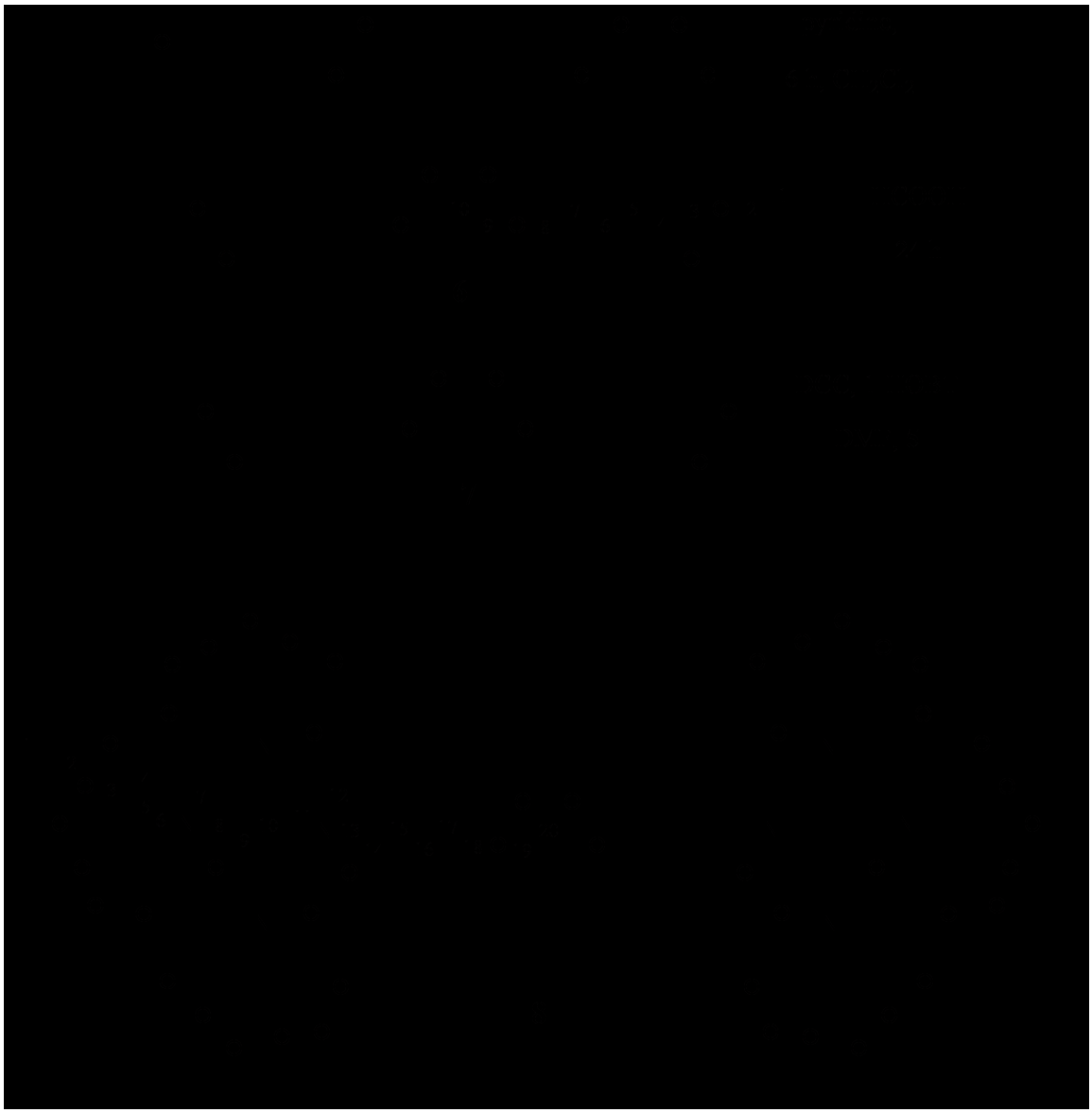

**Figure 5.16**. Synthesis of the didendro malonate **8**.

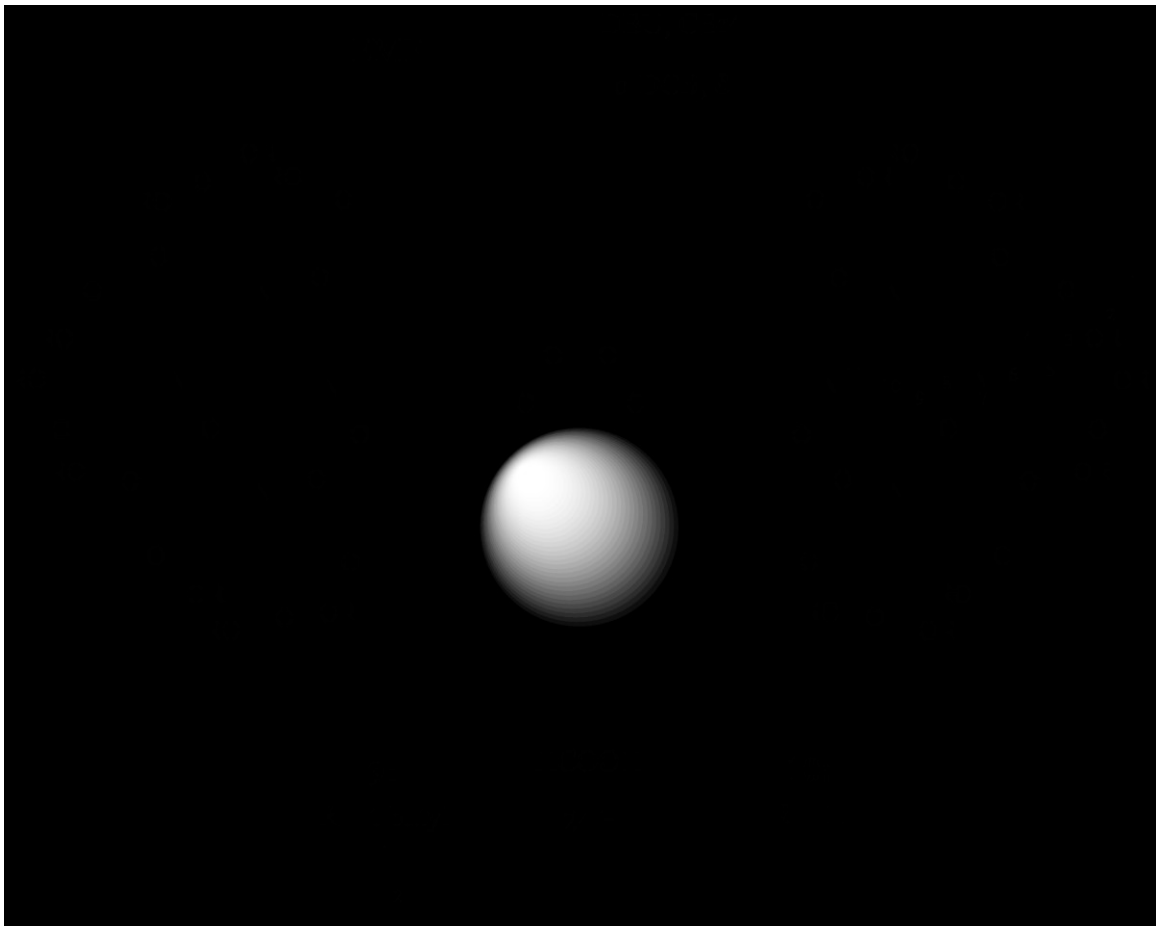

**Figure 5.17**. [2 + 1] cycloaddition reaction of fullerenes with the didendro malonate **8** to afford water soluble fullerenes.

The reaction of the didendro malonate with $Gd_3N@I_h$-$C_{80}$ in the presence of DBU and $CBr_4$ in *o*-DCB afforded 1.2 mg of the protected dendron gadolinium nitride [$I_h$-$C_{80}$] endohedral metallofullerene **9** in 20% yield (see Figure 5.17). This compound was purified by silica gel chromatography, first eluting with toluene to separate the unreactive EMFs, then with toluene: ethyl acetate (1:1) and finally with hexane: ether (6:1). Due to the paramagnetic character of $Gd_3N@I_h$-$C_{80}$ we were unable to characterize this

compound by NMR spectroscopy. Therefore the same reaction was conducted with $Sc_3N@I_h$-$C_{80}$ whose metallic cluster is diamagnetic to allow the characterization of ~0.9 mg of the dendritic compound by $^{13}C$ and $^{1}H$ NMR spectroscopy (see Figures 5.18-5.19) and MALDI-TOF mass spectrometry (Figure 5.20). Unfortunately, the small amount of compound obtained only allowed us to observe the signals from the dendritic carbons and not those of the fullerene cage, thus preventing the assignment of the addition site of the malonate on the fullerene cage. This compound was isolated by HPLC chromatography similarly to its dendro- $Gd_3N@I_h$-$C_{80}$ counterpart.

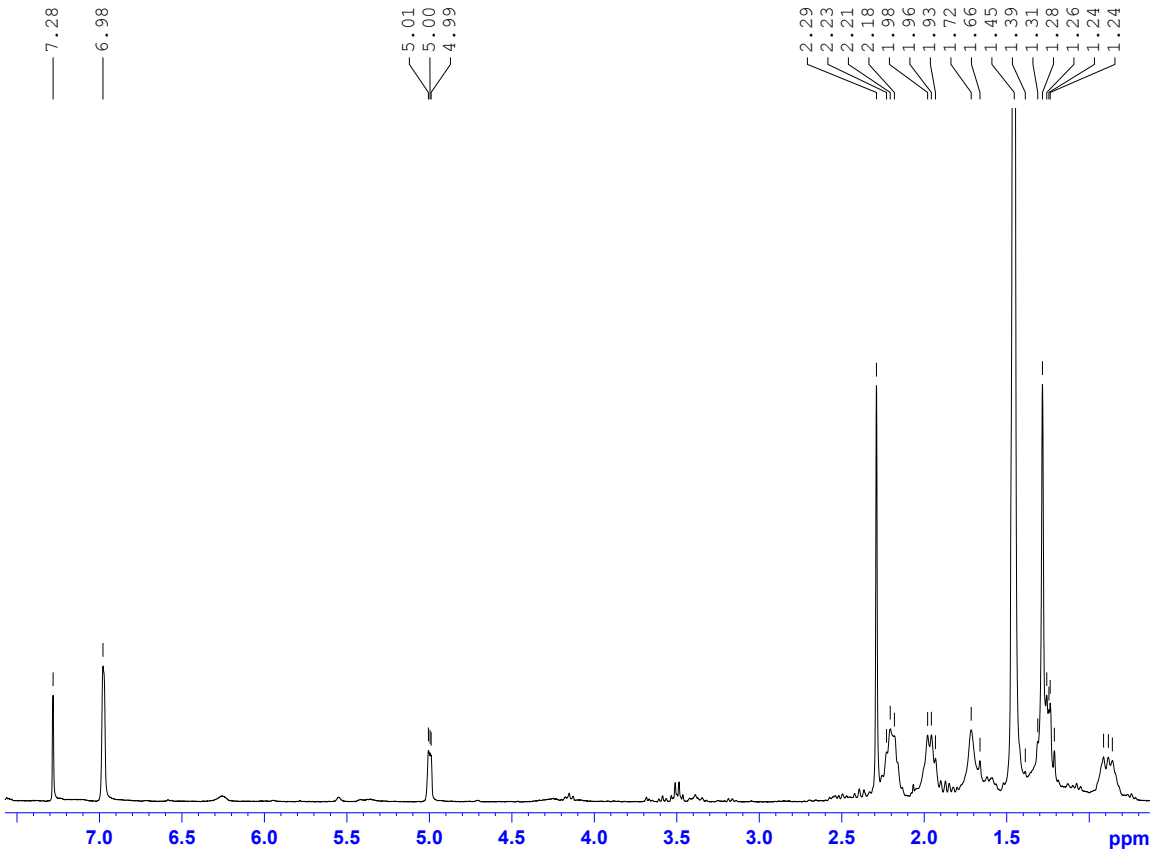


**Figure 5.18**. $^{1}H$ NMR spectrum of the dendro-$Sc_3N@I_h$-$C_{80}$. (500 MHz in $CHCl_3/CS_2$).

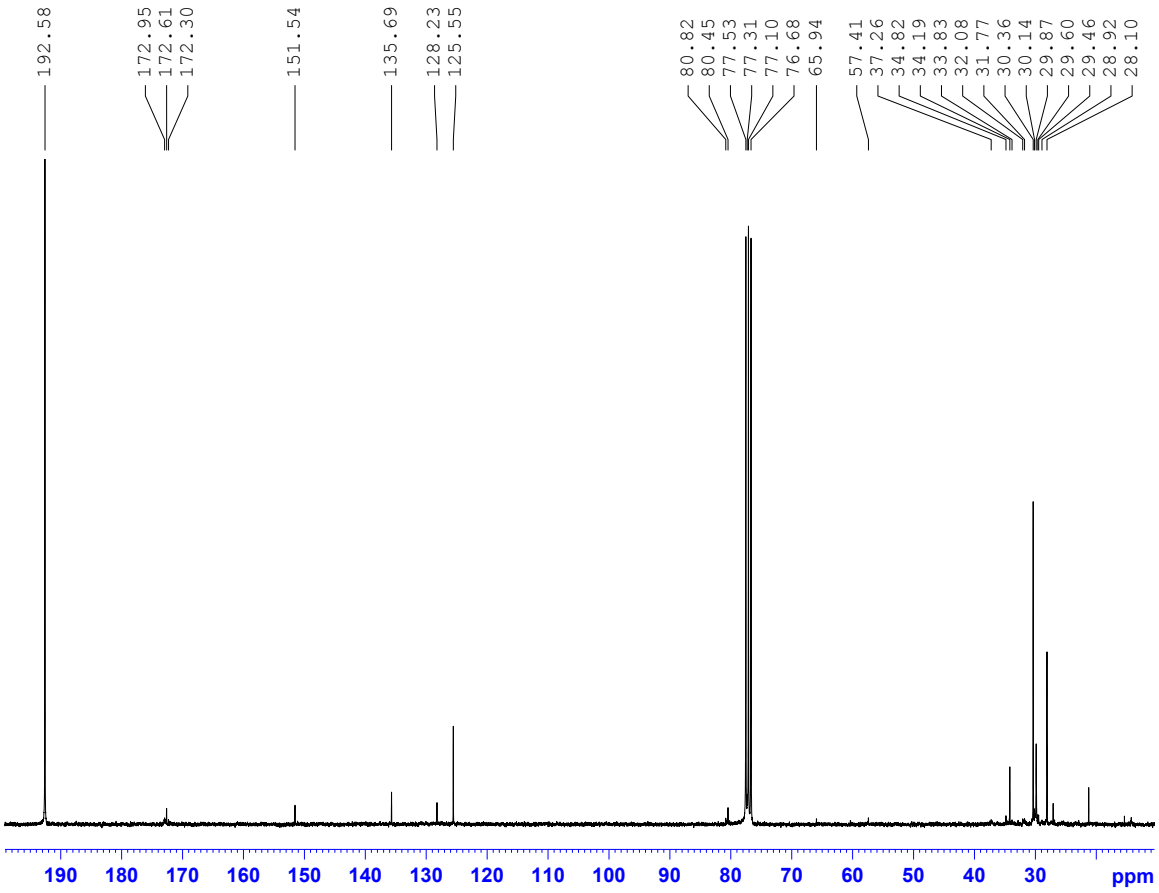


**Figure 5.19**. $^{13}C$ NMR spectrum of the dendro-$Sc_3N@I_h$-$C_{80}$. (500 MHz in $CHCl_3/CS_2$).

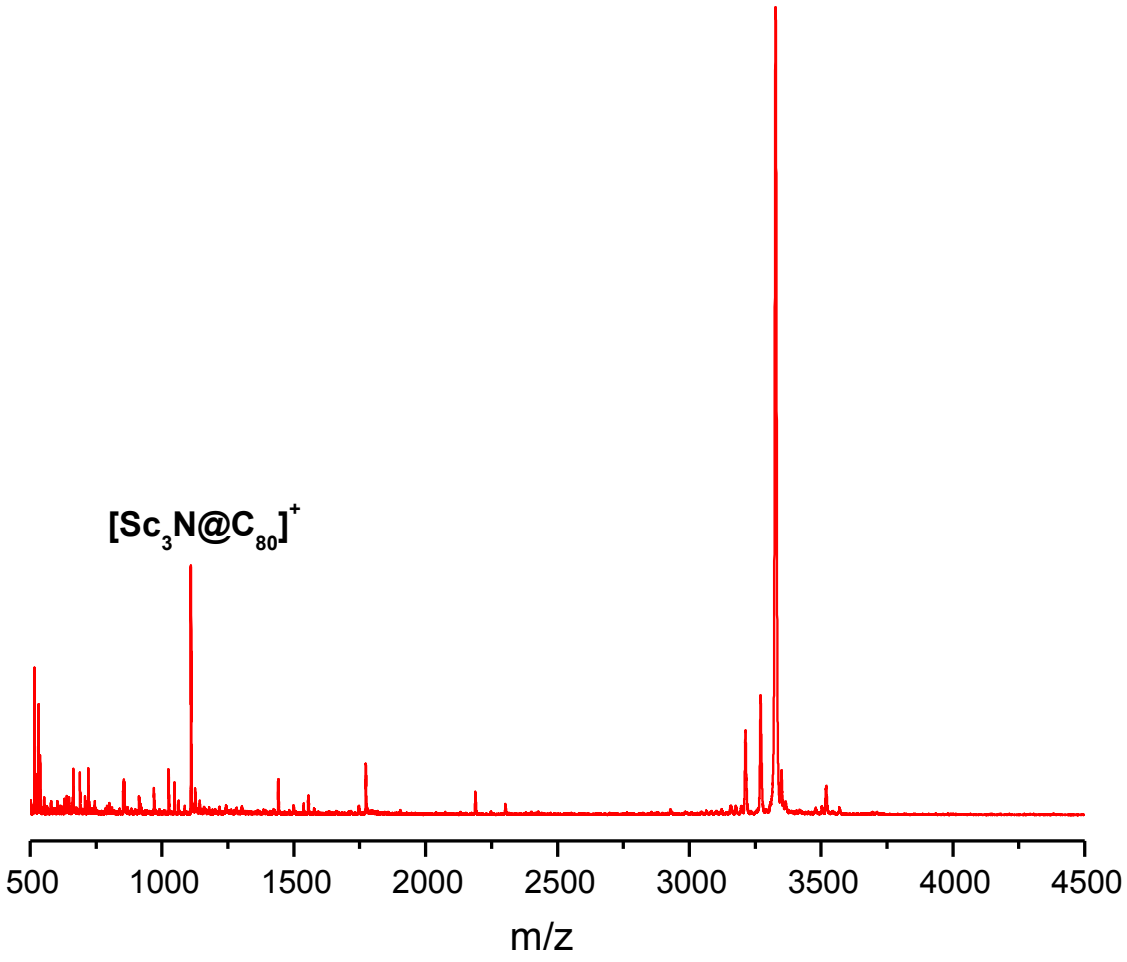


**Figure 5.20**. MALDI TOF spectrum of the dendro-$Sc_3N@I_h$-$C_{80}$.

The didendro malonate **8** is a versatile unit that can be attached not only to $Sc_3N@I_h$-$C_{80}$ and $Gd_3N@I_h$-$C_{80}$ but also to other members of the $Gd_3N@C_{2n}$ (2n = 78, 82, 84 and 86) family that have been isolated in our group (see Chapter 2). After the attachment of the dendritic unit the next step is the deprotection of the *tert*-butyl groups by dissolving the sample in formic acid for 24 hours. At the time this thesis is being

written larger quantities of dendritic-EMFs are being prepared, to characterize the hydrolyzed dendritic structures.

## Conclusions

In this chapter we have studied the reactivity of $Gd_3N@C_{2n}$ (2n=80, 82, 84 and 88) EMFs towards the [2 + 1] cyclopropanation reaction and observed a gradual decrease of reactivity upon increasing the fullerene size. This behavior is attributed to the degree of pyramidalization of the C atoms in the smaller cages.

We have synthesized a didendro malonate that can be attached to fullerenes via a [2+1] cyclopropanation reaction, and the resulting dendro-fullerenes can be easily deprotected to yield highly water soluble compounds that can be of potential use in MRI. Special cases are the metallic nitride EMFs with gadolinium which can be functionalized with the synthesized dendro malonate and deprotected to obtain a potential MRI contrast enhancing agents.

## Experimental section

**Di-*tert*-butyl 4-[2-(*tert*-butoxycarbonyl)ethyl]-4-nitroheptanedicarboxylate (1):** Nitromethane (108 mL, 2.02 mol) was dissolved in DME (500 mL) and heated up to 65-70°C. When the desired temperature was reached, Triton B (20 mL) was added. Slightly more than three equivalents of *tert*-butyl acrylate (908 mL, 6.26 mol) were added while keeping the temperature of the solution at 75-85°C. After 2h stirring more Triton B (4 x 10 mL) was added dropwise. The solution was stirred for another 2 h. The solution was concentrated

in *vacuo* to obtain a brown yellowish solid. After dissolving the solid in ether it was washed with HCl (10%, 2 x 40 mL), a saturated solution of $NaHCO_3$ (2 x 40 mL) and water (2 x 40 mL). The washed solution was then dried over $Na_2SO_4$ and Celite. The solution was filtered and the ether was removed in vacuo in order to give a yellowish residue which was recrystallized affording a white crystalline powder of **1**. $^1$H-NMR (500 MHz, $CDCl_3$): δ = 1.45 (s, C*H*$_3$, 27H), 2.21 (s, C*H*$_2$, 12H); $^{13}$C-NMR (500 MHz, CDCl3): δ = 28.03 (*C*$H_3$), 29.81 (*C*$H_2$CO), 30.36 (*C*$CH_2$), 81.16 (*C*$CH_3$), 92.20 (*C*$NO_2$), 171.08 (*C*$O_2$); MS (FAB-TOF): m/z = 444.3 $[M]^+$-H, 468.3 $[M]^+$+Na

**4-(2-carboxyethyl)-4-nitroheptanedioic acid (2):** A solution of 40 mL of formic acid and nitroester **1** (50 g, 112.2 mmol) was stirred for 24 h. The solution was concentrated under vacuum to obtain a fine white powder in a 95 % yield. $^1$H-NMR (500 MHz, CDCl3): δ = 2.15 (m, C*H*$_2$, 12H), 12.32 (s, O*H*, 3H); $^{13}$C-NMR (500 MHz, CDCl3): δ = 28.65 (*C*$H_2$CO), 30.21 (*C*$H_2$), 93.27 (*C*$NO_2$), 173.61 (*C*$O_2$); MS (FAB-TOF): m/z = 278.1 $[M]^+$+H, 300.1 $[M]^+$+Na

**Di-t-butyl 4-[2-(t-butoxycarbonyl)ethyl]-4-aminoheptanedicarboxylate (3):** Nitroester **1** (1.5 g, 3.29 mmol) was dissolved in dry EtOH (10 mL) and filled into a hydrogenation bottle charged with Raney-Nickel (1.2 g). The hydrogenation was performed at a pressure of 50 psi for 24 hours. In order to remove the Nickel the solution was filtered with a fritted funnel charged with celite and then washed with EtOH. The solution was concentrated in *vacuo* to obtain yellowish oil **3** in a 94 % yield. $^1$H-NMR (500 MHz, CDCl3): δ = 1.38 (s, C*H*$_3$, 27H), 1.55 (t, C*H*$_2$, 6H), 2.17 (t, C*H*$_2$CO, 6H), 7.28 (s, N*H*$_2$, 2H); $^{13}$C-NMR (500

MHz, CDCl3): δ = 27.94 ($CH_3$), 29.85 ($CH_2CO$), 34.21 ($CCH_2$), 80.34 ($CNH_2$), 173.04 ($CO_2$); MS (FAB-TOF): m/z = 416.3 $[M]^+$+H, 417.3 $[M]^+$+2H

**2nd-Generation Newkome-type nitrodendrimer (Nitroamide) (4):** Aminoester **3** (13.17 g, 31.7 mmol), DCC (6.54 g, 31.7 mmol), 1-HOBT (4.29 g, 31.7mmol) and nitroacid **2** (1.95 g) were dissolved in dry DMF (250 mL). The solution was stirred for 48 h at room temperature. The white precipitate was filtered. The filtrate was concentrated in *vacuo* and redissolved in ethyl acetate. The solution was then washed with 10% HCl, water, saturated $NaHCO_3$ and brine solutions and dried over $MgSO_4$. The product was puryfied by flash chromatography (ethyl acetate: hexane 1:1) affording compound **4** in a 79 % yield. $^1$H-NMR (500 MHz, CDCl3): δ = 1.44 (s, H-1,81H), 1.96 (t, H-5, 18H), 2.12 (m, H-9/10, 12H), 2.20 (t, H-4, 18H), 6.21 (s, H-7, 3H); $^{13}$C-NMR (500 MHz, CDCl3): δ = 28.10 (C-1), 29.80 (C-10), 29.92 (C-9), 30.36 (C-5), 31.29 (C-4), 57.71 (C-6), 80.71 (C-2), 92.56 (C-11), 171.10 (C-8), 172.79 (C-3); MS (FAB-TOF): m/z = 1469.9 $[M]^+$, 1470.9 $[M]^+$+H

**2nd-Generation Newkome-type aminodendrimer (Aminoamide) (5):** Amide **4** (25 g, 17.0 mmol) was dissolved in dry EtOH (100mL) and Raney-Nickel (20 g) was added. The hydrogenation was performed at a pressure of 30 psi for 24 hours. In order to remove the Nickel the solution was filtered with a fritted funnel charged with celite and then washed with EtOH. The solution was concentrated and purified by flash chromatography (ethyl acetate/cyclohexane 1:2) affording compound **5** in a 84 % yield. $^1$H-NMR (500 MHz, CDCl3): δ = 1.43 (s, H-1, 81H), 1.61 (m, H-10, 6H), 1.95 (m, H-5, 18H), 2.17 (m,

H-9, H6), 2.21 (m, H-4, 18H), 6.04 (s, H-7, 3H); $^{3}$C-NMR (500 MHz, CDCl3): δ = 27.98 (C-1), 29.70 (C-10), 29.79 (C-9), 31.45 (C-5), 35.02 (C-4), 52.68 (C-6), 57.29 (C-11), 80.45(C-2), 172.35 (C-8), 172.64 (C-3).

**Bis(6-tert-butoxy-6-oxohexyl) malonate (6):** tert-butyl 6-hydroxyhexanoate (5 g, 26.6 mmol) was dissolved in dry $CH_2Cl_2$ (105 mL) and pyridine (2.23 mL, 27.7 mmol) was added. Malonyl dichloide (1.26 mL, 13.0 mmol) was diluted with dry $CH_2Cl_2$ (4.17 mL) and added dropwise to the solution. The solution was stirred for 6 h at room temperature and then washed with water (3 x 65 mL). The solution was dried over $MgSO_4$ and the solvent was removed in vacuo. The product was purified by flash chromatography (hexane: ethyl acetate 4:1) to obtain a yellow oil **6** in a 69 % yield. $^{1}$H-NMR (500 MHz, CDCl3): δ = 1.41 (m, H-6, 4H), 1.45 (s, H-1, 18H), 1.58 (m, H-5/7, 8H), 2.23 (t, H-4, 4H), 3.38 (s, H-10, 2H), 4.17 (t, H-8, 4H); $^{13}$C-NMR (500 MHz, CDCl3): δ = 24.5, 25.2, 28.2 (C-5, C-6, C-7), 28.1 (C-1), 35.2 (C-4), 41.5 (C-10), 65.2 (C-8), 79.9 (C-2), 166.5 (C-9), 172.7 (C-3).

**Bis(5-carboxypentyl) malonate (malonate acid) (7):** Malonate **6** was dissolved in formic acid and stirred for 24 h at room temperature. The solvent was removed in *vacuo* and the residue dried under high vacuum to give a yellow oil **7** in a 98 % yield. $^{1}$H-NMR (500 MHz, CDCl3): δ = 1.39 (m, H-6, 4H), 1.63 (m, H-5/7, 8H), 2.39 (m, H-4, 4H), 3.39 (s, H-10,2H), 4.16 (m, H-8, 4H), 9.15 (bs, H-2, 2H); $^{13}$C-NMR (500 MHz, CDCl3): δ = 24.2 , 25.3, 28.1 (C-5, C-6, C-7), 33.8 (C-4), 41.6 (C-10), 65.3 (C-8), 166.7 (C-9), 179.6 (C-3).

**(Didendroester malon amide) (8):** Aminoamide **5** (24,5 g, 17.0 mmol), DCC (3.13 g, 15.2 mmol), 1-HOBT (2.05 g, 15.2 mmol) and Malonic Acid **7** (2.15 g, 6.5 mmol) were added to a 500 mL three necked flask followed by dry DMF (500 mL). The solution was stirred for 48 h. The precipitate was removed by filtering. The solution was concentrated in *vacuo* and the residue was dissolved in ethyl acetate. The solution was washed with 10% HCl, water, $NaHCO_3$ and brine solutions and dried over $MgSO_4$. The product was puryfied by flash chromatography (ethyl acetate: hexane 1:1) to obtain compound **8** in 29% yield. $^{1}$H-NMR (500 MHz, CDCl3): δ = 1.43 (s, H-1, 162H), 1.95 (m, H-4, H-9, H-15, 28H), 1.63 (m, H-17, H-16, 8H), 2.19 (m, H-14, H-10, H-5, 28H), 3.38 (s, H-20, 2H), 4.17 (t, H-18, 4H); $^{13}$C-NMR (500 MHz, CDCl3): δ = 24.4, 25.2, 28.02, 28.11, 29.3, 29.88, 31.4, 31.56, 32, 8, 41.3, 57.0, 57.44, 65.0, 82.0, 166.5, 171.20, 172.7, 172.9. FAB-MS, m/z 3276 $((M+Cs)^{+})$.

## References


[1] Vlaardingerbroek, M.T.; den Boer, J.A. *Magnetic Resonance Imaging. Theory and Practice*, Springer Verlag, (Germany), **1996**.

[2] Chaur, M.N.; Melin, F.; Ortiz, A.L.; Echegoyen, L. *Angew. Chem. Int. Ed.* **2009**, 48, 7514-7538.

[3] Chaur, M.N.; Melin, F.; Athans, A.J.; Elliott, B.; Walker, K.; Holloway, B.C.; Echegoyen, L. *Chem. Commun*. **2008**, 2665-2667.

[4] Chaur, M.N.; Melin, F.; Elliot, B.; Athans, J.A.; Walker, K.; Holloway, B.C.; Echegoyen, L. *J. Am. Chem. Soc*. **2007**, 129, 14826-14829.

[5] Cardona, C.M.; Elliott, B.; Echegoyen, L. *J. Am. Chem. Soc*. **2006**, 128, 6480-6485.

[6] Zuo, T., Walker, K., Olmstead, M. M., Melin, F., Holloway, B. C., Echegoyen, L., Dorn, H. C., Chaur, M. N., Chancellor, C. J., Beavers, C. M., Balch, A. L., Athans, A. J. *Chem. Commun.* **2008**, 1067.

[7] Cai, T.; Xu, L.; Anderson, M.R.; Ge, Z.; Zuo, T.; Wang, X.; Olmstead, M.M.; Balch, A.L.; Gibson, H.W.; Dorn, H.C. *J. Am. Chem. Soc*. **2006**, 128, 8581-8589.

[8] Campera, J.P.; Bo, C.; Poblet, J.M. *J. Org. Chem*. **2006**, 71, 46-54.

[9] Lee, H.M.; Olmstead, M.M.; Iezzi, E.; Duchamp, J.C.; Dorn, H.C.; Balch, A.L. *J. Am. Chem. Soc*. **2002**, 124, 3494-3495.

[10] Hirsch, A.; Brettreich, M. *Fullerenes: Chemistry and Reactions*, Wiley-VCH, New York, **2005**.

[11] Popov, A. A.; Dunsch, L. *J. Am. Chem. Soc*. **2007**, *129*, 11835-11849.

[12] Zuo, T.; Beavers, C. M.; Duchamp, J. C.; Campbell, A.; Dorn, H. C.; Olmstead, M. M.; Balch, A. L. *J. Am. Chem. Soc*. **2007**, *129*, 2035-2043.

[13] Lukoyanova, O.; Cardona, C.M.; Rivera, J.; Lugo-Morales, L.Z.; Chancellor, C.; Olmstead, M.M.; Rodriguez-Fortea, A.; Poblet, J.M.; Balch, A.L.; Echegoyen, L. *J. Am. Chem. Soc.*, **2007**, 129, 10423–10430.

[14] Caravan, P.; Ellison, J. J.; McMurry, T. J.; Lauffer, R. B. *Chem. Rev.***1999**, 99, 2293−2352.

[15] a) Parker, D.; Williams, J. A. *J. Chem. Soc., Dalton Trans.* **1996**, 3613−3628. b) Aime, S.; Botta, M.; Fasano, M.; Terreno, E. *Chem. Soc. Rev.* **1998**, 27, 19−29. c) Aime, S.; Botta, M.; Fasano, M.; Crich, S. G.; Terreno, E. *Coord. Chem. Rev.* **1999**, 186, 321−333. d) Comblin, V.; Gilsoul, D.; Hermann, M.; Humblet, V.; Jacques, V.; Mesbahi, M.; Sauvage, C.; Desreux, J.F. *Coord. Chem. Rev.* 1999, *186*, 451−470. e) Thunus, L.; Lejeune, R. *Coord. Chem. Rev.* 1999, *184*, 125−155. f) Meade, T. J.; Taylor, A. K.; Bull, S.R. *Curr. Opinion Neurobiol.* **2003**, 13, 597−602.

[16] Caminade, A.M.; Hameaus, A.; Majoral, J.P. *Chem. Eur. J*. **2009**, 15, 9270-9285.

[17] Newkome, G.R.; Behera, R.K.; Moorefield, C.N.; Baker, G.R. *J. Org. Chem*. **1991**, 56, 7162; b) Newkome, G.R.; Nayak, A.; Behera, R.K.; Moorefield, C.N.; Baker, G.R. *J. Org. Chem*. **1992**, 57, 358.

CHAPTER SIX

# ELECTROCHEMICAL PROPERTIES OF CARBON RICH MACROCYCLES: RADIALENES, EXPANDED RADIALENES AND RADIAANNULENES

The chemistry of carbon rich compounds has become an area of intensive study since the discovery of new carbon allotropes, the fullerenes, in 1985.[1] Given their interesting structural, optical and electrochemical properties, most of these compounds are new promising materials for molecular electronics and optics.[2] Therefore conjugated organic compounds play a primary role in the development of a new generation of optical and electronic materials. Molecules, oligomers, and polymers with carbon, heteroatomic, or organometallic frameworks have been widely explored as media for electroluminescence, data storage, and nonlinear optics.[2,3] The most intensely studied conjugated molecules with carbon-rich frameworks feature extended, linearly-conjugated π-systems. There are, however, alternative modes of π-electron communication, including cross conjugation and omniconjugation that can also produce electronically interesting materials.[2]

Shape-persistent, conjugated macrocycles, on the other hand, have been considered to exhibit a broad spectrum of remarkable attributes and topologies.[2] Over the past two decades amazing progress has been made towards the synthesis of these macrocycles, which have remarkable electronic, optical, nonlinear optical, and supramolecular properties.[2,3] A subset of this general class of molecules are the radialenes (**1**) and expanded radialenes (**2** and **3**; see Figure 6.1), which arise from the

formal insertion of acetylene units into the framework of a radialene molecule. A related class of macrocycles, radiaannulenes (**4**,Figure 6.1), contain both endo- and exocyclic vinyl fragments within the conjugated core. Both the expanded radialenes and the radiaannulenes are cross-conjugated macrocycles, and their rigid two-dimensional structure provides a useful framework for the development of fundamentally interesting π-rich molecules.

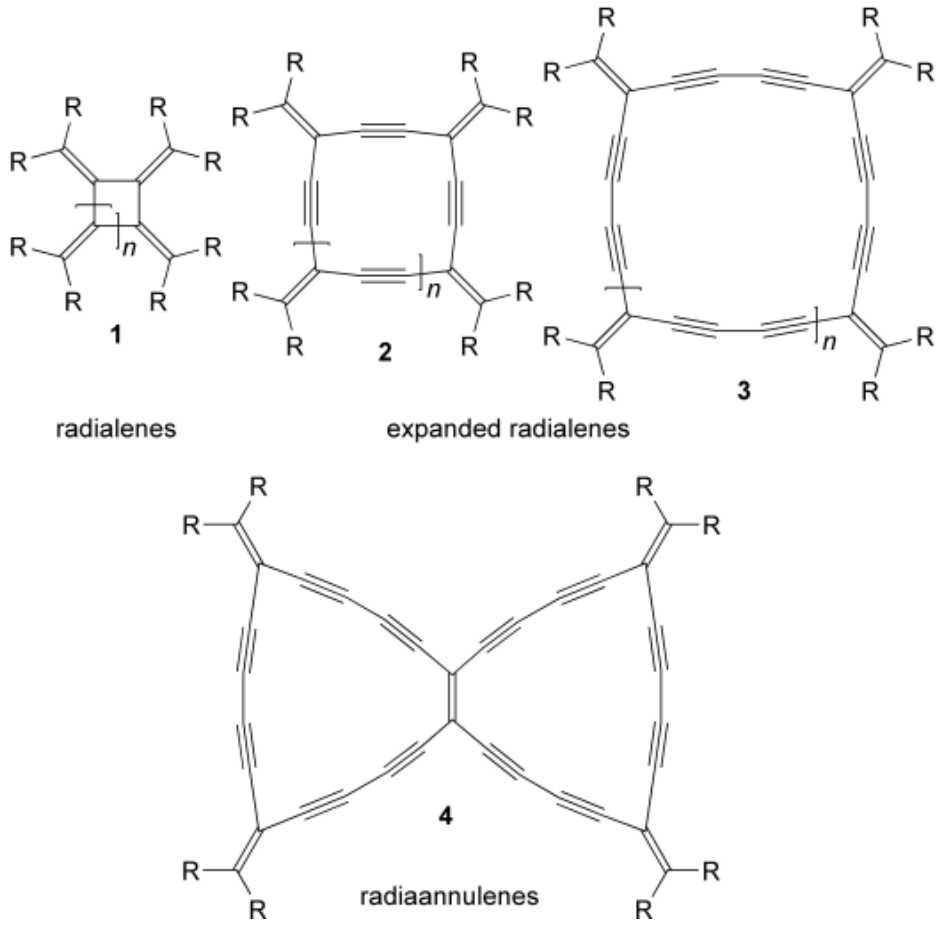


**Figure 6.1**. Structures of radialenes, expanded radialenes, and radiaannulenes.

The study of expanded radialenes was initiated by Diederich and co-workers, who explored the rich chemistry of butadiynyl-based radialenes **3** and radiaannulenes **4**. These studies, and others, used a combination of functional group variation and extensive analysis of their physical properties, and have suggested that molecules such as **3** and **4** can be generated with intriguing optical and electronic properties. Radialenes **2** would be expected to share many of the attractive electronic characteristics of their larger analogues **3**. Furthermore, a recent computational study has suggested that upon a single-electron reduction, a trimeric derivative of **2** (*n*=0) should become antiaromatic. To date, however, the synthesis of radialenes **2** has proved challenging, and only a single example has been reported (**2**, *n*=3, R=alkyl).[2]

In this Chapter we will describe the electrochemical properties of different radialenes, expanded radialenes and radiaannulenes. These compounds were synthesized in Prof. Rik Tykwinski's laboratory. At first the electrochemistry of two particular radiaannulenes will be described followed by those of [3] radialenes with different architectures and finally the electrochemical properties of expanded radialenes with different spacers such as acetylene units and metals will be described.

## Radiaannulenes: synthesis and electrochemistry [4]

A variety of conjugated cyclic topologies can be accessed on the basis of enyne building blocks, including linearly-conjugated dehydroannulenes/dehydrobenzannulenes **1** and cross-conjugated radialenes **2** (Figure 6.2).[2] Intermediate between these two limiting structures are the radiaannulenes **3** and the *meta*-substituted aryl analogues **4**.

Several molecules based on the general structure of **4** have been described, while only a single report of radiaannulenes **3** has appeared, where Zhao and co-workers incorporated π-extended tetrathiafulvalene moieties at the alkylidene positions. In this Chapter we are particularly interested in the electrochemical properties of macrocycles **3** with a minimalistic all carbon structure in comparison to radialenes **2**, and we report the characterization of two examples, **3a** and **3b** (Figures 6.3 and 6.4).

**Figure 6.2**. Annulenes, radialenes and hybrid systems.

**Figure 6.3**.Synthesis of radiaannulene **3a**.

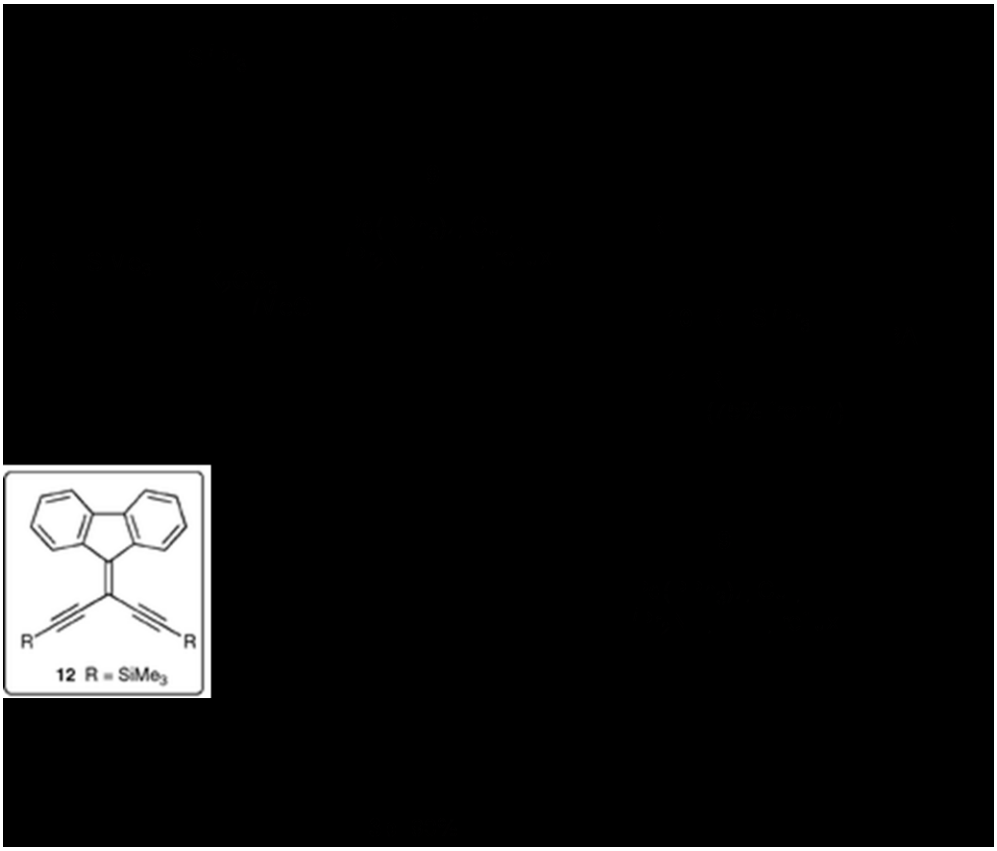


**Figure 6.4**. Synthesis of radiaannulene **3b**.

Radiaannulene **3a** was synthesized in Prof. Tykwinski's laboratories from enediyne **5** *via* desilylation to give **6** and a one-pot Sonogashira cross-coupling reaction with 1,2-diiodobenzene to give the desired macrocycle in 31% yield. $^{13}C$ NMR spectroscopy provided convincing evidence of the ascribed structure, showing each of the expected 11 unique resonances. A parent peak at *m*/*z* 604.2185 in the MALDI TOF HRMS ($M^+$) confirmed the molecular formula as $C_{48}H_{28}$.

The synthesis of radiaannulene **3b** was also attempted *via* an analogous one-pot reaction of 9-[bis(ethynyl)methylene]-9*H*-fluorene with 1,2-diiodobenzene, but the

desired macrocycle could not be isolated. Thus, a stepwise formation of the conjugated core was employed. The known diyne **7** was subjected to $K_2CO_3$ in THF–MeOH to give **8**, which was then utilized in a Sonogashira cross-coupling reaction with dibromoolefin **9**. This gave **10**, which was then desilylated with TBAF in THF to remove the triisopropylsilyl groups, providing **11**. Subsequent reaction of **11** with dibromoolefin **9** gave **3b** in excellent yield. Even more so than **3a**, radiaannulene **3b** was sparingly soluble in most organic solvents, which made NMR spectroscopic characterization a challenge. Ultimately, $^{13}C$ NMR analysis was accomplished in deuterated 1,1,2,2-tetrachloroethane at 65 °C, showing the expected signals of the 13 unique carbons. A parent peak at *m*/*z* 600.1870 in the MALDI TOF HRMS ($M^+$) confirmed the molecular formula as $C_{48}H_{24}$.

Cyclic Voltammetry (CV) and Osteryoung Square Wave Voltammetry (OSWV) for radiaannulenes **3a** and **3b** were performed in $CH_2Cl_2$ containing 0.1M of $NBu_4PF_6$ as the supporting electrolyte. The concentration of the analyte was about $5.10^{-4}$ M. A 2 mm diameter glassy carbon disk was used as the working electrode and a platinum wire as the counter electrode. A silver wire served as a pseudo reference electrode. A small amount of Ferrocene was added at the end of each experiment and used as a reference for measuring the potentials.

**Table 6.1** Electrochemical data for macrocycles **3a** and **3b**.[a]

| Compound | $E_p$ $ox_1$ [V] | $E_{1/2}$ $red_1$ [V] | $E_{1/2}$ $red_2$ [V] | $E_p red_3$ [V] |
|---|---|---|---|---|
| **3a** | 0.75 | –1.97 | –2.15 | –2.41 |
| **3b** | | –1.50 | –1.65 | –2.30 |
| **2** (R=Ph) | 0.78[b] | –1.94 | –2.2 | – |
| **5** | – | -2.03 | –2.23 | – |
| **12** | 0.95 | –1.82 | –2.14 | –2.39 |

[a] Measured in $CH_2Cl_2$ + 0.1 M *n*-$Bu_4NPF_6$ at a scan rate 100 mV/s. All potentials are reported versus the ferrocenium/ferrocene couple. [b] $E_{1/2}$ ox.

Cyclic voltammetry (CV) shows two very closely spaced oxidation processes for **3a**, the first occurring at 0.75 V (Figure 6.5 and Table 6.1), and this is confirmed by OSWV (Figure 6.7). Conversely, **3b** does not exhibit well resolved anodic behavior, although a very weak oxidation event can be discerned at 0.88 V. Macrocycles **3a** and **3b** both exhibit three one-electron reductions (Figure 6.6). In each case, the first two reductions are reversible, while the third is quasireversible. Fluorenylidene substitution provides for a much more facile first reduction, which occurs at −1.50 V for **3b** *versus* −1.97 V for the diphenylalkylidene counterpart **3a**. It is worth emphasizing that the difference in the first reduction potentials of **3a** and **3b** (0.47 V) is much greater than that of the individual alkylidene units, as revealed by the analysis of **5** (−2.03 V) and **12** (−1.82 V) (Table 6.1). Furthermore, there is surprisingly little difference between the redox behavior of radiaannulene **3a** and the radialene **2** (R = Ph), even though the former contains a longer linearly-conjugated segment as a result of the *ortho* fused benzene ring.

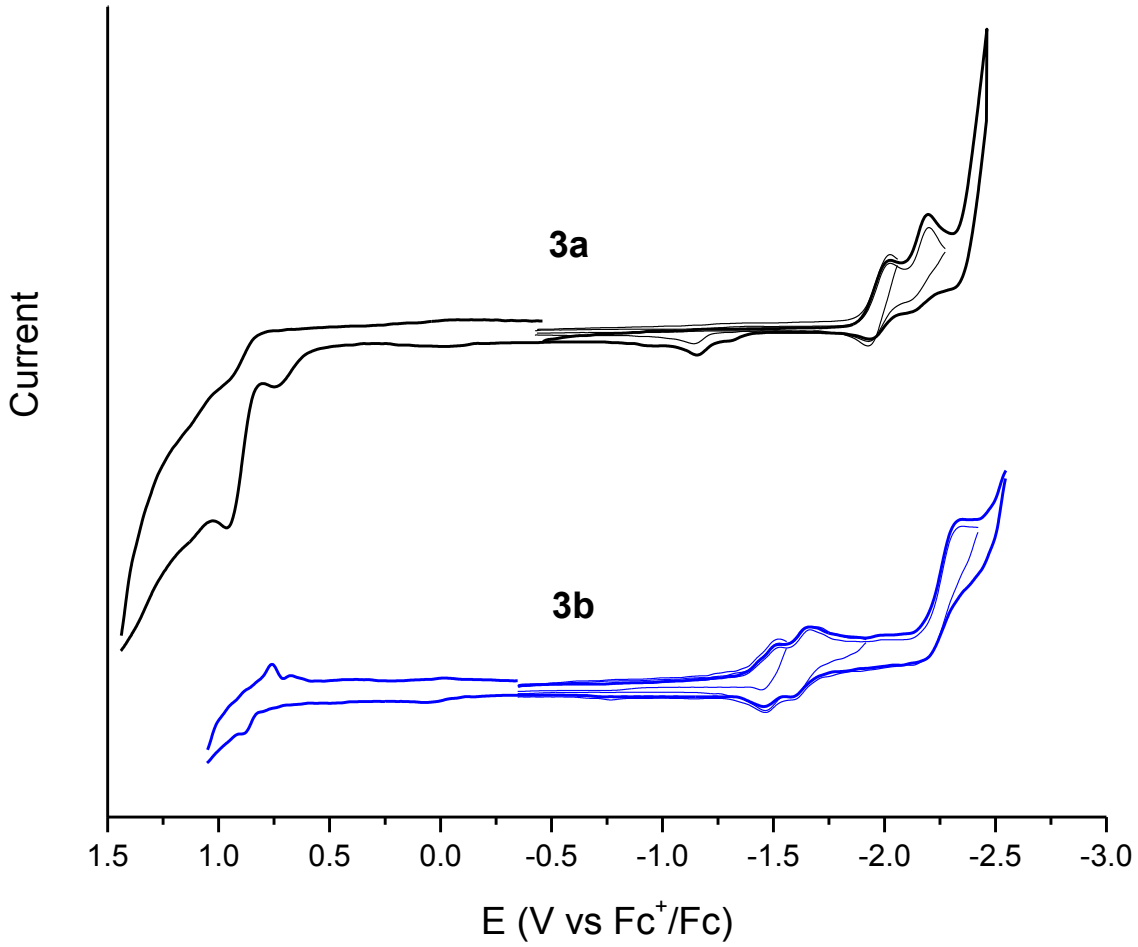


**Figure 6.5**. Cyclic voltammograms of compounds **3a** and **3b** obtained In *o*-DCB + 0.05 M $(nBu)_4NPF_6$ (scan rate 0.1 $Vs^{-1}$).

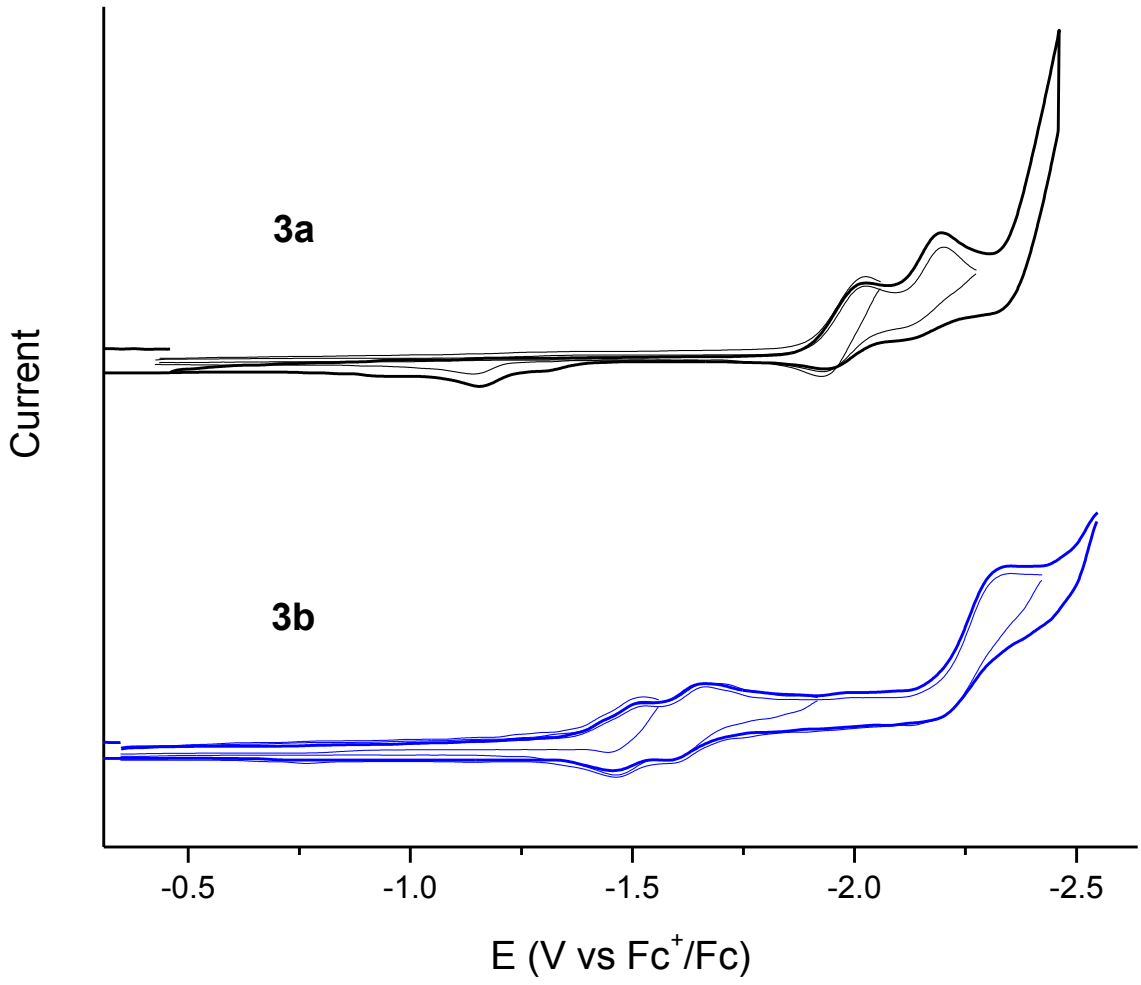


**Figure 6.6**. Cathodic section of the CV of compounds **3a** and **3b** obtained In *o*-DCB + 0.05 M $(nBu)_4NPF_6$ (scan rate 0.1 $Vs^{-1}$).

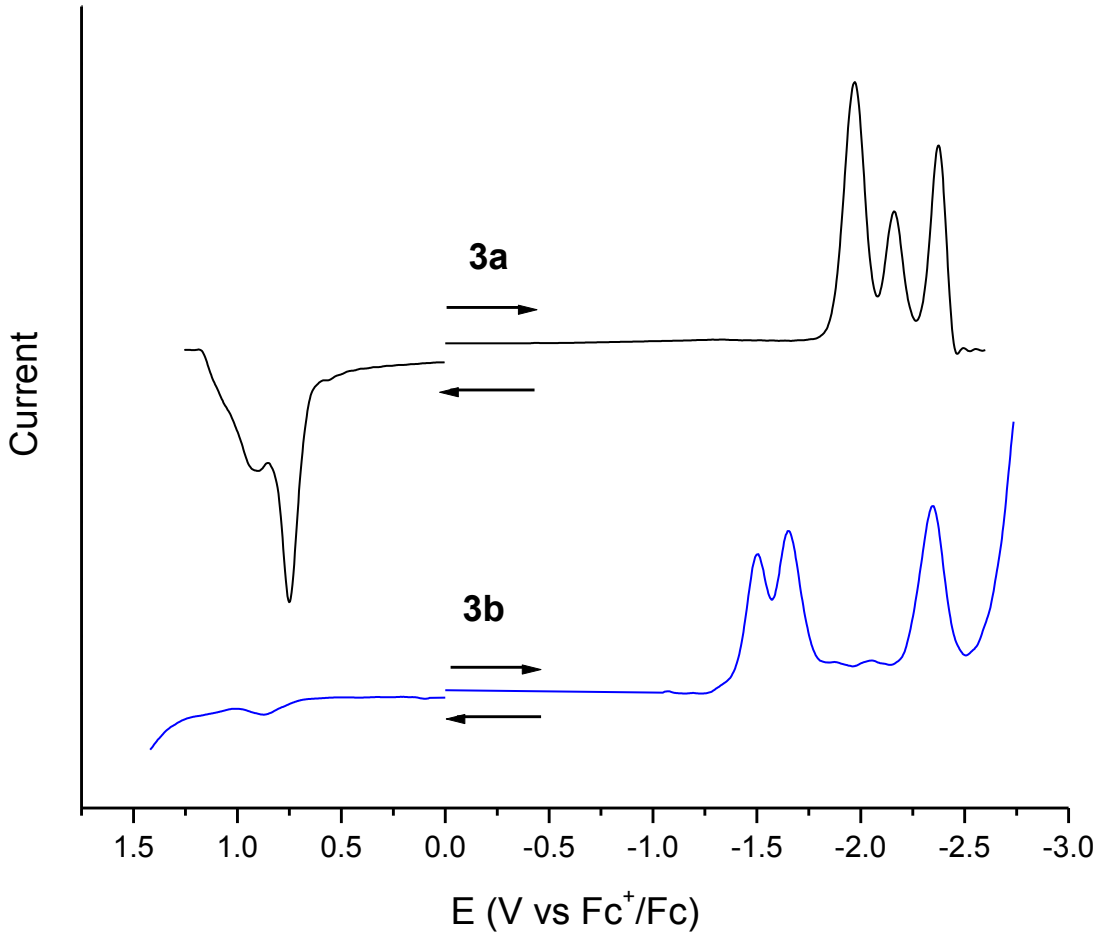


**Figure 6.7**. OSWV of radiaannulenes **3a** and **3b** obtained In *o*-DCB + 0.05 M $(nBu)_4NPF_6$ (scan rate 0.1 $Vs^{-1}$).

**Electrochemistry of radialenes and expanded radialenes**

During the past two decades, shape-persistent conjugated macrocycles with a broad spectrum of attributes and topologies have been synthesized. This includes macrocycles with remarkable electronic, optical, and supramolecular properties, as well as intriguing frameworks. The rigid, conjugated framework of macrocycles provides an outstanding means of examining the fundamental aspects of electronic coupling in

carbon-rich molecules. In this regard, cross–conjugated macrocycles, the expanded radialenes, have been synthesized, characterized, and studied by Tykwinski's group due to their potential applications in materials science and their unique optical, electronic, and structural properties.

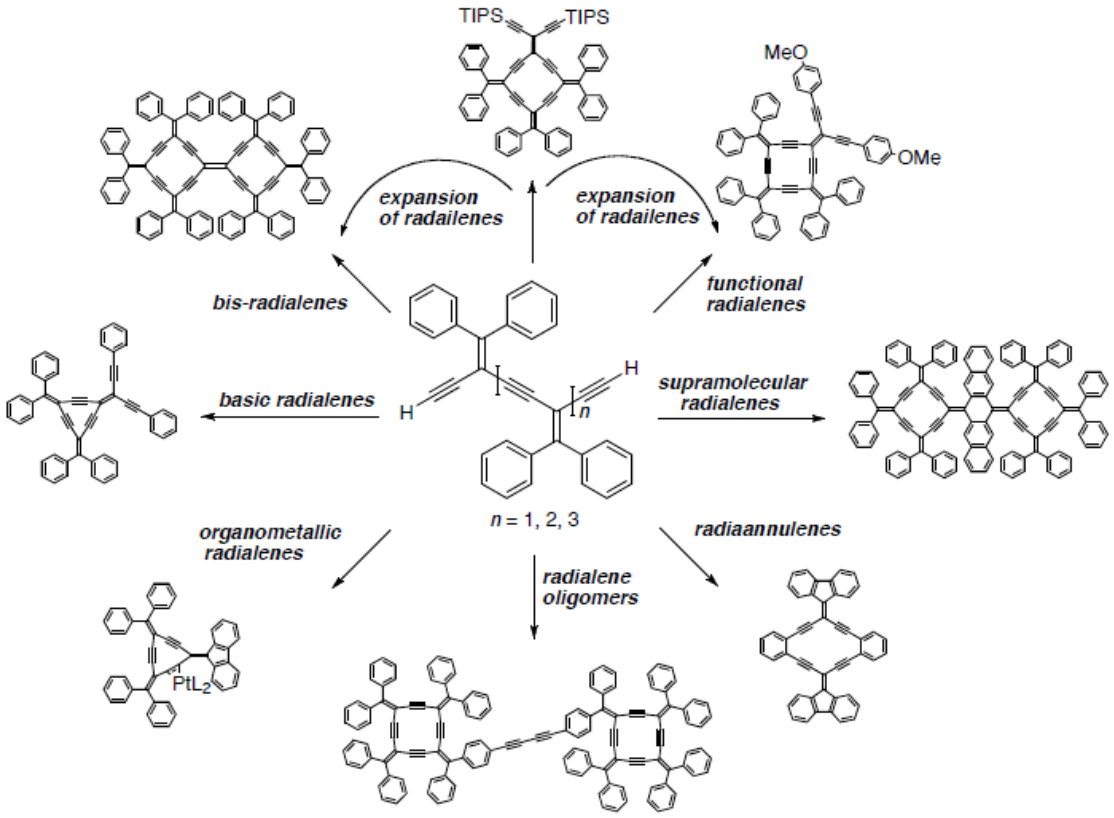


**Figure 6.8**. Representative expanded radialenes.

Tykwinski's synthetic strategy solidly establishes a divergent and versatile method for the synthesis of not only expanded radialenes, but also for unprecedented compounds that derive from this general sub-structure, including bis-radialenes, radiaannulenes, functionalized expanded radialenes, and larger derivatives of the

expanded radialenes. Two synthetic strategies were developed by this group. In the first strategy, the palladium-mediated cross coupling reaction of an *iso*–polydiacetylene with a dibromoolefin or tetrabromoolefin affords a series of the expanded radialenes and related derivatives.[2] In the second strategy, the synthesized radialenes that carry a silylacetylene can be desilylated and then employed in palladium cross-coupling or oxidative coupling reactions to provide interesting carbon-rich skeletons (Figure 6.8).

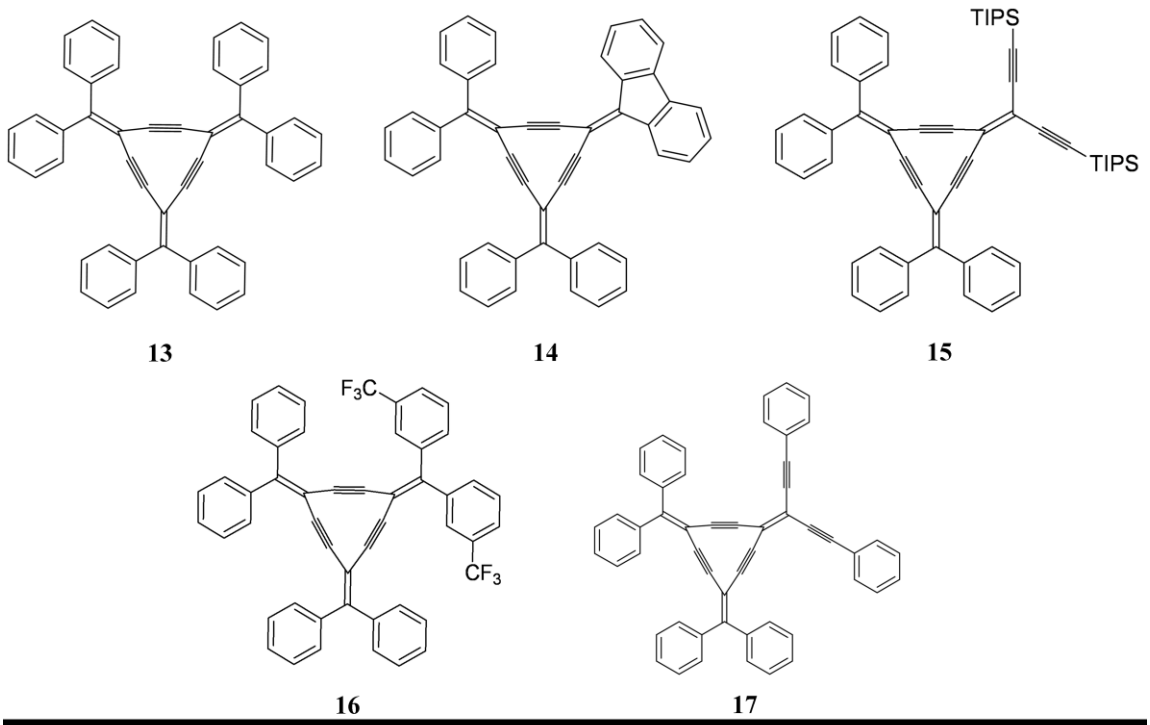


**Figure 6.9**. Structures of different [3] radialenes. Compounds **13**-**17**.

Figure 6.9 shows the chemical structures of compounds **13**-**17**. This family of [3] radialenes exhibits in general similar electrochemical behavior with two one-electron oxidative steps and three one-electron reductive steps (Figures 6.10 and 6.11). The first

cathodic process is reversible except for **16** which presents irreversible cathodic processes. The first oxidative steps are reversible for compounds **13**-**15** while irreversible for **16** and compound **17**. The latter exhibits the lowest HOMO-LUMO gap (2.34 V) among all these five compounds, due to its very low first reduction potential (-1.42 V) followed by four more reductive steps that overlap each other. Surprisingly the two $CF_3$ substituents in **16** do not seem to shift the reduction potentials anodically.

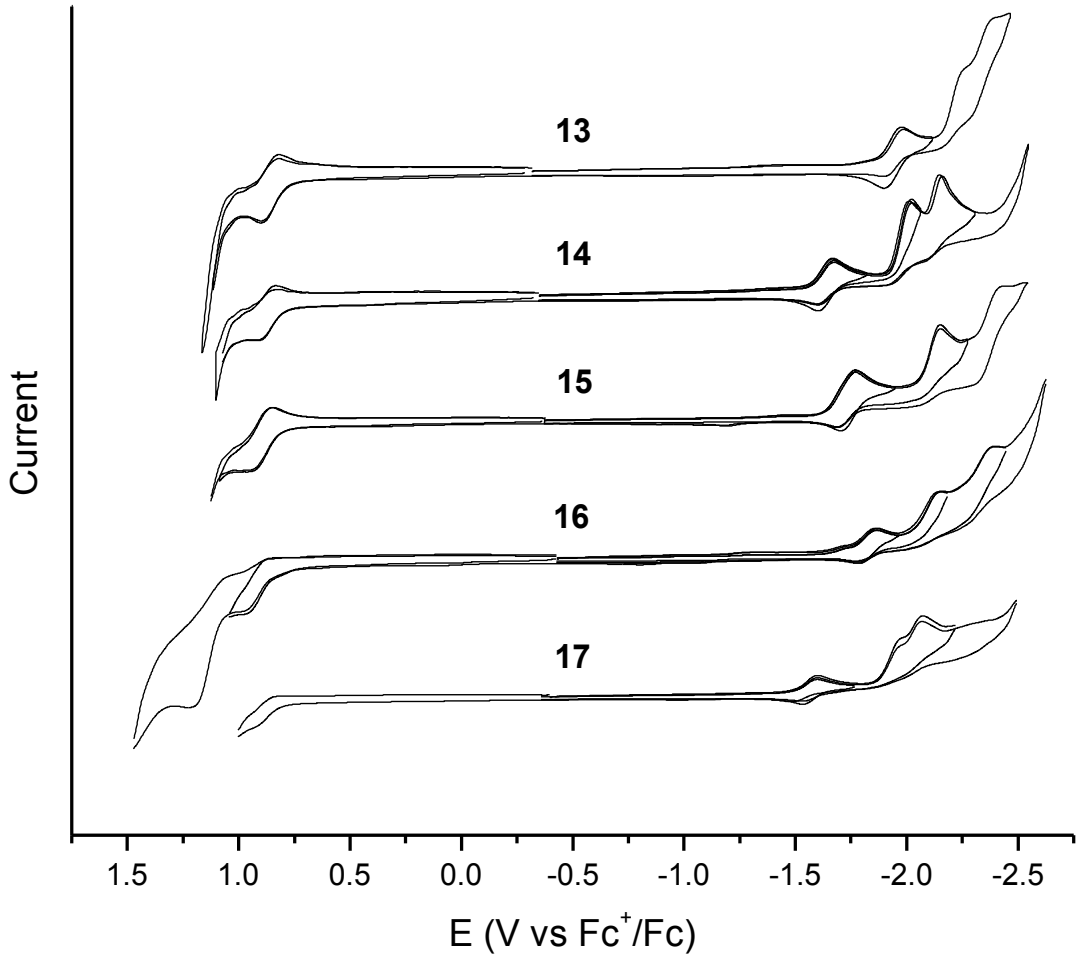


**Figure 6.10**. Cyclic Voltammetry (CV) of compounds **13**-**17** (scan rate 0.1 Vs-1).

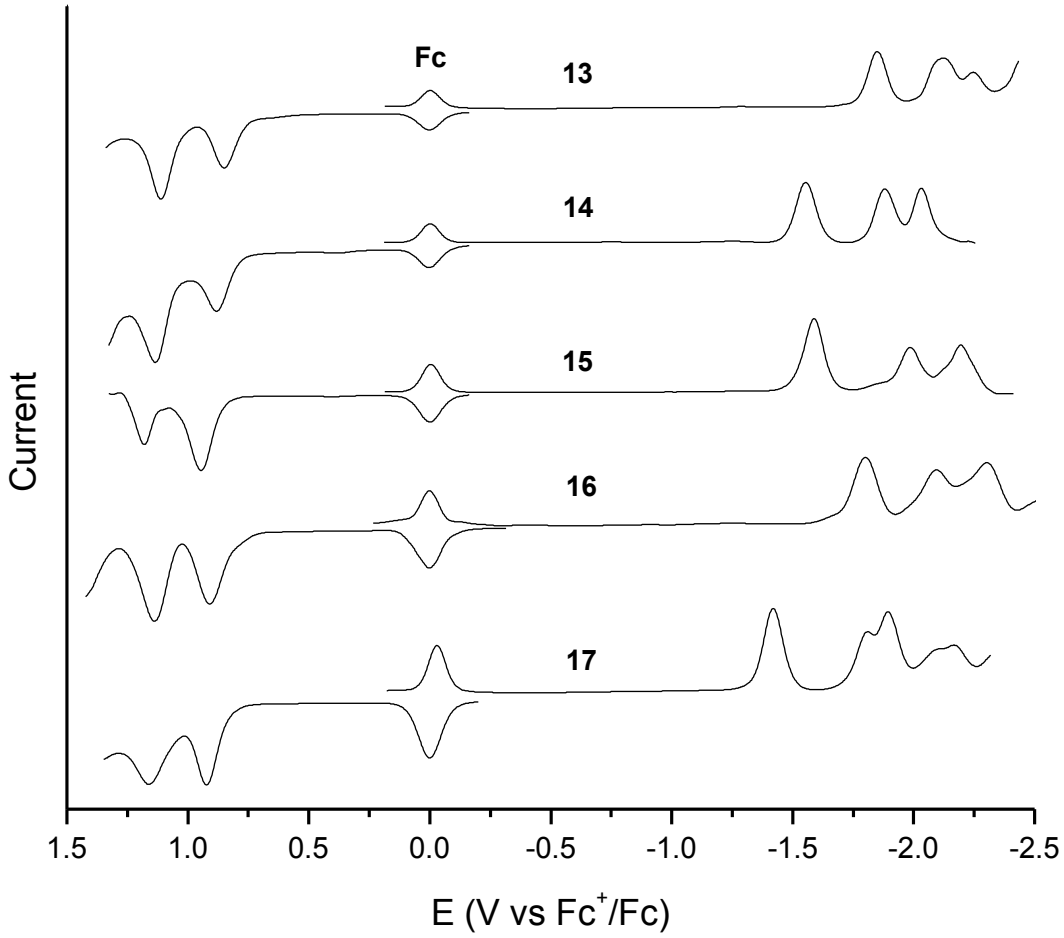


**Figure 6.11**. Osteryoung Square Wave Voltammetry (OSWV) of compounds **13**-**17** (scan rate 0.1 $V.s^{-1}$).

Figure 6.12 shows the structures of expanded radialenes **18**-**20**. These compounds exhibit in general three one-electron reductive processes, the first reduction is reversible for all of them (Figure 6.13 and 6.14). The OSWVs of **18** and **20** show three anodic steps while **19** exhibits a multielectronic oxidative step at 0.92 V. It is interesting to note that despite the well known electron donor properties of the silyl grops these three compounds

exhibit an enhanced reductive ability. Unexpectedly **20** exhibits a first reductive step at a very low potential (-1.61 V).

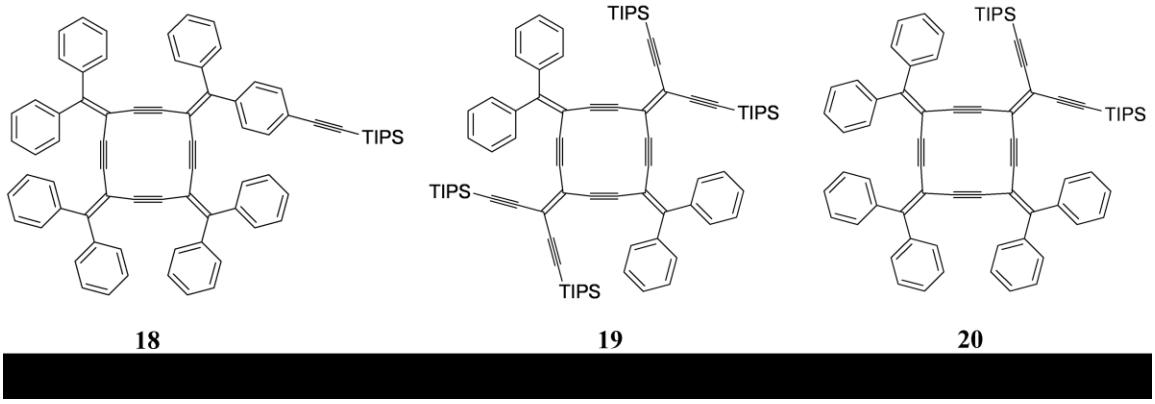


**Figure 6.12**. Structures of different expanded [4] radialenes. Compounds **18**-**20**.

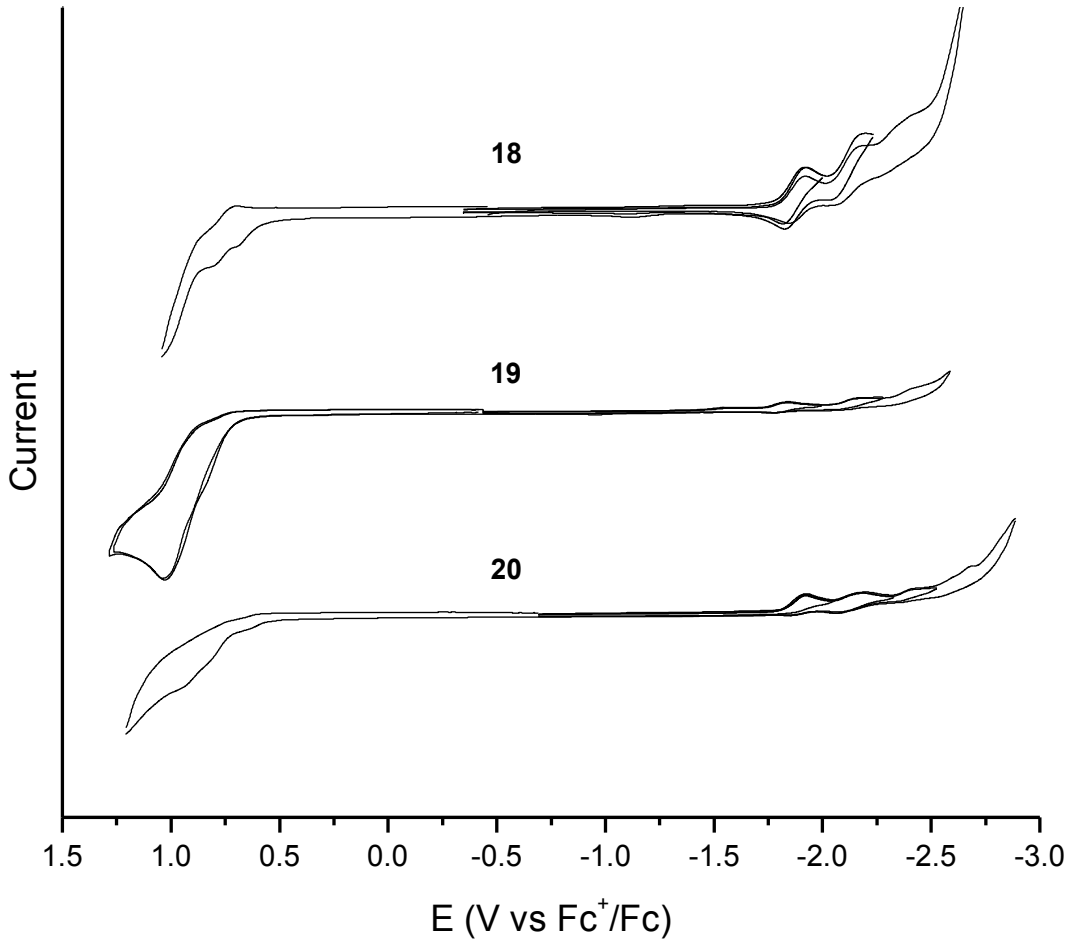


**Figure 6.13**. Cyclic Voltammetry (CV) of compounds **18**-**20** (scan rate 0.1 $Vs^{-1}$).

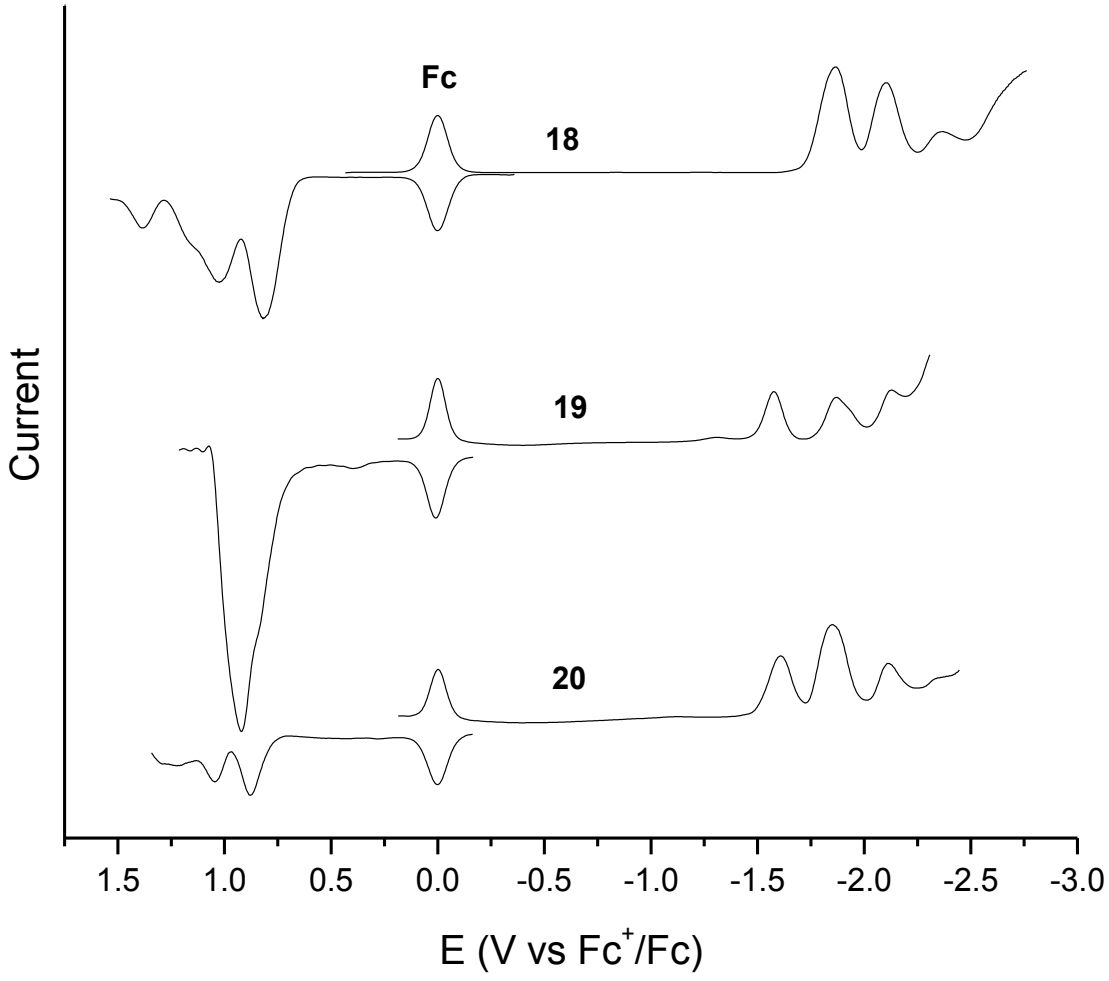


**Figure 6.14**. Osteryoung Square Wave Voltammetry (OSWV) of compounds **18**-**20** (scan rate 0.1 $Vs^{-1}$).

The redox properties of compounds **21-25** (Figure 6.15) can be classified in two groups. The first group with compounds **21-23**, where the reductive and oxidative ability is notably increased going from **21** to **23**, the latter exhibits three reversible one-electron reductions (Figure 6.16).

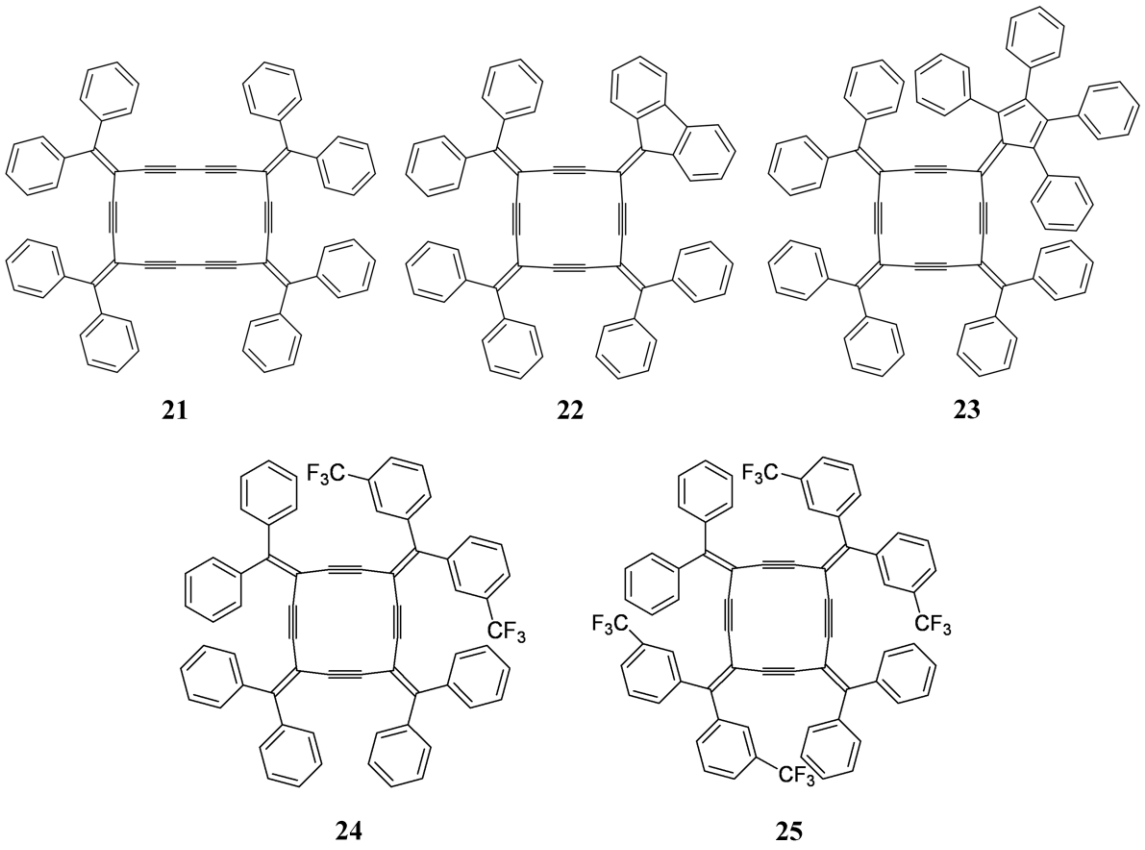


**Figure 6.15**. Structures of compounds **21**-**25**.

By OSWV two oxidation steps were observed and as noted from the CV the first one is reversible (Figure 6.17). Apparently the TPCPC group brings higher reductive-oxidative ability to the radialene framework, most likely because the five membered ring becomes aromatic after ionization. Therefore, it would be interesting to observe the redox potentials of extended radialenes with more than one TPCPC groups. On the other hand, **24** and **25** exhibit similar HOMO-LUMO gaps with a first reduction around -1.80 V, and in the case of **25** it is reversible.

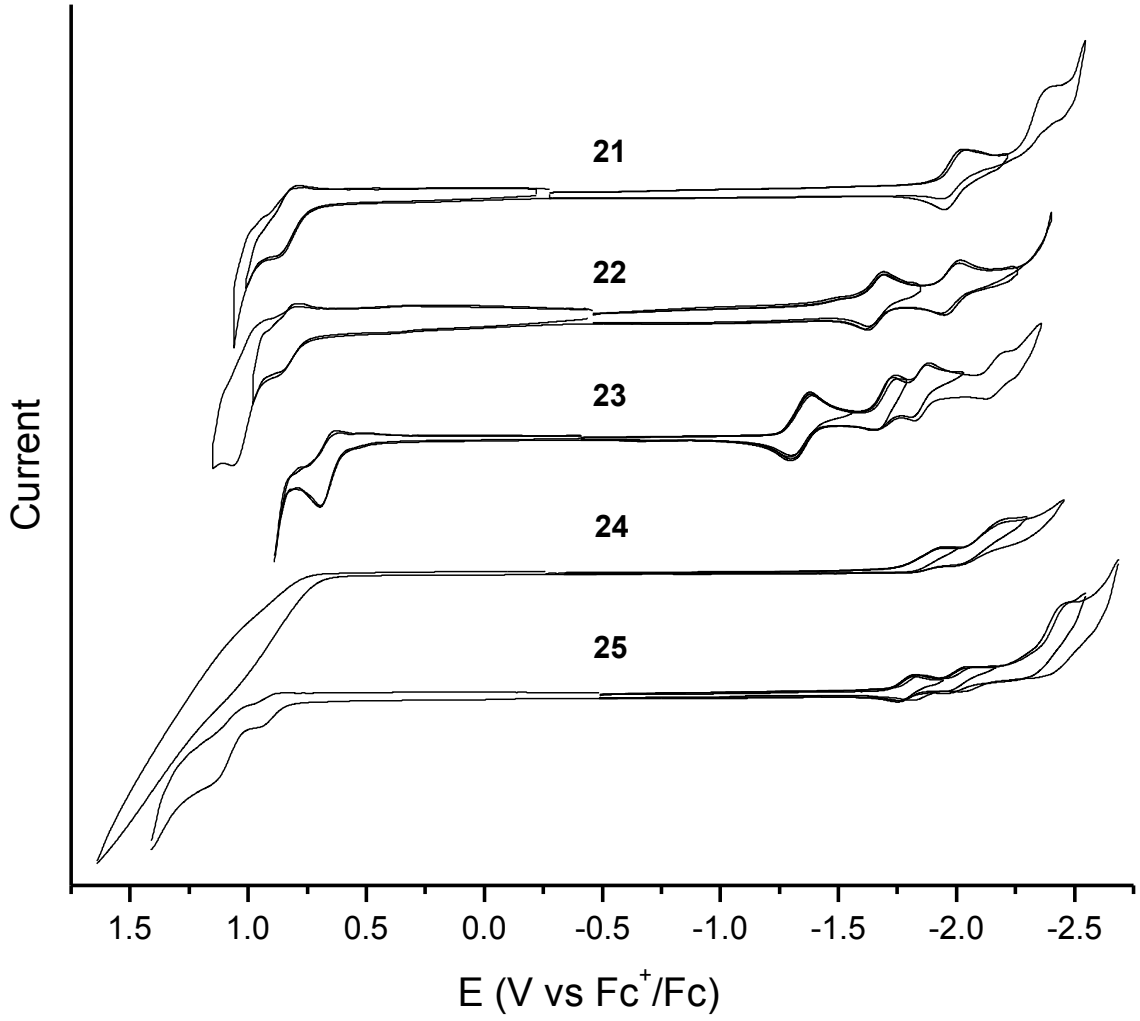


**Figure 6.16**. Cyclic Voltammetry (CV) of compounds **21**-**25** (scan rate 0.1 $Vs^{-1}$).

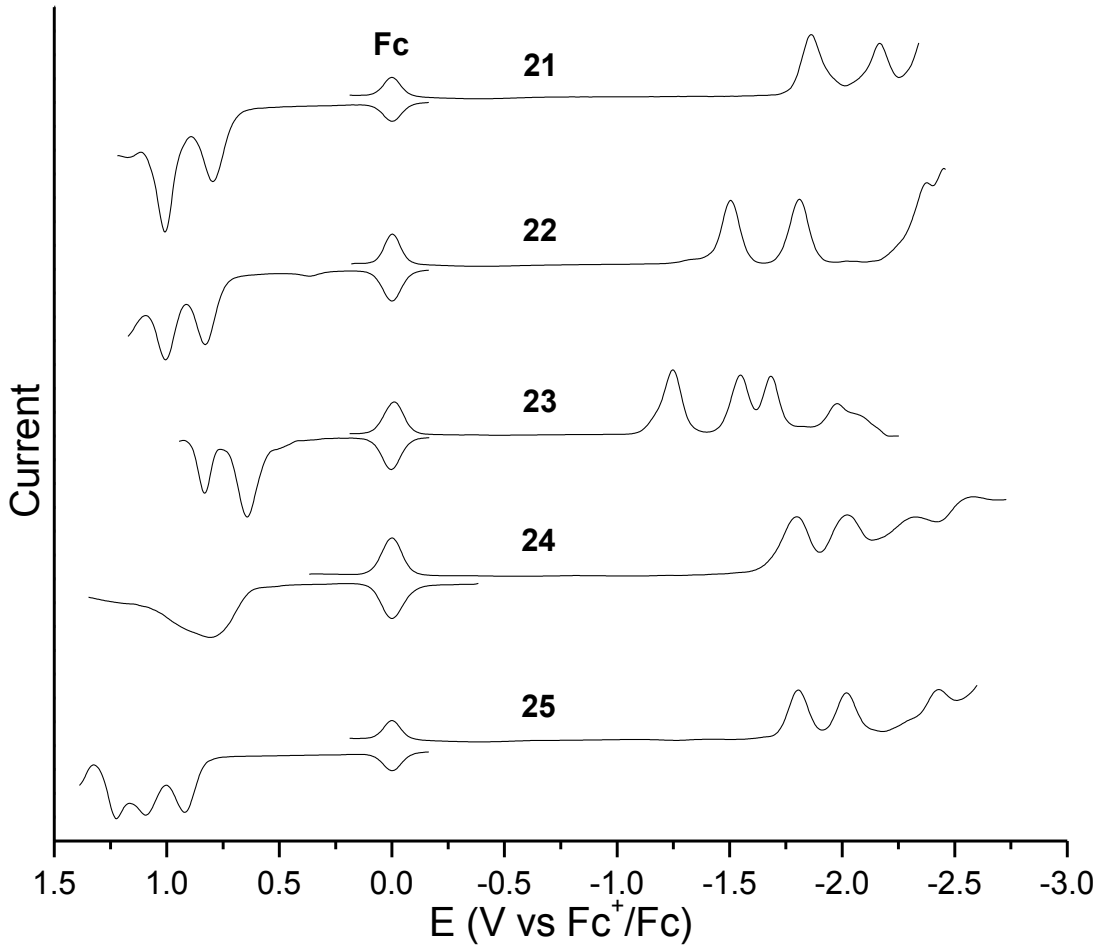


**Figure 6.17**. Osteryoung Square Wave Voltammetry (OSWV) of compounds **21**-**25** (scan rate 0.1 $Vs^{-1}$).

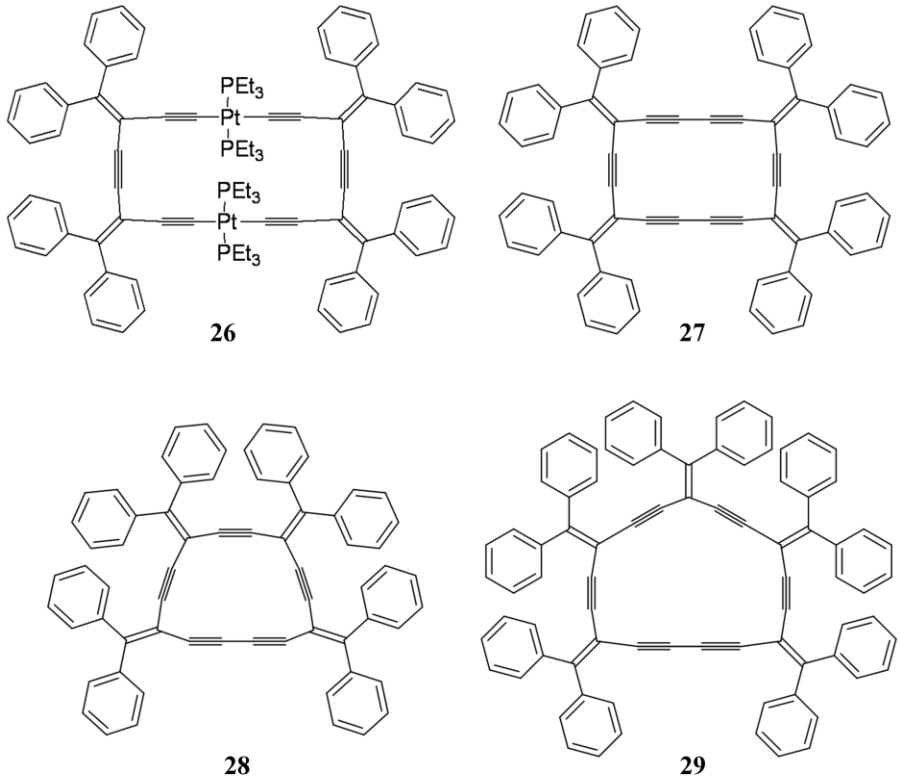


**Figure 6.18**. Structures of compounds **26**, **27**, **28**, and **29**.

Figure 6.18 shows the structure of compounds **26**, **27**, **28** and **29**. These compounds are expanded radialenes with different spacers, in the case of compounds **27**, **28** and **29** the spacers are acetylene units whereas for compound **26** the spacer contains a platinum metal. Surprisingly compound **26** does not exhibit any reduction steps within the solvent window but exhibits a very low first reversible oxidation step at 0.37 V with a second oxidation at 0.56 V and a third one at 0.82 V. The framework of the radialene does not seem to affect considerably the redox potentials of the compound as is observed for compounds **27**, **28** and **29** where these radialenes exhibit similar reductive and oxidative steps with HOMO-LUMO gaps around 2.62 V.

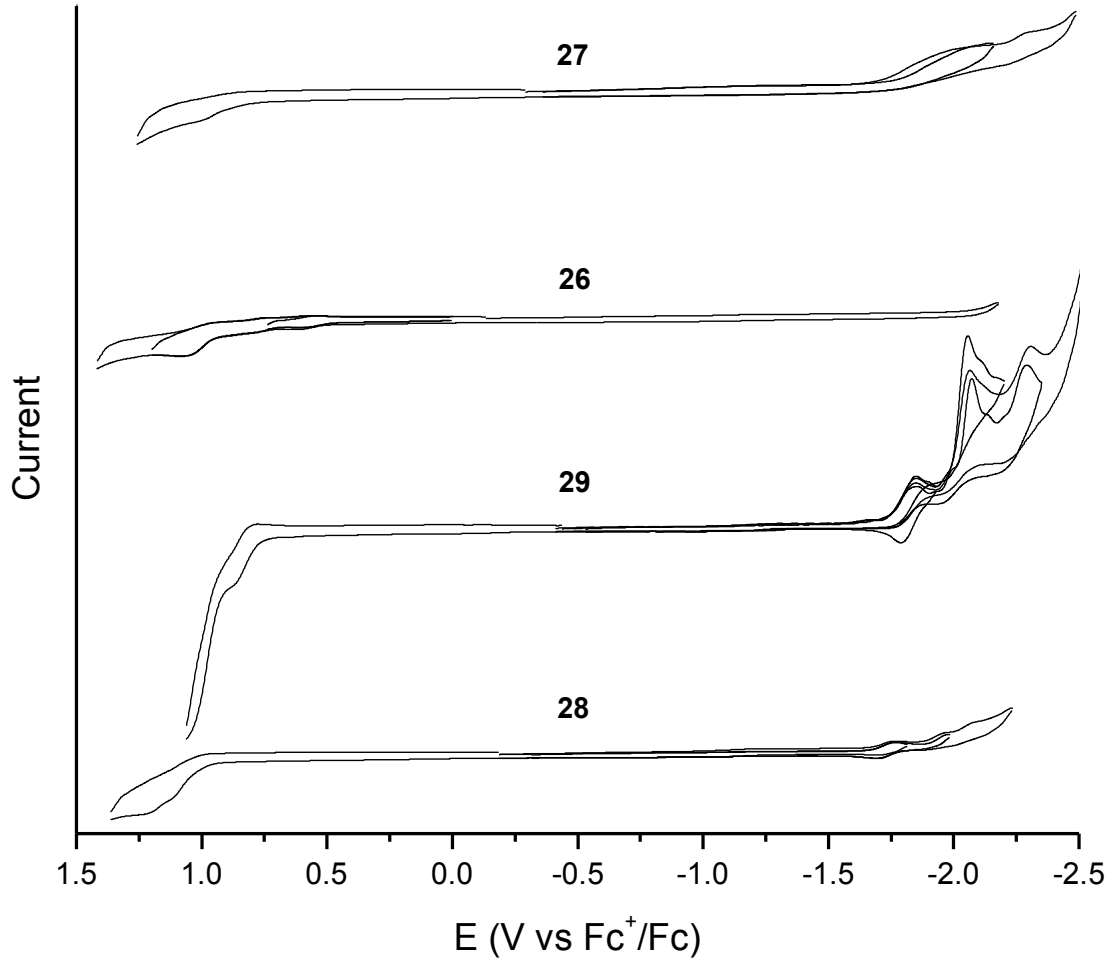


**Figure 6.19**. Cyclic Voltammetry (CV) of compounds **26-29** (scan rate 0.1 $Vs^{-1}$).

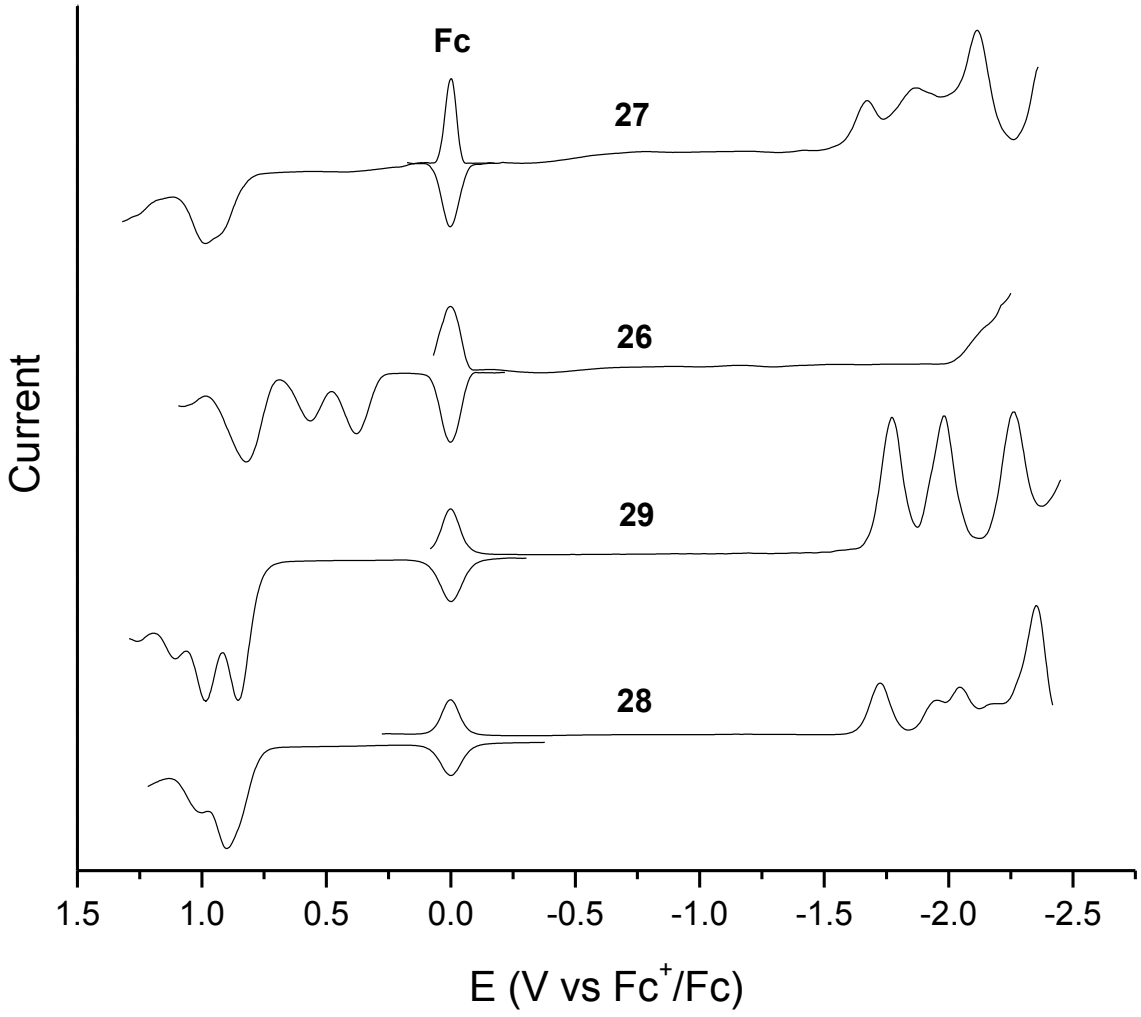


**Figure 6.20**. Osteryoung Square Wave Voltammetry (OSWV) of compounds **26**-**29** (scan rate 0.1 $Vs^{-1}$).

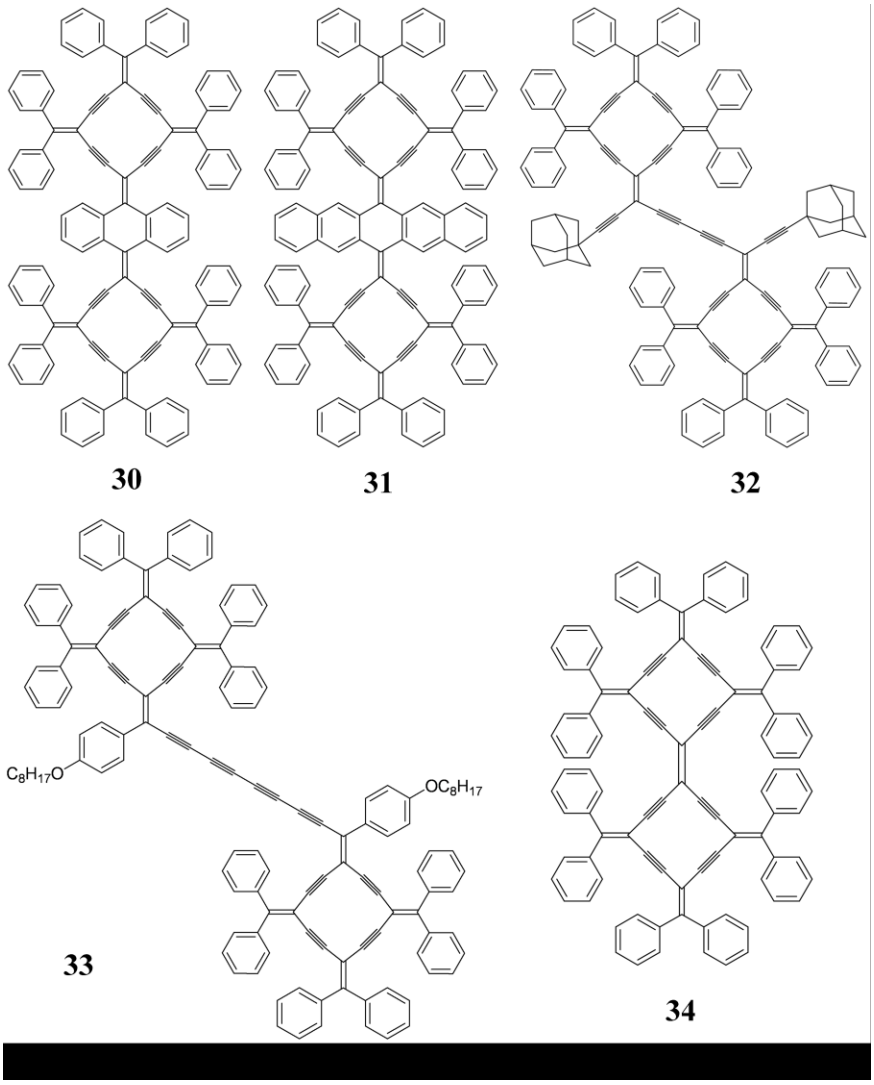


**Figure 6.21**. Structures of compounds **30-34**.

The last series of compounds (Figure 6.21) shows a similar electrochemical behavior (Figure 6.22). In the case of **32** OSWV (Figure 6.23) shows that the first two reductive steps are processes where two electrons go to the same molecular orbital (LUMO) while the third and fourth reductive steps are processes in which two electrons

occupy the same LUMO+1 orbital. In all these compounds the first reduction is reversible and the first oxidation irreversible.

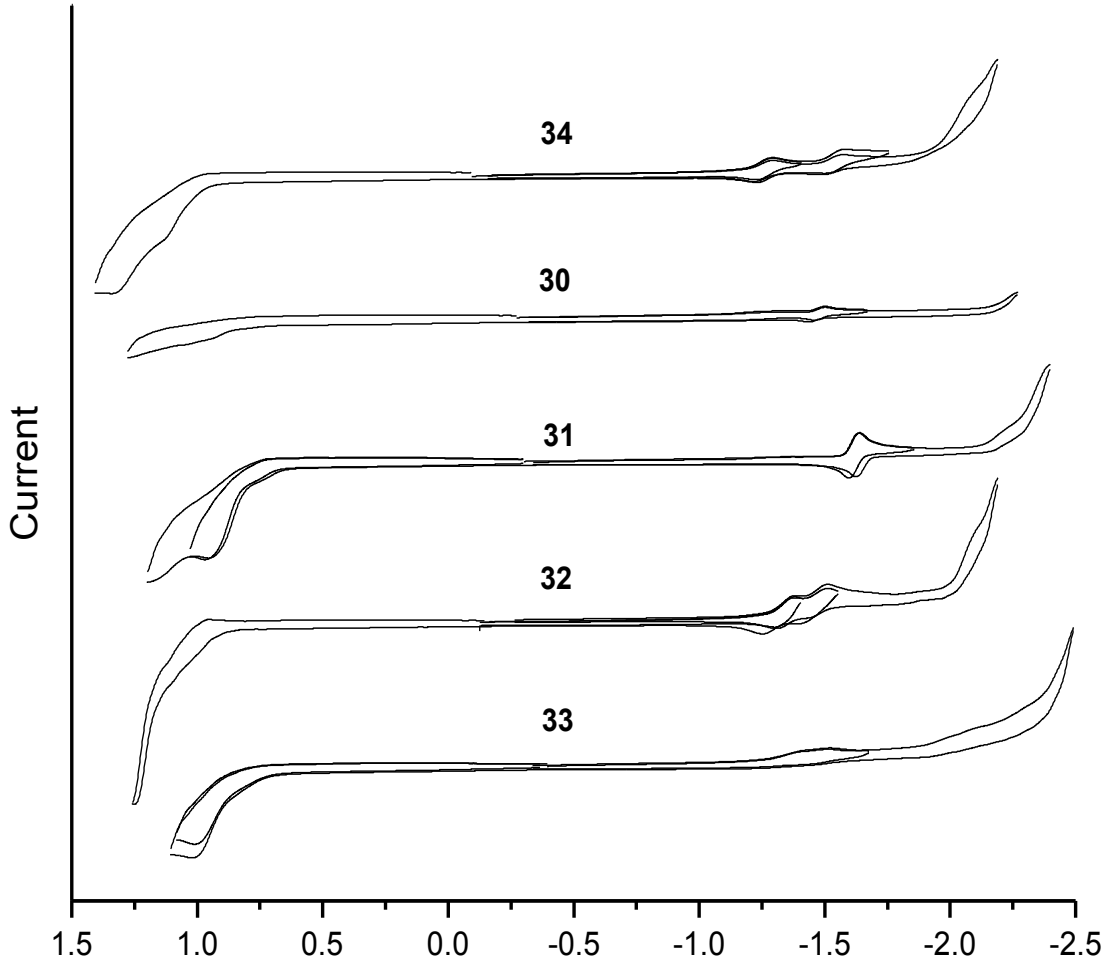


**Figure 6.22**. Cyclic Voltammetry (CV) of compounds **30-34** (scan rate 0.1 $Vs^{-1}$).

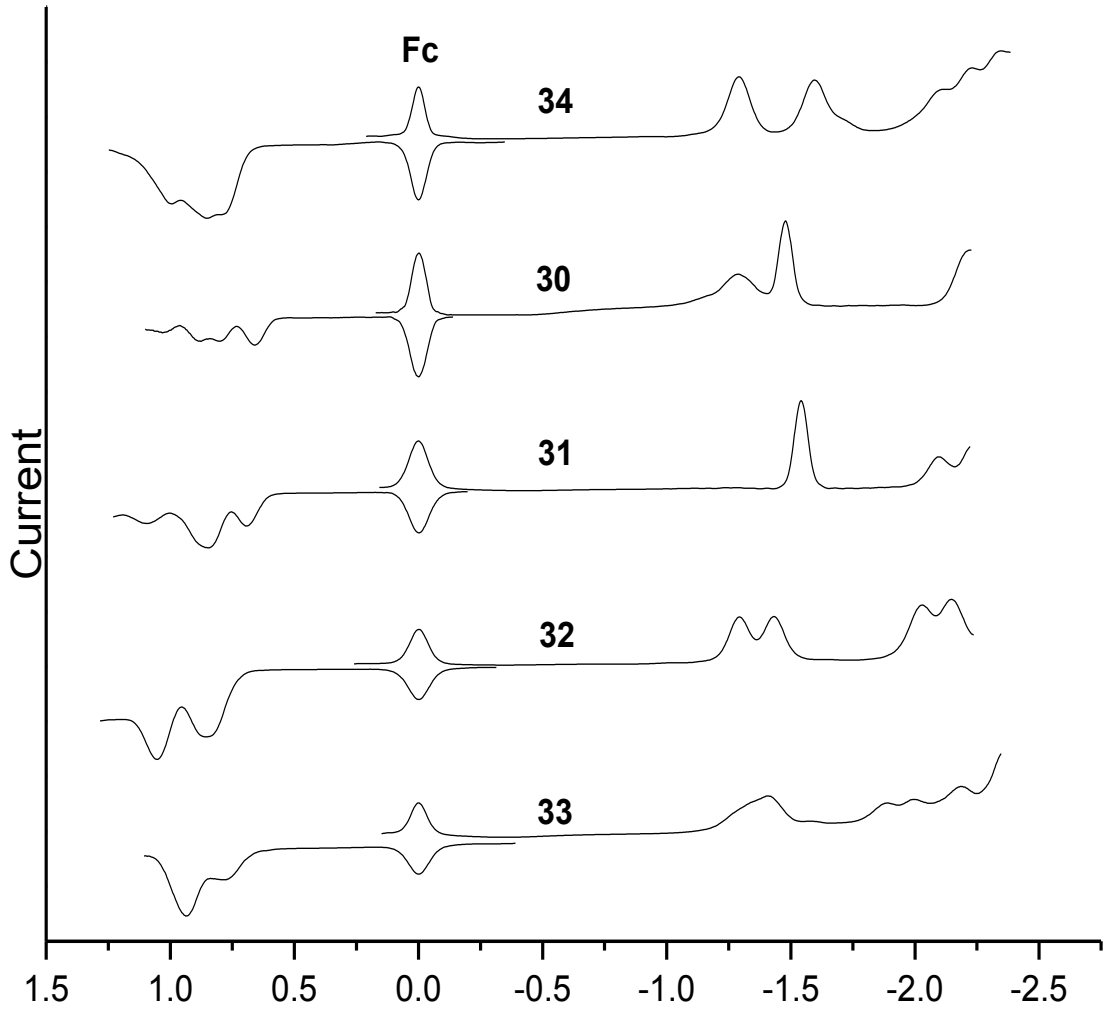


**Figure 6.23**. Osteryoung Square Wave Voltammetry (OSWV) of compounds **30**-**34** (scan rate 0.1 $Vs^{-1}$).

Table 6.2 summarizes the electrochemical potentials of the compounds studied in this Chapter.

**Table 6.2**. Redox potentials for the macrocycles studied in this Chapter.

| Compound | $E_p$, $ox_1$ | $E_{1/2}$, $ox_1$ | $E_p$, $ox_2$ | $E_p$, $red_1$ | $E_{1/2}$, $red_1$ | $E_p$, $red_2$ | $E_{1/2}$, $red_2$ | $E_p$, $red_3$ | $E_p$, $red_4$ | $\Delta E_{gap}$ [V] |
|---|---|---|---|---|---|---|---|---|---|---|
| 13 | | 0.82 | 1.11 | | -1.9 | -2.12 | | -2.25 | | 2.72 |
| 14 | | 0.88 | 1.13 | | -1.55 | -1.88 | | -2.03 | | 2.43 |
| 15 | | 0.94 | 1.19 | | -1.59 | -1.98 | | -2.2 | | 2.53 |
| 16 | 1.08 | | | -2.15 | | -2.28 | | -2.45 | | 3.23 |
| 17 | 0.92 | | 1.16 | | -1.42 | -1.8 | | -1.89 | | 2.34 |
| 18 | 0.81 | | 1.03 | | -1.87 | -2.19 | | | | 2.68 |
| 19 | | 0.92 | | | -1.58 | -1.88 | | | | 2.5 |
| 20 | 0.95 | | | | -1.61 | | -1.85 | -2.11 | | 2.56 |
| 21 | | 0.81 | 1.01 | | -1.9 | -2.16 | | | | 2.71 |
| 22 | | 0.83 | 1.01 | | -1.51 | | -1.81 | -2.37 | | 2.34 |
| 23 | 0.65 | | 0.83 | | -1.26 | | -1.54 | -1.69 | | 1.91 |
| 24 | 0.79 | | | -1.79 | | -2.02 | | | | 2.58 |
| 25 | 0.93 | | 1.14 | | -1.80 | | -2.01 | -2.42 | | 2.73 |
| 27 | 0.96 | | | -1.67 | | -1.86 | | -2.11 | | 2.63 |
| 26 | | 0.37 | 0.56 | | | | | | | |
| 29 | 0.85 | | 0.98 | | -1.77 | | -1.98 | -2.26 | | 2.62 |
| 28 | 0.89 | | | | -1.72 | -1.94 | | -2.04 | -2.35 | 2.61 |
| 34 | 0.78 | | 0.86 | | -1.29 | | -1.59 | | | 2.07 |
| 30 | 0.66 | | 0.8 | | -1.48 | | | | | 2.14 |
| 31 | 0.69 | | 0.85 | | -1.54 | -2.09 | | | | 2.23 |
| 32 | 0.85 | | 1.05 | | -1.29 | | -1.43 | -2.03 | -2.14 | 2.14 |
| 33 | 0.77 | | 0.93 | | -1.4 | -1.88 | | -1.99 | -2.19 | 2.17 |

**Final remarks on the electrochemical properties of carbon rich macrocycles**

In general the studied macrocycles exhibit at least two oxidative events which are shifted depending on the electronic properties of the respective addend. For instance, compound **26** exhibits three one-electron oxidation steps occurring at very low potentials (0.37, 0.56 and 0.84 V respectively) as a consequence of the metallic nature of the incorporated spacer in the macrocycle framework.

It is interesting to note that addends containing a five member ring core can lower the first reduction step of the respective macrocycle. For instance, for compounds **13**, **22** and **23** the first reductive process is shifted anodically. Among these three compounds, **23** exhibits a very interesting electrochemistry with up to four reductive steps and two oxidation processes. The first reduction occurs at -1.26 V, the lowest value within the whole series of macrocycles studied here and the first oxidation occurs at 0.65 V. These features make compound **23** a very good candidate for many applications due to its versatile electrochemistry. It would be very interesting in the future to explore the electrochemistry of compounds with more than one TPCPC groups in the macrocycle framework. In order to understand better the electronic properties of these compounds, additional characterization should include EPR experiments along with calculations which can give insight on the localization of the molecular orbital distribution.

## References


[1] Kroto,H.W.; Heath,J.R.; O'Brien,S.C.; Curl, R.F.; Smalley, R.E. *Nature* **1985**, 318, 162.

[2] Gholami, M.; Tykwinski, R.R. *Chem. Rev*. **2006**, 106, 4997-5027.

[3] a) Meier, H. *Angew.Chem.,Int.Ed.***2005**, 44, 2482.;b) Martin, R. E.; Diederich, F. *Angew.Chem.Int.Ed.***1999**, 38, 1350.

[4] Gholami, M.; Chaur, M.N.; Wilde, M.; Ferguson, M.J.; McDonald, R.; Echegoyen, L.; Tykwinski, R.R. *Chem. Commun*. **2009**, 21, 3038-3040.


.

CHAPTER SEVEN

# FUTURE DIRECTIONS IN THE FIELD OF METALLOFULLERENES

As described in this dissertation, EMFs are fullerenes that encapsulate metals in their interior; therefore these types of compounds combine the metallic properties of the incarcerated moiety with those of the carbon fullerene host. The interaction between the metallic cluster and the carbon cage is mostly ionic since there is an electron transfer from the encapsulated moiety to the carbon cage and this electron transfer accounts for their stability and most of their electronic properties. To date, several types of EMFs have been synthesized, which include single and multiple metals (classical EMFs), metal carbides, trimetallic nitrides and metal oxide EMFs.[1] Of all of these families the metallic nitride is the largest one. Metals from group III and lanthanides have been found to form metallic nitride EMFs thus offering a broad variety of properties of potential use in different fields. One of the most interesting properties of EMFs is the strong interaction between the entrapped metal(s) and the carbon cage, which provides the main driving force for the formation of carbon cages that have never been isolated independently. For instance, many violations of the IPR rule have been reported for EMFs but not for empty fullerenes and $I_h$-$C_{80}$ easily forms with a wide variety of the metallic nitrides inside but has not been isolated independently.

Chemical functionalization has also revealed that EMFs are chemically different from empty cages. It seems that the metallic cluster has a considerable influence on the carbon cage, making certain bonds more reactive towards some reactions.[1] However, the low yields of some EMFs and the difficulty of isolating and purifying mono and bis-

adducts have restrained progress in this field. On the other hand, functionalized and non-functionalized EMFs feature interesting electrochemical properties that expand the number of possible applications of these compounds.

Even though there are many significant contributions in the field of EMF research, there are still many questions that need to be addressed in the near future such as the influence of the metal on the carbon cage, what are the rules of stabilization of non-IPR EMFs, which other types of endohedral confinement are possible, how to selectively control the synthesis of EMFs and how to increase their yields as well as finding non-HPLC purification methods. Clearly the EMF field remains as a fascinating, challenging and still largely unexplored arena with multiple potential applications and many directions to be addressed.

As a final part of this dissertation the question about the possibility of having other endohedral entities is addressed as well as future applications of these compounds. As described earlier, metallic nitride EMFs are compounds with general formula $M_3N@C_{2n}$, where M is a metal and 2n corresponds to the given fullerene cage. In these compounds the nitrogen atom plays the role of central atom connecting the three metals, but in principle other central atoms could be used, and phosphorous would be the most obvious replacement.

Though phosphorus is directly below nitrogen in Group 15 of the periodic table because of its similar electronic configuration, its chemical behavior is quite different. For example, while the largest number of ligands that nitrogen can bind is 3, phosphorus can also be found in the 4+ and 5+ oxidation states. Metal-phosphorus bonds are

considerably longer than metal-nitrogen bonds due to the larger van der Waals radius and smaller electronegativity of phosphorus. Simply replacing a nitrogen source with a phosphorus source during endohedral fullerene synthesis is not straightforward. The phosphorous analogue of ammonia, $PH_3$, phosphine, is not just toxic like ammonia, it is a deadly poison. Therefore, extending the reactive gas synthetic method is not easily feasible. Alternative sources of phosphorus such as solid state phosphorus containing compounds are in general very unstable towards high temperatures. On the other hand, sulfur appears as an interesting alternative not only because it can bind to a larger number of ligands than nitrogen but also because there are sources of sulfur containing gases that can be adapted to the reactive gas atmosphere method for the production of EMFs.

With this in mind, attempts to synthesize sulfur containing EMFs where done. Core drilled graphite rods were packed with scandium oxide and graphite powder in a weight ratio of 1:3. The rods were then annealed at 1000 $^{o}$C for 12 hours. The annealed rods were finally arc-burned under an atmosphere of helium and sulfur dioxide (200 torr and 20 torr respectively).

The resulting carbon soot was placed in a Soxhlet extractor apparatus. Using toluene as a solvent the EMFs were extracted for 24 hours. Preliminary mass spectrometry results showed the presence of considerably large amounts of empty fullerenes. These empty fullerenes were removed by passing the extracted fullerenes throughout a column containing a cyclopentadiene-functionalized resin as described by Dorn and co-workers.[2] In this method, a stationary phase composed of a cyclopentadiene-functionalized resin undergoes Diels-Alder reactions with the fullerenes

as they are eluted through the column. Since empty fullerenes and classical EMFs are more reactive than the metallic nitride EMFs, they are retained longer in the column. Therefore the metallic nitride EMFs are eluted first. In our case we were expecting to elute only those EMFs containing sulfur.

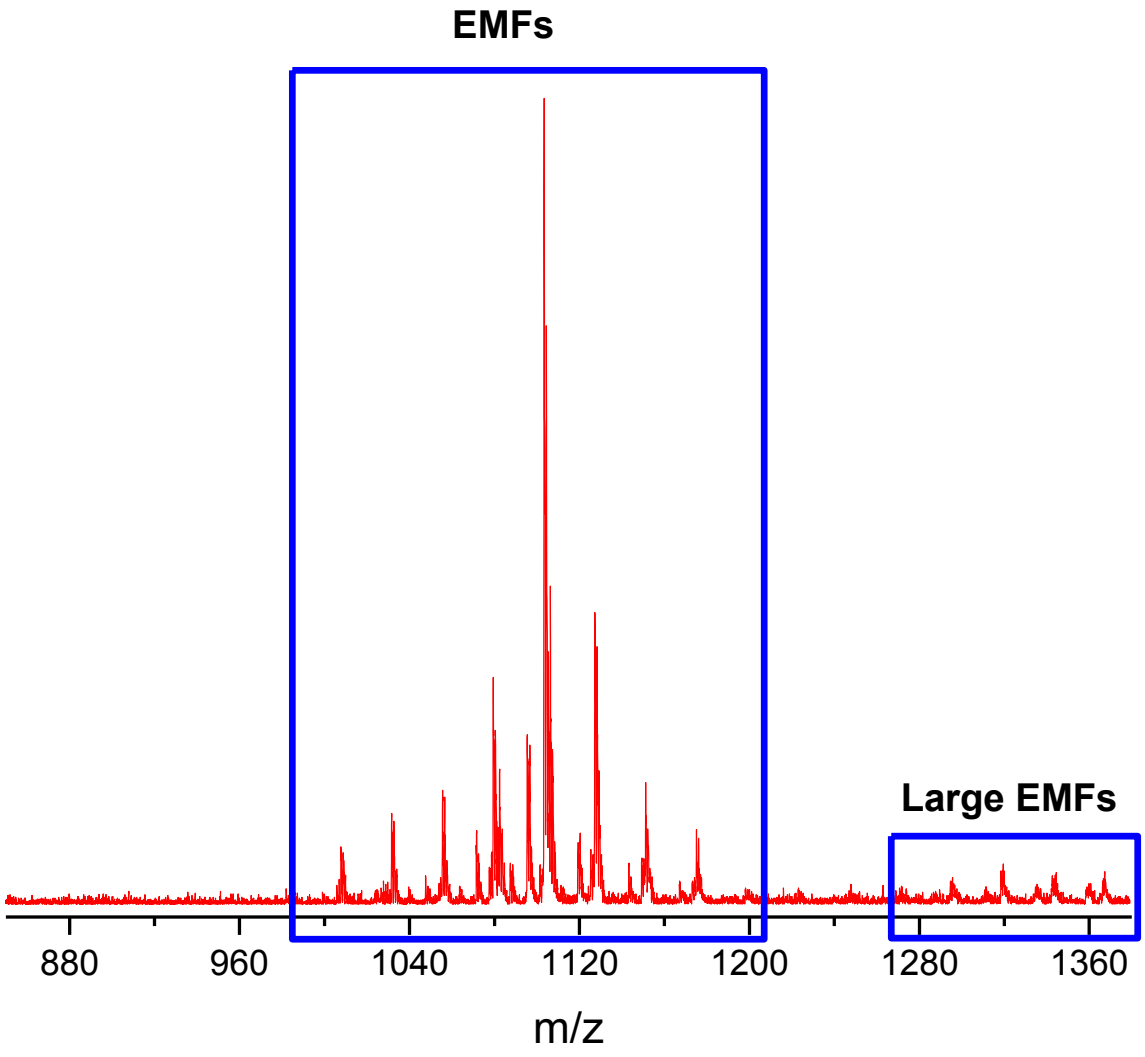


**Figure 7.1**. MALDI-TOF mass spectrum of the extracted fullerenes during the sulfur containing gas experiment.

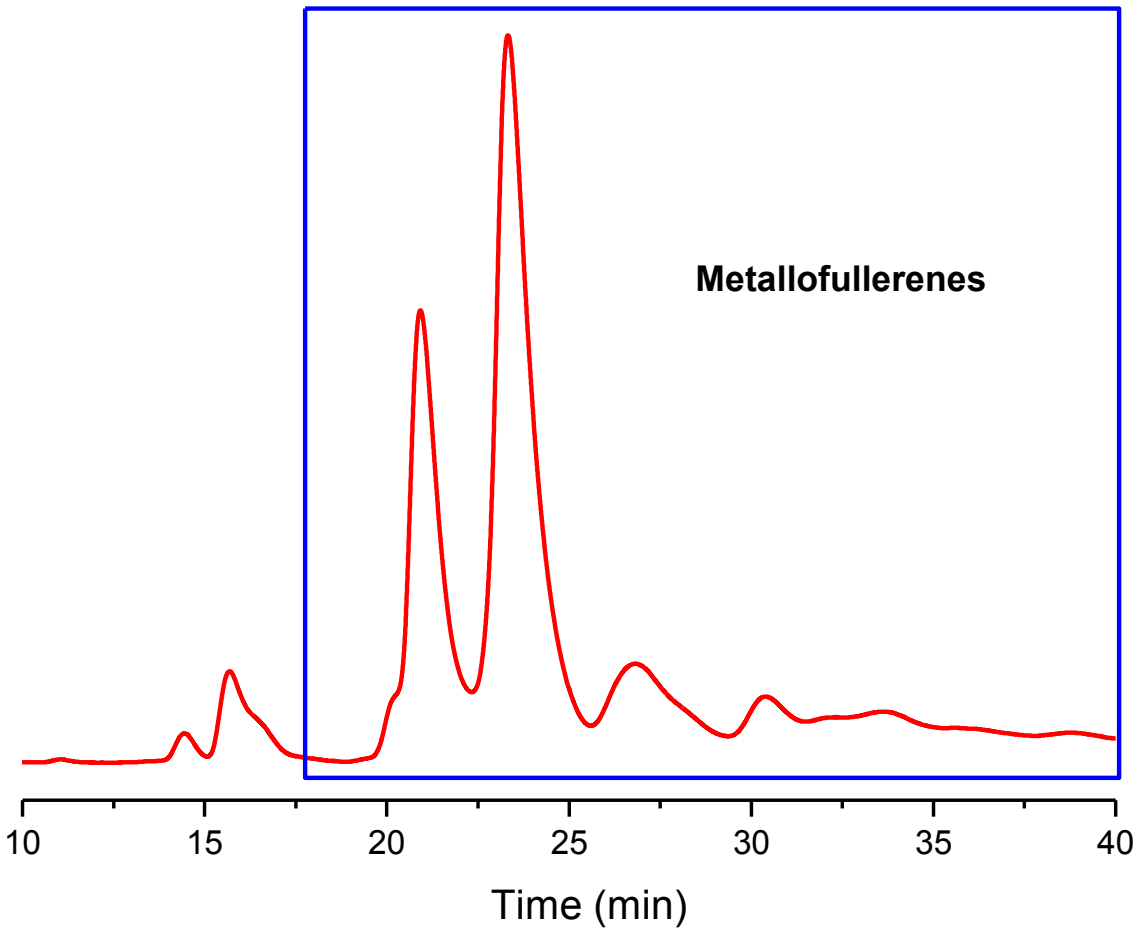


**Figure 7.2**. HPLC chromatogram of the extracted fullerenes during the sulfur containing gas experiment. Solvent: toluene; Column: Buckyprep-M, detection: 372 nm.

Figures 7.1 and 7.2 show the MALDI-TOF MS and HPLC chromatogram of the extracted fullerenes. From these analyses it can be inferred that compounds of general formula $Sc_2SC_{2n}$ are formed. The endohedral character of the metallic moiety is still not confirmed. However, EDS analysis of a collected sample from the HPLC shows the presence of sulfur in the sample as indicated in Figure 7.3.

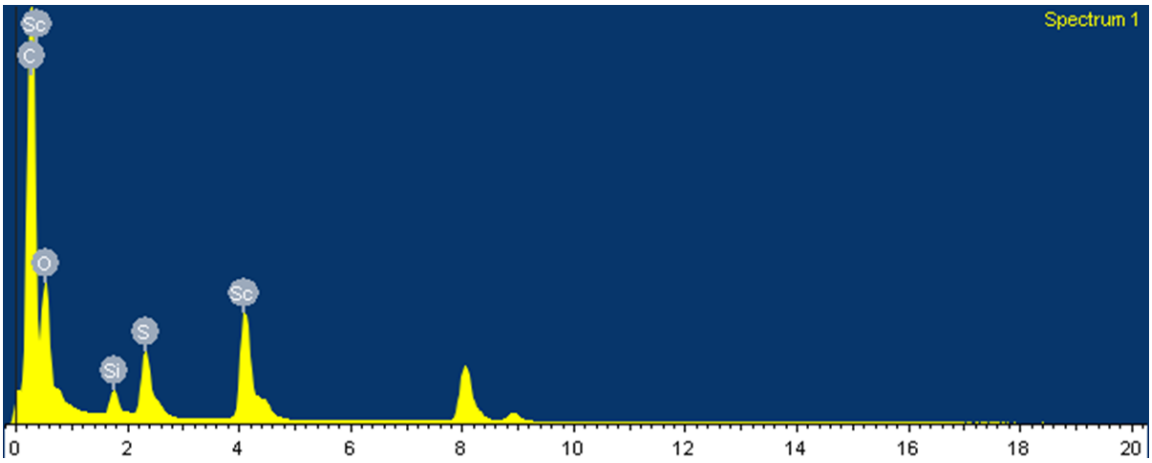


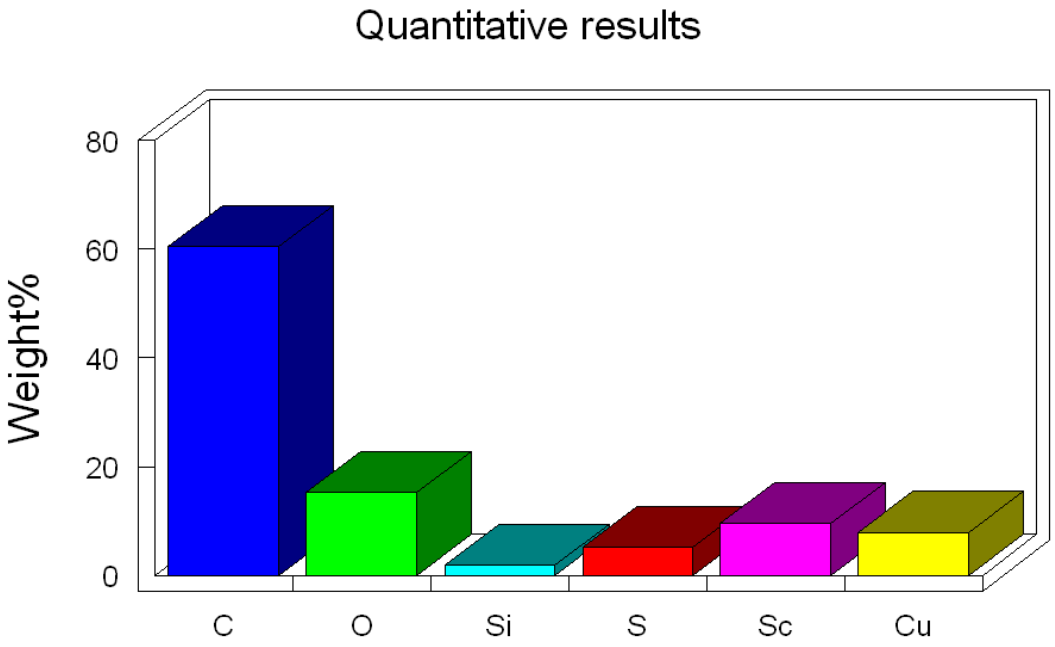


**Figure 7.3**. Energy Dispersive Spectroscopy (EDS) spectrum of a fraction collected from the HPLC chromatogram obtained from the extracted EMFs after the sulfur containing experiment. Copper and silisium are coming from the grid and sample holder. Oxygen is probably coming from the solvent used to manipulate the sample (ether).

These preliminary results are promising and should be extended in the future. Further work should be expanded to obtain larger amounts of these compounds in order

to fully characterize them, especially by X-ray diffraction to determine the endohedral character of the sulfur.

On the other hand, not only the central atom of the cluster can be changed, as it was suggested previously, but also the metallic nature of the entrapped moiety. Recently Dunsch and co-workers reported the synthesis of an endohedral titanium (III) in a fullerene cage.[3] As mentioned earlier, the encaged metals for all reported metallic nitride EMFs are limited to group III (Sc, Y and lanthanides) metals. Therefore the encapsulation of titanium (III) represents the first non-group III metal that is successfully encapsulated inside a fullerene cage. These results open the possibility of the encapsulation of many other metals from the transition metal series inside fullerenes thus widening the potential use of these compounds in many areas.

In the past years organic photovoltaics (OPVs) has become a very attractive field of research for their potential use in solar energy conversion. However, OPVs efficiencies are very low (lower than 10%), and these low efficiencies are partly due to the energy mismatch between the donor and acceptor materials used in OPV devices. In other words, the molecular orbitals involved in the electron transfer of the donor and the acceptor should match in energy in order to obtain better efficiencies.

With this in mind, it is interesting to explore the synthesis of novel acceptor materials with LUMO energies closer to that of the donor, in this case, metallic nitrides EMFs are appealing compounds whose first reduction potentials (~-1.22 to -1.55V) are around 280 mV larger than those observed for empty fullerenes. Based on the systematic electrochemical analysis reported in this thesis novel acceptor materials can be explored

based on the EMFs studied in this thesis. For instance, Dress and co-workers reported a considerable reduction in energy losses during the charge transfer process using acceptors based on $Lu_3N@C_{80}$ and a larger efficiency than the reported for $C_{60}$-PCBM, a traditional acceptor used in OPVs.[4] A recently reported ferrocene adduct of $Sc_3N@C_{80}$,[5] for which photoinduced electron transfer between the ferrocene moiety and the fullerene was detected, showed that the radical ion pair was significantly stabilized relative to the analogous ferrocene-$C_{60}$ dyad. Therefore, the potential use of metallic nitride EMFs in the field of photovoltaics seems promising.

Aside from the large range of HOMO-LUMO gaps exhibited by these compounds, some show very interesting electronic and electro-optical properties which have widened their potential applications. However, only a few reports of the full incorporation of endohedral metallofullerenes in nanoelectronic devices have been published so far.

Fullerenes, in particular higher order ones ($C_{70}$ and above) usually show large Non Linear Optical (NLO) responses, due to their highly polarizable π-electron cloud. In metallofullerenes, the charge transfer between the encapsulated moiety and the cage leads to an even larger π-electron density on the cage (six electron transfer in the case of metallic nitride EMFs), and therefore these compounds are expected to show even better NLO properties. These properties have been either measured or calculated with DFT for some metallofullerenes.[6] Encapsulation of one metal seems to result effectively in enhancement of NLO properties of fullerenes such as $C_{74}$[6c] and $C_{82}$.[6b,d] However, the size of the metal encapsulated is an important factor, and large metals, such as La, are

preferable to smaller ones like Sc.[6e] In the case of metallic nitride EMFs no reports on the NLO properties have been published so far. Therefore the NLO properties of metallic nitride EMFs based on the larger metals such as Nd, Pr, Ce and La should be addressed in the future.

Although the aforementioned potential applications of metallic nitride EMFs are almost unexplored, there is also a lot of fundamental research that needs to be addressed, for example, the structural characterization of EMFs with cages larger than $C_{88}$. It was shown in this thesis that larger metals are preferentially encapsulated inside larger cages, however, nothing is known about the structures of these large EMFs. Attempts to crystallize metallic nitride EMFs of the type $M_3N@C_{96}$, $M_3N@C_{92}$, and $M_3N@C_{88}$ have been unfruitful so far, most likely because of the small amount of available. Previous results have shown that in the case of the $Pr_3N@C_{2n}$ family, the metallic nitride cluster is diamagnetic, therefore it is possible to conduct NMR studies with these compounds. Electron paramagnetic resonance (EPR) studies on ionized samples of the $Pr_3N@C_{2n}$ family should be also attempted in order to understand the electronic distribution for these compounds. At the time this thesis is being written, the chemical properties of the larger metallic nitride EMFs remain totally unexplored so these remain as future avenues with potential interesting and useful applications to pursue.

The mentioned future directions are just a few examples of the many unanswered questions in this interesting field and clearly show that EMFs remain as challenging, fascinating and still largely unexplored compounds.

## References


[1] Chaur, M.N.; Melin, F.; Ortiz, A.L.; Echegoyen, L. *Angew. Chem. Int. Ed.* **2009**, 48, 7514-7538.

[2] Ge, Z.; Duchamp, J.C.; Cai, T.; Gibson, H.W.; Dorn, H.C. *J. Am. Chem. Soc*. **2005**, 127, 16292-16298.

[3] Yang, S.; Chen, C.; Popov, A.A.; Zhang, W.; Liu, F.; Dunsch, L. *Chem. Commun*. **2009**, 6391-6393.

[4] Ross, R.B.; Cardona, C.M.; Guldi, D.M.; Sankaranarayanan, S.G.; Reese, M.O.; Kopodakis, N.; Peet, J.; Walker, B.; Bazan, G.C.; Keuren, E.V.; Holloway, B.C.; Drees, M. *Nature Materials*, **2009**, 8, 208-212.

[5] Pinzon, J.R.; Plonska-Brzezinska, M.E.; Cardona, C.M.; Athans, J.A.; Gayathri, S.S.; Guldi, D.M.; Herranz, M.A.; Martin, N.; Torres, T.; Echegoyen, L. *Angew. Chem. Int. Ed*. **2008**, 47, 4173-4176.

[6] a) Huang, H.; Gu, H.; Yang, S.; Fu, J.; Yu, P.; Wong, G.K.; Du, Y. *Proc. Electrochem. Soc.* **1997**, 401-407; b) Gu, G.; Huang, H.; Yang, S.; Yu, P.; Fu, J.; Wong, G.K.; Wan, X.; Dong, J.; Du, Y. *Chem. Phys. Lett.* **1998**, 289, 167-173. c) Hong, C.; Ji-Kang, F.; Xin, Z.; Ai-Min, R.; Qua, J.; Goddard, J.D. *THEOCHEM* **2003**, 629, 271-277; d) Xenogiannopoulou, E.; Couris, S.; Koudoumas, E.; Tagmatarchis, N.; Inoue, T.; Shinohara, H. *Chem. Phys. Lett.* **2004**, *394*, 14-18; e) Hu, H.; Cheng, W.D.; Huang, S.P.; Xie, Z.; Zhang, H. *Journal of Theoretical & Computational Chemistry* **2008**, 7, 737-749.